Photometric Mass Determinations of Eclipsing Cataclysmic Variables

Martin J. McAllister

Department of Physics & Astronomy
The University of Sheffield

A dissertation submitted in candidature for the degree of
Doctor of Philosophy at the University of Sheffield

September 2017

Declaration

I declare that no part of this thesis has been accepted, or is currently being submitted, for any degree or diploma or certificate or any other qualification at this University or elsewhere.

This thesis is the result of my own work unless otherwise stated.

The following Chapters have been based on publications:

Chapter 4 - McAllister et al. (2015)

Chapter 5 - McAllister et al. (2017a)

Chapter 6 - McAllister et al. (2017b)

Summary

Cataclysmic variables (CVs) are a type of close, interacting binary system containing a white dwarf primary and a low-mass, Roche lobe-filling secondary/donor. Mass is commonly transferred from the donor to an accretion disc around the white dwarf, due to the conservation of angular momentum, before eventually reaching the surface of the white dwarf. A region of increased luminosity, termed the 'bright spot', exists at the intersection of accretion disc and mass transfer stream. The transfer of mass within the system is a turbulent process, giving rise to random photometric variations commonly referred to as 'flickering'.

For high inclination systems, the donor eclipses all other components within the system, resulting in complex eclipse light curves that can be fit with a parameterised model to obtain system parameters. Eclipses of the white dwarf and bright spot occur in quick succession, and therefore precise eclipse modelling requires high-time-resolution photometry. Flickering is a hindrance to eclipse modelling, however, as it can obscure ingress/egress features of the component eclipses, and therefore existing studies use eclipse averaging to minimise its effects. In this thesis, a new approach to eclipse modelling is introduced, which involves modelling flickering through the utilisation of Gaussian processes (GPs).

The new modelling approach is implemented on ULTRACAM/ULTRASPEC eclipse light curves of 18 eclipsing CVs, returning 18 sets of precise system parameters. Four of these systems have been modelled previously using the existing approach, while 14 are modelled for the first time. The 18 new/revised white dwarf and donor masses from this work are used alongside other CV component masses from the literature in an attempt to secure a better understanding of CVs and their evolution. One of the outcomes is a new estimate for the CV orbital period minimum, 79.57 ± 0.22 min, which is over 2 min shorter than previously thought.

Acknowledgements

I would like to begin by thanking my supervisor, Stuart Littlefair. Without all of your invaluable help, guidance, support, and incredible knowledge, I genuinely could not have made it to this point. Additional thanks to Vik Dhillon and Tom Marsh, as if it weren't for your dedication towards the instrumentation and software behind ULTRACAM/ULTRASPEC, none of this work would have been possible. Thank you to Liam Hardy for the many in-depth discussions we've shared, from which I've learned so much. Our work together has been one of the most rewarding aspects of the PhD. Also, a big thank you to Paul Kerry for all your IT expertise and help throughout the years.

I would like to acknowledge the Science and Technology Facilities Council (STFC) for providing the funding for this PhD. Also, the Isaac Newton Group (ING), European Southern Observatory (ESO) and National Astronomical Research Institute of Thailand (NARIT) for the use of their observing facilities.

A huge thank you to everyone who has been a part of these past four years, and who have in some way or another helped get me across the finish line. Special thanks to Manu Bernhard, Rob Spence, Dan Griffiths and Dave Sahman for the many great laughs we've shared, and for keeping me sane throughout this whole process. Thanks to Saida Caballero, Chris Rosslowe, Pavel Lee, Patricia Bessiere, Marvin Rose, Steven Parsons, Martin Dyer, Katie Tehrani, Claire Esau, Héloïse Stevance, Becky Arnold, Jonny Pierce and the rest of the Sheffield Astro group for making my time as a PhD student both enjoyable and memorable. I will miss

working with you all.

Thanks to Rekha Wilson for your support and invaluable proof reading, for which I am very grateful. Thanks to Amber Wilson for the endless help and advice you have given me over the past few years, and for just generally being such an amazing person. I'm excited for what's to come my love. Last but not least, I would like to thank my family and friends for your continued encouragement. In particular my sister Nicola and my Mum and Dad; for who I am so grateful to be able to call my parents. Without your unconditional support and belief in me, none of this would have been possible. Thank you for everything.

Contents

List of Figures

List of Tables

Chapter 1

Introduction

1.1 Cataclysmic Variables

1.1.1 CV Structure

Cataclysmic variables (CVs) are a type of close, interacting binary system. They contain a white dwarf primary and a low-mass secondary, most commonly a red dwarf star. The secondary star's radius is sufficiently large enough for it to fill its Roche lobe, allowing for the transfer of material/gas from the secondary to the white dwarf via the inner Lagrangian point (L1) (see Section 1.1.2). The secondary acts as the donor in CV systems, and is frequently referred to as the 'donor' star throughout this work.

In systems with a non- or weakly-magnetic white dwarf, the transferred material cannot immediately reach the white dwarf due to the need to conserve angular momentum, so instead forms an accretion disc around it. Material in the disc gradually makes its way inwards towards the white dwarf, where it is eventually accreted (see Section 1.1.3 for further details).

The gas stream from the secondary makes contact with the outer edge of the accretion disc. With stream and disc material travelling at different velocities, collisions between the two release large amounts of energy. This is observed as a region

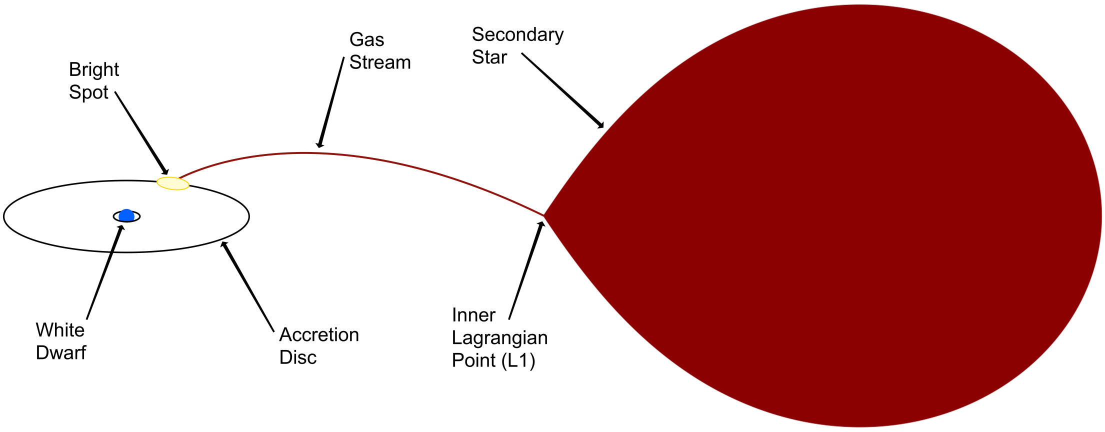

Figure 1.1: A schematic diagram showing the main components of a typical non-magnetic CV system.

of increased luminosity at the intersection of disc and stream termed the bright spot. Figure 1.1 shows the structure of a typical non-magnetic CV system in schematic form.

The transfer of mass from the donor, through the accretion disc, and onto the surface of the white dwarf is a turbulent process, which gives rise to random photometric variations in the light emitted by a CV. To an observer, these photometric variations from mass transfer within the system make a CV appear to 'flicker', and are therefore commonly referred to as 'flickering' (Warner, 1995). Flickering is discussed further in Section 3.3.

In systems with strong magnetic white dwarfs, the gas stream from the secondary can travel down the magnetic field lines of the white dwarf, directly onto its surface. Such systems do not possess an accretion disc and their nature is discussed further in Section 1.2.6.

1.1.2 Roche Lobe Geometry

The proximity of the primary and secondary within a CV system enables them to tidally interact with each other. From early on in the lifetime of a CV, tidal interactions establish synchronisation of the secondary, in addition to the removal of any existing binary eccentricity (Warner, 1995). All CVs therefore possess circular orbits, enabling their orbital motion to be described by Kepler's 3rd law,

$$P_{\mathrm{orb}}^2 = \frac{4\pi^2 a^3}{G(M_1 + M_2)}, \tag{1.1}$$

where P_{orb} is the orbital period, a is the binary separation, G is the gravitational constant and M_1, M_2 are the masses of the primary and secondary, respectively. As CVs typically have orbital periods of a few hours and masses of order $M_1 = 1\,\mathrm{M}_\odot$, $M_2 = 0.1\,\mathrm{M}_\odot$, a typical CV separation is of the order $1\,\mathrm{R}_\odot$.

It is clear from Figure 1.1 that while the white dwarf is spherical, the secondary appears misshapen. To understand why this is the case, we need to consider Roche equipotentials, lines of equal potential that exist around a rotating binary system. By considering a set of cartesian coordinates (x, y, z) in the frame of the rotating binary – with origin at the primary, x-axis along line of separation, y-axis in the direction of orbital motion and z-axis perpendicular to the orbital plane – the potential at any point within the system (Φ) can be determined through:

$$\Phi = -\frac{GM_1}{(x^2 + y^2 + z^2)^{1/2}} - \frac{GM_2}{[(x-a)^2 + y^2 + z^2]^{1/2}} - \frac{2\pi^2}{P_{\mathrm{orb}}^2}[(x - \mu a)^2 + y^2], \tag{1.2}$$

where $\mu = M_2/(M_1 + M_2)$. Equation 1.2 is comprised of the potential contribution from the primary (first term), the potential contribution from the secondary (second term), and the potential arising from centrifugal force (third term).

Roche equipotentials in the x-y plane are shown in Figure 1.2. Close to the centre of each component the equipotentials are spherical, but moving further out this is no longer the case due to the gravitational effect from the other body. The largest closed equipotential is called the Roche lobe, and represents the spatial limit within which a star can be contained. In CVs, the radius of the secondary is sufficiently large for it to fill its Roche lobe and consequently takes its shape. The point at which the Roche lobes of each component meet is referred to as the inner Lagrangian point

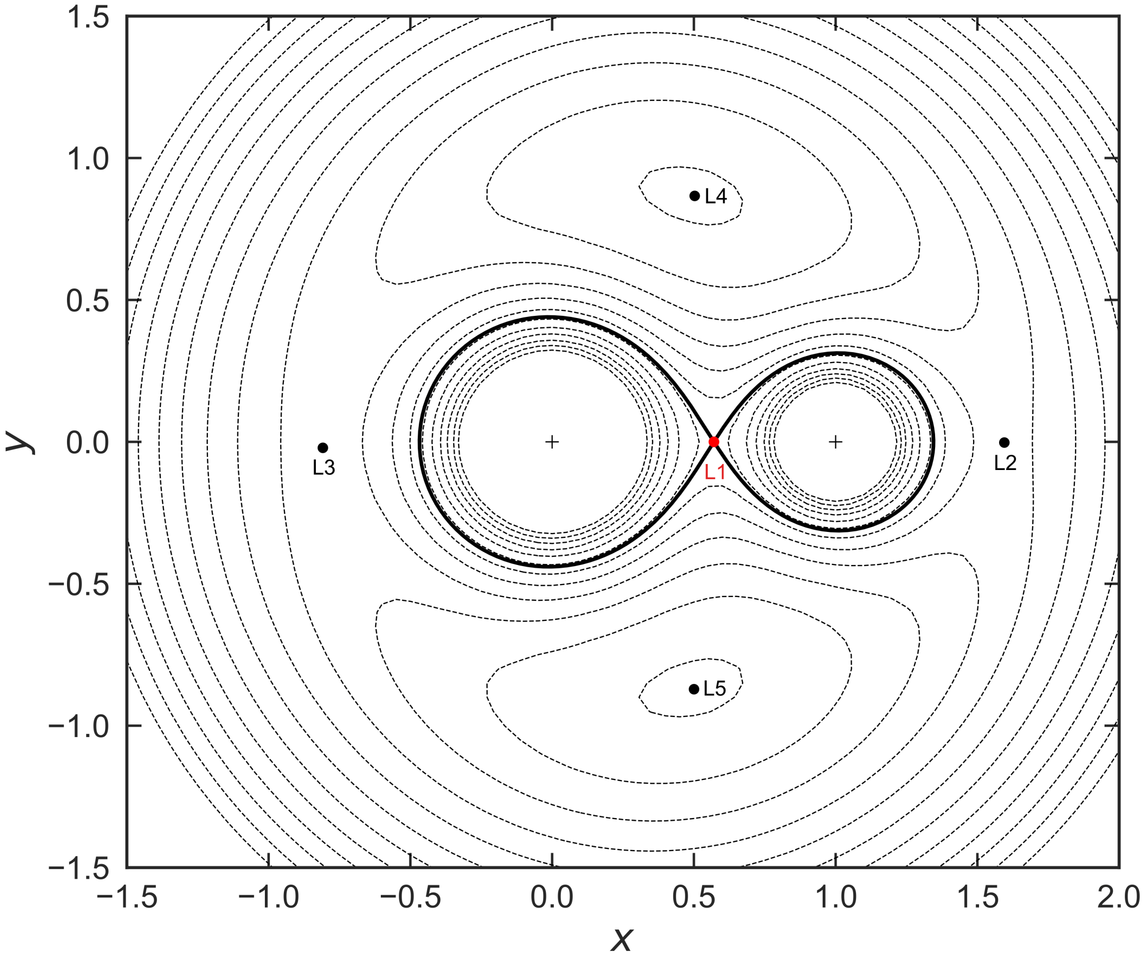

Figure 1.2: Roche equipotentials in the x-y plane. The crosses at (0,0) and (1,0) represent the centres of the primary and secondary, respectively. The black line indicates the Roche lobe. The red point shows the location of the inner Lagrangian point (L1), while the black points represent the locations of additional Lagrangian points (L2–5).

(L1), and it is from here that material from the secondary leaves its own Roche lobe and enters the primary's. The shape of the Roche lobe is dependent only on the mass ratio (q) of the CV (defined as $q = M_2/M_1$), while the scale is dependent on a. The volume-equivalent radius ($R_{\rm L}$) of the secondary's Roche lobe can be approximated by

$$\frac{R_{\rm L}}{a} = \frac{0.49q^{2/3}}{0.6q^{2/3} + \ln(1 + q^{1/3})}, \tag{1.3}$$

valid for all values of q and accurate to $< 1\%$ (Eggleton, 1983), or alternatively:

$$\frac{R_{\rm L}}{a} = 0.47 \left(\frac{q}{1+q} \right)^{1/3}, \tag{1.4}$$

valid for $0.01 < q < 1.0$ and accurate to 3% (Paczyński, 1971; Smith & Dhillon, 1998). Although slightly less accurate, this latter expression for $R_{\rm L}$ is much simpler and easier to manipulate than equation 1.3. As the secondary fills its Roche lobe, $R_{\rm L}$ can be used as a reliable measurement of the secondary's radius. The mean density of a Roche lobe-filling secondary is therefore:

$$\langle \rho_2 \rangle = \frac{3M_2}{4\pi R_{\rm L}^3}. \tag{1.5}$$

This can be combined with equations 1.1 and 1.4 to form the following period-density relationship for stars filling their Roche lobe

$$\langle \rho_2 \rangle = \frac{3M_2}{4\pi R_2^3} \simeq 1.05 \times 10^5 \, P_{\rm orb}^{-2}, \tag{1.6}$$

where $P_{\rm orb}$ is in units of hrs and $\langle \rho_2 \rangle$ in units of $\rm kg\,m^{-3}$.

1.1.3 Accretion in CVs

Accretion is not unique to CVs, and is observed in numerous types of objects throughout the Universe, from protostars to active galactic nuclei (AGN). CVs provide arguably the best opportunity for studying the physics of accretion, however, due to their proximity and relative clarity (Hellier, 2001).

Mass supplied to the accretion disc from the donor star begins in an orbit towards the outermost edge of the disc, then gradually migrates radially to smaller orbits. However, for this to be possible there must be a property of the disc which allows mass to lose both angular momentum and gravitational potential energy. This property is viscosity, and enables mass to flow inwards through the disc, with angular momentum moving in the opposite direction. Viscosity arising from interactions on a molecular scale alone cannot explain observed CV accretion rates, mainly due to the diffuse nature of accretion discs (Warner, 1995). An additional source of viscosity in discs is thought to be due to turbulence, which involves the movement of mass to different radii via random eddies. The idea of turbulent viscosity led to Shakura & Sunyaev (1973) proposing the ‘alpha disc’ model, which handles viscosity ν through the introduction of a free parameter α:

$$\nu = \alpha c_{\mathrm{s}} H, \tag{1.7}$$

where c_{s} is the sound speed in the disc, and H is the disc scale height. No turbulent eddies within the disc can be larger than H or have velocities greater than c_{s}, so $c_{\mathrm{s}}H$ is treated as the viscosity limit. α can therefore take any value between 0 and 1. CV accretion discs (in quiescence) have $\alpha \sim 0.01$–0.05 (Hellier, 2001).

Approximately half of all the gravitational potential energy lost by mass moving to smaller orbits is emitted as light, giving rise to a luminous disc. This is otherwise known as accretion luminosity. The remaining fraction is converted into kinetic energy, as mass at smaller radii have higher Keplerian velocities, and results in the innermost edge of the disc containing mass with the highest velocities. These velocities are an order of magnitude higher than the rotational velocity of the white dwarf surface, so mass must lose kinetic energy and decelerate before it can be accreted. The region of deceleration between the white dwarf surface and inner disc is called the boundary layer, and can be especially luminous given the large amounts of kinetic energy that is radiated away as light.

If the rate at which mass entering each orbit equals that of mass leaving, the disc is said to be in a 'steady state'. For an orbit at radius r in a steady-state disc: temperature $T \propto r^{-3/4}$ and luminosity $L \propto T^4 r^2 \propto r^{-1}$. Both temperature and luminosity should therefore decrease for orbits at larger radii (Warner, 1995). Interestingly, CV accretion discs only display this temperature distribution when in outburst (discussed further in Section 1.2.3), whereas there is a much flatter distribution observed in quiescent discs. This is most likely due to the presence of an optically thin component to the disc during quiescence[1] (Horne & Cook, 1985; Wood et al., 1986).

1.2 Types of CV

Cataclysmic variables are named as such due to their innate tendency to exhibit drastic increases in brightness over a wide range of amplitudes and timescales. The observed variation in these cataclysmic events has multiple origins, with the possibility for both eruptions on the surface of the white dwarf and outbursts within the accretion disc to occur. The differing nature of these events can be used – along with other intrinsic properties – to categorise CVs.

1.2.1 Classical Novae

Classical novae (CNe) are a category of CV systems for which a solitary nova eruption has been observed. Nova eruptions are the most extreme event inherent to CVs and can temporarily increase a system's brightness by anywhere between 6 to 19 magnitudes (Warner, 1995). Novae can be either fast, lasting for a few days with

---

[1] The optically thin component is also responsible for the observation of emission lines in quiescent CV spectra.

large eruption amplitudes, or slow, lasting for much longer (hundreds of days) along with smaller eruption amplitudes (Warner, 1995). The number of Galactic novae per year is estimated at ~ 50, although this is many more than are actually observed as a high proportion are thought to originate in the Galactic plane and consequently obscured by dust (Shafter, 2017).

The origin of a nova eruption is at the boundary between the degenerate core of the white dwarf and the newly accreted, hydrogen-rich surface layer. The high gravity of the white dwarf, coupled with a substantial amount of accreted hydrogen create a region of very high density at the base of the surface layer. As a consequence, the material at the boundary is degenerate, forcing electrons into higher energy levels and increasing the temperature. The temperature eventually becomes sufficiently high enough for nuclear reactions to commence, which increases the temperature further, leading to higher reaction rates. The degenerate nature of the material means there is no expansion in response to an increase in temperature and therefore no cooling. With no cooling possible, there is a runaway increase in temperature, culminating in the point where the gas pressure exceeds the degeneracy pressure, removing the degeneracy and giving way to a violent expansion. As this expansion surpasses the escape velocity of the white dwarf, the hydrogen surface layer is ejected, whilst being further energised by the decay of the radioactive products from the nuclear reactions (Warner, 1995).

The amount of accreted hydrogen required before a thermonuclear runaway occurs is highly dependent on the mass of the white dwarf. High-mass white dwarfs have higher surface gravity and therefore don't need as much accreted hydrogen in order to create the densities required. For example, a white dwarf with a high mass of $1.3\,\mathrm{M}_\odot$ requires approximately $3 \times 10^{-5}\,\mathrm{M}_\odot$ of accreted hydrogen, which would take of order 10 000 yrs with a typical mass transfer rate of $10^{-9}\,\mathrm{M}_\odot\,\mathrm{yr}^{-1}$. Alternatively, a white dwarf with a low mass of $0.6\,\mathrm{M}_\odot$ requires approximately $5 \times 10^{-3}\,\mathrm{M}_\odot$, taking of order millions of years. Importantly, this is much less than the typical lifetime of a CV, so all CVs must undergo multiple nova eruptions in their lifetime (Hellier, 2001).

1.2.2 Recurrent Novae

There are a total of 10 systems within the Galaxy that have been observed to undergo two or more nova eruptions (Schaefer, 2010), and are referred to as recurrent novae (RNe). Considering that comprehensive novae records only date back one and a half centuries, all known RNe must have recurrence times no greater than $\sim 100\,\mathrm{yrs}$. Such a rapid nova cycle requires a high-mass white dwarf and a significantly higher than average mass transfer rate of $\sim 10^{-7}\,\mathrm{M}_\odot\,\mathrm{yr}^{-1}$. Although there is a high probability that some CNe have undergone additional, unobserved nova eruptions since their discovery, the small number of known RNe is evidence that systems with these specific characteristics are rare.

Based on orbital period, RNe can be put into three categories: very short periods ($< 8\,\mathrm{h}$), periods of order $1\,\mathrm{d}$ and periods of order $1\,\mathrm{yr}$ (Schaefer, 1990; Schaefer & Ringwald, 1995). The two known RNe with periods $< 8\,\mathrm{h}$ (T Pyx and IM Nor) contain low-mass main sequence donors like the majority of CNe, while those with longer periods contain either sub-giant or giant donors. RNe with main sequence donors are thought to be in unsustainable, temporary states of high mass transfer, driven by the heating of the donor by a very hot white dwarf undergoing steady hydrogen burning – otherwise known as a super-soft X-ray source (Knigge, King & Patterson, 2000; Schaefer, Pagnotta & Shara, 2010). RNe with evolved donors have their high mass transfer rates driven by expansion of the donor and will continue to be RNe for the foreseeable future (Schaefer, 2010).

1.2.3 Dwarf Novae

The other type of cataclysm a CV can undergo is a dwarf nova (DN) outburst. These events cannot reach the same energies, and therefore outburst amplitudes, as nova eruptions (hence the *dwarf* prefix), but are still able to increase the brightness of a system between 2 to 5 magnitudes (Warner, 1995). DN outburst lengths are comparable to the fastest CNe ($< 20\,\mathrm{d}$), but with much shorter recurrence times, ranging from days to decades (Warner, 1995). Any CVs observed to have undergone a DN outburst – but with no record of a nova eruption – are classed as dwarf novae (DNe); also known as U Geminorum (U Gem) stars after the first such system observed.

Disc Instability Model

DN outbursts arise from a brightening of the accretion disc, triggered by increases in the rates of both mass transfer through the disc and accretion onto the white dwarf. Osaki (1974) was the first to put forward a model – based on disc instability – to successfully explain the origin of DN outbursts. Only the fundamentals of the disc instability model are discussed here, see Cannizzo (1993), Osaki (1996) and Lasota (2001) for in-depth reviews.

More precisely, it is a thermal instability within the disc that drives cycles from quiescence to outburst and back again. Figure 1.3 shows the thermal equilibrium curve in surface density (Σ) and temperature (T) parameter space for an accretion disc annulus. The thermal equilibrium curve forms the shape of an ‘S’, and illustrates the thermal instability cycle that is responsible for DN outbursts – the bottom and top ‘rungs’ representing quiescence and outburst, respectively.

In quiescence, a disc annulus is stable, with low temperature, surface density and viscosity ($\alpha \sim 0.01$–0.05), and is therefore situated on the bottom rung of the S-curve in Figure 1.3. The low α value associated with viscosity in quiescence results in a low mass transfer rate through the annulus, and mass accumulates. This build-up results

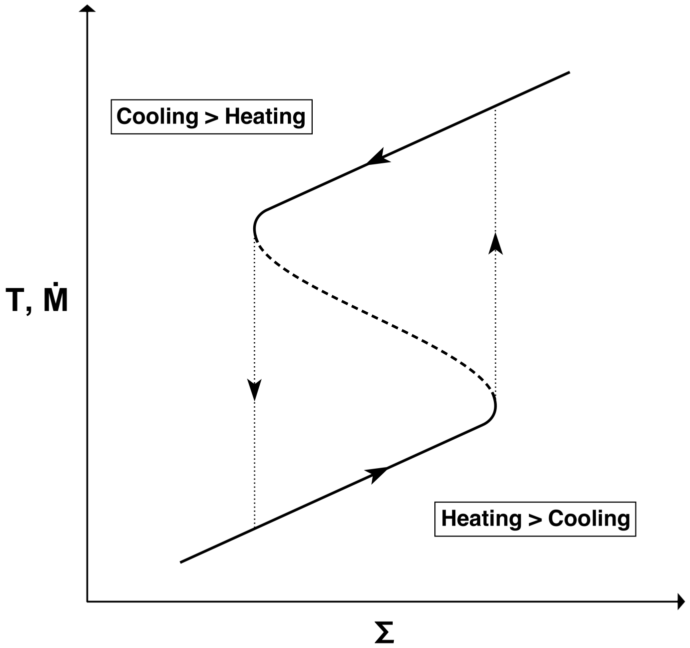

Figure 1.3: Thermal equilibrium curve – representing the thermal instability cycle – in surface density (Σ) and temperature (T) parameter space for an accretion disc annulus.

in an increase in both surface density and temperature, and the annulus moves up the bottom rung of the S-curve. The annulus typically spends the majority of its time in this phase of the DN outburst cycle. Once temperatures reach $\sim 7000\,\mathrm{K}$ and hydrogen starts becoming partially ionised, the thermal instability initiates, resulting in a dramatic increase in temperature, which sends the annulus onto the top rung in Figure 1.3.

The annulus is once again in a stable state, but is now in outburst, with a significantly higher temperature, viscosity ($\alpha \sim 0.1$–0.5, Hellier 2001) and now contains fully ionised hydrogen. Even with a similar α value, viscosity is increased in outburst due to an increased value of c_{s} (see equation 1.7), a consequence of higher temperatures. However, a larger α value is also inferred during outburst, and is thought to be linked with a magnetorotational instability – otherwise known as the Balbus-Hawley instability (Balbus & Hawley, 1991, 1992a,b, 1994). Briefly, the Balbus-Hawley instability arises due to the presence of fully ionised hydrogen in the disc, which couples to magnetic field lines and in doing so increases the ease at which material can move radially through the disc.

Once one annulus enters outburst, those that are adjacent follow suit, and so on until the entire disc is in an outburst state. The rate of mass transfer through the disc is increased, and accretion onto the white dwarf occurs at a much higher rate than at quiescence. The rate of mass leaving the disc is typically greater than that supplied by the donor, so the annuli within the disc begin to gradually decrease in both surface density and temperature, and consequently slide down the top rung in Figure 1.3. Once a temperature is reached where recombination of hydrogen becomes important, an annulus becomes partially ionised once again. The thermal instability now has the effect of rapidly decreasing the temperature, so the annulus falls back down to the bottom rung and into quiescence. The same domino effect occurs, bringing the entire disc back into quiescence, from where the whole cycle repeats.

Some DNe exhibit departures from the outburst cycle outlined above, and it is variation in outburst behaviour that allows DNe to be split into three sub-groups (after three prototypical systems): SS Cygni (SS Cyg), SU Ursae Majoris (SU UMa) and Z Camelopardalis (Z Cam) stars.

SS Cyg

SS Cyg is one of the earliest known DN and – similar to U Gem – displays outbursts that vary in length, shape and recurrence time but have almost constant amplitudes. It shows no deviations from the standard outburst cycle and similar systems are referred to as SS Cyg stars.

SU UMa

In addition to regular outbursts, some DNe are observed to undergo superoutbursts. These superoutbursts occur less frequently, last longer and have greater amplitudes compared to regular outbursts. They are also synonymous with periodic brightness variations called *superhumps*, which are discussed further in Section 1.5.2. DNe that experience superoutbursts are called SU UMa stars, and notably all have orbital periods $< 3\,\mathrm{h}$.

A superoutburst is initiated when, during a regular outburst, the accretion disc reaches a large enough radius for it to be perturbed by the donor, where a 3:1 tidal resonance between the orbit of material in the disc and the orbit of the donor star can drive the disc elliptical. The required disc radius for such a resonance can only be reached within systems with $q \lesssim 0.33$, which explains – as q scales with orbital period – why only short period systems experience superoutbursts (Hellier, 2001).

The period of time between two successive superoutbursts is called a supercycle, and its structure – numerous regular outbursts followed by a superoutburst – can be explained by the thermal-tidal instability model (Osaki, 1989). During each regular outburst, less material is accreted onto the white dwarf than is supplied to the disc by the donor since the previous outburst, so the disc grows in mass and size. Eventually, the start of a regular outburst pushes the disc to a radius that enables the tidal instability to drive it eccentric, consequently inducing a superoutburst. The additional tidal interactions involved with a superoutburst allow a much higher mass flow through the disc, which significantly drains the disc during the prolonged outburst. The supercycle then begins again, starting from a sufficiently depleted disc.

The supercycle length in a typical system is $\sim 400\,\mathrm{d}$, but some systems exhibit supercycles of just 20–50 d (ER UMa stars), while others have decade-long cycles (WZ Sge stars). The length of the supercycle is related to the mass transfer rate of the system, with short supercycles indicative of a high mass transfer rate and vice versa.

Z Cam

Z Cam stars have very short outburst recurrence times ($< 30\,\mathrm{d}$), which means they go through the outburst cycle very rapidly (Warner, 1995). This is possible due to a high mass transfer rate from the donor that fills up the quiescent disc very quickly. However, Z Cam stars are better known for their long periods of sustained outburst called standstills. These standstills always follow a regular outburst, and it is thought that irradiation of the donor from the disc during said outburst can increase the mass transfer rate entering the disc, enough to sustain a prolonged outburst state. Once the mass transfer rate decreases – possibly due to a starspot passing through the L1 point – the standstill comes to an end and the rapid outburst cycles recommence (Hellier, 2001).

1.2.4 Nova-like Variables

Not all CVs are observed to erupt/outburst, and such systems are referred to as nova-like variables, novalikes (NLs) or even UX UMa stars. The nova-like nomenclature originates from their similarities to CNe in their pre- and post-nova states (Hellier, 2001). It is logical to conclude that they are both the same type of system, but with the majority (current known NLs) yet to undergo an observed nova eruption due to such a short observational baseline. The absence of DN outbursts in NLs can be explained by a sufficiently high mass transfer rate from the donor star that enables the disc to reach and maintain temperatures consistent with those found on the upper rung of the ‘S’-curve in Figure 1.3. The disc is essentially in a permanent outburst state.

The majority of NLs show very little in the way of brightness variations, however a select few – known as VY Scl stars – enter low states in which their brightness can decrease by several magnitudes. These low states are the product of a significant decrease in the mass transfer rate from the donor, again possibly due to a starspot passing through L1 (Livio & Pringle, 1994).

A group of spectroscopically peculiar eclipsing NLs were found by Thorstensen et al. (1991) to share many similar properties, leading to the creation of a new NL sub-group called SW Sex stars (after a member of the group). They are among the most luminous NLs, and therefore have the highest mass transfer rates, although the cause of this cannot yet be fully explained. Systems showing SW Sex star traits have since been discovered over a wide range of inclinations, making the class no longer exclusive to eclipsers. They currently make up approximately 40% of the entire NL population, which rises to 50% when just focussing on the 3–4.5 h orbital period range (Rodríguez-Gil et al., 2007; Rodríguez-Gil, Schmidtobreick & Gänsicke, 2007). As further SW Sex stars are found or identified from the existing NL population, it is expected for them to make up the majority of systems in the 3–4.5 h period range, with consequences for our understanding of CV evolution (see Section 1.4).

1.2.5 Helium-rich Systems

There exists a rare subgroup of CVs – known as AM CVn stars – that contain a donor rich in helium rather than hydrogen. The different composition of their donor make them ultracompact systems with short orbital periods (<65 min). The helium donor can either be a less-massive helium white dwarf, a semi-degenerate helium star or the core of a heavily-evolved main sequence star. AM CVn systems containing the latter are the final evolutionary state of CVs with a donor that evolves off the main sequence prior to the start of mass transfer (Podsiadlowski, Han & Rappaport, 2003). See Solheim (2010) for an in-depth review of AM CVn stars.

1.2.6 Magnetic Systems

Systems containing strongly magnetic white dwarfs with field strengths of order 10–100 MG are known as polars or AM Her stars. The accretion stream from the donor, instead of forming a disc, follows the magnetic field lines directly onto the white dwarf. The interaction between both star's magnetic fields enables synchronous rotation, where the spin of the white dwarf is matched to the orbital motion of the system. There are an additional class of magnetic CVs called intermediate polars (also referred to as DQ Her stars), which as their name suggests have intermediate strength (1–10 MG) magnetic white dwarfs. These field strengths are not sufficient for synchronous rotation and the smaller magnetosphere surrounding the white dwarf can allow a partial disc to form. The rest of this work will only focus on CVs with non- or weakly-magnetic white dwarfs.

1.3 CV Formation

1.3.1 CV Progenitors

The progenitors of CVs are low- to intermediate-mass main sequence binaries with wide separations, significantly larger than the typical CV separation. The more massive of the two stars in the binary – defined as the primary – is the first to experience core hydrogen depletion, and consequently evolves off the main sequence. It ascends the red-giant branch (RGB) while hydrogen shell burning commences, a process that leads to the expansion of the star's outer layers. This dramatic increase in radius can result in the red giant primary filling its large Roche lobe, and in doing so initiate an evolutionary phase exclusive to binaries (see Section 1.3.2). In progenitor systems with wider separations – and therefore larger Roche lobes – the red giant may not fill its Roche lobe until it is on the asymptotic-giant branch (AGB), where there is both helium shell and hydrogen shell burning above an inert carbon-oxygen core.

1.3.2 Common Envelope Phase

Approximately 1/4 of all binary systems have initial separations that enable the filling of the primary's Roche lobe (Willems & Kolb, 2004), a situation which leads to the transfer of mass from primary to secondary. Not only is this in the opposite direction compared to mass transfer in CVs, but it is also unstable. This is due to the shrinking of the primary's Roche lobe with response to mass loss, a consequence of the transfer of mass from the more massive to the less massive component in the binary. The primary is not able to adjust as quickly as the contracting Roche lobe, and runaway mass transfer takes place. Mass transfer is discussed in much more detail in Sections 1.4.1 and 1.4.2.

The secondary is subsequently inundated with mass from the primary, arriving quicker than it can be assimilated. The outcome is the rapid formation of a common envelope (CE) that surrounds both the primary's core and the secondary (Paczynski, 1976; Iben & Livio, 1993). The binary – now orbiting within the CE – experiences drag, with both energy and angular momentum transferred from the binary to the CE. The loss of angular momentum from the binary results in a dramatic reduction in binary separation. The increasing energy of the envelope eventually surpasses its binding energy and is ejected from the binary, which now takes on the appearance of a planetary nebula (PN).

1.3.3 Pre-CV Phase

The CE phase is expected to last for no longer than 10^3 yrs (Taam & Sandquist, 2000), which in most cases is short enough to avoid the merger of the two components. What remains after the CE is referred to as a post-common envelope binary (PCEB), typically a close, detached binary consisting of a the remnant degenerate core of the primary (otherwise known as a white dwarf) and a low-mass secondary.

The mass and composition of the white dwarf is heavily dependent on the mass of the initial primary and at what stage it filled its Roche lobe. If this occurs while on the RGB, the white dwarf will be predominantly helium (He-WD) and low mass (0.15–0.50 $\mathrm{M}_{\odot}$). A star that reaches the AGB before filling its Roche lobe will have previously undergone core helium burning whilst on the horizontal branch (HB), resulting in a remnant white dwarf composed of carbon and oxygen (CO-WD) and of a higher mass (0.50–1.10 $\mathrm{M}_{\odot}$). If the initial mass of the primary is between 8–10 $\mathrm{M}_{\odot}$, the core can become sufficiently hot for carbon burning, leaving behind an oxygen-neon white dwarf (ONe-WD) with an even higher mass ($1.10 - 1.44\,\mathrm{M}_{\odot}$). The evolutionary endpoints for stars of mass greater than 10 $\mathrm{M}_{\odot}$ are no longer white dwarfs, as their cores collapse to form either a neutron star or black hole.

Approximately 25–30% of all white dwarf-main sequence binaries are PCEBs (Rebassa-Mansergas et al., 2010, 2012). The PCEB's separation gradually decreases through angular momentum losses (see Sections 1.4.3 and 1.4.4). This has the effect of shrinking the secondary's Roche lobe, eventually coming into contact with the secondary[2]. It is at this point the system becomes a CV, with mass from the secondary transferred to the primary. The progenitors of the present-day CV population ('pre-CVs') can be inferred from those current PCEBs that will reach semi-detached status within the age of the Galaxy (Zorotovic, Schreiber & Gänsicke, 2011).

1.4 CV Evolution

1.4.1 Response to Mass Transfer

Knowledge of the response of CVs to mass transfer is key to understanding CV evolution. The movement of mass between components, invariably to a new distance from the system's centre of mass, requires a response from the binary in order to conserve angular momentum. First, consider the following expression for the total

---

[2] It is also possible for contact to occur through nuclear expansion of the secondary.

angular momentum of a binary (J):

$$J = M_1 a_1 v_1 + M_2 a_2 v_2 = M_1 a_1 \frac{2\pi a_1}{P_{\rm orb}} + M_2 a_2 \frac{2\pi a_2}{P_{\rm orb}}, \tag{1.8}$$

where a_1, a_2 are the distances from the centre of mass and v_1, v_2 are the velocities of the binary components. Through taking advantage of both $a = a_1 + a_2$ and $a_1 M_1 = a_2 M_2$, in addition to the substitution of Kepler's 3rd law (equation 1.1), equation 1.8 can be transformed into

$$J = M_1 M_2 \left(\frac{Ga}{M}\right)^{1/2}, \tag{1.9}$$

where $M = M_1 + M_2$. Differentiating logarithmically (taking natural logs and differentiating with respect to time) and rearranging gives

$$\frac{\dot{a}}{a} = 2\frac{\dot{J}}{J} + \frac{\dot{M}}{M} - 2\frac{\dot{M}_1}{M_1} - 2\frac{\dot{M}_2}{M_2}. \tag{1.10}$$

For the conservative case, where both the total mass and angular momentum within the binary is conserved ($\dot{M} = 0, \dot{M}_1 = -\dot{M}_2, \dot{J} = 0$):

$$\frac{\dot{a}}{a} = 2(q-1)\frac{\dot{M}_2}{M_2}. \tag{1.11}$$

As $P_{\rm orb}^2 \propto a^3$ (equation 1.1), this can also be expressed as

$$\frac{\dot{P}_{\rm orb}}{P_{\rm orb}} = \frac{3}{2}\frac{\dot{a}}{a} = 3(q-1)\frac{\dot{M}_2}{M_2}. \tag{1.12}$$

Equations 1.11 and 1.12 convey how the binary separation and period respond ($\dot{a}, \dot{P}_{\rm orb}$) to mass transfer within the system ($\pm\dot{M}_2$). As mass transfer in CVs is from secondary to primary ($-\dot{M}_2$), systems with $q > 1$ should have their binary separation and period decrease ($-\dot{a}, -\dot{P}_{\rm orb}$) in response to mass transfer, while the opposite should occur for those with $q < 1$.

In addition to the binary separation and period, the response of the secondary's Roche lobe to mass transfer ($\dot{R}_{\rm L}$) must also be considered. Differentiating equation 1.4 logarithmically and substituting for equation 1.11 gives

$$\frac{\dot{R}_{\rm L}}{R_{\rm L}} = \frac{\dot{a}}{a} + \frac{1}{3}\frac{\dot{M}_2}{M_2} = \left(2q - \frac{5}{3}\right)\frac{\dot{M}_2}{M_2}. \tag{1.13}$$

This shows that for CVs with $q < 5/6$, the secondary's Roche lobe increases in response to mass transfer, and therefore continuous mass transfer should not be possible[3]. This directly contradicts the observation that the majority of CVs have $q < 5/6$ and main sequence secondaries, and therefore the assumptions of the conservative case ($\dot{M} = 0, \dot{J} = 0$) must be incorrect. Angular momentum loss from the system has the effect of shrinking the secondary's Roche lobe, counteracting any expansion and enabling mass transfer in CVs with $q < 5/6$. The two mechanisms thought to be responsible for these angular momentum losses are gravitational radiation and magnetic braking, the focus of Sections 1.4.3 and 1.4.4, respectively.

1.4.2 Stability and Timescale of Mass Transfer

The stability and timescale of mass transfer is dependent on the response of both secondary and Roche lobe as mass is lost from the secondary. This response can be expressed as the exponent of a mass-radius relationship, e.g. $R \propto M^{\xi}$. The response of the secondary (ξ) is therefore:

$$\xi = \frac{{\rm d}\ln R_2}{{\rm d}\ln M_2}. \tag{1.14}$$

A similar expression can be constructed for the response of the secondary's Roche lobe ($\xi_{\rm L}$), which combined with equation 1.13 becomes:

---

[3] Unless the radius of the secondary also increases (e.g. nuclear expansion in evolved secondaries).

$$\xi_{\mathrm{L}} = \frac{\mathrm{d}\ln R_{\mathrm{L}}}{\mathrm{d}\ln M_2} = 2q - \frac{5}{3}. \tag{1.15}$$

For stable mass transfer, the response of the secondary must be greater than the response of the Roche lobe ($\xi > \xi_{\mathrm{L}}$), which puts the following stability condition on q (from equation 1.15):

$$q < \frac{1}{2}\xi + \frac{5}{6}. \tag{1.16}$$

The relevant value of ξ to use here is dependent on how the mass loss timescale,

$$\tau_{\mathrm{ML}} = \frac{M_2}{\dot{M}_2}, \tag{1.17}$$

compares to the thermal (Kelvin-Helmholtz) timescale (τ_{KH}), the timescale on which the star reaches thermal equilibrium,

$$\tau_{\mathrm{KH}} \sim \frac{GM_2^2}{R_2 L_2}. \tag{1.18}$$

This is one of two timescales on which the secondary adjusts to mass loss. The other is the dynamical timescale (τ_{dyn}), the timescale on which the star adiabatically reaches hydrostatic equilibrium,

$$\tau_{\mathrm{dyn}} \sim \left(\frac{R_2^3}{GM_2}\right)^{1/2}. \tag{1.19}$$

As $\tau_{\mathrm{KH}} \gg \tau_{\mathrm{dyn}}$, a star reaches hydrostatic equilibrium much quicker than it reaches thermal equilibrium.

If $\tau_{\mathrm{ML}} \gg \tau_{\mathrm{KH}}$, mass loss proceeds slowly, with a thermal-equilibrium response from the secondary analogous to that of a low-mass, main sequence star ($\xi = \xi_{\mathrm{KH}} \simeq 0.8$; e.g. Knigge, Baraffe & Patterson 2011). Inserting this value of ξ into equation 1.16 gives a requirement for thermal stability of $q < 1.23$. Alternatively, if $\tau_{\mathrm{ML}} \ll \tau_{\mathrm{KH}}$, mass loss is rapid and there is instead a dynamical response from the secondary. Secondaries with $M_2 \lesssim 0.43\,\mathrm{M}_\odot$ are deeply convective and therefore $\xi = \xi_{\mathrm{dyn}} \simeq -1/3$ (Paczyński, 1965; Rappaport, Joss & Webbink, 1982), but ξ_{dyn} increases sharply for more massive secondaries ($0.43\,\mathrm{M}_\odot \lesssim M_2 < 0.8\,\mathrm{M}_\odot$) due to the decreasing depth of the convective region. This produces the following dynamical stability limits for q (Hjellming, 1989; Politano, 1996):

$$q = \begin{cases} \frac{2}{3} & M_2 \leq 0.4342\,\mathrm{M}_\odot \\ 2.244(M_2 - 0.4343)^{1.364} + \frac{2}{3} & 0.4342 \leq M_2 < 0.8\mathrm{M}_\odot. \end{cases} \tag{1.20}$$

Consequently, for CVs with $M_2 < 0.8\,\mathrm{M}_\odot$, mass transfer will be stable so long as they have $q \lesssim 2/3$. If this condition is not met, unstable mass transfer will take place on a dynamical timescale, possibly leading to the formation of a second CE phase (see Section 1.3.2). For CVs with $M_2 > 0.8\,\mathrm{M}_\odot$, mass transfer will be stable for those systems with $q < 1.23$, while the remainder will transfer mass on a thermal timescale, and may be responsible for the high mass transfer rates of super-soft X-ray sources (see Section 1.2.2).

1.4.3 Angular Momentum Loss: Gravitational Radiation

Due to their relatively small separations, it is possible for CVs to lose a significant amount of angular momentum through gravitational radiation (Paczyński, 1967; Faulkner, 1971; Webbink, 1976):

$$\frac{\dot{J}_{\mathrm{GR}}}{J} = -\frac{32}{5}\frac{G^3}{c^5}\frac{M_1 M_2 M}{a^4}, \tag{1.21}$$

where c is the speed of light. For a system with $M_1 = 1.0\,\mathrm{M}_\odot$, $M_2 = 0.1\,\mathrm{M}_\odot$ and $P_{\mathrm{orb}} = 1.5\,\mathrm{h}$, gravitational radiation angular momentum loses equate to $\dot{M}_2 \sim -3.7 \times 10^{-11}\,\mathrm{M}_\odot\,\mathrm{yr}^{-1}$ (Warner, 1995). This is towards the lower end of observed mass transfer rates in CVs, but rates can reach orders of magnitude larger than this, especially at longer periods where gravitational radiation is less effective. An additional mechanism for losing angular momentum in CVs is therefore required.

1.4.4 Angular Momentum Loss: Magnetic Braking

The additional mechanism is termed magnetic braking, which – as the name suggests – is associated with the magnetic field of the secondary star. The ionised stellar wind from the secondary follows, and therefore co-rotates with, its magnetic field lines out to radii much larger than that of the secondary. This induces a spin-down torque on the secondary, and ultimately a loss in angular momentum. As the secondary is synchronously rotating with the primary due to tidal forces, angular momentum is not only lost from the secondary, but from the whole system.

Conventionally, magnetic braking was thought to contribute to angular momentum loss in partially radiative secondary stars only, following the belief that the origin of the magnetic field is the tachocline – the interface between the radiative core and convective envelope (MacGregor & Charbonneau, 1997; Charbonneau & MacGregor, 1997). The change in the secondary star from partially radiative to fully convective, and the subsequent cessation of magnetic braking, was long considered the cause of the period gap in the orbital period distribution of CVs (see Section 1.4.5 for further details).

However, there is now a wealth of evidence for the existence of fully convective stars (with no tachocline) having sizeable magnetic fields (e.g. Basri 2009; Donati & Landstreet 2009; Reiners 2011; Reiners, Joshi & Goldman 2012), which contradicts the existing theoretical understanding. It is now postulated that magnetic fields are generated in fully convective stars through a turbulent dynamo (Knigge, Baraffe & Patterson, 2011), as opposed to an interface dynamo in partially radiative stars. This may enable magnetic braking to continue in CVs towards short orbital periods, and is given the term 'residual' magnetic braking. There is also evidence suggesting a change in the magnetic field's geometry across the partially radiative/fully convective transition (e.g. Reiners & Basri 2008, 2009, 2010; Morin et al. 2010), and it is the subsequent disruption of the magnetic braking mechanism at this boundary that is now thought to be responsible for the period gap (Section 1.4.5).

There have been numerous attempts to try and model magnetic braking (e.g. Verbunt & Zwaan 1981; Rappaport, Verbunt & Joss 1983; Kawaler 1988; Mestel & Spruit 1987; Andronov, Pinsonneault & Sills 2003; Ivanova & Taam 2003; Matt et al. 2012), resulting in a wide range of predictions for the effectiveness of the mechanism. The vast differences between the many models is evidence that the intricacies of the magnetic braking mechanism are far from fully understood.

1.4.5 Orbital Period Distribution

The timescales on which CVs evolve are many orders of magnitude greater than those we can observe. We cannot follow a system through its evolution, only observe it for a short period of its lifetime. Although very little about CV evolution can be extracted from a single system, the distributions of the CV population as a whole can reveal insights into the evolutionary process. An example is the orbital period distribution of CVs, which can be used to trace CV evolution due to the decrease in orbital period with continued mass transfer in CVs (equation 1.12). The orbital period distribution of all (~ 1100) CVs within the Ritter & Kolb (2003) catalogue (v7.20) is shown by the white histogram in Figure 1.4. There are two main features to this distribution that need explaining, namely the lack of CVs within the ~ 2–$3\,$h period range (the ‘period gap’) and the sharp edge at $\sim 80\,$min (the ‘period minimum’).

Period Gap

The existence of a gap in the orbital period distribution – commonly referred to as the period gap (light grey band in Figure 1.4) – is evidence for a significant disruption to the evolution of a CV at the point it reaches the top of the gap ($P_{\mathrm{orb}} \sim 3\,\mathrm{h}$). An orbital period of $\sim 3\,$h corresponds to a donor mass of $\sim 0.2\,\mathrm{M}_{\odot}$, the point at

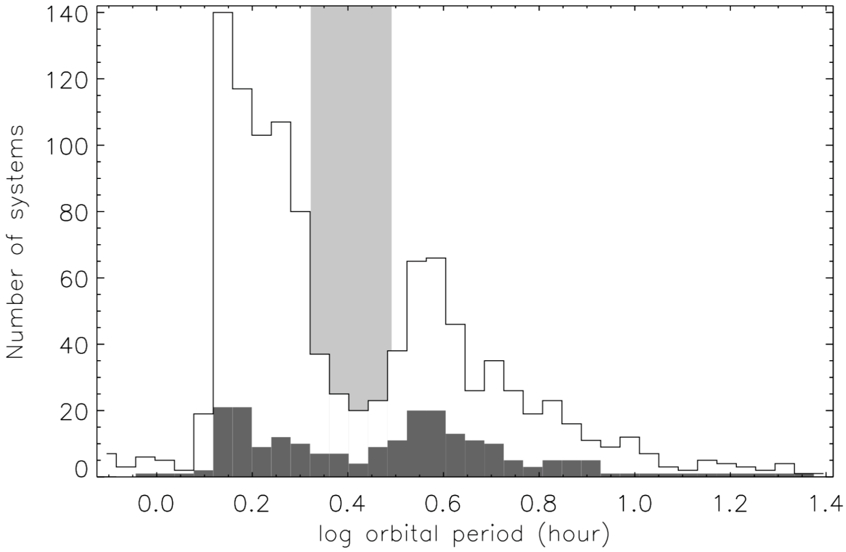

Figure 1.4: The orbital period distribution of all CVs (white) and eclipsing CVs (dark grey) from the Ritter & Kolb (2003) catalogue (v7.20). The light grey band indicates the CV period gap. From Southworth et al. (2015).

which the donor becomes fully convective (Knigge, Baraffe & Patterson, 2011). As mentioned in Section 1.4.4, there is evidence to suggest that the donor's transition from partially radiative to fully convective involves a change in the geometry of its magnetic field.

The donor is out of thermal equilibrium when in reaches the top of the period gap, a result of high mass transfer rates (a consequence of magnetic braking) within the system at long orbital periods. The change in the geometry of the magnetic field at this point weakens the magnetic braking mechanism, leading to abrupt reductions in both angular momentum loss and mass transfer rate. The donor's $\tau_{\rm ML}$ increases accordingly, causing the donor to rapidly shrink and return to thermal equilibrium. The donor no longer fills its Roche lobe and the CV now takes on the appearance of a detached system. Although there is no mass transfer whilst in this state, the system is still losing angular momentum via gravitational radiation and residual magnetic braking, which gradually reduces the size of the Roche lobe. At an orbital period of $\sim 2\,$h, the donor – now in thermal equilibrium – can once again fill its Roche lobe and mass transfer restarts.

The period gap therefore exists due to CVs evolving through the orbital periods of approximately 3 h to 2 h whilst detached. The period gap is not completely arid, however. The few CVs occupying the period gap either began mass transfer within this period range, have an evolved donor (see Section 1.4.6) or are magnetic systems (see Section 1.2.6).

Period Minimum

As the donor is in thermal equilibrium at the bottom of the period gap, its response to mass loss is $\xi = \xi_{\mathrm{KH}} \simeq 0.8$. The continuation of mass loss from the donor causes τ_{KH} to increase, which, as τ_{ML} is relatively constant, causes ξ to decrease as a CV evolves to shorter orbital periods. The donor is consequently pushed further and further from thermal equilibrium.

Substituting equation 1.16 into equation 1.12 gives the following relation between $\dot{P}_{\mathrm{orb}}$ and ξ:

$$\frac{\dot{P}_{\mathrm{orb}}}{P_{\mathrm{orb}}} = \frac{3\xi - 1}{2} \frac{\dot{M}_2}{M_2}. \tag{1.22}$$

It is apparent from equation 1.22 that a decreasing ξ will eventually change the direction of orbital period evolution – a phenomena known as period ‘bounce’ – as the donor begins to expand in response to further mass loss. This indicates the existence of a minimum period that a CV reaches before evolving to larger orbital periods, corresponding to $\dot{P}_{\mathrm{orb}} = 0$ and therefore $\xi = 1/3$ (from equation 1.22).

This can explain the sharp cut-off around 80 min in the orbital period distribution (Figure 1.4), commonly referred to as the period minimum. It also explains why there is a build-up of CVs at the period minimum, known as the period ‘spike’ (Gänsicke et al., 2009). The time taken for a CV to evolve through a particular orbital period range is the reciprocal of the average $\dot{P}_{\mathrm{orb}}$ of the range. The period bounce effect, in addition to low angular momentum loss rates, result in reduced values for $\dot{P}_{\mathrm{orb}}$ around the period minimum, and as a consequence CVs spend a large amount of time evolving through this regime. It is therefore no surprise to see a build-up of systems in the orbital period distribution at the period minimum.

Binary population synthesis (BPS) studies (e.g. Kolb 1993; Howell, Nelson & Rappaport 2001; Willems et al. 2005; Goliasch & Nelson 2015) predict period-bounce systems to make up a significant fraction ($\sim$40–70%) of the total CV population. Until recently, very few such systems had been discovered, resulting in a big discrepancy between theory and observation. This was likely due to considerable undersampling of the period bouncer population, as they characteristically have faint quiescent magnitudes and long outburst recurrence times (Patterson, 2011). The emergence of the Sloan Digital Sky Survey (SDSS; York et al. 2000) finally enabled this population to be uncovered (Littlefair et al., 2006b, 2008; Savoury et al., 2011), thanks to its reasonable completeness down to $g \sim 19$ mag and selection from spectral analysis (Gänsicke et al., 2009).

The evolutionary path described here is followed by the vast majority of CVs, namely those possessing a main sequence donor. The small proportion of CVs containing an alternative donor instead follow different paths, which is why there is a handful of systems with orbital periods below this period minimum in Figure 1.4. These systems either contain an evolved, helium-rich donor (i.e. AM CVn stars, see Section 1.2.5), a donor with low-metallicity (e.g. a member of the Galactic halo; Patterson, Thorstensen & Knigge 2008; Uthas et al. 2011) or have harboured a brown dwarf donor from formation. This latter case is discussed further in the following section.

1.4.6 CVs with Brown Dwarf Donors from Formation

The evolution of a CV can differ markedly if the progenitor system (see Section 1.3.1) contains a substellar/brown dwarf secondary. For starters, the most massive brown dwarf secondaries cannot fill their Roche lobes – and therefore begin mass transfer – until the system reaches a P_{orb} of 46 min (Politano, 1996, 2004), which is well below the period minimum of the standard evolutionary track. Once such a system begins mass transfer, its $P_{\rm orb}$ increases and will eventually join the evolutionary path of the period bouncers. A BPS study by Politano (2004) predicted that approximately 15% of *all* CVs should lie below the period minimum due to forming with brown dwarf secondaries, but only a handful of CVs actually do and most do so due to evolved secondaries (e.g. Augusteijn et al. 1996; Thorstensen et al. 2002; Breedt et al. 2012).

The distinct lack of close ($< 3\,$AU) binary systems observed with a main sequence primary and brown dwarf secondary has led to the coining of the term 'brown dwarf desert' (e.g. Duquennoy & Mayor 1991; Marcy & Butler 2000; Grether & Lineweaver 2006a). The progenitors of CVs formed with brown dwarf donors are expected to fall within this 'desert', which may explain the dearth of observed CVs with brown dwarf secondaries below the period minimum. The 'desert' is not completely arid (Duchêne & Kraus, 2013), however, so it is possible that CVs formed with brown dwarf secondaries do exist, although any such systems are expected to be vastly outnumbered by those formed with main sequence secondaries.

1.5 Using Donor Stars to Trace CV Evolution

While the orbital period distribution is able to uncover a few broad aspects of CV evolution, it cannot be used to examine the evolutionary process in detail. To achieve this requires focusing on the driver of CV evolution – mass transfer (which is itself driven by angular momentum losses from the system, as discussed in Section 1.4.1). More specifically, it is the *secular* mass transfer rate – varying on an evolutionary timescale ($\tau_{\rm ev} \sim P_{\rm orb}/\dot{P}_{\rm orb} \sim 10^8$–$10^{10}\,$yrs) – that needs tracing. Obtaining an estimate for the secular mass transfer rate is made harder due to the existence of mass transfer rate fluctuations occurring on long timescales, though shorter than $\tau_{\rm ev}$. These fluctuations can arise due to irradiation from the donor (e.g. King et al.

1995, 1996; Ritter, Zhang & Kolb 2000; Büning & Ritter 2004) or the nova cycle (e.g. MacDonald 1986; Shara et al. 1986; Livio & Shara 1987; Livio, Govarie & Ritter 1991; Schenker, Kolb & Ritter 1998; Kolb et al. 2001). It is important that this is taken into consideration when estimating the mass transfer rate observationally.

1.5.1 Tracers of Mass Transfer Rate and the Importance of CV Donor Stars

An example of an observational tracer of the mass transfer rate is the time-averaged absolute magnitude of the accretion disc. This provides an estimate of the accretion rate from disc to white dwarf, which is indicative of the transfer of mass through the system (Patterson, 1984, 2011). The absolute magnitude must be time-averaged, preferably across at least one DN outburst cycle in order to obtain an accurate estimate. This method is only able to measure the mass transfer rate over the timescale of observations, ranging from years to decades. The observational timescale is many orders of magnitude shorter than the evolutionary timescale, and is therefore not able to trace the secular mass transfer rate given current understanding about long-term mass transfer rate fluctuations (Knigge, Baraffe & Patterson, 2011).

Another way to estimate the accretion rate, and therefore mass transfer rate, is through the mass and effective temperature of the white dwarf in quiescence (Townsley & Bildsten, 2003, 2004; Townsley & Gänsicke, 2009):

$$\langle \dot{M}_{\rm acc} \rangle ({\rm M}_\odot\,{\rm yr}^{-1}) = 10^{-10} \left(\frac{T_{\rm eff}}{1.7 \times 10^4{\rm K}} \frac{0.9{\rm M}_\odot}{M_1} \right)^4 , \tag{1.23}$$

where $\langle \dot{M}_{\rm acc} \rangle$ is the mean accretion rate onto the white dwarf during the current nova cycle. The nova timescale ($\tau_{\rm nova} \sim 10^4$–$10^7\,$yrs) is typically much longer than the observational timescale, but still much lower than $\tau_{\rm ev}$. This method is an improvement over time-averaged disc absolute magnitudes, but is still unable to trace the true secular mass transfer rate of CVs.

When attempting to obtain a mass transfer rate estimate somewhere close to the secular value, it is requisite to focus on the donor. More specifically, the donor radius (R_2), as the timescale on which R_2 adjusts to mass loss ($\tau_{\rm adj}$) is comparable to the thermal timescale of the donor in thermal equilibrium ($\tau_{\rm KH,eq}$):

$$\tau_{\rm adj} \simeq 0.05\tau_{\rm KH,eq}, \tag{1.24}$$

(for substantially convective stars; Stehle, Ritter & Kolb 1996) and therefore $\tau_{\rm ev}$ (as $\tau_{\rm KH,eq} \sim \tau_{\rm ev}$ for CVs; Knigge, Baraffe & Patterson 2011). A comparison of R_2 with the radius of a main sequence star of the same mass is therefore the closest possible estimate of the secular mass transfer rate.

Precise donor masses and radii can be obtained from eclipsing CV systems (see Section 3.2), but these make up only a small fraction of the overall CV population ($<10\%$, Figure 1.4). A much larger (though less precise) sample of donor masses and radii can be acquired through the help of the superhump phenomena observed to occur in superoutbursts of SU UMa-type DNe.

1.5.2 Superhumps and the $\epsilon(q)$ Relation

The superoutburst phenomena was briefly discussed in Section 1.2.3, but what is the origin of the associated periodic brightness variations that are referred to as superhumps? As mentioned previously, during superoutburst the accretion disc is driven into an elliptical state by resonances between the donor star and material within the disc. Tidal interaction between the donor and the disc results in an extended area of increased luminosity at the edge of the disc, centred at the point closest to L1 (Warner & O'Donoghue, 1988; O'Donoghue, 1990). The increased luminosity originates from an increase in collisions between orbiting material, and therefore dissipated energy within the area of the disc closest to the donor. A consequence of the elliptical nature of the disc is a variable distance between the disc edge and donor. This leads to fluctuations in luminosity as the orbiting donor sweeps around the disc, which are observed as superhumps (Hellier, 2001).

Another consequence of an elliptical disc is precession. The disc precesses at a slow rate, with a period ($P_{\rm prec}$) significantly longer than $P_{\rm orb}$. These two periods therefore both contribute to the formation of the superhump period ($P_{\rm sh}$), which is simply the 'beat period' of $P_{\rm prec}$ and $P_{\rm orb}$ (Hellier, 2001):

$$\frac{1}{P_{\rm sh}} = \frac{1}{P_{\rm orb}} - \frac{1}{P_{\rm prec}}. \tag{1.25}$$

$P_{\rm sh}$ is therefore usually a few percent longer than $P_{\rm orb}$, but does not stay constant throughout the superoutburst. In fact, a superoutburst can be split up into three distinct stages (A, B and C), with sharp transitions observed between each stage. Stage A represents the start of the superoutburst, with a long, stable $P_{\rm sh}$. Stage B is the middle part of the superoutburst, with a shorter, unstable $P_{\rm sh}$. The final stage (C) exhibits the shortest $P_{\rm sh}$, which is stable once again (Olech et al., 2003; Kato et al., 2009). The general trend of decreasing $P_{\rm sh}$ across the superoutburst hints at an increasing $P_{\rm prec}$ (from equation 1.25) and therefore a dwindling disc radius (Murray, 2000).

The superhump excess (ϵ) is defined as the difference between $P_{\rm sh}$ and $P_{\rm orb}$ as a fraction of the latter:

$$\epsilon = \frac{P_{\rm sh} - P_{\rm orb}}{P_{\rm orb}}. \tag{1.26}$$

Equations 1.25 and 1.26 also show ϵ to be a measure of $P_{\rm prec}$, which is itself dependent on disc radius and q (Murray, 2000; Patterson, 2001). Theoretically, ϵ must scale with q, which is an important relation as ϵ is relatively easy to measure accurately, while q is much harder to measure and critical for acquiring component masses. The exact scaling between ϵ and q can be determined empirically from a set of calibration systems with independently derived values of ϵ and q. The first attempts at this were made by Patterson (1998, 2001) and Patterson et al. (2005). The systems used

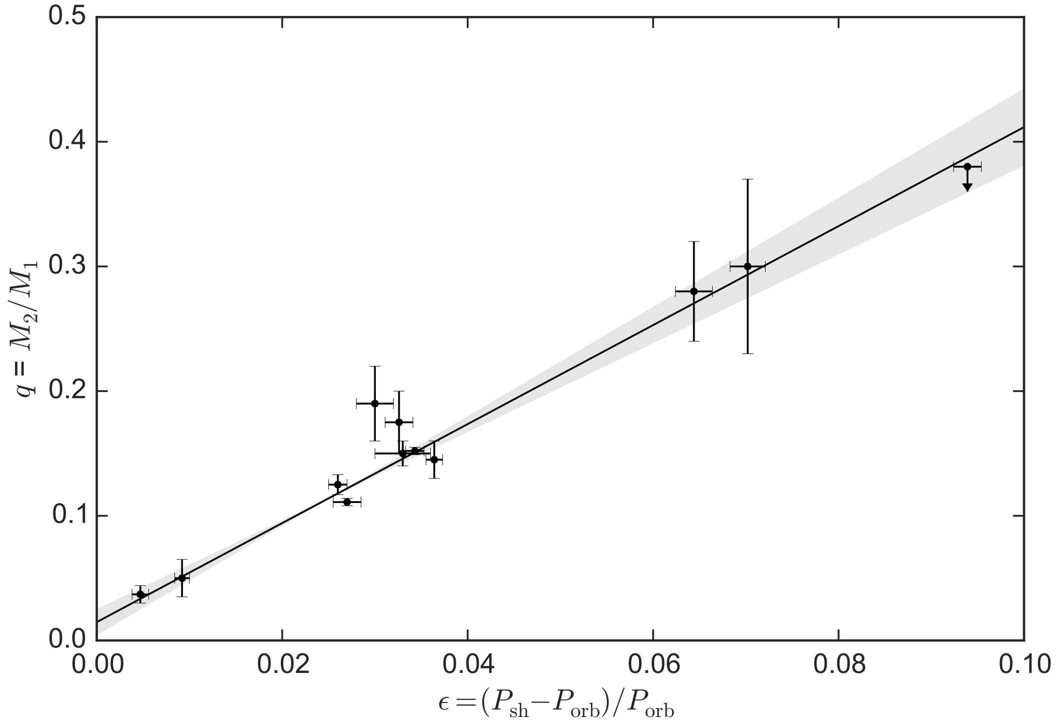

Figure 1.5: Measured ϵ and q values of superhumping and eclipsing CVs (from Patterson et al. 2005). The black line shows the linear calibration of the $\epsilon(q)$ relation for superhumping CVs, with 1σ errors (shaded region), from Knigge (2006).

as calibrators are mostly eclipsing SU UMa DNe, with precise values of q obtained through eclipse studies (see Section 3.2) and ϵ values derived using P_{sh} measurements from 'common' superhumps[4]. Using the same set of calibration systems as Patterson et al. (2005), Knigge (2006) produced the following linear calibration of $\epsilon(q)$:

$$q(\epsilon) = (0.114 \pm 0.005) + (3.97 \pm 0.41) \times (\epsilon - 0.025), \qquad (1.27)$$

where the -0.025 shift in ϵ is included to ensure the fit parameters (and errors) are uncorrelated. This calibration is also plotted in Figure 1.5, along with the calibrators used.

---

[4] No differentiation made between the three stages of superoutburst, but typically comparable to $P_{\mathrm{sh}}^{\mathrm{B}}$.

1.5.3 Semi-Empirical Mass-Radius Relation for CV Donor Stars

For superhumping systems with accurately measured $P_{\rm sh}$ and $P_{\rm orb}$, an estimate of the donor mass can be attained through use of the $\epsilon(q)$ relation (equation 1.27) and the assumption of a constant white dwarf mass. The period-density relation for Roche lobe secondaries (equation 1.6) can then be used to obtain a measure of the donor radius. Using their $\epsilon(q)$ calibration and a constant white dwarf mass of $\langle M_1 \rangle = 0.75\,{\rm M}_\odot$, Patterson et al. (2005) were able to supplement the existing, limited sample of donors with measured parameters (all from eclipsing systems) with those from superhumping systems, with the aim of investigating the mass-radius relation for CV donors.

Patterson et al. (2005) found that at almost all donor masses the donor radius was slightly larger than a main sequence star of identical mass, which is a direct consequence of mass transfer. Another finding was how relatively well constrained the relation is, suggesting there is a single evolutionary path that all non-evolved CV donors follow as they evolve towards $P_{\rm min}$. This is expected, since the timescale on which R_2 adjusts to mass loss ($\tau_{\rm adj}$) is an order of magnitude smaller than the evolutionary timescale ($\tau_{\rm ev}$), as equation 1.24 shows. Patterson et al. (2005) fit the donor mass-radius relation linearly, accounting for a clear break around $M_2 = 0.2\,{\rm M}_\odot$, which is a consequence of the period gap (Section 1.4.5).

The donor mass-radius relation was initially revised by Knigge (2006) using the same data set and constant M_1 [5], but the alternative $\epsilon(q)$ calibration shown in equation 1.27. A further revision was made by Knigge, Baraffe & Patterson (2011), with the inclusion of additional precise masses and radii from Littlefair et al. (2008). This latest optimal mass-radius relation, in the form of a broken-power-law, is shown by

---

[5] From the average M_1 of an eclipsing CV sample: $\langle M_1 \rangle = 0.75 \pm 0.05\,{\rm M}_\odot$.

the black line in Figure 1.6 and given by:

$$\frac{R_2}{\mathrm{R}_\odot} = \begin{cases} 0.118 \pm 0.004 \left(\frac{M_2}{M_\mathrm{bounce}}\right)^{0.30\pm0.03} & M_2 < M_\mathrm{bounce} \\ 0.225 \pm 0.008 \left(\frac{M_2}{M_\mathrm{conv}}\right)^{0.61\pm0.01} & M_\mathrm{bounce} < M_2 < M_\mathrm{conv} \\ 0.293 \pm 0.010 \left(\frac{M_2}{M_\mathrm{conv}}\right)^{0.69\pm0.03} & M_\mathrm{conv} < M_2 < M_\mathrm{evol}, \end{cases} \tag{1.28}$$

where M_bounce is the donor mass at period minimum, M_conv is the donor mass within the period gap and M_evol is the donor mass at which evolved systems start to dominate. The broken-power-law mass-radius relation shown above was obtained by carrying out three separate fits – via minimisation of the χ^2 statistic (see Appendix C of Knigge 2006) – to the data shown in Figure 1.6. This required assumptions for M_conv and M_evol, along with locations for the period minimum P_min (from period spike; Gänsicke et al. 2009), and upper $P_\mathrm{gap,+}$ and lower $P_\mathrm{gap,-}$ bounds of the period gap (Knigge, 2006):

$$\begin{array}{lll} M_\mathrm{bounce} = 0.069 \pm 0.009\,\mathrm{M}_\odot, & M_\mathrm{conv} = 0.20 \pm 0.02\,\mathrm{M}_\odot, & M_\mathrm{evol} \simeq 0.6{-}0.7\,\mathrm{M}_\odot. \\ P_\mathrm{min} = 82.4 \pm 0.7\,\mathrm{min}, & P_\mathrm{gap,-} = 2.15 \pm 0.03\,\mathrm{hrs}, & P_\mathrm{gap,+} = 3.18 \pm 0.04\,\mathrm{hrs}. \end{array}$$

The value of M_bounce was found through optimising the short-period (non-period-bouncer) fit. Using a data set almost identical to that of Patterson et al. (2005), it is no surprise that Knigge, Baraffe & Patterson (2011) report similar findings: the bloated nature of CV donor stars in comparison to their identical-mass main sequence counterparts, and the existence of a unique evolution track followed by all non-evolved CVs (evidence for both clearly visible in Figure 1.6).

1.5.4 Semi-Empirical Donor-Based CV Evolution Track

In order to try and quantify the secular mass transfer rate in CVs (and therefore the rate of angular momentum loss), Knigge, Baraffe & Patterson (2011) also attempted the construction of a semi-empirical evolutionary track. This involved tuning the

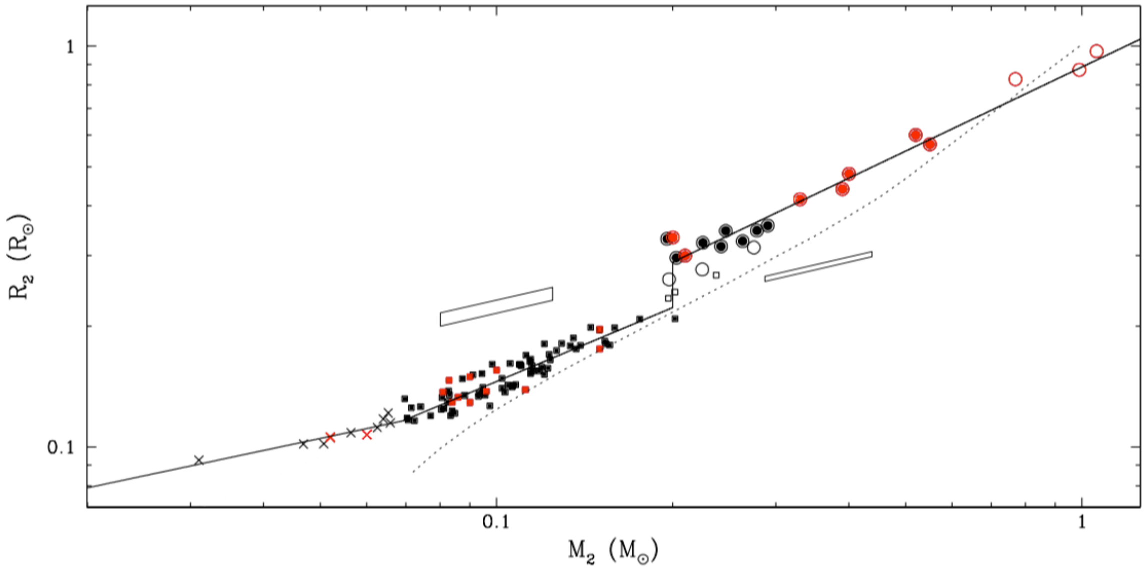

Figure 1.6: Mass-radius relation for CV donor stars from Knigge, Baraffe & Patterson (2011). The black data points represent masses/radii inferred from superhumps (Knigge, 2006), while the red are measured from eclipsing systems (Patterson et al., 2005; Littlefair et al., 2008). The error bars have been removed for clarity, with the typical errors associated with any short- or long-period superhump system shown by the parallelograms. Circles, squares and crosses represent long-period, short-period and candidate period bounce systems. An optimal broken-power-law fit to the data (excluding unfilled data points) is shown by the solid black line. For comparison, the mass-radius relation for main sequence stars (5 Gyr isochrone; Baraffe et al. 1998) is also shown (dashed line). Figure from Knigge, Baraffe & Patterson (2011).

angular momentum loss rate to match the observed inflation of CV donor stars. Main sequence stellar models from Baraffe et al. (1998) were used as a basis for donor evolution sequences, after correction for non-mass-loss related causes of donor inflation[6], e.g. starspot coverage, low convective efficiency and tidal/rotational deformation (e.g. Renvoizé et al. 2002).

The self-consistent donor evolution sequences were completed with the addition of angular momentum loss recipes for both gravitational radiation and magnetic braking. As mentioned in Section 1.4.4, there exist a wide range of different magnetic braking models, and the consideration of many different recipes can be very computationally expensive. Therefore, only the model from Rappaport, Verbunt & Joss (1983) was employed by (Knigge, Baraffe & Patterson, 2011), chosen due to its adjustable normalisation and power-law index (γ). A range of self-consistent evolution tracks were calculated for a range of normalisation factors for the two different angular momentum-loss recipes used ($f_{\rm GR}, f_{\rm MB}$), then fit to the empirical data set (same as used for mass-radius relation from previous section) through χ^2 minimisation.

The resulting best-fit evolutionary track, in both $P_{\rm orb}$-M_2 and M_2-R_2 planes, is shown in Figure 1.7 (red lines). In order to reproduce the empirical data, normalisation factors of $f_{\rm GR} = 2.47 \pm 0.22$ and $f_{\rm MB} = 0.66 \pm 0.05$ were required below and above the period gap, respectively. For comparison, a 'standard model' evolutionary track with $f_{\rm GR} = f_{\rm MB} = 1$ is also shown in Figure 1.7 (black dot-dashed lines), which poorly represents the empirical data, particularly below the period gap. The most notable difference between the two tracks is their contrasting predictions of $P_{\rm min}$. The standard track severely underpredicts $P_{\rm min}$ ($\sim 73\,$min) based on the observed location of the period spike ($82.4 \pm 0.7\,$min; Gänsicke et al. 2009), while the best-fit track is in excellent agreement ($81.8 \pm 0.9\,$min), as shown in the top panel of Figure 1.7. The requirement of additional angular momentum loss below the gap

---

[6] Irradiation is another cause of donor inflation, but as its impact is limited and complicated to implement, Knigge, Baraffe & Patterson (2011) choose not to correct for it.

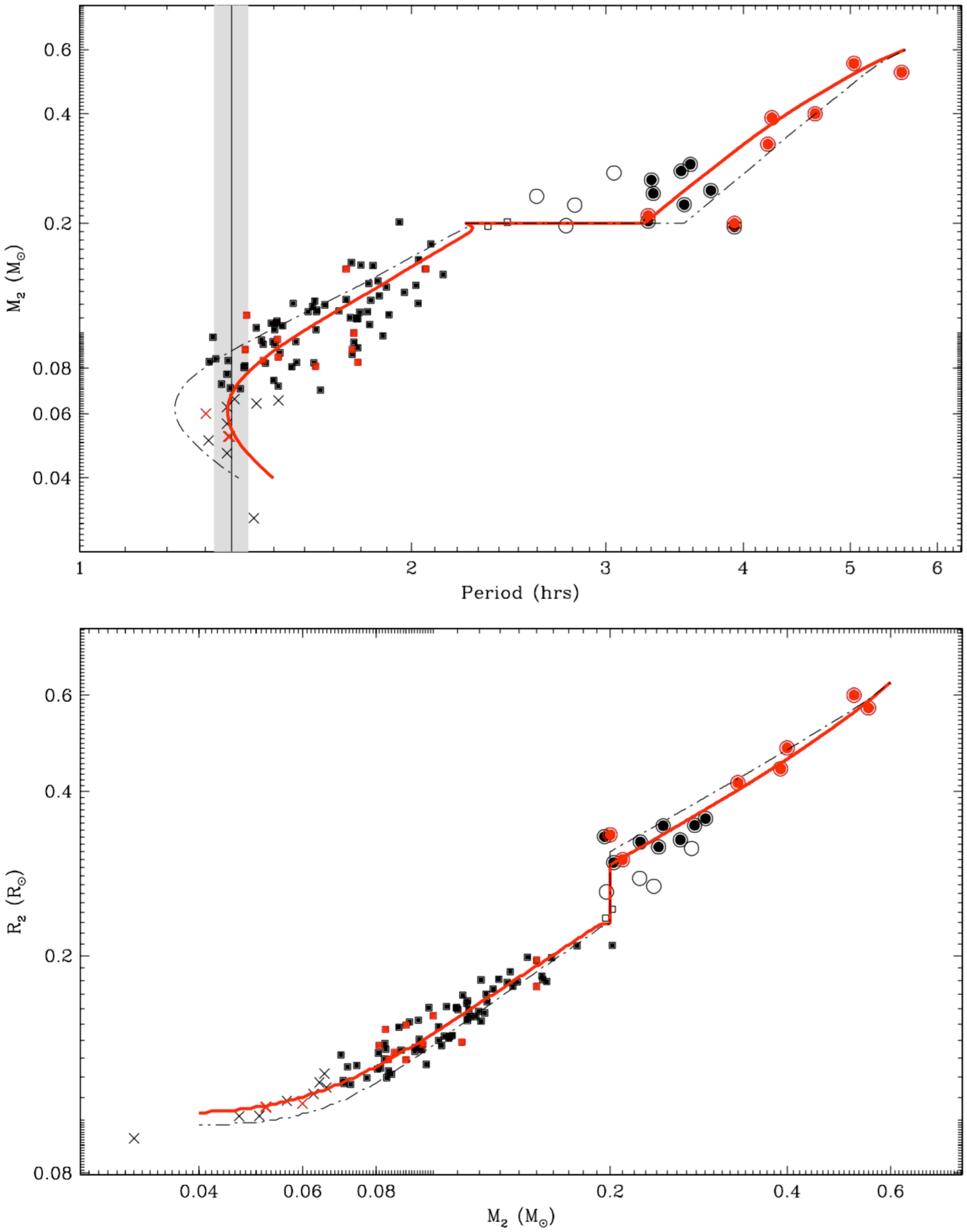

Figure 1.7: Semi-empirical, best-fit evolutionary track ($f_{\rm GR} = 2.47 \pm 0.22$, $f_{\rm MB} = 0.66 \pm 0.05$; red lines) for CV donor stars in the $P_{\rm orb}$-M_2 (top) and M_2-R_2 (bottom) planes, from Knigge, Baraffe & Patterson (2011). For comparison, the 'standard model' evolutionary track ($f_{\rm GR} = f_{\rm MB} = 1$) is shown by black dot-dashed lines. Data set (including data point colour/shape scheme) same as that used in Figure 1.6. The vertical line in the top panel represents the observed location of the period spike and assumed to correspond to $P_{\rm min}$, while the width of the shaded region corresponds to FWHM of the spike (Gänsicke et al., 2009). Figure from Knigge, Baraffe & Patterson (2011).

points to an additional angular momentum loss mechanism (or mechanisms) working alongside gravitational radiation. Residual magnetic braking (see Section 1.4.3) is thought to be responsible for this additional angular momentum loss (Knigge, Baraffe & Patterson, 2011), but contribution from consequential angular momentum loss (see Section 1.6.2) is also a possibility (e.g. Willems et al. 2005).

1.6 CV White Dwarf Mass Problem

It has long been an issue that the white dwarfs within CVs are on average significantly more massive than single white dwarfs, as this contradicts what is predicted from population studies (e.g. Politano 1996). White dwarfs within CVs should have lower masses due to the expected stunting effect of CE evolution (Section 1.3.2) and erosion from nova eruptions (Sections 1.2.1 & 1.6.2). Selection effects were once a popular explanation for this discrepancy, on the basis that accretion luminosity (and therefore intrinsic brightness) scales with white dwarf mass (Ritter & Burkert, 1986). However, this does not seem to be the case, as a group of intrinsically faint, white dwarf-dominated CVs from the SDSS were discovered to have white dwarfs just as – if not more – massive as those within intrinsically bright CVs (Littlefair et al., 2008; Savoury et al., 2011).

Using robust CV white dwarf masses from the Ritter & Kolb (2003) catalogue (v7.14) and Savoury et al. (2011), Zorotovic, Schreiber & Gänsicke (2011) found a mean CV white dwarf mass of $\langle M_1 \rangle = 0.82 \pm 0.15\,\mathrm{M}_\odot$ (where the uncertainty refers to the standard deviation of the mass distribution). This is not just significantly higher than the mean single white dwarf mass of $\langle M \rangle = 0.62 \pm 0.11\,\mathrm{M}_\odot$ (Tremblay et al., 2016), but also the mean pre-CV (see Section 1.3.3) white dwarf mass of $\langle M_1 \rangle = 0.67 \pm 0.21\,\mathrm{M}_\odot$ (Zorotovic, Schreiber & Gänsicke, 2011). This also rules out the CE phase as a possible explanation for the higher than predicted masses, as both CVs and pre-CVs are post-CE systems. As the mass discrepancy appears unique to CV white dwarfs, it must be as a consequence of mass transfer.

1.6.1 Do CV White Dwarfs Grow in Mass?

One explanation put forward by Zorotovic, Schreiber & Gänsicke (2011) for high white dwarf masses in CVs involves the growth in mass through sustained accretion. If this were to be the case, CVs would have to be considered a likely progenitor channel for Type Ia Supernovae, the thermonuclear explosion of a white dwarf after reaching the Chandrasekhar mass limit of $1.44\,\mathrm{M}_{\odot}$ (see Maoz, Mannucci & Nelemans 2014 for a review).

Evidence for mass growth over time would be a notable increase in white dwarf mass with decreasing P_{orb}, but this is not observed, with similar values for $\langle M_1 \rangle$ both above and below the period gap found by Zorotovic, Schreiber & Gänsicke (2011). However, these average masses are based on just 32 white dwarf mass measurements (most below the gap), and therefore additional precise white dwarf masses – especially from CVs at longer P_{orb} – are needed in order to investigate this further. Additional evidence against mass growth in CV white dwarfs comes from nova simulation studies, which overwhelmingly favour net mass loss from the white dwarf across the nova cycle (e.g. Prialnik & Kovetz 1995; Yaron et al. 2005; Epelstain et al. 2007; Idan, Shaviv & Shaviv 2013). A recent BPS study by Wijnen, Zorotovic & Schreiber (2015) corroborates these findings, by showing that while an increase in mass accretion efficiency does increase the overall white dwarf mass, it cannot reproduce the observed white dwarf mass distribution, with many more low-mass ($\lesssim 0.6\,\mathrm{M}_{\odot}$) white dwarfs predicted than are actually observed.

Another explanation outlined by Zorotovic, Schreiber & Gänsicke (2011) is a short phase of thermal-timescale mass transfer (TTMT; see Section 1.4.2) early on in the lifetime of a CV. The high mass transfer rate involved allows sustained hydrogen burning on the surface of the white dwarf and in the process increasing the white dwarf's mass before the CV enters its main evolutionary (stable mass transfer) stage. This option was also considered by Wijnen, Zorotovic & Schreiber (2015), but once again a large number of low-mass white dwarfs were predicted.

1.6.2 Consequential Angular Momentum Loss

So far, only angular momentum loss associated with either gravitational radiation or magnetic braking has been considered (Sections 1.4.3 & 1.4.4, respectively). Both remove angular momentum loss from the system gradually (driving stable mass transfer) and are therefore referred to as sources of systematic angular momentum loss ($\dot{J}_{\rm sys}$). Another source of angular momentum loss from the system is related to mass transfer/accretion, and is commonly referred to as consequential angular momentum loss ($\dot{J}_{\rm CAML}$). The total angular momentum loss from the system is therefore

$$\dot{J} = \dot{J}_{\rm sys} + \dot{J}_{\rm CAML}. \tag{1.29}$$

Examples of viable CAML mechanisms include an accretion disc wind (e.g. Livio & Pringle 1994), interactions with a circumbinary disc (e.g. Willems et al. 2005) and nova eruptions (e.g. King & Kolb 1995; Kolb et al. 2001). The latter of these CAML mechanisms is the most commonly considered and will therefore be the focus of the remaining discussion. For the classical case of CAML associated with nova eruptions – where the mass ejected is assumed to have the same specific angular momentum as that of the white dwarf (King & Kolb (1995)) – $\dot{J}_{\rm CAML}$ is defined as

$$\frac{\dot{J}_{\rm CAML}}{J} = \nu \frac{\dot{M}_2}{M_2}, \tag{1.30}$$

where $\nu = M_2^2/(M_1(M_1 + M_2))$.

The mass and angular momentum losses resulting from a nova eruption have an effect on the response of the donor's Roche lobe ($\xi_{\rm L}$) to mass transfer, and hence the required value of q to ensure stable mass transfer (see Section 1.4.2 for simple, conservative case). Schreiber, Zorotovic & Wijnen (2016) considered whether an alternative stability limit on q due to CAML could explain the lack of observed CVs with low-mass white dwarfs. The reasoning behind this is that a lower stability limit on q would make CVs with low-mass white dwarfs (and therefore higher values of q) unstable to mass transfer and remove them from the CV population. For the classical $\dot{J}_{\rm CAML}$ case described above, the value of q required for stable mass transfer actually increases compared to that of the conservative case (derived in Section 1.4.2), creating an even larger discrepancy between theory and observations.

1.6.3 An Empirical Consequential Angular Momentum Loss Model

The work of Schreiber, Zorotovic & Wijnen (2016) culminates in the introduction of an empirical CAML (eCAML) model that *is* capable of lowering the stability limit on q, and therefore able to reproduce the observed CV white dwarf mass distribution[7]. The amount of CAML in the empirical model scales with the inverse of white dwarf mass, so that ν (equation 1.30) now has the form

$$\nu = \frac{C}{M_1}, \tag{1.31}$$

where $C = 0.3$–0.4 (Schreiber, Zorotovic & Wijnen, 2016). This requires an additional source of CAML, with a contribution inversely proportional to the mass of the white dwarf. Another predicted source of CAML connected to nova eruptions is from frictional losses associated with the nova ejecta and donor (e.g. Schenker, Kolb & Ritter 1998; Shen 2015; Nelemans et al. 2016). If the expansion velocity of the ejecta is low, it should be able to form a CE around the system, allowing large amounts of angular momentum to be removed due to friction between the CE and the donor. Interestingly, nova models show evidence for a relation between white dwarf mass and expansion velocity of nova ejecta (Yaron et al., 2005). This essen-

---

[7] Unsurprising, given the empirical nature of the model.

tially provides a physical interpretation to Schreiber, Zorotovic & Wijnen (2016)'s empirical model, and a potential solution to the long-standing CV white dwarf mass problem.

1.7 This Thesis

This thesis presents precise system parameters – including component masses – for 18 eclipsing CVs, obtained through the modelling of high-time-resolution eclipse light curves. Chapter 2 outlines the procedure involved in transforming raw observational data into eclipse light curves ready for modelling. Details of the eclipse model and existing modelling approach are included in Chapter 3, in addition to the introduction of a new modelling approach developed as part of this work. Chapter 4 presents results from modelling eclipses – using the existing modelling approach – of a period-minimum system, with the aim of determining its evolutionary status. The new modelling approach is tested on a short-period system in Chapter 5, in addition to the system from Chapter 4, thereby providing a comparison of the two approaches. Chapter 6 comprises of an eclipse modelling study of a suspected period-bounce system. The results from the eclipse modelling of a further 15 systems are presented in Chapter 7. In Chapter 8, the 18 precise CV component masses from this work are utilised in an attempt to try and improve the current understanding of CV evolution.

Chapter 2

Observations and Data Reduction

2.1 High-Time-Resolution Photometry

For CVs with inclinations $\gtrsim 80^{\circ}$ [1], it is possible for the donor star to eclipse all other components within the system once every orbital period. A typical eclipse light curve of a CV therefore includes individual eclipses of the white dwarf, bright spot and accretion disc, with all occurring in quick succession. This results in a complex overall CV eclipse shape, which can be exploited to enable the attainment of system parameters (e.g. component masses, radii etc.). This technique is discussed in detail within Section 3.2, but briefly, it relies on light curves with clearly resolved white dwarf and bright spot eclipses, which can subsequently be modelled to obtain system parameters. Typically, the bright spot eclipse begins directly after that of the white dwarf, and therefore high-time-resolution photometry is an important requirement to performing precise eclipse modelling. All photometry included in this thesis has been acquired with one of two high-speed imaging cameras; ULTRACAM (Dhillon et al., 2007) and ULTRASPEC (Dhillon et al., 2014).

---

[1] A system's eclipsing potential is also dependent on q (see Section 3.2).

2.1.1 ULTRACAM

ULTRACAM (ULTRA-fast CAMera) is an instrument purposefully built for the study of high-speed astrophysics. It utilises frame-transfer CCDs to enable rapid frame rates of up to 500 Hz, and possesses an image area of $1024 \times 1024\,\mathrm{pixel}^2$. A very useful feature of ULTRACAM is its multi-channel capability, which permits simultaneous photometry in three different wavelength bands. The primary filter set used by ULTRACAM is the SDSS photometric system (Fukugita et al., 1996), which covers the wavelength range $\sim$3000–11000 Å and consists of five pass-bands with negligible overlap: u', g', r', i' and z'.

ULTRACAM was first commissioned in May 2002, and its portability has allowed it to see time on each of the following telescopes over the past $\sim$15 yrs:

– 4.2-m William Herschel Telescope (WHT), operated at the Spanish Observatorio del Roque de Los Muchachos of the Instituto de Astrofísica de Canarias, La Palma, Spain by the Isaac Newton Group (ING).

– 8.2-m Very Large Telescope (VLT), operated at the Paranal Observatory, Chile by the European Southern Observatory (ESO).

– 3.5-m New Technology Telescope (NTT), operated at the La Silla Observatory, Chile by ESO.

2.1.2 ULTRASPEC

ULTRASPEC started out life as a spectroscopic alternative to ULTRACAM, consisting of a frame-transfer CCD detector and cryostat, which could be attached to the external foci of existing spectrographs. This design also enabled ULTRASPEC to perform (single-channel) photometry, with the removal of certain spectroscopic-based components (e.g. grisms, slits etc.). This capability was briefly demonstrated in Jun 2009 whilst on the NTT.

Since Nov 2013, ULTRASPEC has been solely used as an photometer, and is permanently mounted at the 2.4-m Thai National Telescope (TNT), operated at the Thai National Observatory, Thailand by the National Astronomical Research Institute of Thailand (NARIT). The conversion to a dedicated imager required a few modifications to the instrument, with a chassis, re-imaging optics and filter wheel being the main additions (Dhillon et al., 2014). ULTRASPEC shares the same primary filter set (SDSS) as ULTRACAM, but with an additional Schott *KG5* filter. The *KG5* filter is a broad filter, covering approximately $u'+g'+r'$ and useful for when observing faint objects with the TNT. Both instruments share the same image area (1024×1024 pixel^2), although ULTRASPEC's frame rate limit (~ 200 Hz) – while still rapid and more than satisfactory for CV eclipse observations – is a factor of $\sim 2.5\times$ lower than that of ULTRACAM.

2.2 Eclipsing CV Observations

Eclipsing CVs have been a popular target for ULTRACAM throughout its ~ 15 yrs of operation. This has resulted in a large archive of eclipse data corresponding to a vast number of systems. In recent years, the archive's growth has accelerated thanks to additional, regular CV eclipse observations with ULTRASPEC. At present, the ULTRACAM/ULTRASPEC data archive contains eclipses from over 90 different eclipsing CVs. Around a quarter of these have been confirmed as either AM CVn (Section 1.2.5), NL/SW Sex (Section 1.2.4), magnetic (Polar/IP; Section 1.2.6) or grazing/partial eclipsing systems, all of which are not suitable for eclipse modelling and therefore not considered further.

Approximately 70 of these eclipsing CVs have some level of modelling potential, and all feature within the upcoming four tables (2.1–2.4). The information given in each table include coordinates, magnitudes (SDSS g' band), orbital ephemerides (T_0 and $P_{\rm orb}$, see Section 3.1), number of ULTRACAM/ULTRASPEC eclipses obtained and comments. These comments primarily describe the structure of a typical eclipse light curve and contribution from each of the individual components (white dwarf, bright spot, accretion disc and donor), but also refer to the strength of flickering present (Section 1.1.1). Flickering can be a serious issue when attempting to model eclipses, especially if the flickering amplitude is comparable to that of the white dwarf or bright spot (see Sections 3.2 and 3.3 for more details). The $\sim$70 systems suitable/potentially suitable for modelling can be categorised as follows:

- Eclipsing CVs modelled prior to this work (Table 2.1).
- Eclipsing CVs with currently sufficient data for modelling (Table 2.2).
- Eclipsing CVs with a *high* future modelling potential (Table 2.3).
- Eclipsing CVs with a *lower* future modelling potential (Table 2.4).

Table 2.1 contains the 16 systems for which ULTRACAM eclipse data has been modelled and system parameters published (see caption of Table 2.1 for references). Four of these systems (indicated by an asterisk in Table 2.1) have been re-modelled in Chapter 7. Table 2.2 lists the 25 systems for which – at time of writing – there is sufficient and suitable ULTRACAM/ULTRASPEC data available for eclipse modelling. Additional eclipses may still be useful in a number of cases, however, in order to improve the accuracy of the calculated system parameters. Eleven of these systems (indicated by an § in table) are modelled in Chapter 7, while the modelling of PHL 1445, ASASSN-14ag and SDSS J105754.25+275947.5 are the subjects of Chapters 4, 5 and 6, respectively. Details of the individual eclipse observations for all eclipsing CVs modelled in this thesis can be found in Appendix A.

The final two tables (2.3 and 2.4) show those systems that are – given current data – not suitable for modelling. This is due to either poor quality data or lack of clear bright spot ingress/egress features in their eclipse light curves. Systems with high future modelling potential are those with evidence of bright spot eclipse features, but which are lacking clarity, either due to poor SNR or merged white dwarf and bright spot ingresses. The latter is a common issue, but may not be the case in future eclipses due to disc radius changes. Systems with lower future modelling potential, on the other hand, have eclipse light curves typically dominated by the accretion disc and heavy flickering, with little (if any) sign of bright spot features. While these systems have a lower modelling potential, they cannot be disregarded completely, as it is possible that the contribution of the accretion disc may decrease (and vice versa for the bright spot) in future eclipses. It is worth noting that no obvious selection biases are introduced here, as the suitability of modelling an eclipsing system depends only on disc radius changes and the shortest-term mass transfer rate, which both occur on timescales considerably shorter than the evolutionary timescale of a CV (see Section 1.5).

2.3 Data Reduction

All ULTRACAM and ULTRASPEC photometry was reduced with the dedicated ULTRACAM pipeline data reduction system software (Dhillon et al., 2007), while all light curve plotting, examination and manipulation was carried out using Tom Marsh's PONTO software[2].

2.3.1 Bias Subtraction

The readout process from the instrument CCDs is not perfect, with an uncertainty introduced to each pixel when its charge is measured. This is referred to as *readout noise* and should ideally be as low as possible. The existence of readout noise opens up the possibility for a pixel to contain negative charge, but the analog to digital converter (ADC), that turns this charge into counts, can only assign positive values. To overcome this issue, a voltage offset is added to each pixel by default. The exact number of added counts – the 'bias level' – varies across the frame, and must be accounted for in the data reduction process.

---

[2] No longer available online.

Object	Right Ascension	Declination	Mag. (g')	T_0 (MJD)	$P_{\rm orb}$ (d)	$P_{\rm orb}$ (m)	$N_{\rm ecl}$	Comments	Pub.	Eph.	Add. Ecl. Times
CTCV J1300−3052* (V1258 Cen)	13 00 29.05	−30 52 57.1	18.6	54262.099166(18)^h	0.0889406998(17)	128.07	4	Prominent BS, clear ingress/egress, moderate flickering	8	10	11
CTCV J2354−4700 (DI Phe)	23 54 20.4	−47 00 20.0	19.6	54261.383885(5)^h	0.065550270(1)	94.39	19	Disc dominated, weak BS	8	8	11
DV UMa*	09 46 36.65	+44 46 45.1	18.7	52782.973948(10)^h	0.0858526308(7)	123.63	4	'Classic' eclipse shape, components clearly distinguishable, minimal flickering	1,8	10	12,13,14
IP Peg	23 23 08.55	+18 24 59.3	15.3	53594.206270(1)^b	0.1582061029(3)	227.82	18	Prominent BS that dominates WD, moderate flickering	7	7	15,16,17
KIS J192748.53+444724.5	19 27 48.49	+44 47 24.6	19.4	56205.5845(17)^b	0.165308(5)	238.04	4	Prominent BS, moderate flickering	9	18	–
OU Vir	14 35 00.22	−00 46 06.3	18.2	51724.53283(7)^h	0.072706113(5)	104.70	8	Notable disc and donor contribution	2,8	2	19
SDSS J090350.73+330036.1	09 03 50.73	+33 00 36.1	19.2	53799.894707(2)^b	0.059073543(9)	85.07	12	WD dominated, very weak BS	6,8	6	–
SDSS J103533.03+055158.4	10 35 33.02	+05 51 58.4	18.8	53798.981469(8)^b	0.0570067(2)	82.09	17	WD dominated, weak BS	4,6,8	6	–

Table 2.1: Eclipsing CVs observed with ULTRACAM/ULTRASPEC – systems modelled previously, with system parameters published in: (1) Feline et al. (2004a), (2) Feline et al. (2004b), (3) Littlefair et al. (2006a), (4) Littlefair et al. (2006b), (5) Littlefair et al. (2007), (6) Littlefair et al. (2008), (7) Copperwheat et al. (2010), (8) Savoury et al. (2011), (9) Littlefair et al. (2014). T_0 is the mid-eclipse time of cycle 0, while $N_{\rm ecl}$ is total number of eclipses obtained. BS and WD abbreviations used for bright spot and white dwarf, respectively. Further references for orbital ephemerides and additional eclipse times: (10) This work (see Section 3.1), (11) Tappert, Augusteijn & Maza (2004), (12) Howell et al. (1988), (13) Patterson et al. (2000), (14) Nogami et al. (2001), (15) Goranskii, Lyutyi & Shugarov (1985), (16) Wood et al. (1989b), (17) Wolf et al. (1993), (18) Scaringi, Groot & Still (2013), (19) Vanmunster (priv. comm.), (20) Southworth et al. (2010), (21) Shears et al. (2008), (22) Szkody et al. (2007), (23) Boyd, Oksanen & Henden (2006), (24) Woudt & Warner (2001), (25) Uemura et al. (2004).

*Re-modelled in Chapter 7, ^{h}Heliocentric (HMJD), ^{b}Barycentric (BMJD)

Object	Right Ascension	Declination	Mag. (g')	T_0 (MJD)	P_{orb} (d)	P_{orb} (m)	N_{ecl}	Comments	Pub.	Eph.	Add. Ecl. Times
SDSS J115207.00+404947.8*	11 52 07.01	+40 49 48.0	19.5	55204.101279(6)^h	0.0677497026(3)	97.56	7	Comparable WD/BS contribution, moderate flickering, low SNR	8	10	20
SDSS J122740.82+513925.0 (GP CVn)	12 27 40.82	+51 39 25.0	18.8	53796.2482451(5)^b	0.062959041(7)	90.66	3	Comparable WD/BS contribution, minimal flickering	6,8	6	21
SDSS J143317.78+101123.3	14 33 17.79	+10 11 23.5	18.5	53858.35689(2)^b	0.054240679(2)	78.11	7	WD dominated, clear BS, minimal flickering	6,8	6	22
SDSS J150137.22+550123.4*	15 01 37.24	+55 01 23.5	19.0	56178.870444(8)^h	0.05684126603(21)	81.85	12	WD dominated, very weak BS, low SNR	6,8	10	–
SDSS J150240.98+333423.9 (NZ Boo)	15 02 40.98	+33 34 23.9	17.4	53799.140607(3)^b	0.05890961(5)	84.83	15	Strong WD, notable disc contribution, clear BS	6,8	6	–
SDSS J150722.30+523039.8 (OV Boo)	15 07 22.26	+52 30 40.2	18.3	53798.239587(3)^b	0.04625828(4)	66.61	8	WD dominated, clear BS, minimal flickering	5,6,8	6	–
SDSS J170213.24+322954.2 (V1239 Her)	17 02 13.25	+32 29 54.3	17.9	53647.736507(29)^h	0.10008215(1)	144.12	14	Clear BS, notable disc and donor contribution	3,8	23	–
XZ Eri	04 11 25.76	−15 23 24.3	19.0	52667.54099(2)^h	0.061159491(5)	88.07	5	WD dominated, clear BS, low SNR	1,8	1	24,25

Table 2.1: *Continued.*

Object	Right Ascension	Declination	Mag. (g')	T_0 (MJD)	$P_{\rm orb}$ (d)	$P_{\rm orb}$ (m)	$N_{\rm ecl}$	Comments	Add. Ecl. Times
ASASSN-14ag[†]	08 13 18.45	−01 03 27.7	16.0	$56990.867004(12)^h$	0.060310665(9)	86.85	14	Visible BS features despite heavy flickering	–
ASASSN-14hq	06 38 19.59	−48 59 16.1	18.1	$57703.277456(14)^h$	0.074326968(10)	107.03	5	‘Classic’ eclipse shape, components clearly distinguishable, low flickering	1
ASASSN-15pb	20 14 22.92	−63 37 58.6	19.5	$57626.142035(14)^h$	0.09328967(3)	134.34	7	WD and BS ingresses just about separated, low flickering	1
AY For	02 42 34.82	−28 02 44.0	18.2	$57701.108854(5)^h$	0.07461448(26)	107.44	5	Strong WD, clear BS, moderate flickering	–
CSS080623 J140454−102702[§]	14 04 53.97	−10 27 02.3	19.5	$55329.234631(13)^h$	0.059578971(3)	85.79	10	Comparable WD/BS contribution, WD egress begins before BS ingress finishes, minimal flickering	–
CSS090102 J132536+210037	13 25 36.06	+21 00 36.8	19.8	$55943.120678(5)^h$	0.0623849110(5)	89.83	9	Comparable WD/BS contribution, visible BS features, low SNR	2
CSS090419 J162620−125557	16 26 19.83	−12 55 56.5	20.5	$56498.927851(19)^h$	0.07544698(8)	108.64	7	Visible BS features, moderate flickering, low SNR	1
CSS090622 J215636+193242	21 56 36.34	+19 32 41.5	19.3	$56874.201951(21)^h$	0.07092930(12)	102.14	7	Visible BS features despite heavy flickering, significant disc contribution	–
CSS110113 J043112−031452[§]	04 31 12.45	−03 14 51.6	19.5	$55942.014642(15)^h$	0.0660508707(18)	95.11	12	Comparable WD/BS contribution, WD egress begins before BS ingress finishes, minimal flickering	–
CSS111003 J054558+022106 (Te 11)	05 45 58.00	+02 21 06.0	19.0	$57730.24240(3)^h$	0.120971471(9)	174.20	8	Prominent BS, significant disc contribution	1
GY Cnc[§]	09 09 50.55	+18 49 47.5	16.7	$55938.263734(22)^b$	0.175442399(6)	252.64	12	Prominent BS, WD/BS ingresses separated large donor contribution, moderate flickering	–

Table 2.2: Eclipsing CVs observed with ULTRACAM/ULTRASPEC – systems ready for modelling. T_0 is the mid-eclipse time of cycle 0, while $N_{\rm ecl}$ is total number of eclipses obtained. BS and WD abbreviations used for bright spot and white dwarf, respectively. All orbital ephemerides shown are from this work (see Section 3.1). References for additional eclipse times: (1) Woudt (priv. comm.), (2) Southworth et al. (2015), (3) Steeghs et al. (2003), (4) Soszyński et al. (2015), (5) Soszyński et al. (2016), (6) Dillon et al. (2008), (7) Southworth et al. (2009), (8) Southworth et al. (2010), (9) Baptista et al. (2003), (10) Vrielmann, Stiening & Offutt (2002), (11) Qian et al. (2015), (12) Bours (priv. comm.).

[*]Modelled in Chapter 4, [†]Modelled in Chapter 5, [‡]Modelled in Chapter 6, [§]Modelled in Chapter 7, ^{h}Heliocentric (HMJD), ^{b}Barycentric (BMJD)

Object	Right Ascension	Declination	Mag. (g')	T_0 (MJD)	$P_{\rm orb}$ (d)	$P_{\rm orb}$ (m)	$N_{\rm ecl}$	Comments	Add. Ecl. Times
IY UMa§	10 43 56.73	+58 07 31.9	17.1	56746.6395010(9)^h	0.07390892818(21)	106.43	10	‘Classic’ eclipse shape, components clearly distinguishable, minimal flickering	3
OGLE BLG-ECL-000082	17 54 16.19	−35 26 39.5	18.0	57623.033842(4)^h	0.0719308073(14)	103.58	2	‘Classic’ eclipse shape, components clearly distinguishable, minimal flickering, crowded field may be issue	4,5
OY Car§	10 06 22.07	−70 14 04.6	15.6	55353.996477(3)^h	0.06312092545(24)	90.89	7	Comparable WD/BS contribution, clear BS features, moderate flickering	–
PHL 1445* (KN Cet)	02 42 42.86	−11 46 45.5	18.0	55867.123983(12)^h	0.0529848892(11)	76.30	19	WD dominated, very heavy flickering, BS features visible in some eclipses	–
SDSS J090103.94+480911.0§ (PU UMa)	09 01 03.94	+48 09 11.0	19.5	55942.116358(8)^h	0.0778805321(5)	112.15	10	Comparable WD/BS contribution, clear BS features, minimal flickering	6
SDSS J100658.40+233724.4§	10 06 58.42	+23 37 24.6	18.6	56682.72973(5)^h	0.185913107(13)	267.71	11	Prominent BS, moderate flickering, large disc contribution	2,7
SDSS J105754.25+275947.5‡	10 57 54.25	+27 59 47.5	19.6	56046.002389(8)^h	0.0627919557(6)	90.42	12	WD dominated, BS features in averaged eclipses, minimal flickering	–
SDSS J152419.33+220920.0	15 24 19.33	+22 09 20.1	19.1	56486.913762(4)^h	0.0653187306(8)	94.06	15	BS egress not clear, moderate flickering, large disc contribution	8
SSS100615 J200331−284941§	20 03 31.27	−28 49 41.3	19.6	56873.023625(5)^h	0.0587045(4)	84.53	3	WD dominated, minimal flickering	–
SSS130413 J094551−194402§	09 45 51.00	−19 44 00.8	16.7	56683.673971(12)^h	0.0657692903(12)	94.71	17	Comparable WD/BS contribution, clear BS features, moderate flickering	1
V2051 Oph	17 08 19.08	−25 48 31.7	15.7	55314.156237(4)^b	0.06242785751(8)	89.90	38	BS features discernible in handful of eclipses, very large disc contribution, heavy flickering	9,10,11
V713 Cep§	20 46 38.70	+60 38 02.8	18.5	56176.936402(7)^h	0.0854185080(12)	123.00	15	WD dominated, moderate flickering	12
Z Cha§	08 07 27.75	−76 32 00.7	15.6	53498.011471(4)^h	0.0744992631(3)	107.28	14	‘Classic’ eclipse shape, components clearly distinguishable, minimal flickering	–

Table 2.2: *Continued.*

Object	Right Ascension	Declination	Mag. (g')	T_0 (MJD)	$P_{\rm orb}$ (d)	$P_{\rm orb}$ (m)	$N_{\rm ecl}$	Comments	Add. Ecl. Times
ASASSN-13cx	00 02 22.40	+42 42 14.2	18.6	56989.689133(17)^h	0.079650060(9)	114.70	6	Clear BS egress but ingresses merged	–
ASASSN-15aa	10 49 25.91	−21 47 35.9	16.8	57773.806750(10)^b	0.37553966(17)	540.78	2	Clear BS egress but ingresses possibly merged, very large donor contribution	1
CSS080306 J082655-000733	08 26 54.70	−00 07 33.1	19.9	56693.898770(13)^h	0.0597644249(19)	86.06	4	BS features not clear, moderate flickering, low SNR	2
CSS081220 J011614+092216	01 16 13.76	+09 22 16.0	19.1	56489.176270(14)^h	0.065843016(3)	94.81	16	BS features not clear, moderate flickering	3
CSS110513 J210846−035031	21 08 46.43	−03 50 31.8	18.0	56489.11448(6)^h	0.15692657(3)	225.97	5	Prominent BS with clear egress but not ingress, large disc contribution	–
CSS131106 J052412+004148	05 24 12.15	+00 41 48.1	18.3	56990.830611(22)^h	0.174666454(19)	251.52	10	Clear BS egress but ingresses merged, large disc contribution	–
MASTER OT J001400.25−561735.0	00 14 00.25	−56 17 35.0	18.3	57625.295956(11)^h	0.071529488(22)	103.00	5	Comparable WD/BS contribution, BS egress not clear, moderate flickering	–
SDSS J074859.55+312512.6	07 48 59.56	+31 25 12.7	17.8	57808.629530(21)^h	0.05831114(5)	83.97	12	Clear BS egress but ingresses merged	–
SDSS J075059.97+141150.1	07 50 59.98	+14 11 50.2	19.0	56658.955303(16)^h	0.093165497(3)	134.16	12	Comparable WD/BS contribution, BS features not clear, heavy flickering	4,5
SDSS J125023.85+665525.5 (OV Dra)	12 50 23.85	+66 55 25.5	18.5	55204.136356(12)^h	0.0587356812(5)	84.58	15	Comparable WD/BS contribution, BS features not clear, heavy flickering	6
SDSS J155531.99−001055.0 (V489 Ser)	15 55 31.99	−00 10 55.0	19.0	54260.226214(5)^h	0.0788455502(3)	113.54	18	WD dominated, faint BS features, minimal flickering	7
V1032 Oph	16 26 09.71	−03 53 24.2	17.5	57795.90439(17)^b	0.081051(7)	116.71	5	Clear BS egress but ingresses merged	–

Table 2.3: Eclipsing CVs observed with ULTRACAM/ULTRASPEC – systems with a *high* future modelling potential (further observations required). T_0 is the mid-eclipse time of cycle 0, while $N_{\rm ecl}$ is total number of eclipses obtained. BS and WD abbreviations used for bright spot and white dwarf, respectively. All orbital ephemerides shown are from this work (see Section 3.1). References for additional eclipse times: (1) Thorstensen, Alper & Weil (2016), (2) Woudt (priv. comm.), (3) Coppejans (priv. comm.), (4) Southworth et al. (2010), (5) Southworth et al. (2015), (6) Dillon et al. (2008), (7) Southworth et al. (2007). ^{h}Heliocentric (HMJD), ^{b}Barycentric (BMJD)

Object	Right Ascension	Declination	Mag. (g')	T_0 (MJD)	$P_{\rm orb}$ (d)	$P_{\rm orb}$ (m)	$N_{\rm ecl}$	Comments	Add. Ecl. Times
ASASSN-15af	01 57 54.91	−54 30 38.0	17.0	57622.17633(8)^h	0.149834(8)	215.76	3	BS features not visible, very large disc contribution, moderate flickering	–
ASASSN-15au	07 44 08.57	+15 39 10.1	17.8	57076.54612(3)^h	0.068949738(14)	99.29	5	BS features not visible, large disc contribution, moderate flickering	–
ASASSN-15bu	02 54 43.68	+22 44 02.7	17.8	57080.523351(25)^h	0.076830311(8)	110.64	5	BS features not visible, large disc contribution, moderate flickering	1
ASASSN-15cw	08 08 18.98	+00 59 00.1	18.0	57777.68106(3)^b	0.079126006(19)	113.94	1	BS features not visible, large disc contribution, moderate flickering	2
ASASSN-15pw	04 46 39.41	−51 32 54.9	19.5	57626.36957(5)^h	0.183439	264.15	1	BS ingress not visible, large disc contribution, moderate flickering. [$P_{\rm orb}$ from Woudt (priv. comm.)]	–
CSS080227 J112634−100210	11 26 33.98	−10 02 10.1	18.8	55333.986155(18)^h	0.0774215733(11)	111.49	7	BS features mostly not visible, large disc contribution, moderate flickering	3
CSS100218 J043829+004016	04 38 29.10	+00 40 15.9	19.5	56657.958272(9)^h	0.0654948(8)	94.31	3	BS features mostly not visible, heavy flickering, caution: uncertain ephemeris	–
CzeV404 Her	18 30 01.76	+12 33 46.1	17.0	56871.91730(4)^b	0.098021254(2)	141.15	7	No WD eclipse visible, only disc and BS, due to high state?	–
GALEX J003535.7+462353	00 35 35.72	+46 23 52.4	17.0	55940.82430(5)^h	0.172274910(12)	248.08	16	BS features not visible, very large disc contribution, moderate flickering	4
GSC 04560−02157	15 43 36.65	+75 15 41.2	15.1	57462.88371(5)^h	0.265360053(23)	382.12	2	BS ingress not visible, WD not clear, large donor and disc contribution	5,6

Table 2.4: Eclipsing CVs observed with ULTRACAM/ULTRASPEC – systems with a *lower* future modelling potential (further observations required). T_0 is the mid-eclipse time of cycle 0, while $N_{\rm ecl}$ is total number of eclipses obtained. BS and WD abbreviations used for bright spot and white dwarf, respectively. The orbital ephemerides shown are from this work (see Section 3.1), with the exception of ASASSN-15pw, IR Com and V4140 Sgr (see comments for references). References for additional eclipse times: (1) Watson (priv. comm.), (2) Thorstensen, Alper & Weil (2016), (3) Southworth et al. (2015), (4) Wils et al. (2011), (5) Khruslov et al. (2015), (6) Han et al. (2016), (7) Pyrzas et al. (2012), (8) Kennedy et al. (2016).

^{h}Heliocentric (HMJD), ^{b}Barycentric (BMJD)

Object	Right Ascension	Declination	Mag. (g')	T_0 (MJD)	P_{orb} (d)	P_{orb} (m)	N_{ecl}	Comments	Add. Ecl. Times
HS 2325+8205	23 26 50.30	+82 22 11.2	16.7	56487.19545(5)^h	0.194334532(6)	279.84	3	No WD eclipse visible, only disc and BS, due to high state?	7
HT Cas	01 10 13.13	+60 04 35.4	16.5	56874.050584(16)^h	0.0736471745(5)	106.05	15	BS ingress sometimes visible, egress lost in heavy flickering	–
IR Com	12 39 32.02	+21 08 06.2	18.3	49485.9818691(26)^h	0.08703862787(20)	125.34	9	BS ingress sometimes visible, egress lost in heavy flickering. [Ephemeris from Feline et al. (2005)]	–
MASTER OT J003059.39+301634.3	00 30 59.40	+30 16 34.4	18.1	57199.18598(3)^h	0.07026252(3)	101.18	4	BS features not visible, moderate flickering	–
MASTER OT J192328.22+612413.5	19 23 28.36	+61 24 13.8	18.5	56873.057146(19)^h	0.16764650(6)	241.41	2	BS features not visible, large disc contribution, moderate flickering	8
MASTER OT J232100.42+494614.0	23 21 00.42	+49 46 14.7	18.6	56992.62087(10)^h	0.2123774(8)	305.82	3	Cannot comment on eclipse structure due to very low SNR	–
SDSS J040714.78−064425.1 (LT Eri)	04 07 14.78	−06 44 25.0	17.8	54396.23376(8)^h	0.170203913(7)	245.09	6	BS features not visible, large disc contribution	–
SDSS J155656.92+352336.6 (BT Crb)	15 56 56.93	+35 23 36.6	18.8	56046.02626(5)^h	0.088091485(9)	126.85	8	No WD eclipse visible, only disc and BS, due to high state?	–
V4140 Sgr	19 58 49.70	−38 56 13.3	17.8	46261.17145(6)^b	0.0614296779(9)	88.46	6	BS features not visible, large disc contribution, moderate flickering. [Ephemeris from Baptista et al. (2003)]	–

Table 2.4: *Continued.*

The bias level of each pixel can be acquired by reading out the CCD without a prior exposure. The result is a 'bias frame', which can be subtracted from each exposure to remove the bias level of each pixel. Biases are usually taken at the start of every observing night with ULTRACAM/ULTRASPEC, with each bias run consisting of typically 50+ individual frames. In the reduction process, these multiple bias frames were averaged to create a 'master bias', which was subsequently subtracted from each exposure.

2.3.2 Flat Fielding

All pixels within a CCD will have slightly different sensitivities to incoming light, and this must also be be accounted for in the reduction process, especially when performing aperture photometry (see Section 2.3.4). A measure of the sensitivity of each pixel is obtained by exposing the CCD to a light source as close to uniform as possible. The twilight sky is typically used for this, providing conditions are clear. Counts are kept below $\sim 30\,000$, as above this limit structure begins to form within the ULTRACAM CCDs – a phenomena referred to as 'peppering'. The resulting frame is called a 'flat field', and can be normalised by dividing the counts in each pixel by the average counts within the frame. Pixels with greater than average sensitivity now have values greater than one, while those below average will have values less than one. Dividing an exposure by a normalised (and bias-subtracted) flat field can correct for variations in pixel sensitivity.

Flat fields of the twilight sky are taken each clear observing night with ULTRACAM/ULTRASPEC, either at evening twilight, morning twilight or sometimes both. The telescope is pointed towards an empty sky field and set to track a spiral pattern. This minimises the contamination from any stars in the field which may start to become visible in twilight. Flat fields are obtained in each filter, with exposures taken until a sufficient number (>10) have counts within the suitable range of $\sim 10\,000$–$30\,000$. In the reduction process, a flat field's exposures were firstly bias-subtracted, for the same reasons described in the previous section. Those exposures with counts outside of the suitable range were discarded, while the rest were averaged to produce a 'master flat field', which was subsequently normalised. Every exposure of the observation being reduced was then divided by this master flat field.

2.3.3 Dark Frames

Not all charge within a CCD pixel is the result of photometrically excited electrons. It is also possible for electrons to be thermally excited from the random motion of silicon atoms in the lattice (Hellier, 2001). Such a contribution to the overall charge is referred to as *dark current* and while it is a very significant issue at room temperature, it can be negated by cooling the CCD to much lower temperatures. The dark current can be measured by taking a 'dark frame', an exposure of same length as that of the observation, but without the CCD exposed to light. A dark frame can then be subtracted from each exposure of the observation, in order to correct for dark current.

The ULTRACAM CCDs are Peltier-cooled to $-40°$C, while ULTRASPEC's CCD is cooled to approximately $-110°$C by liquid nitrogen. A consequence of these very low operating temperatures – together with short exposures times (typically 1–10 s) – is a negligible dark current associated with all observations included in this work. The subtraction of dark frames to correct for dark current was therefore not necessary here.

2.3.4 Aperture Photometry

In the data reduction pipeline, counts from objects in ULTRACAM/ULTRASPEC data images are measured through use of apertures, a technique known as *aperture photometry*. Figure 2.1 shows a section of an ULTRACAM data image with two objects surrounded by overlaid apertures. The object at the centre of aperture one

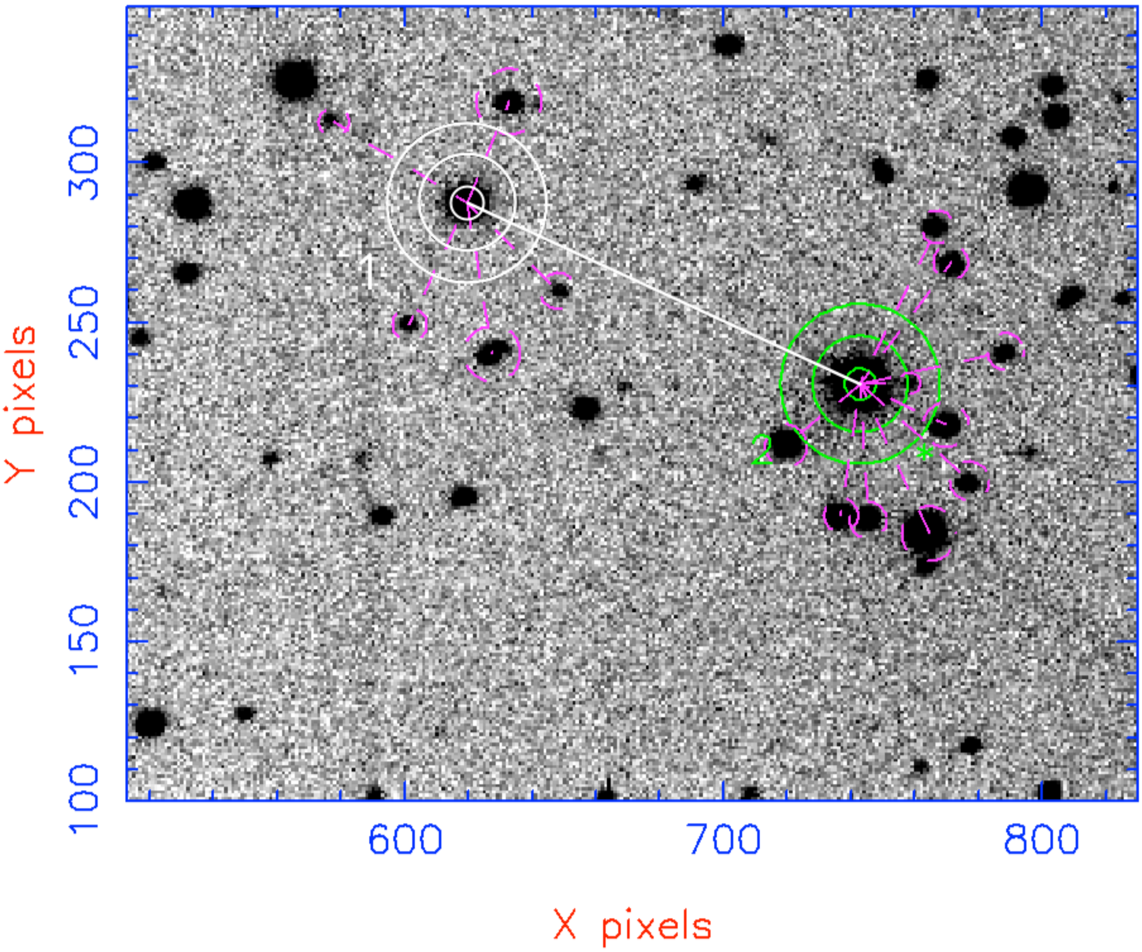

Figure 2.1: Section of an ULTRACAM data image with overlaying apertures. Aperture one (white) is centred on the target, while aperture two (green) is centred on the comparison star. Counts from the pixels enclosed by an aperture's inner circle contribute to the central object's signal, while those within the outer annulus contribute to the sky signal. The straight white line shows that the two apertures are linked. The smaller purple apertures show objects that are 'masked' to avoid contamination in the sky annulus. Note that the colours of the image have been inverted for the purpose of clarity.

(white) is the target eclipsing CV. The counts from all pixels within this aperture's inner circle are summed and attributed to the target. However, in addition to counts originating from the target, these pixels contain counts from the sky background, which need subtracting. Obtaining a measurement of the sky background is the purpose of the two larger circles of the aperture. They create an annulus around the target that covers an area of pixels largely free of any sources[3], and therefore any counts can be attributed to the sky background. The counts from all of the pixels within the annulus are summed and divided by the number of pixels to find the typical sky background counts per pixel. This value can then be subtracted from all pixels within the inner circle to remove the contribution from the sky background.

Not all variations in the target signal are intrinsic, as variations associated with the transparency and stability of Earth's atmosphere can also have an affect. Atmospheric variations are accounted for by using a *comparison star*, which must be a bright[4] and non-variable star within the same image frame as the target. The comparison star in Figure 2.1 is the object at the centre of aperture two (green). This second aperture – importantly the same size as used for the target in order to obtain the same percentage of counts as the target – is used to measure a comparison star signal (in the same way as described for aperture one). Any atmospheric variations should affect both target and comparison equally, and can therefore be removed by calculating the ratio of target and comparison star signals.

When performing aperture photometry, it is important to maximise the SNR of the output data produced. The variable with the biggest impact on the SNR is the size of the inner aperture. As the size of the inner aperture increases, more sky background pixels become enclosed and as a consequence additional noise is introduced, thus decreasing SNR. This suggests that smaller apertures are more

---

[3] In the majority of cases there is at least one object located within the annulus. This would create an inaccurate sky background measurement, and therefore any such objects must be 'masked', i.e. have their pixel's counts ignored. All objects surrounded by pink apertures in Figure 2.1 have been masked.

[4] At least brighter than the target, in order to minimise noise.

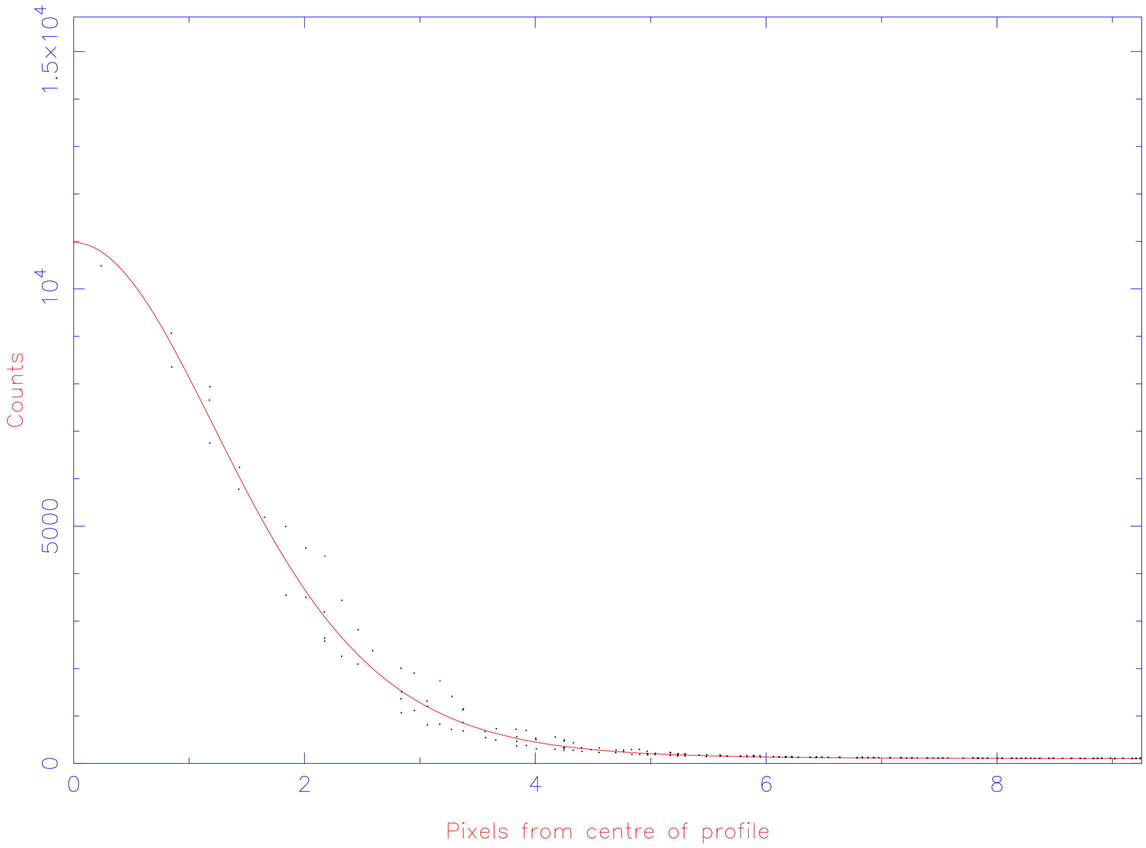

Figure 2.2: Moffat fit (red line) to profile of comparison star (black points). Each point represents an individual pixel.

favourable, but smaller apertures result in less signal from both target and comparison being recorded and SNR once again decreases. Consequently, there exists an optimal scaling relation between the full-width at half maximum (FWHM) of the sources and size (radius) of inner aperture used which needs utilising. It is possible for the atmospheric seeing – and therefore source FWHM – to vary significantly across an observation, and so a varying aperture size from exposure to exposure is also highly desirable.

The ULTRACAM reduction pipeline is able to accommodate both fixed and variable apertures. For variable apertures, the source FWHM for each exposure is measured through fitting a Moffat[5] distribution (Moffat, 1969) to the comparison star profile, as shown in Figure 2.2. Variable apertures were used in the reduction of all observations, while each observation was reduced multiple times – each using

---

[5] Able to achieve a better fit to source profiles than both Gaussian and Lorentzian distributions.

a different scaling relation – in an attempt to maximise SNR. For bright systems ($g' \lesssim 17$), a scaling factor of ~ 1.5 was commonly chosen, while a lower value of ~ 1.0 was often preferred for fainter systems. For those observations with the lowest SNR – due to poor conditions or an intrinsically very faint target – 'optimal' extraction was used (see Naylor 1998).

2.4 Flux Calibration

The eclipse light curves resulting from the aperture photometry reduction process described in the previous section have y-axis units of target counts as a fraction of comparison star counts ($C_{\rm CV}/C_{\rm c}$). However, units of absolute flux ($F_\nu^{\rm CV}$) are required for eclipse modelling, so that the temperature of the white dwarf can be estimated. A white dwarf temperature estimate is important, as the calculation of system parameters utilises a temperature-dependent white dwarf mass-radius relation (See Section 3.7.2).

2.4.1 Calibrating Comparison Star Magnitudes

The first step towards acquiring $F_\nu^{\rm CV}$ involves converting $C_{\rm c}$ into a calibrated comparison star magnitude ($m_{\rm c}$). As the following equation shows, this conversion requires correcting for both atmospheric extinction ($\kappa_\lambda X_{\rm c}$) and instrumental response (c):

$$m_{\rm c} = -2.5 \log_{10}\left(\frac{C_{\rm c}}{t_{\rm exp}}\right) - \kappa_\lambda X_{\rm c} + c, \tag{2.1}$$

where $t_{\rm exp}$ is the exposure time. The value of $C_{\rm c}$ included here is obtained from a second reduction of the data, but this time using only a single aperture centred on the comparison star, with an inner aperture sufficiently large enough to comfortably surround the entire star. As there is a value of $C_{\rm c}$ associated with each exposure, the mean value is taken.

Atmospheric Extinction

When observing from the surface of the Earth, the light from a source must pass through the Earth's atmosphere before it is detected. The atmosphere absorbs and scatters a proportion of this light, causing the source to appear fainter than it actually is, and therefore this needs correcting for when calibrating magnitudes. The level of absorption and scattering is dependent on the wavelength of light, the atmospheric composition, and the amount of atmosphere between source and detector, otherwise known as airmass.

The composition (e.g. amount of dust present) of the local atmosphere is addressed using atmospheric extinction coefficients (κ_λ), with a unique coefficient for each wavelength band to account for the wavelength dependent nature of extinction. For WHT observations up to Aug 2013, nightly measured r'-band extinction coefficients were available – courtesy of the Carlsberg Meridian Telescope (CMT)[6] – and subsequently converted into the other wavelength bands using the information provided in La Palma Technical Note 31[7]. For nights where extinction wasn't measured, the typical values from the CMT for a good quality, dust free night were used. No nightly extinction measurements exist for the NTT, so typical values[8] were used for all NTT observations. It is the same situation for the TNT, with extinction measurements obtained during the commissioning phase (Nov 2013) of ULTRASPEC (Dhillon et al., 2014) used for all TNT observations.

The airmass (X) differs depending on the position of the source on the sky, and is defined as the secant of the zenith angle (z). The airmass at zenith ($z = 0^{\mathrm{o}}$) is therefore 1, and increases towards lower altitudes. Airmasses of 2 and 3 correspond to altitudes of 30^{o} ($z = 60^{\mathrm{o}}$) and $\sim 20^{\mathrm{o}}$ ($z \sim 70^{\mathrm{o}}$), respectively. X can be calculated with knowledge of the telescope's geographical coordinates, target's celestial coordinates and time of observation.

---

[6] http://www.ast.cam.ac.uk/ioa/research/cmt/camc_extinction.html

[7] http://www.ing.iac.es/astronomy/observing/manuals/ps/tech_notes/tn031.pdf

[8] https://www.eso.org/sci/observing/tools/Extinction.html

Instrumental Response

Each individual telescope+instrument setup will obtain a unique number of counts – and therefore magnitude – from the exact same star in the same filter and atmospheric conditions. This is primarily due to differing telescope sizes, but is also affected by the efficiencies of the optics, coatings and detectors involved. All of these factors are combined to form the instrumental response of a telescope+instrument, which must be accounted for when calibrating magnitudes, hence the inclusion of a constant term (c) in equation 2.1.

Unlike the calibration for atmospheric extinction, instrumental response is not calculated, but dealt with through observations of standard stars. Standard stars are non-variable stars with calibrated magnitudes available in the literature. The counts obtained from a standard star observation (C_{std}) can be converted to a calibrated standard star magnitude (m_{std}) in a similar way to equation 2.1:

$$m_{\mathrm{std}} = -2.5 \log_{10} \left(\frac{C_{\mathrm{std}}}{t_{\mathrm{exp}}} \right) - \kappa_{\lambda} X_{\mathrm{std}} + c. \tag{2.2}$$

Providing the standard star was observed using the same telescope+instrument setup, filter(s) and in the same atmospheric conditions[9] as the comparison star observation requiring calibration, equation 2.2 can be subtracted from equation 2.1 to remove the unknown constant c. Rearranging then gives the following:

$$m_{\mathrm{c}} = m_{\mathrm{std}} - 2.5 \log_{10} \left(\frac{C_{\mathrm{c}}}{C_{\mathrm{std}}} \right) - \kappa_{\lambda} (X_{\mathrm{c}} - X_{\mathrm{std}}), \tag{2.3}$$

where C_{c} and C_{std} are now in units of counts per second. It is also important that the same aperture size used for the comparison star reduction is also used for the standard star reduction.

The ULTRACAM/ULTRASPEC data archive contains a multitude of standard

---

[9] preferably observed during the same night.

star observations, the majority from the u', g', r', i', z' standard star system (Smith et al., 2002). Standards from this system were used to calibrate all magnitudes in this work. Values for $m_{\rm std}$ in u', g', r', i' and z' were obtained from Table 8 of Smith et al. (2002), however no such values for the *KG5* filter exist in the literature due to no prior calibration of the filter. With no *KG5* magnitudes for these SDSS standards available, calculation of theoretical magnitudes – and therefore calibration of the *KG5* filter – was necessary.

Calibration of *KG5* Filter

The vast majority of the work involved in calibrating the *KG5* filter was carried out by fellow PhD candidate (since graduated) Liam Hardy. See Appendix A of Hardy et al. (2017) for an in-depth report into the calibration process, as only a brief overview is included here.

Theoretical magnitudes can be calculated through use of bolometric corrections (BCs; e.g. Bell et al. 2012). The BC of a star in a specific filter is defined as the difference in magnitude in that filter compared to the bolometric magnitude, $M_{\rm bol}$. For example, in the SDSS g' and *KG5* filters:

$$\mathrm{BC}_{g'} = M_{\rm bol} - m_{g'}, \tag{2.4}$$

$$\mathrm{BC}_{\mathit{KG5}} = M_{\rm bol} - m_{\mathit{KG5}}. \tag{2.5}$$

Making $M_{\rm bol}$ the subject of both equation 2.4 and 2.5, they can be equated and rearranged to form:

$$m_{\mathit{KG5}} - m_{g'} = \mathrm{BC}_{g'} - \mathrm{BC}_{\mathit{KG5}}. \tag{2.6}$$

The difference between a star's magnitude in g' and *KG5* filters can therefore be obtained if the BCs for each filter are known. The BC of a star in a particular filter can be calculated with knowledge of both the star's spectrum and throughput model of

$T_{\rm eff}$(K)	$m_{KG5} - m_{g'}$	$T_{\rm eff}$(K)	$m_{KG5} - m_{g'}$	$T_{\rm eff}$(K)	$m_{KG5} - m_{g'}$
3500	−0.841	5500	−0.254	7500	0.011
3600	−0.814	5600	−0.233	7600	0.021
3700	−0.798	5700	−0.215	7700	0.030
3800	−0.780	5800	−0.198	7800	0.039
3900	−0.762	5900	−0.181	7900	0.048
4000	−0.748	6000	−0.167	8000	0.056
4100	−0.703	6100	−0.151	8100	0.066
4200	−0.672	6200	−0.137	8200	0.074
4300	−0.631	6300	−0.123	8300	0.083
4400	−0.585	6400	−0.109	8400	0.090
4500	−0.553	6500	−0.097	8500	0.098
4600	−0.503	6600	−0.084	8600	0.104
4700	−0.467	6700	−0.072	8700	0.110
4800	−0.431	6800	−0.060	8800	0.116
4900	−0.397	6900	−0.049	8900	0.121
5000	−0.370	7000	−0.038	9000	0.125
5100	−0.340	7100	−0.027	9100	0.129
5200	−0.316	7200	−0.017	9200	0.134
5300	−0.293	7300	−0.007		
5400	−0.271	7400	0.003		

Table 2.5: Differences in magnitude between *KG5* and g' filters ($m_{KG5} - m_{g'}$) for theoretical star effective temperatures in the range 3500–9200 K.

telescope+instrument+detector+filter as a function of wavelength (see equation A2 of Hardy et al. 2017). A throughput model already existed from the commissioning phase of ULTRASPEC on the TNT (Dhillon et al., 2014), while model spectra for a range of theoretical main sequence ($\log g < 4$) stars with unique $T_{\rm eff}$ and $\log g$ pairs were produced using both the Dartmouth stellar evolution database (Dotter et al., 2008) and the spectral atlas of Castelli & Kurucz (2004). Calculating the BC for each theoretical star in both *KG5* and g' filters enabled the magnitude difference ($m_{KG5} - m_{g'}$) to be found (from equation 2.6).

The final product of the calibration process is shown in Table 2.5, which contains the magnitude differences in *KG5* and g' filters ($m_{KG5} - m_{g'}$) for theoretical star effective temperatures in the range 3500–9200 K. Table 2.5 allowed m_{KG5} to be estimated for any SDSS standard used, with both $m_{g'}$ and spectral type (an indicator of T_{eff}) of all SDSS standards contained within Smith et al. (2002).

2.4.2 Absolute Fluxes

The SDSS photometric system utilised by both ULTRACAM and ULTRASPEC is designed so that its zero point is on the spectrophotometric AB magnitude system. As a consequence, an SDSS magnitude of zero corresponds to a flux per unit frequency (F_ν) of 3631 Jy (Oke & Gunn, 1983), where $1\,\mathrm{Jy} = 10^{-23}\,\mathrm{erg\,s^{-1}\,cm^{-2}\,Hz^{-1}}$. The conversion between the SDSS magnitude of the comparison star (m_{c}) and its absolute flux (in mJy) in that particular wavelength band (F_ν^{c}) is as follows (Oke & Gunn, 1983):

$$F_\nu^{\mathrm{c}}(\mathrm{mJy}) = 3.631 \times 10^6 \times 10^{-0.4 m_{\mathrm{c}}}. \tag{2.7}$$

The eclipse light curve y-axis can be converted from units of $C_{\mathrm{CV}}/C_{\mathrm{c}}$ to F_ν^{CV} through simply multiplying by F_ν^{c}:

$$F_\nu^{\mathrm{CV}}(\mathrm{mJy}) = F_\nu^{\mathrm{c}}(\mathrm{mJy}) \left(\frac{C_{\mathrm{CV}}}{C_{\mathrm{c}}}\right). \tag{2.8}$$

Chapter 3

Data Analysis Techniques

3.1 Orbital Ephemerides

All eclipsing systems have their own unique orbital ephemeris, which can be used as a tool for predicting times of future eclipses. A linear orbital ephemeris consists of the following terms:

$$T_{\mathrm{mid}}^{E} = T_0 + P_{\mathrm{orb}} E, \tag{3.1}$$

where T_{mid}^{E} and T_0 are the mid-eclipse times of cycles E and 0, respectively, and P_{orb} is the orbital period of the system. With a typical CV P_{orb} being a few hours, across the space of a year they can clock up thousands of cycles. Any inaccuracies in P_{orb} – even on the order of tenths of a second – can therefore lead to significantly erroneous eclipse timing predictions after just one year. It is therefore imperative for long-term eclipse timing prediction that P_{orb} and T_0 are measured with the highest accuracy possible.

Updated orbital ephemerides for the majority of eclipsing CVs with modelling potential in the ULTRACAM/ULTRASPEC archive were calculated for this work, and are included in Tables 2.1–2.4. This required measurement of mid-eclipse times for all eclipses, a task carried out in Tom Marsh's PONTO software. The x-axis of each eclipse light curve from the reduction process is Coordinated Universal Time

(UTC), in the form of Modified Julian Date (MJD), which first had to be corrected for light-travel time corrections. MJD was corrected for the changing position of the Earth with respect to either the Sun (Heliocentric MJD or HMJD) or barycentre of the Solar System (Barycentric MJD or BMJD). The correction used was decided upon a system-to-system basis, and depended on previous mid-eclipse times and ephemeris in the literature (see below). Mid-eclipse times were taken to be the mid-eclipse time of the white dwarf, as this allowed the most precise timing measurement for each eclipse. Times of white dwarf mid-ingress ($T_{\rm wi}$) and mid-egress ($T_{\rm we}$) were measured from the light curves, with visual help from an overlaid smoothed light curve derivative plot. In the derivative of the light curve, $T_{\rm wi}$ and $T_{\rm we}$ are a sharp minimum and maximum, respectively. The time of mid-eclipse ($T_{\rm mid}$) was then calculated:

$$T_{\rm mid} = \frac{(T_{\rm wi} + T_{\rm we})}{2}. \tag{3.2}$$

It must be noted that for eclipses with no clear white dwarf features, mid-eclipse was taken as the point of minimum light. For each system, one eclipse was chosen – typically the one with the clearest white dwarf features – to be cycle 0. The mid-eclipse time of this eclipse ($T_{\rm mid} = T_0$), along with a value of $P_{\rm orb}$ from the literature were then used to assign cycle numbers to all eclipses, along with any other available mid-eclipse times in the literature[1]. The cycle numbers and mid-eclipse times of all non-outburst eclipses from a given system were then fit linearly, with the intercept and gradient of the line of best fit representing T_0 and $P_{\rm orb}$, respectively. The errors on the mid-eclipse times of the ULTRACAM/ULTRASPEC eclipses were adjusted so that the reduced $\chi^2 = 1$. A linear ephemeris was found to be suitable for almost all systems, however a handful show evidence for small variations in $P_{\rm orb}$ (of order 20–40 s over a timescale of years). Period variations in CVs are thought to be caused by a magnetically-driven process within the donor, such as Applegate's mechanism

---

[1] Not all mid-eclipse times within the literature are measured using the white dwarf, creating a shift in mid-eclipse times compared to those from this work. This was accounted for by adding necessary offsets to the times from alternate methods.

(e.g. Applegate 1992; Bours et al. 2016), although in many cases variations are too large for Applegate's mechanism itself (e.g. Brinkworth et al. 2006; Bours et al. 2014).

The orbital ephemeris can also be used to phase-fold eclipse light curves, converting the x-axis from MJD into orbital phase, with a phase of 0 corresponding to the time of (white dwarf) mid-eclipse. All eclipse light curves included in this work were phase-folded using the updated ephemerides located in Tables 2.1 and 2.2.

3.2 Physical Model of a CV

At the beginning of the previous Chapter it was briefly mentioned that the complex shape of a CV eclipse light curve can be used to obtain system parameters, under the provision that the individual eclipses of the white dwarf and bright spot by the secondary star are present and clearly resolved. This technique is based on a number of important relations and assumptions. Firstly, assuming the secondary star fills its Roche lobe, the radius depends solely on q (see equation 1.3). The width of white dwarf eclipse ($\Delta\phi$) is therefore strictly a function of q and i: $\Delta\phi = f(q,i)$ (Bailey, 1979). Secondly, assuming the gas stream emanating from the secondary star follows a ballistic trajectory (path determined by q[2]; Lubow & Shu 1975), the timings of bright spot ingress (ϕ_{bi}) and egress (ϕ_{be}) are also dependent on q and i, in addition to the disc radius as a fraction of the distance to L1 ($R_{\mathrm{disc}}/x_{\mathrm{L1}}$). $\Delta\phi$, ϕ_{bi} and ϕ_{be} can all be measured from an eclipse light curve, providing the three constraints required in order to solve these two relations and acquire values for q, i and $R_{\mathrm{disc}}/x_{\mathrm{L1}}$. A third assumption that the white dwarf is unobscured with an unmodified surface brightness allows the radius of the white dwarf as a fraction of the distance to L1 (R_1/x_{L1}) to be calculated from q, i and the measured length of white dwarf ingress/egress. Under a fourth and final assumption that the white

---

[2] A lower q results in the gas stream following a wider trajectory.

dwarf can be accurately described by a theoretical mass-radius relation, values for q, i and R_1/x_{L1} can be used to calculate the remaining system parameters, e.g. M_1, M_2, R_1, R_2, a, etc. (see Section 3.7.2 for more details).

Early studies developing this technique measured eclipse contact phases either directly from the eclipse light curve (e.g. Smak 1979; Vogt et al. 1981; Cook & Warner 1984; Cook 1985) or its derivative[3] (e.g. Wood, Irwin & Pringle 1985; Wood et al. 1986, 1989a). An alternative approach – pioneered by Horne et al. (1994) – involves the construction of a physical model of the CV system, which can be used to produce individual eclipse light curves for each of the system components. The model parameters control the shape and scale of the individual eclipse light curves, and can be adjusted to create an aggregate eclipse light curve that best fits the data. The best-fitting model parameters (namely q, $\Delta\phi$ and R_1/x_{L1}) can then be used to calculate system parameters (see Section 3.7.2). This modelling technique has been utilised in a number of studies over the past two decades (e.g. Feline et al. 2004a; Littlefair et al. 2008; Copperwheat et al. 2010; Savoury et al. 2011), and has gradually increased in complexity during this period. A comparison of these two approaches was made by Feline et al. (2004a), who found that while they both produce consistent results, the model is preferred over the contact phase approach due to the exploitation of a significantly larger proportion of the eclipse light curve. This is especially advantageous in the presence of flickering (see Section 3.3).

The physical CV model also relies on the four assumptions mentioned above, and therefore the accuracy of this technique is dependent on their validity. While it is difficult to test each of these assumptions directly, it is reassuring that spectroscopically determined system parameters appear to be largely in agreement with those obtained from the model (e.g. Tulloch, Rodríguez-Gil & Dhillon 2009; Copperwheat et al. 2010, 2012; Savoury et al. 2012; Littlefair et al. 2013). The validity of one of these assumptions, namely that of an unobscured white dwarf, has recently been

---

[3] Similar to that used to measure mid-eclipse times in this work (see Section 3.1).

questioned by Spark & O'Donoghue (2015) following fast photometric observations of the dwarf nova OY Car. However, it is not yet completely clear that the results of Spark & O'Donoghue (2015) cannot be explained by flickering in the boundary layer and inner disc, and the agreement between photometric and spectroscopic parameter estimates suggest an unobscured white dwarf is still a reasonable assumption to make.

The model used throughout this work is the same as that used by Savoury et al. (2011). There are 18 model parameters in total (see Section 3.2.1 for a full list), which control the shape and scale of light curves for the four components within the CV system: white dwarf, bright spot, accretion disc and secondary star. The following subsections include a brief description of how each component is incorporated into the model.

Secondary Star

As the secondary star is the eclipsing object within the model, its light curve does not include an eclipse. The secondary star light curve does, however, possess ellipsoidal variation – a consequence of its distorted shape due to filling its Roche lobe. The secondary star has flux F_2.

White Dwarf

The white dwarf is represented in the model as an unobscured sphere that is eclipsed by the secondary star. It has flux F_1, radius R_1, and is linearly limb-darkened:

$$\frac{I_1^l}{I_1^0} = 1 - U_1(1 - \cos\beta), \tag{3.3}$$

where I_1^l and I_1^0 are the intensities at the limb and centre of the white dwarf, respectively, β is the angle between a line normal to the surface of the white dwarf and the observer's line of sight, and U_1 is the white dwarf linear limb-darkening coefficient.

U_1 is included as a parameter of the model.

Accretion Disc

The accretion disc is modelled as a disc within the orbital plane that is comprised of a series of concentric annuli. The intensity at each annuli depends on its radius R, and is determined by the following radial intensity distribution for the disc: $I_{\rm disc} \propto R^{-b}$. The value of b determines the power-law of the disc's intensity distribution and is included as a parameter of the model. The disc has total flux $F_{\rm disc}$ and radius $R_{\rm disc}$[4].

Bright Spot

The bright spot is the most complex component to model. It is characterised – with no physical motivation – as two linear strips with emitting surfaces perpendicular to the orbital plane that pass through the point where the gas stream and disc intersect. Both strips occupy the same physical space, with one emitting isotropically and the other emitting/beaming in a specific direction. The bright spot has flux $F_{\rm bs}$, with the fraction of $F_{\rm bs}$ emitted isotropically defined as $f_{\rm iso}$.

The direction of the bright spot strips in the orbital plane, relative to the line passing through both the centre of the white dwarf and secondary star is determined by the bright spot angle, $\theta_{\rm az}$ (see Figure 3.1). Including $\theta_{\rm az}$ as a parameter of the model ensures that any variation in the orbital phase of the bright spot orbital hump can be accommodated for. The schematic of the bright spot model in Figure 3.1 shows that the beaming angle of the non-isotropic strip is determined by two angles: tilt ($\theta_{\rm tilt}$) and yaw ($\theta_{\rm yaw}$). $\theta_{\rm tilt}$ controls the beaming angle out of the orbital plane, while $\theta_{\rm yaw}$ controls the beaming angle within the orbital plane. For eclipse light curves with less prominent bright spot features, it is possible to reduce the complexity of the bright spot model by removing $\theta_{\rm tilt}$ and $\theta_{\rm yaw}$ as model parameters

---

[4] Determined from the distance between bright spot and white dwarf, as bright spot is expected to lie at the edge of the disc.

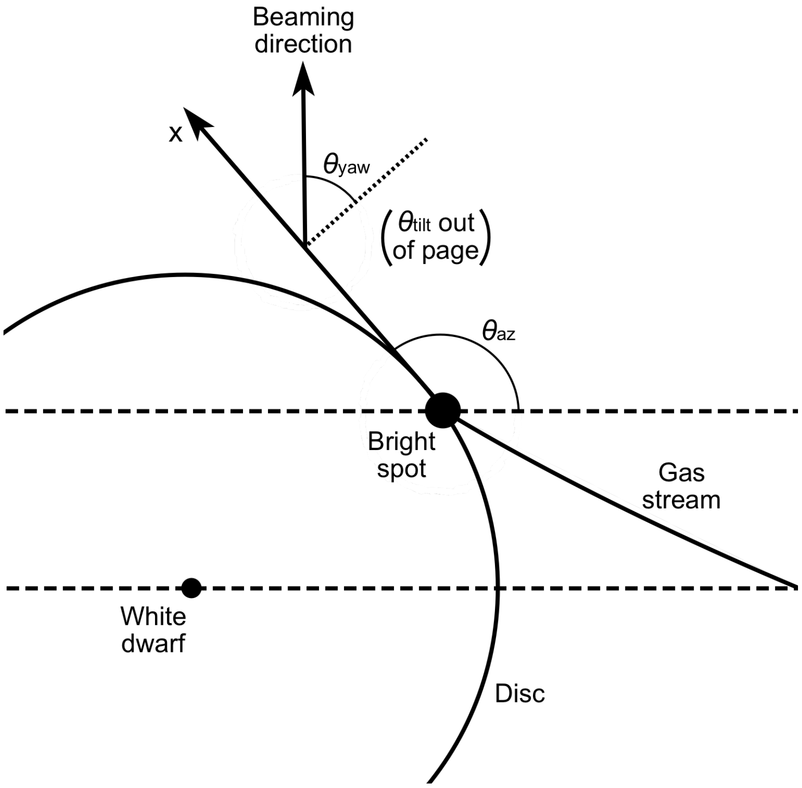

Figure 3.1: A schematic diagram of the bright spot model. The lower of the two dashed parallel lines passes through both the centre of the white dwarf and secondary star (located to the right of diagram), while the other passes through the centre of the bright spot. The dotted line is perpendicular to the the bright spot strip's surface and indicates the (fixed) beaming direction of the simple bright spot model.

and fixing the beaming angle to be perpendicular to the non-isotropic strip's surface. This is equivalent to holding θ_{tilt} and θ_{yaw} to 90° and 0°, respectively.

The intensity distribution of the bright spot strips is described by:

$$I_{\text{bs}} \propto \left(\frac{X}{S}\right)^{Y} \exp\left[-\left(\frac{X}{S}\right)^{Z}\right], \tag{3.4}$$

where X is the distance along the strips and S is the bright spot scale, while Y and Z are the first and second exponents, respectively. S, Y and Z are all included as parameters of the model, enabling the construction of a wide range of different bright spot intensity distributions. This is an important capability for when modelling eclipses with prominent bright spots that have complex ingress/egress shapes. However, just as the bright spot beaming direction can be fixed for less prominent bright spot eclipses, so can the exponents of the intensity distribution. This involves both Y and Z being removed as model parameters and fixing their values to 2 and 1, respectively. With these four bright spot parameters ($\theta_{\rm tilt}$, $\theta_{\rm yaw}$, Y, Z) removed, the model is referred to as the 'simple' bright spot model (as opposed to 'complex' bright spot model with them included).

The model defines the point of intersection between gas stream and disc as the distance along the bright spot strip where the maximum of the intensity distribution occurs, $X(I_{\rm bs,max})$. From equation 3.4, this corresponds to:

$$X(I_{\rm bs,max}) = S\left(\frac{Y}{Z}\right)^{1/Z}. \tag{3.5}$$

For the simple bright spot model ($Y = 2$, $Z = 1$), this simplifies to $X(I_{\rm bs,max}) = 2S$.

3.2.1 Model Parameters

To summarise, here is a list of all 18 model parameters (the final four parameters can be excluded if only a simple bright spot model is required):

- White dwarf flux contribution, F_1.
- Disc flux contribution, $F_{\rm disc}$.
- Bright spot flux contribution, $F_{\rm bs}$.
- Secondary star flux contribution, F_2.
- Mass ratio, $q = M_2/M_1$.
- White dwarf eclipse phase full-width at half-depth, $\Delta\phi$.
- White dwarf radius (R_1) as a fraction of the distance to L1 ($x_{\rm L1}$), $R_1/x_{\rm L1}$.
- Disc radius ($R_{\rm disc}$) as a fraction of the distance to L1, $R_{\rm disc}/x_{\rm L1}$
- White dwarf limb-darkening coefficient, U_1.
- Bright spot scale (S) as a fraction of the distance to L1, $S/x_{\rm L1}$.
- Bright spot angle, $\theta_{\rm az}$.
- Fraction of bright spot light emitted isotropically, $f_{\rm iso}$.

- Disc exponent, b.
- Phase offset, ϕ_0.
- First exponent of bright spot intensity distribution, Y. (Complex bright spot model only)
- Second exponent of bright spot intensity distribution, Z. (Complex bright spot model only)
- Bright spot beaming tilt angle, θ_{tilt}. (Complex bright spot model only)
- Bright spot beaming yaw angle, θ_{yaw}. (Complex bright spot model only)

Figure 3.2 contains an example corner-plot produced from model fitting, displaying various degeneracies between model parameters. See Sections 3.5 and 3.6 for details of how the model is fit to eclipse light curves through Markov Chain Monte Carlo (MCMC) analysis. The subsequent procedure for converting the resulting optimal model parameters into system parameters is outlined in Section 3.7.

3.3 Overcoming Flickering

As mentioned briefly at the start of Chapter 1, CV light curves can also contain random photometric variations, which are commonly referred to as flickering. Flickering exists due to turbulent nature of mass transfer within CVs, and has been found to originate from both the bright spot and the inner accretion disc/boundary layer (Bruch, 1992, 2000, 2015; Baptista & Bortoletto, 2004; Scaringi et al., 2012; Scaringi, 2014). The strength of flickering varies from system to system, as well as over time within a single CV. The presence of flickering within an eclipse light curve can deform the ingress/egress features of the component eclipses, which complicates the process of eclipse modelling and introduces additional uncertainty. Flickering even has the ability to completely conceal an ingress/egress feature, if its amplitude is comparable to the size of either white dwarf or bright spot eclipse. For these reasons, it is necessary to try and minimise the effects of flickering when attempting to model eclipse light curves.

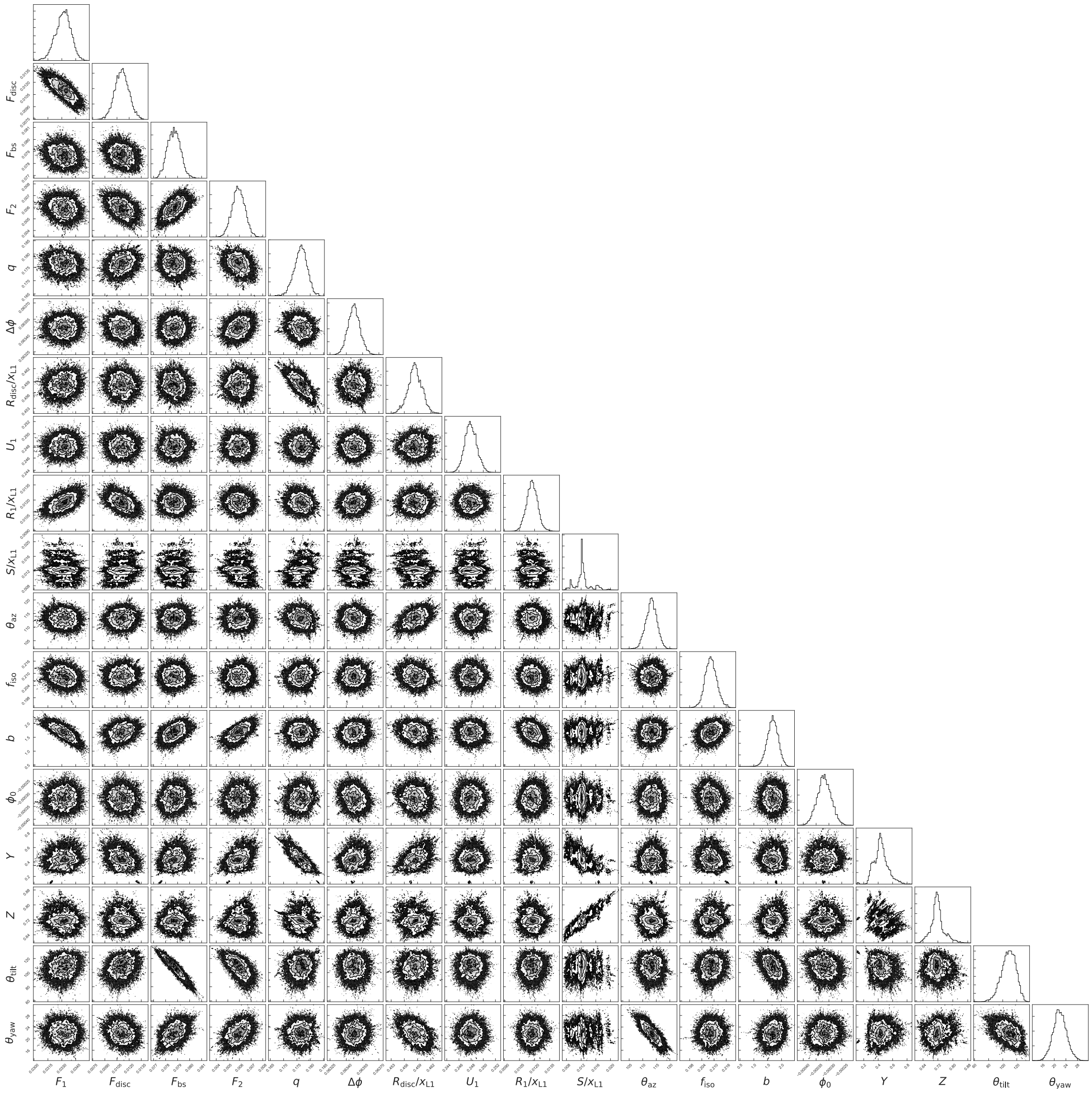

Figure 3.2: Example corner-plot of model parameters (complex BS included) post-model fitting.

3.3.1 Eclipse Light Curve Averaging

In the vast majority of previous eclipse modelling studies, flickering is minimised through the averaging of multiple eclipse light curves (e.g. Copperwheat et al. 2010; Savoury et al. 2011; Littlefair et al. 2014). Eclipse averaging has the effect of strengthening eclipse features relative to the random variations contributed to flickering. The eclipse model is then fit to the average eclipse light curve. This approach is valid so long as the eclipse features within each individual eclipse used in the construction of the average occur at the same phase and have (roughly) the same shape. This is always true for the white dwarf eclipse, but not for the eclipse of the bright spot. A change in disc radius can shift the phases of bright spot ingress/egress, while the shapes of bright spot ingress/egress can also be very changeable. Averaging eclipse light curves can therefore lead to bright spot features that appear diminished and broadened, which introduces inaccuracies into the model fitting process and beyond. As changes in disc radius and bright spot eclipse shape are observed in the majority of systems, it is clear that an alternative approach for overcoming flickering is required.

3.3.2 Modelling of Flickering

One particular alternative approach involves the introduction of a flickering model, which can be fit to individual eclipse light curves alongside the eclipse model. The successful implementation of such a model – outlined in Section 3.6.2 – was one of the main objectives of this work, and was achieved through the utilisation of Gaussian processes (GPs). An introduction to GPs and their application in a model for flickering are the subject of the next Section.

3.4 Gaussian Processes

Gaussian processes (GPs) have been used for many years in the machine learning community (Rasmussen & Williams, 2006; Bishop, 2006), and have recently started to be used in many areas of astrophysics. Some examples include photometric redshift prediction (Way & Srivastava, 2006; Way et al., 2009), modelling instrumental systematics in transmission spectroscopy (Gibson et al., 2012; Evans et al., 2015), modelling stellar activity signals in radial velocity studies (Rajpaul et al., 2015; Rajpaul, Aigrain & Roberts, 2016), and inference of both stellar (Angus et al., 2018) and brown dwarf (Littlefair, Burningham & Helling, 2017) rotation periods. The textbooks of Rasmussen & Williams (2006) and Bishop (2006) are recommended as general overviews of the topic, while useful introductions to the use of GPs for modelling time-series data can be found in Roberts et al. (2013) and the appendices of Gibson et al. (2012).

The formal definition of a GP is a collection of random variables, any finite number of which have a joint Gaussian distribution (Rasmussen & Williams, 2006). An example of a joint Gaussian distribution between two variables (t_1, t_2) is shown by the blue ellipse in the left plot of Figure 3.3. Also shown is the effect an observation of t_1 has on the marginal (conditional) distribution of t_2. GPs are defined by just two functions, one representing the *mean* $\mu(t)$ and another specifying the *covariance* $k(t_i, t_j)$:

$$y(t) \sim \mathcal{GP}(\mu(t), k(t_i, t_j)), \tag{3.6}$$

where t_i and t_j represent the times of any two data points. A light curve of observables/fluxes $\mathbf{y}$ located at inputs/times $\mathbf{t}$ (see right plots of Figure 3.3 for a simple example) can therefore be represented by a joint distribution $P(\mathbf{y}|\mathbf{t})$ which takes the form of a multivariate Gaussian [$\mathcal{N}()$]:

$$P(\mathbf{y}|\mathbf{t}) = \mathcal{N}(\boldsymbol{\mu}(\mathbf{t}), \mathbf{K}). \tag{3.7}$$

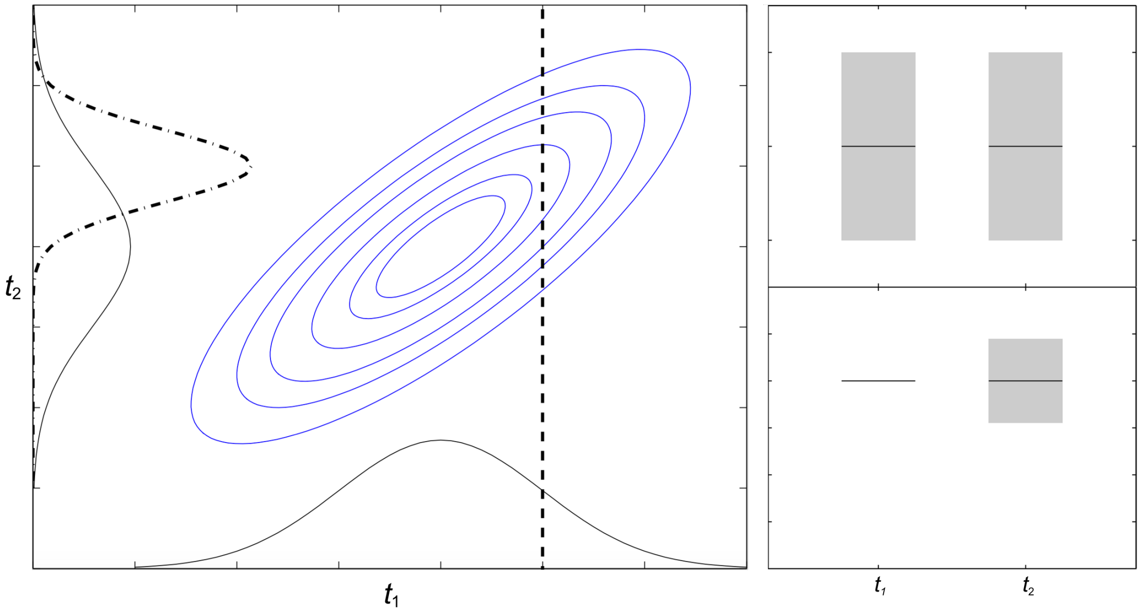

Figure 3.3: Two variables (t_1, t_2) defined by a joint Gaussian distribution. *Left:* Joint Gaussian distribution shown as a covariance ellipse (blue), with each contour representing equal probability. Marginal Gaussian distributions for each variable are also shown as solid black lines along on each axis. Dashed vertical line indicates an observation of t_1, with the resultant conditional distribution of t_2 shown by the dash-dot line. *Right:* Marginal Gaussian distributions of t_1 and t_2 (grey shaded regions represent $\pm\sigma$) in light curve form, both before (top) and after (bottom) observation of t_1. Figure adapted from Roberts et al. (2013).

The covariance of $P(\mathbf{y}|\mathbf{t})$ is specified by a *covariance matrix* $\mathbf{K}$ with the following structure:

$$\mathbf{K} = \mathbf{K}(\mathbf{t}, \mathbf{t}) = \begin{pmatrix} k(t_1, t_1) & k(t_1, t_2) & \dots & k(t_1, t_n) \\ k(t_2, t_1) & k(t_2, t_2) & \dots & k(t_2, t_n) \\ \vdots & \vdots & \vdots & \vdots \\ k(t_n, t_1) & k(t_n, t_2) & \dots & k(t_n, t_n) \end{pmatrix}. \tag{3.8}$$

Each element of the covariance matrix is defined by the covariance function, enabling trends in the light curve to be captured by correlations between nearby data points; i.e off-diagonal entries in the covariance matrix. The covariance function is crucial to the function of a GP, as without it the covariance matrix would contain an unfeasibly large n^2 free parameters. Many different types of covariance function exist, see Section 3.4.3 for examples of those most commonly used.

3.4.1 GP Regression

A GP can utilise the finite number of observed data points $(\mathbf{t}, \mathbf{y})$ in a light curve to produce predicted observables $\mathbf{y}_*$ at inputs $\mathbf{t}_*$ where no observed data is available. The observed and predicted data are commonly referred to as the training and test data, respectively. The joint probability distribution of $\mathbf{y}$ and $\mathbf{y}_*$ is as follows[5]:

$$P\left(\begin{bmatrix} \mathbf{y} \\ \mathbf{y}_* \end{bmatrix}\right) = \mathcal{N}\left(\begin{bmatrix} \boldsymbol{\mu}(\mathbf{t}) \\ \boldsymbol{\mu}(\mathbf{t}_*) \end{bmatrix}, \begin{bmatrix} \mathbf{K}(\mathbf{t}, \mathbf{t}) & \mathbf{K}(\mathbf{t}, \mathbf{t}_*) \\ \mathbf{K}(\mathbf{t}_*, \mathbf{t}) & \mathbf{K}(\mathbf{t}_*, \mathbf{t}_*) \end{bmatrix}\right). \tag{3.9}$$

Through manipulation using Gaussian identities (see Appendix A.2 of Rasmussen & Williams 2006), the conditional joint posterior probability distribution of $\mathbf{y}_*$ – given $\mathbf{y}$ – can be determined:

$$P(\mathbf{y}_*|\mathbf{t}_*, \mathbf{y}, \mathbf{t}) = \mathcal{N}(\mathbf{m}_*, \mathbf{C}_*). \tag{3.10}$$

---

[5] It is important to note that, for simplicity, it is assumed that observations are noise-free. This is obviously not the case for real data, where noise must be taken into account (see Section 3.4.5).

The posterior mean $\mathbf{m}_*$ and covariance $\mathbf{C}_*$ have the following form (Roberts et al., 2013):

$$\mathbf{m}_* = \boldsymbol{\mu}(\mathbf{t}_*) + \mathbf{K}(\mathbf{t}_*, \mathbf{t})\mathbf{K}(\mathbf{t}, \mathbf{t})^{-1}\mathbf{r}, \tag{3.11}$$

$$\mathbf{C}_* = \mathbf{K}(\mathbf{t}_*, \mathbf{t}_*) - \mathbf{K}(\mathbf{t}_*, \mathbf{t})\mathbf{K}(\mathbf{t}, \mathbf{t})^{-1}\mathbf{K}(\mathbf{t}_*, \mathbf{t})^\top, \tag{3.12}$$

where $\mathbf{r} = \mathbf{y} - \boldsymbol{\mu}(\mathbf{t})$ represents the residuals after subtraction of the mean function from the observed data.

3.4.2 GP Modelling of Light Curves

GPs offer an alternative approach to modelling light curves. This can be performed through the maximisation of the light curve's *marginal likelihood* $\mathcal{L}$. As all the data points within a light curve can be represented by a joint multivariate Gaussian distribution (equation 3.7), the marginal likelihood[6] $\mathcal{L}$ of the light curve is therefore (Rasmussen & Williams, 2006):

$$\mathcal{L} = P(\mathbf{r}|\mathbf{t}) = \frac{1}{(2\pi)^{n/2}|\mathbf{K}|^{1/2}} \exp\left(-\frac{1}{2}\mathbf{r}^\top\mathbf{K}^{-1}\mathbf{r}\right), \tag{3.13}$$

where n is the number of data points. This is commonly expressed logarithmically:

$$\log\mathcal{L} = -\frac{1}{2}\mathbf{r}^\top\mathbf{K}^{-1}\mathbf{r} - \frac{1}{2}\log|\mathbf{K}| - \frac{n}{2}\log(2\pi). \tag{3.14}$$

3.4.3 Covariance Functions

As equation 3.6 shows, the covariance function – also known as the *covariance kernel* – is an integral component of a GP, defining the covariance between any two data points. There exists a wide range of valid[7] covariance functions, enabling the modelling of many different forms of data. It is also possible to combine numerous

---

[6] Likelihood marginalised over all possible functions within the distribution defined by the GP (Gibson et al., 2012).

[7] A covariance function is valid if the resulting covariance matrix is positive semidefinite (Rasmussen & Williams, 2006).

covariance functions, further increasing the flexibility of GPs.

It is important to choose the most suitable covariance function for the data that is to be modelled. In this particular case, GPs are used in the modelling of CV flickering (see Section 3.4.5), which is assumed to be a stationary time-series[8,9]. Only stationary covariance functions – which have a dependence on $|t_i - t_j|$ – are therefore considered here. Below are some commonly used examples of stationary covariance functions.

Squared Exponential Covariance Function

Arguably the most widely used covariance function, at least in the field of machine learning, is the squared exponential function (Rasmussen & Williams, 2006). It has the following form:

$$k(t_i, t_j) = h^2 \exp\left(-\frac{|t_i - t_j|^2}{2\lambda^2}\right), \tag{3.15}$$

where h and λ are free parameters which define the output scale (amplitude) and input scale (time), respectively. Free parameters that control the input/output scales are referred to as *hyperparameters* of the GP, and can be optimised through the maximisation of $\mathcal{L}$ (see Section 3.4.5 for further details).

A GP using a squared exponential covariance function is infinitely differentiable, resulting in smooth, gradual variations. According to Stein (1999), the smoothness of the squared exponential covariance function makes it a poor choice for modelling the majority of physical processes.

Matérn Class of Covariance Functions

The Matérn[10] class of covariance functions are defined by:

$$k(t_i, t_j) = \frac{2^{1-\nu} h^2}{\Gamma(\nu)} \left(\sqrt{2\nu}\frac{|t_i - t_j|}{\lambda}\right)^{\nu} \mathbb{B}_{\nu}\left(\sqrt{2\nu}\frac{|t_i - t_j|}{\lambda}\right), \tag{3.16}$$

---

[8] Stationary time-series: the mean and variance do not change with time.

[9] This is not strictly true, see Sections 3.4.4 and 3.4.5.

[10] Named after the work of Matérn (1960).

where ν is a positive parameter, $\Gamma(\nu)$ is the Gamma function[11] of ν, and $\mathbb{B}_\nu$ is the second order modified Bessel function of ν (Abramowitz & Stegun, 1964). A GP using a Matérn covariance function is $\nu + 1/2$ times differentiable, and therefore the chosen value of ν has a large impact on the GP's structure.

As $\nu \to \infty$, the Matérn function becomes the squared exponential function[12] (equation 3.15), while it becomes greatly simplified for half-integer values of ν. For example, this is the form of the Matérn-3/2 ($\nu = 3/2$) covariance function:

$$k(t_i, t_j) = h^2 \left(1 + \sqrt{3}\frac{|t_i - t_j|}{\lambda}\right) \exp\left(-\sqrt{3}\frac{|t_i - t_j|}{\lambda}\right). \tag{3.17}$$

The Matérn-3/2 covariance function results in a GP with much sharper variations compared to the squared exponential covariance function, and is considered the most interesting of the Matérn functions for use in machine learning (Rasmussen & Williams, 2006).

Exponential Covariance Function

Substituting $\nu = 1/2$ into equation 3.16 gives the exponential covariance function:

$$k(t_i, t_j) = h^2 \exp\left(-\frac{|t_i - t_j|}{\lambda}\right). \tag{3.18}$$

A GP using this covariance function is only once differentiable, resulting in rough, sharp variations. The exponential covariance function is used in the Ornstein-Uhlenbeck process, which models a particle's velocity whilst undergoing Brownian motion (Uhlenbeck & Ornstein, 1930).

---

[11] $\Gamma(n) = (n-1)!$

[12] In reality, the Matérn function is practically indistinguishable from the squared exponential function when $\nu \geq 7/2$ (Rasmussen & Williams, 2006).

3.4.4 Changepoints

It is possible for a time-series to suddenly depart from stationarity, and therefore using a GP with a single stationary covariance function is no longer practical. Two separate covariance functions are now necessary, one for before and the other for after the point in the time-series where the characteristics suddenly changed – commonly termed as a *changepoint*. The two covariance functions typically only differ in hyperparameter values, but can have different functional forms if required. For further information regarding changepoints, see Garnett et al. (2010).

3.4.5 GP Model for Flickering

GPs are an ideal tool for the construction of a non-parametric model for CV flickering. As equation 3.7 shows, it is possible for the flickering within a CV eclipse light curve – taken as the residuals resulting from the subtraction of the eclipse model from the data – to be represented by a multivariate Gaussian distribution with a mean function $\boldsymbol{\mu}$ and covariance matrix $\mathbf{K}$. The structure of the covariance matrix is an important consideration. In this application, the structure of $\mathbf{K}$ was specified so that each element has the form:

$$\mathbf{K}_{ij} = k(t_i, t_j) + \sigma_i^2 \delta_{ij}, \tag{3.19}$$

where $k(t_i, t_j)$ is a chosen covariance function and $\sigma_i^2 \delta_{ij}$ is a white noise component.

It was necessary to decide on a covariance function that best represents the variations associated with CV flickering, and all three of the stationary covariance functions discussed in Section 3.4.3 were considered. Sample functions from GPs using each of the three covariance functions (squared exponential, Matérn-3/2 and exponential), in addition to a range of input scales (λ = 1, 0.1, 0.01, 0.001), are shown in Figure 3.4. Also included in Figure 3.4 are the power spectral densities (PSDs) for each function shown. For all inputs scales, the squared exponential

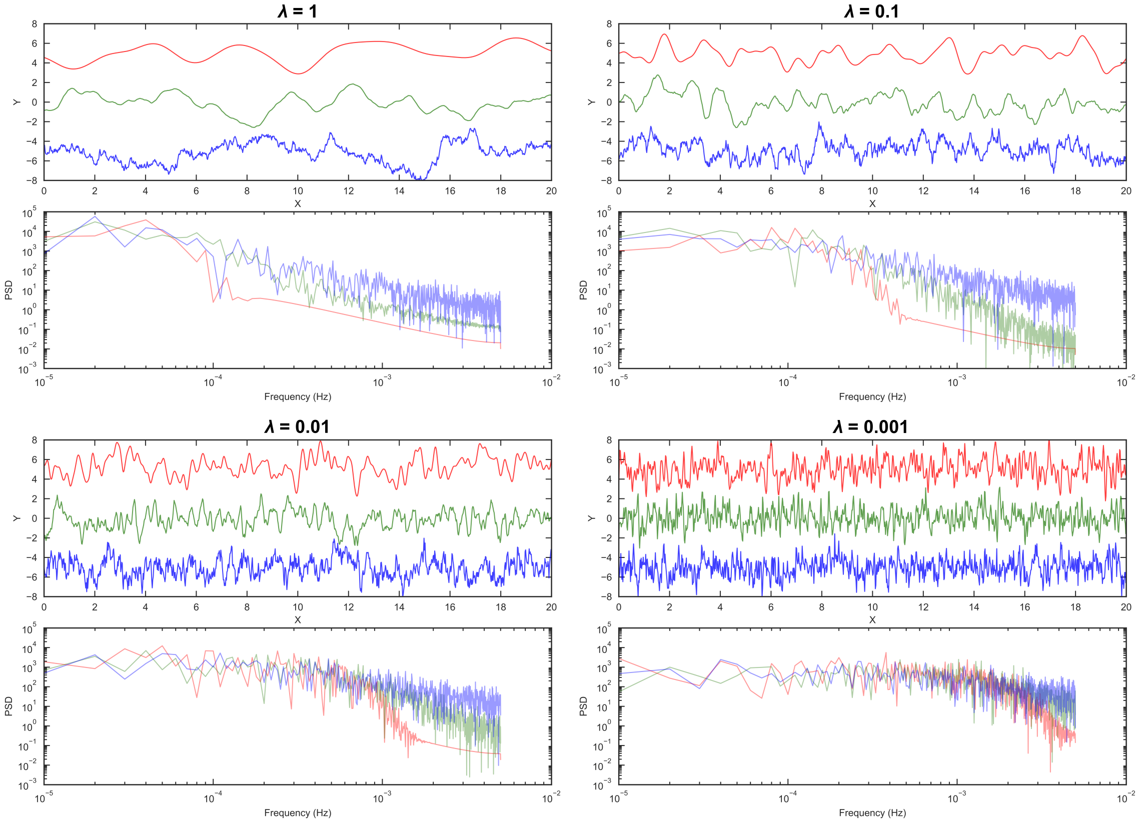

Figure 3.4: Sample functions (upper plot of each quadrant), and corresponding power spectral densities (PSDs) (lower plot of each quadrant), from GPs with different combinations of covariance functions and input scales (λ). The three covariance functions shown are: squared exponential (red, +5 shift in Y direction), Matérn-3/2 (green) and exponential (blue, -5 shift in Y direction). Each quadrant represents a different input scale: $\lambda = 1$ (top-left), 0.1 (top-right), 0.01 (bottom-left) and 0.001 (bottom-right).

covariance function PSDs appear to lack high frequency signals, while both the exponential and Matérn-3/2 PSDs compare reasonably well to those of CV light curves (Scaringi et al., 2012; Scaringi, 2014; Van de Sande, Scaringi & Knigge, 2015). During initial testing of the new modelling approach, the Matérn-3/2 function (equation 3.17) was determined the most suitable for replicating flickering, as when fit to test data it returned the highest likelihood out of the three covariance functions. The squared exponential and exponential functions appear too smooth and too sharp to replicate flickering, respectively.

As mentioned in Section 3.3, there are multiple sources of flickering in CVs, and therefore more than one flickering amplitude. The observed amplitude should vary across the eclipse as the different components are individually eclipsed. To accommodate for the anticipated changes in flickering amplitude, two changepoints (Section 3.4.4) were introduced. These changepoints are positioned at the white dwarf's ingress start, t_{in}, and egress end, t_{e}. This enabled the covariance function amplitude hyperparameter outside white dwarf eclipse, h_1, to differ from that inside, h_2. The location of the changepoints were chosen on the basis that the inner disc is a main source of flickering, but not the only source. The covariance function form (Matérn-3/2) and input scale hyperparameter, λ, were kept the same across the whole time-series. The changepoints were implemented in accordance with the drastic changepoint approach from Garnett et al. (2010), with the covariance function taking the following form:

$$k(t_i, t_j; h_1, h_2, \lambda) \triangleq \begin{cases} k(t_i, t_j; h_1, \lambda), & t_i, t_j < t_{\mathrm{in}} \\ k(t_i, t_j; h_2, \lambda), & t_{\mathrm{in}} \leq t_i, t_j \leq t_{\mathrm{e}} \\ k(t_i, t_j; h_1, \lambda), & t_i, t_j > t_{\mathrm{e}} \\ 0, & \text{otherwise.} \end{cases} \tag{3.20}$$

The implementation of changepoints results in a total of three GP hyperparameters, which can be thought of as the three free parameters of the GP flickering model. The GP model is fit to the light curve residuals through the calculation and maximisation of the GP likelihood $\mathcal{L}$ (equation 3.14), and takes place alongside the fitting of the eclipse model to the eclipse light curve (see Section 3.6.2 for further details).

As equation 3.14 shows, the computation of the likelihood necessitates the inversion of the $n \times n$ covariance matrix ($\mathbf{K}^{-1}$). This is computationally expensive, requiring $\mathcal{O}(n^3)$ operations, and therefore has the potential to significantly limit the size of $\mathbf{K}$, with large matrices becoming impractical. It was possible to speed this step up, however, through use an alternative solver, based on an $\mathcal{O}(n \log^2 n)$ algorithm for inversion (Ambikasaran et al., 2016).

3.5 Markov Chain Monte Carlo

Markov Chain Monte Carlo (MCMC) is a powerful, efficient way of performing Bayesian inference, and is widely used throughout the field of astronomy and beyond. Included in this Section is a brief introduction to Bayesian inference and MCMC; see Gregory (2005) for a detailed review.

3.5.1 Bayesian Inference

Bayesian inference is a form of statistical inference that enables the derivation of posterior probability from prior knowledge and new information/data. In this particular case, Bayesian inference can be used to obtain a posterior probability density function (PDF) for the parameters of the model(s), M, from the available eclipse light curve data, D. The posterior PDF, denoted by $P(M|D)$, is the subject of Bayes' theorem:

$$P(M|D) = \frac{P(D|M) \times P(M)}{P(D)}, \tag{3.21}$$

where $P(D|M)$ is the likelihood of the model parameters, $P(M)$ is the prior PDF of the model parameters, and $P(D)$ is the marginal likelihood. The likelihood can be thought of as the probability of obtaining the dataset in question, assuming a particular set of model parameters represent the true values. The prior PDF represents the – in this case limited – state of knowledge prior to the consideration of the data. The marginal likelihood is included for normalisation, but it can be ignored in instances of parameter estimation (Gregory, 2005).

3.5.2 MCMC Basics

For models with large numbers of parameters, the calculation of equation 3.21 is far from straightforward due to the involvement of multi-dimensional integrals. MCMC is a mathematical tool that enables the approximation of these integrals through random sampling of parameter space. This random sampling is achieved through use of a Markov chain, with a specified initial set of model parameters and transition probability (Gregory, 2005). The ultimate aim of MCMC is to generate a chain of model parameter sets that are sampled from the posterior PDF (Ford, 2005).

3.5.3 MCMC Requirements

In order for a Markov chain to converge to $P(M|D)$, it must be the following (e.g. Roberts 1996):

- *Irreducible*: Able to eventually reach all non-zero probability states, regardless of starting position.
- *Aperiodic*: Able to prevent a periodic oscillation between two states.
- *Positive recurrent*: Able to revisit a particular state within a finite amount of time.

3.5.4 Metropolis-Hastings

The simplest and most common way to perform MCMC is with the Metropolis-Hastings (M-H) algorithm (Metropolis et al., 1953; Hastings, 1970). The algorithm proceeds by generating a candidate set of model parameters (M') – according to a proposal distribution $q(M'|M_N)$ – which is either accepted or rejected depending on the transition probability $P(M'|M_N)$:

$$P(M'|M_N) = q(M'|M_N)\alpha(M'|M_N), \tag{3.22}$$

where $\alpha(M'|M_N)$ is the acceptance probability. In the M-H algorithm, $\alpha(M'|M_N)$ is defined as (Gregory, 2005):

$$\alpha(M'|M_N) = \min(1, r) = \min\left(1, \frac{P(M'|D)}{P(M_N|D)}\frac{q(M_N|M')}{q(M'|M_N)}\right), \tag{3.23}$$

where r is referred to as the Metropolis ratio. Just as the likelihood function $P(D|M)$ can be estimated using $\exp(-\chi^2/2)$, so can the posterior PDF $P(M|D)$, provided a prior very close to flat ($P(M) \sim 1$) is chosen (equation 3.21). This, together with a symmetric proposal distribution $[q(M'|M_N) = q(M_N|M')]$, enables the following alternative expression for the Metropolis ratio:

$$r \sim \exp\left(\frac{\chi^2(M_N)}{2} - \frac{\chi^2(M')}{2}\right). \tag{3.24}$$

A step by step implementation of the M-H algorithm is as follows (Gregory, 2005; Ford, 2005):

- Initialise chain with initial set of model parameters, $M_{N=0}$, then repeat the following sequence of steps.
- Obtain a new (candidate) set of model parameters, M', from $q(M'|M_N)$.
- Calculate $\chi^2(M')$, $\chi^2(M_N)$ and r (equation 3.24).
- Draw a random number, u, from a uniform distribution in the interval 0 to 1.
- If $u < \alpha(M'|M_N)$ (equation 3.23), then set $M_{N+1} = M'$, otherwise set $M_{N+1} = M_N$.
- Set $N = N + 1$.

3.5.5 Affine Invariant Ensemble Sampling

A consequence of the M-H algorithm's simplicity is that it is inefficient when required to explore a complex parameter space with a large number of dimensions, taking an unfeasibly large amount of time to converge (Foreman-Mackey et al., 2013). Thankfully, there exist a number of alternative methods for performing MCMC that are more complex and powerful than M-H. One such method is affine invariant[13] ensem-

---

[13] Performs equally well under all linear transformations (Foreman-Mackey et al., 2013).

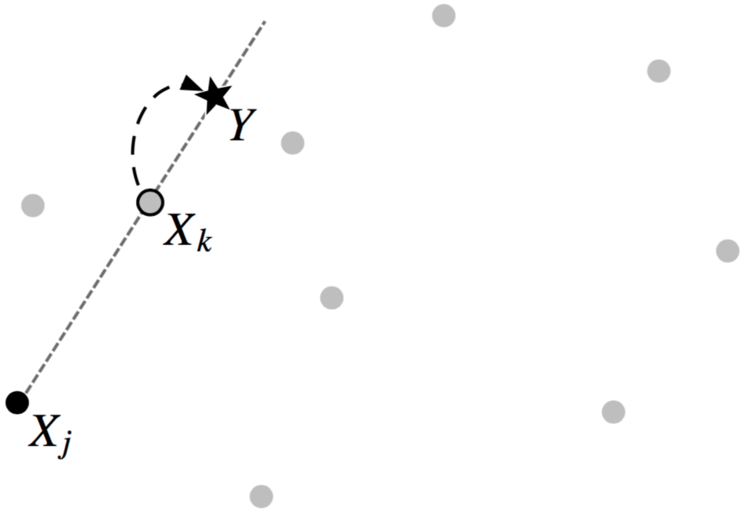

Figure 3.5: A schematic demonstrating the stretch move associated with affine invariant ensemble sampling. The proposal move Y of the walker at X_k is generated through stretching the straight line connecting X_k and another, randomly selected, walker position X_j. The additional dots represent walkers that are not involved in this particular stretch move. Figure from Goodman & Weare (2010).

ble sampling (Goodman & Weare, 2010). This involves an ensemble of K particles or 'walkers' that explore parameter space through affine invariant transformations. Walkers can be thought of as individual MCMC chains, each transformed in series with a proposal distribution dependent on the positions of all other walkers in the ensemble, in addition to the chosen type of affine invariant algorithm (Foreman-Mackey et al., 2013). A walker can therefore 'signal' the existence of high probability regions of parameter space to the other walkers, enabling all walkers to eventually converge on the global solution.

The simplest type of affine invariant ensemble sampler algorithm is referred to as the 'stretch move'. An overview of this algorithm is included here, but the reader should refer to Goodman & Weare (2010) for an in-depth explanation. A walker k, initially at position X_k, has a proposed position Y generated from:

$$X_k \rightarrow Y = X_j + z(X_k - X_j), \tag{3.25}$$

where X_j is the position of a randomly selected walker j, and z is a random variable drawn from a distribution $g(z)$ of the form:

$$g(z) \propto \begin{cases} \frac{1}{\sqrt{z}}, & \frac{1}{2} \leq z \leq 2 \\ 0, & \text{otherwise.} \end{cases} \tag{3.26}$$

The stretch move algorithm is also shown schematically in Figure 3.5. The acceptance probability $\alpha(Y|X_k)$ of the proposed move is

$$\alpha(Y|X_k) = \min\left(1, z^{n-1}\frac{P(Y)}{P(X_k)}\right), \tag{3.27}$$

where n is the number of dimensions of parameter space. As with the M-H algorithm, a proposed move is either accepted or rejected based on how $\alpha(Y|X_k)$ compares to a random number u drawn from a uniform distribution in the interval 0 to 1. If $u < \alpha(Y|X_k)$ then it is accepted, otherwise it is rejected.

It is possible to parallelise the stretch move algorithm, so that walkers can be transformed simultaneously, as opposed to in series (see Foreman-Mackey et al. 2013 for details). This has the beneficial effect of dramatically reducing the required computational time.

3.6 Eclipse Light Curve Fitting

3.6.1 Existing Approach

The existing approach to eclipse light curve fitting outlined here is identical to that used by Savoury et al. (2011); Littlefair et al. (2014), and is used within Chapter 4 of this work. It involves fitting the eclipse model from Section 3.2 to a *single* eclipse light curve with the M-H MCMC algorithm (Section 3.5.4). During the MCMC fitting, each set of model parameters is drawn from a multi-variate Gaussian proposal distribution, which is defined by a covariance matrix.

The MCMC fitting is split into two sections; initial ‘burn-in’ phase and ensuing 'production' phase. The purpose of the burn-in phase – which uses a proposal distribution determined by an initial Levenberg-Marquardt fit (Levenberg, 1944; Marquardt, 1963) – is to converge towards $P(M|D)$, and ultimately produce a proposal distribution resembling $P(M|D)$ that can be used in the production phase. Provided that convergence has been achieved, the production phase is then able to sample from $P(M|D)$. The MCMC fitting is run for total of 200 000 steps, 100 000 per each phase. The MCMC chain from the burn-in phase is discarded and only the chain from the production phase is used going forwards.

All parameters are fit freely, with the exception of the limb darkening parameter (U_1), as it cannot be constrained given the quality of data available. It is instead kept fixed at a suitable value, dependent on the white dwarf temperature (T_1), $\log g$ and the wavelength band used. Estimates of T_1 and $\log g$ are therefore required to acquire an appropriate value of U_1, and so it is necessary to perform a preliminary run through of the complete eclipse modelling procedure (see Figure 3.6 and Section 3.7 for more details). The estimates of T_1 and $\log g$ from the preliminary run are then interpolated with the white dwarf limb-darkening tables of Gianninas et al. (2013) to acquire values for U_1 in each SDSS band. A value for U_1 in the *KG5* band is calculated by taking a weighted mean of the u', g' and r' values, based on the approximate fraction of the *KG5* bandpass covered by each of these three SDSS bands.

Uniform priors are adopted for the majority of model parameters, with only these two following exceptions:

- A joint prior on q and $\Delta\phi$ that disallows combinations resulting in $i > 90^{\circ}$.
- A prior on θ_{az} that constrains the bright spot strip to within 40° of the tangent to the accretion disc.

3.6.2 New Approach

A new, advanced approach to eclipse light curve fitting has been developed as part of this work. The new approach involves a number of changes, including two major modifications. The first of these modifications is the ability to fit the eclipse model from Section 3.2 to *multiple* eclipse light curves from the same system *simultaneously*, whilst sharing parameters intrinsic to that particular system, e.g mass ratio (q), white dwarf eclipse phase full-width at half-depth ($\Delta\phi$) and white dwarf radius (R_1/x_{L1}) between all eclipses. The second is the introduction of a GP model for flickering (See Section 3.4.5), which can be fit to multiple eclipse light curves alongside the eclipse model. As explained in Section 3.4.5, the GP flickering model comprises of three (hyper)parameters, amplitude outside white dwarf eclipse (h_1), amplitude inside white dwarf eclipse (h_2), and timescale (λ), which are shared across all eclipses.

MCMC analysis remains the chosen method for fitting the model(s) to eclipse light curves. However, a consequence of the multi-eclipse fitting ability is the involvement of significantly more parameters – an additional 11 or 15 parameters[14] per eclipse included – and therefore a considerable increase in the size and complexity of the parameter space. In order to successfully explore such a large and complex parameter space, an alternative to the simplistic, inefficient M-H algorithm used previously is required. An affine invariant ensemble sampler, incorporating a 'stretch move' algorithm (see Section 3.5.5), is favoured as a replacement, due to its ensemble configuration being much better suited for exploring complex parameter space. The ensemble sampler is implemented through the PYTHON module EMCEE[15] (Foreman-Mackey et al., 2013).

As with the existing approach (Section 3.6.1), the MCMC fitting is split into burn-in and production phases. The burn-in phase is run for a total of 20 000 steps,

---

[14] Depending on whether the simple or complex bright spot model is used.

[15] http://dan.iel.fm/emcee/current/

while the production phase is run for a total of 10 000 steps. The burn-in is run for longer in order to increase the chances of convergence to $P(M|D)$. It is advisable to use a large number of 'walkers' in the ensemble (Foreman-Mackey et al., 2013), as the number of walkers correlates with the sampling performance, however the use of many walkers also results in a long computation time. A compromise between performance and computation time must therefore be considered when deciding on the number of walkers to use. As an increase in the number of parameters results in a larger parameter space to be explored, the chosen number of walkers is scaled to the number of parameters involved. For all fits in this work using the new approach, the chosen number of walkers outnumber parameters by a factor of ~ 10.

In another effort to increase the chances of convergence, the starting values of the eclipse model parameters are obtained from a by-eye fit of the model to the eclipse light curve(s), while all three GP model hyperparameters are given starting values located towards the lower limit of their priors. The walkers are initiated in parameter space as a ball centred on the starting values. The extent, or more specifically standard deviation, of this ball in each parameter dimension is governed by the parameter's assigned amount of 'scatter'. The typical scatter assigned to each parameter is between a factor of 0.1 and 0.3 times its starting value, which is large enough to prevent the majority of walkers from getting stuck at the local solution associated with the starting values. A consequence of this amount of scatter, however, is a significant number of walkers ending up in invalid parameter space. It is important to ensure that any invalid walkers are re-introduced into valid parameter space before the start of the MCMC fit. This is done by moving each invalid walker to the location of a randomly selected valid walker, at which point it is re-scattered. This process is repeated until all walkers are valid, at which point the MCMC fitting is initiated.

All parameters are fit freely, except for the limb darkening parameters, which – for reasons stated in Section 3.6.1 – are given highly constrained (Gaussian) priors that encompass a suitable value[16]. The majority of remaining parameters have uniform priors, with the following exceptions[17]:

- A joint prior on q and $\Delta\phi$ that disallows values consistent with $i > 90^{\circ}$.
- Priors on $R_{\mathrm{disc}}/x_{\mathrm{L1}}$ parameters that prevent values greater than $0.46a/x_{\mathrm{L1}}$, where a is the binary separation. $R_{\mathrm{disc}} \sim 0.46a$ is the maximum size a disc can reach without precessing (Hellier, 2001).
- Priors on θ_{az} parameters that constrain the bright spot strip to within 80° of the tangent to the accretion disc.
- Priors on S/x_{L1} parameters that limit values to between 1/3 and 3 times R_1/x_{L1}.
- Joint priors on S/x_{L1}, Y and Z to ensure that the distance along the bright spot strip where the intensity distribution peaks ($X(I_{\mathrm{bs,max}})$; equation 3.5) is no greater than $0.5x_{\mathrm{L1}}$.

3.7 Post-Eclipse Light Curve Fitting Procedure

The post-eclipse light curve fitting procedure – transforming model parameters into system parameters – is shown schematically in Figure 3.6. As Figure 3.6 shows, the procedure takes the form of an iterative loop, comprised of two separate processes: white dwarf atmosphere fitting (Section 3.7.1) and the calculation of system parameters (Section 3.7.2). The details of each individual process are the subjects of the following two Sections, but here is a brief overview of the complete procedure:

- Multi-band white dwarf fluxes from eclipse model fitting ($F_{1,1}, F_{1,2}, ..., F_{1,n}$) are fit with white dwarf atmosphere predictions to obtain an estimate for T_1, amongst other white dwarf parameters (Section 3.7.1).

---

[16] The process of obtaining limb darkening parameter values is also explained in Section 3.6.1.

[17] Note that only the first of these non-uniform priors is used in both the new and existing approaches.

- The model parameters q, $\Delta\phi$ and R_1/x_{L1} from eclipse model fitting, along with the estimate for T_1, are used to calculate system parameters, which include $\log g$ (Section 3.7.2).
- The white dwarf atmosphere fitting is repeated, but this time with constraints on the $\log g$ prior that reflect the value of $\log g$ from the system parameter calculation. A new estimate of T_1 is obtained.
- The system parameter calculation is repeated, using the new estimate of T_1.

As mentioned in Section 3.6, the eclipse light curve fitting, and subsequent procedure outlined above, is performed twice. The first (preliminary) run is required in order to obtain accurate white dwarf limb-darkening parameters (U_1). It is the values of T_1 and $\log g$ from the second white dwarf atmosphere fitting and system parameter calculation iteration that are used to extract values of U_1 from the the white dwarf limb-darkening tables of (Gianninas et al., 2013), as illustrated with the grey arrows in Figure 3.6.

3.7.1 White Dwarf Atmosphere Fitting

White dwarf fluxes ($F_{1,1}, F_{1,2}, ..., F_{1,n}$) in a range of wavelength bands resulting from the eclipse light curve fit can be used to obtain estimates for the white dwarf temperature (T_1), $\log g$ and distance (d). This involves fitting the white dwarf fluxes with white dwarf atmosphere predictions[18] (Bergeron, Wesemael & Beauchamp, 1995; Holberg & Bergeron, 2006; Kowalski & Saumon, 2006; Tremblay, Bergeron & Gianninas, 2011), which give the predicted SDSS absolute magnitude of a hydrogen-rich[19] (DA) white dwarf for a given temperature and $\log g$. The models responsible for these absolute magnitude predictions were re-calculated in order to also include *KG5* magnitudes (Bergeron, priv. comm.). An affine invariant MCMC ensemble

---

[18] http://www.astro.umontreal.ca/∼bergeron/CoolingModels

[19] Models assume a carbon-core white dwarf with a thick hydrogen envelope ($M_{\mathrm{H}}/M_1 = 10^{-4}$) (Bergeron, Leggett & Ruiz, 2001).

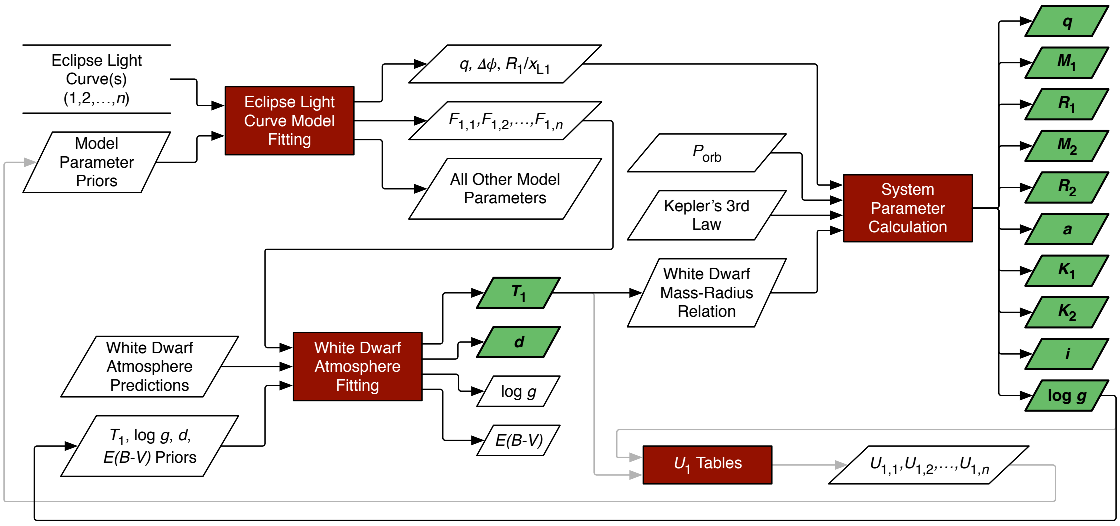

Figure 3.6: A schematic of the procedure followed to obtain system parameters from eclipse light curves. The eclipse light curve fitting process (top left) is performed twice, each time followed by two iterations of a loop involving both the white dwarf atmosphere fitting and system parameter calculation processes. The grey arrows – associated with the white dwarf limb darkening (U_1) tables – show steps only to be taken during the second iteration of the first (post-preliminary eclipse model fitting) white dwarf atmosphere fitting and system parameter calculation loop; necessary in order for updated U_1 priors to be used in the second and final performance of the eclipse light curve model fitting process.

sampler (see Section 3.5.5) is again chosen for these white dwarf atmosphere prediction fits, with the following four parameters used in the fitting:

- White dwarf temperature, T_1.
- White dwarf $\log g$.
- Distance, d.
- Interstellar reddening, $E(B-V)$.

Distance is included as a fitting parameter due to the fact that the fluxes from the eclipse model fit are apparent fluxes, while the atmosphere predictions include absolute magnitudes, and therefore a conversion is required. Interstellar reddening is also included as a parameter, but only for its uncertainty to be taken into account, as it is rarely constrained by the data. Its prior covers the range from 0 to the total amount of reddening measured along the line-of-sight to the system in question (Schlafly & Finkbeiner, 2011). This should be a reasonable upper limit for white dwarfs with lines-of-sight away from the Galactic plane, but will be a significant overestimate for those with lines-of-sight within the Galactic plane, particularly towards the Galactic centre.

The white dwarf fluxes and errors used in the white dwarf atmosphere fitting are taken from the median values and standard deviations of a random sample of the eclipse model fitting MCMC chain. A 3% systematic error is also added to account for uncertainties introduced during the flux calibration process (Section 2.4).

3.7.2 Calculating System Parameters

The posterior PDFs of the model parameters q, $\Delta\phi$ and R_1/x_{L1} resulting from the eclipse model MCMC fit (Section 3.6) can be utilised to obtain the posterior PDFs of the following 10 system parameters:

- Mass ratio, q.
- White dwarf mass, M_1.

- White dwarf radius, R_1.
- Donor mass, M_2.
- Donor radius, R_2.
- Binary separation, a.
- White dwarf radial velocity, K_1.
- Donor radial velocity, K_2.
- Inclination, i.
- White dwarf $\log g$.

While q is acquired directly from the model, the remaining nine system parameters require calculation. The values of q, $\Delta\phi$ and $R_1/x_{\rm L1}$ at each step of the MCMC chain are used to produce an individual set of system parameter values (see below for details). The distributions of system parameter values across all of these individual sets are then taken to be the system parameter posterior PDFs. The final parameter value is taken as the most likely value of its PDF, with upper and lower errors derived from the 67% confidence level.

As mentioned in Section 3.2, $\Delta\phi$ is strictly a function of q and i, and therefore it is $\Delta\phi$ and q that are used to find i. This is achieved with the help of an accurate Roche lobe model and a binary search algorithm.

An expression for R_1 can be formed through rearranging Kepler's 3rd law (equation 1.1) and making substitutions of $q = M_2/M_1$ and $r = R_1/a$:

$$R_1 = \left(\frac{G(1+q)P_{\rm orb}^2 r^3 M_1}{4\pi^2} \right)^{1/3}. \tag{3.28}$$

q is a model parameter, r is obtained from simply multiplying $R_1/x_{\rm L1}$ by $x_{\rm L1}/a$[20] and $P_{\rm orb}$ is known from the orbital ephemeris, but this equation cannot be solved directly due to the presence of M_1, another as-yet-unknown system parameter. However, as equation 3.28 is essentially a geometrically-obtained mass-radius relation for CV

---

[20] Ratio solely dependent on q.

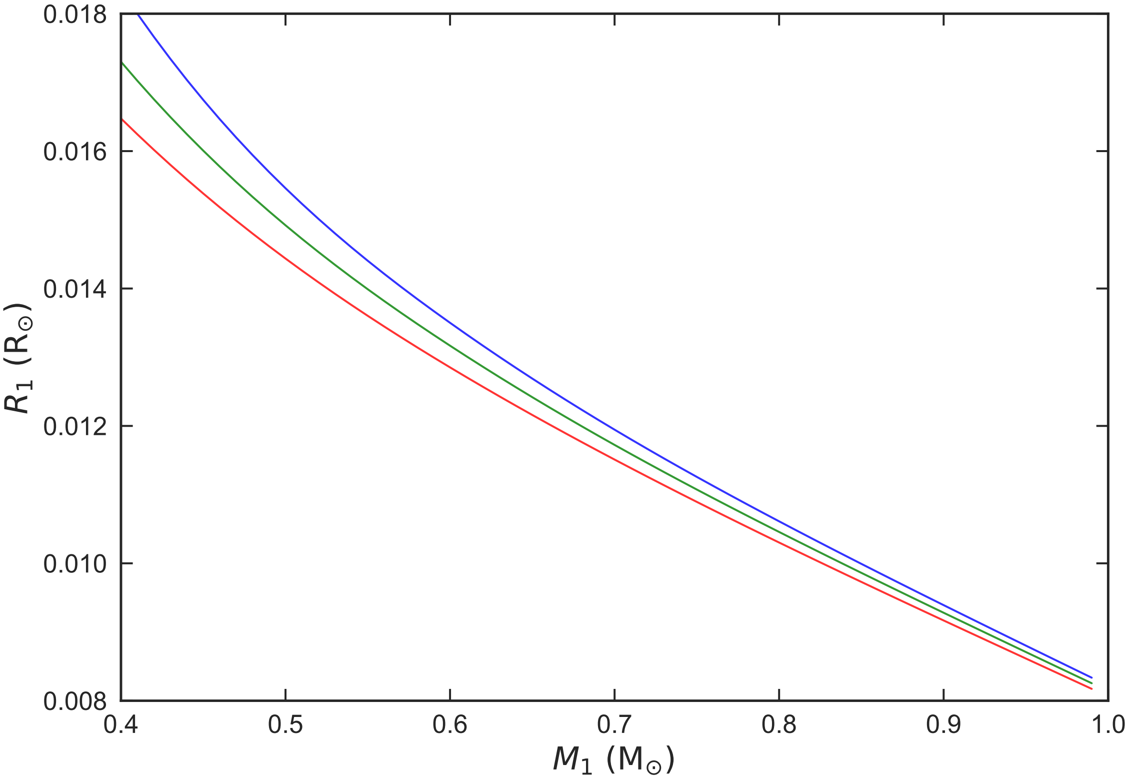

Figure 3.7: Theoretical white dwarf mass-radius relations from Wood (1995), for temperatures of 10 000 K (red), 15 000 K (green) and 20 000 K (blue).

white dwarfs, it can be solved with the aid of an additional, theoretical white dwarf mass-radius relation (see below). A value of M_1 is found which satisfies both relations, which then enables R_1 to be calculated from equation 3.28, a from $r = R_1/a$, and the surface gravity ($\log g$) of the white dwarf from the following expression:

$$\log\, g = \log_{10}\left(\frac{GM_1}{R_1^2}\right). \tag{3.29}$$

The preferred choice of theoretical white dwarf mass-radius relations for use in this work are those deriving from the Wood (1995) thick hydrogen layer CO white dwarf models, examples of which are shown in Figure 3.7. These models have a limited mass range of 0.4–1.0 M$_\odot$, however, so when a higher M_1 is required (up to 1.2 M$_\odot$) the relations from Panei, Althaus & Benvenuto (2000) are used instead. For a mass outside the range of 0.4–1.2 M$_\odot$, the Hamada-Salpeter 0 K relation (Hamada & Salpeter, 1961) is used. The mass-radius relations from Wood (1995) and Panei, Althaus & Benvenuto (2000) are temperature-dependent, and therefore require knowledge of T_1 (see Section 3.7.1).

M_2 is simply obtained from the product of q and M_1, while R_2 is calculated from equation 1.3, under the assumption that the donor fills its Roche lobe. The following expression is used to calculate K_1:

$$K_1 = \frac{2\pi a \sin i}{P_{\rm orb}} \frac{q}{1+q}, \tag{3.30}$$

which is derived from Kepler's 3rd law (equation 1.1), and makes use of both $K_1 M_1 = K_2 M_2$ and $(K_1 + K_2)/\sin i = 2\pi a/P_{\rm orb}$. The first of these equations is also used to obtain K_2.

Chapter 4

A Study of PHL 1445

The contents of this Chapter have been published in the Monthly Notices of the Royal Astronomical Society, **451**, 114–125 as a paper entitled *PHL 1445: an eclipsing cataclysmic variable with a substellar donor near the period minimum*, by McAllister, Littlefair, Baraffe, Dhillon, Marsh, Bento, Bochinski, Bours, Breedt, Copperwheat, Hardy, Kerry, Parsons, Rostron, Sahman, Savoury, Tunnicliffe (McAllister et al., 2015). The following is my own work unless otherwise stated.

4.1 Introduction

As discussed in Section 1.4.5, CV evolution theory predicts the existence of an orbital period minimum. Observational support for a period minimum comes in the form of a sharp cut off at low orbital periods in the CV orbital period distribution (Figure 1.4), whilst the current estimate for the period minimum is 81.8 ± 0.9 min (Knigge, Baraffe & Patterson, 2011).

Not all CVs obey this period minimum, however, as a handful are found to have periods below it. An example of such a CV, with an orbital period of 76.3 min, is PHL 1445[1]. PHL 1445 was first catalogued as a faint blue object by Haro & Luyten (1962) in the Palomar-Haro-Luyten catalogue, and again (as PB 9151) by Berger & Fringant (1984). It was identified as a CV system by Wils (2009) through spectroscopic analysis of the 6dF Galaxy Survey (Jones et al., 2004) target 6dFGS g0242429-114646, which was found to be coincident with PHL 1445. Its spectrum also showed double-peaked emission lines, indicating a high inclination and possibly deeply eclipsing system (Wils, 2009). The eclipsing nature of PHL 1445 was confirmed by Wils et al. (2011) through follow-up photometry, which also resulted in the first determination of the system's orbital period.

There are a number of reasons for a CV to have an orbital period shorter than the period minimum (see Sections 1.4.5 and 1.4.6). Obtaining PHL 1445's system parameters through eclipse modelling may help reveal its evolutionary state, and therefore the particular reason for its unusually low orbital period.

In this Chapter, averaged ULTRACAM eclipse light curves of PHL 1445 are modelled using the existing approach to obtain system parameters. The resulting donor mass, together with the orbital period, is utilised in an attempt to determine PHL 1445's evolutionary state. Additional modelling of individual PHL 1445 eclipse light curves is carried out with the aim of investigating variations in both the accretion disc and bright spot.

4.2 Observations and Light Curve Morphology

A total of 19 PHL 1445 eclipses were observed from Aug 2011–Feb 2014. The majority (15) of these eclipses were obtained with ULTRACAM on the WHT, the remainder with ULTRASPEC on the TNT. A complete journal of observations can be found in Table A.1. Out of the four ULTRASPEC eclipses, one is in outburst and

---

[1] PHL 1445 recently entered the General Catalogue of Variable Stars (GCVS) with the designation KN Cet (Kazarovets et al., 2015), however PHL 1445 is the identifier used throughout this work.

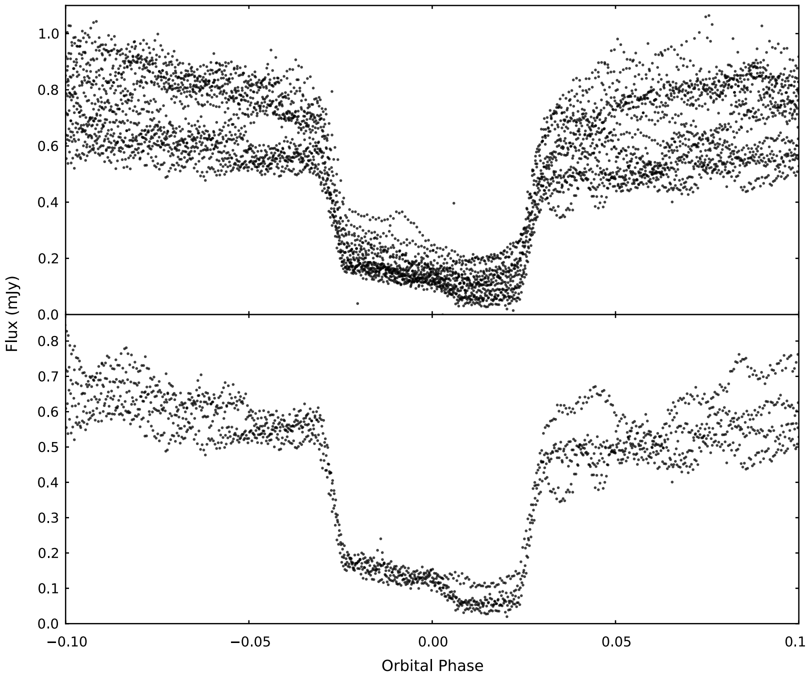

Figure 4.1: *Top*: All 14 quiescent PHL 1445 g'-band eclipse light curves observed with ULTRACAM, phase-folded using the ephemeris within Table 2.2. *Bottom*: The four PHL 1445 g'-band eclipse light curves chosen to create an average eclipse light curve.

the other three suffer from low SNR, so only the ULTRACAM eclipses – observed simultaneously in either SDSS $u'g'r'$ or $u'g'i'$ bands – are considered for this study. One of the ULTRACAM eclipses is also in outburst, but the remaining 14 show a clear white dwarf eclipse feature (see top panel of Figure 4.1).

While the white dwarf eclipse is clearly visible in all these eclipses, the same cannot be said for the bright spot feature. A bright spot ingress can be discerned in most cases, but not one eclipse shows a clear egress. The reason for the lack of clear bright spot egress in any of these light curves is the strong flickering associated with this system. The flickering is dramatically reduced during white dwarf eclipse and appears to begin immediately after white dwarf egress at around phase 0.03 (see Figure 4.1). This implies that its source is close to the white dwarf, either in the inner disc or boundary layer.

To help reduce the prominence of the strong flickering present, and to be able to locate the position of the bright spot egress, it was necessary to average multiple eclipse light curves together. The 10 eclipses appearing to show signs of a bright spot ingress in the g' band were phase-folded using the ephemeris within Table 2.2 and averaged, allowing a broad, faint bright spot egress feature to emerge. Averaging also seemed to reduce the strength of the bright spot ingress. After analysing each individual eclipse, it was apparent that the position of the bright spot ingress varied significantly across the range of observations due to changes in accretion disc radius. This is the reason for the bright spot ingress feature becoming broad and weak in the average eclipse light curve.

To fix this issue, four eclipse light curves (cycle nos. 0, 1413, 1430 and 1431) observed not too far apart in time (Nov 2011–Jan 2012) and with clear bright spot ingresses at a similar position (see bottom panel of Figure 4.1) were averaged. It is evident from Figure 4.1 that these four chosen eclipses occurred when PHL 1445 was in the lower of two distinct photometric states (clear gap visible in top panel just before white dwarf ingress), although this was not necessarily a criterion for choosing candidates for the average. A further two eclipses were observed within this time span (both on 14th Jan), but were not used due to a mixture of poor observing conditions and lack of a visible bright spot ingress. This new average eclipse light curve revealed much sharper bright spot features than that consisting of all 10 eclipses (Figure 4.2), and it is also worth noting that the position of the bright spot egress remained unchanged from the 10-eclipse average. The total rms of this average light curve's residuals is approximately 7%, which is larger than the typical photometric error ($\sim 3\%$) and shows that while flickering has been decreased through averaging, it remains an issue. Average eclipse light curves were also produced in the u' and r' bands, using the same four eclipse numbers as for the g' band.

4.3 Results

4.3.1 Average Eclipse Light Curve Modelling

The three average eclipse light curves – one in each of the u', g' and r' bands – were fit separately with the CV eclipse model (Section 3.2), as outlined in Section 3.6.1[2]. Only the simple bright spot model was used, as the subdued bright spot eclipse in PHL 1445 did not require the additional complexity offered by the complex model. The model fits to the average eclipse light curves are shown in Figure 4.2, while the associated model parameters can be found in Table C.1.

4.3.2 System Parameters

The mass ratio (q), white dwarf eclipse phase full-width at half-depth ($\Delta\phi$), and scaled white dwarf radius ($R_1/x_{\rm L1}$) posterior PDFs returned by each model fit were used to calculate posterior PDFs for the system parameters in each band (coloured PDFs in Figure 4.3), following the procedure described in Section 3.7. Combining the PDFs from the u', g' and r' bands gave the total posterior distributions for each system parameter (black PDFs in Figure 4.3). The value of each system parameter is taken as the most likely value of its PDF, with upper and lower errors derived from the 67% confidence level. The system parameters associated with these PDFs are shown in the first four columns of Table 4.1. Figure 4.4 shows a corner-plot for the g'-band fit, which exposes degeneracies between certain system parameters.

---

[2] Note that this is the existing modelling approach, as this study was carried out prior to the development of the new modelling approach.

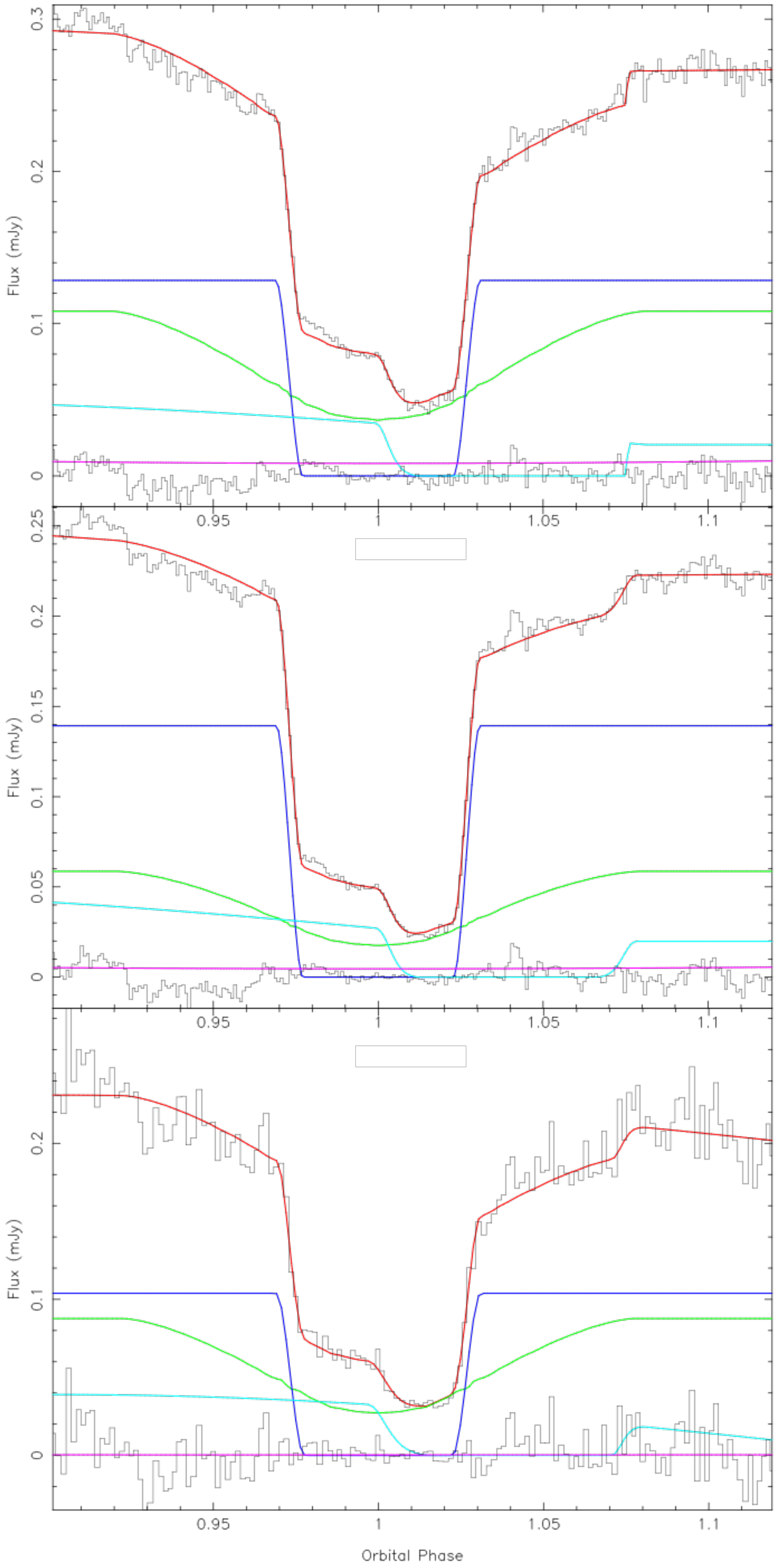

Figure 4.2: Model fits (red) to average PHL 1445 eclipse light curves (black) in r' (top), g' (middle) and u' (bottom) bands. Also shown are the different components of the model: white dwarf (dark blue), bright spot (light blue), accretion disc (green) and donor (purple). The residuals are shown at the bottom of each plot.

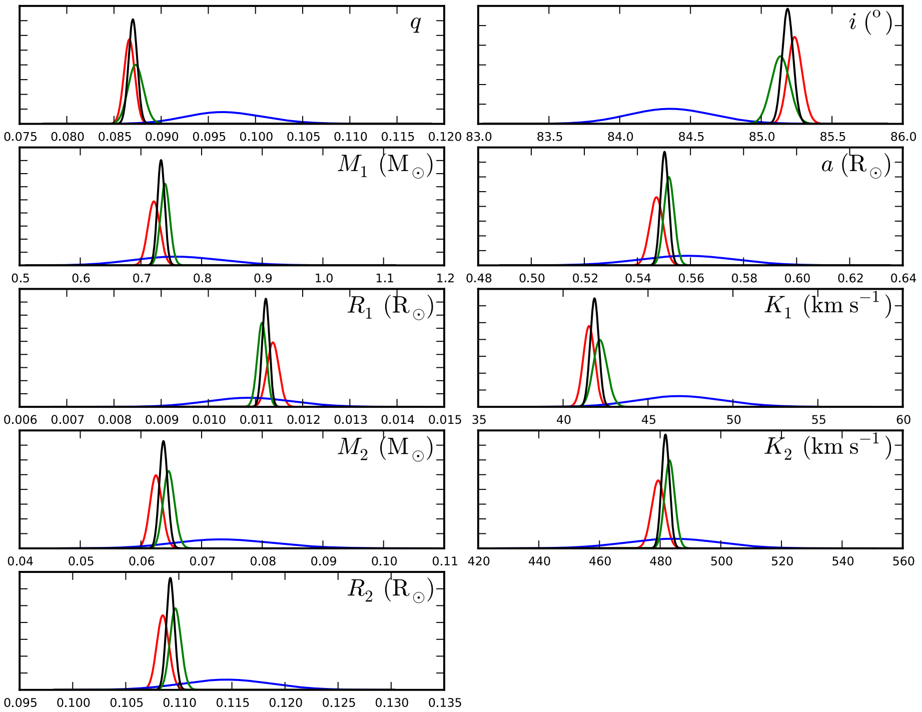

Figure 4.3: Normalised posterior probability density functions (black) for system parameters. The red, green and blue distributions represent the r'-, g'- and u'-band fits, respectively.

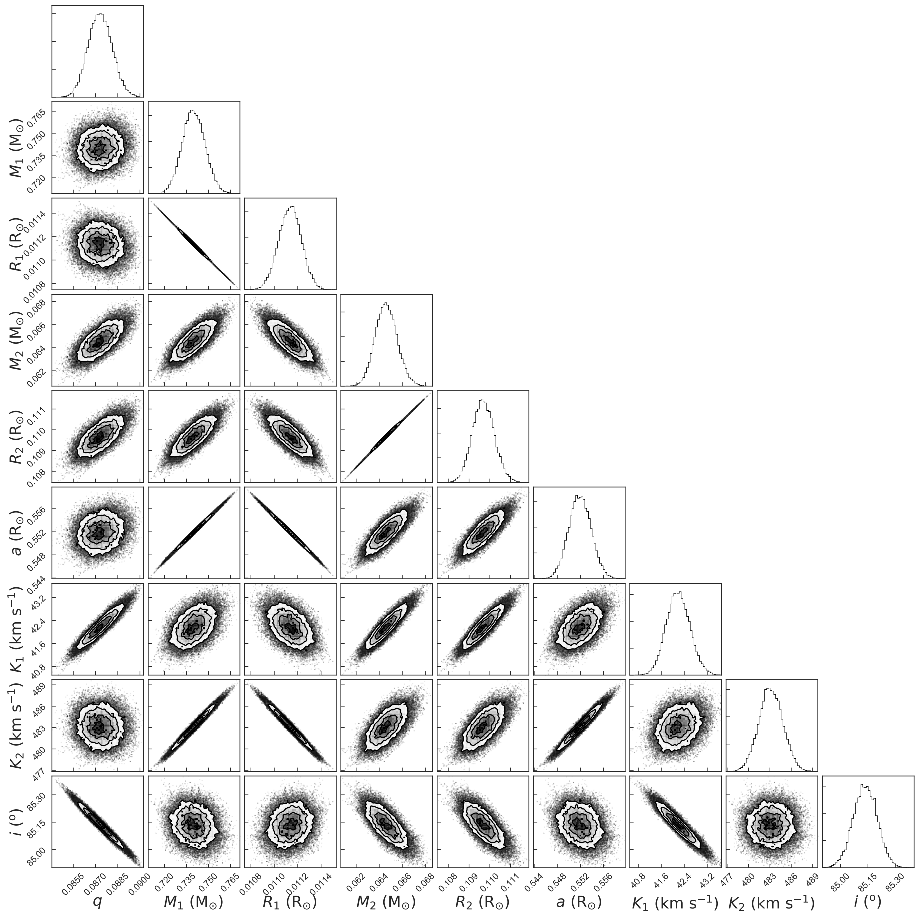

Figure 4.4: Corner-plot of g'-band fit showing correlations of varying strengths between system parameters.

Band	r'	g'	u'	Combined	Sys. error (%) due to flickering	Final estimates
q	0.0866 ± 0.0006	0.0873 ± 0.0008	0.096 ± 0.004	0.08701 ± 0.0005	5	0.087 ± 0.004
M_1 ($M_\odot$)	0.722 ± 0.010	0.740 ± 0.008	0.76 ± 0.08	0.733 ± 0.006	4	0.73 ± 0.03
R_1 ($R_\odot$)	0.01137 ± 0.00013	0.01114 ± 0.00010	0.0109 ± 0.0009	0.01122 ± 0.00008	4	0.0112 ± 0.0005
M_2 ($M_\odot$)	0.0625 ± 0.0010	0.0646 ± 0.0010	0.073 ± 0.009	0.0637 ± 0.0007	9	0.064 ± 0.006
R_2 ($R_\odot$)	0.1085 ± 0.0006	0.1097 ± 0.0006	0.115 ± 0.004	0.1092 ± 0.0004	3	0.109 ± 0.003
a ($R_\odot$)	0.547 ± 0.003	0.552 ± 0.002	0.559 ± 0.018	0.5502 ± 0.0016	2	0.550 ± 0.011
K_1 ($\mathrm{km\,s^{-1}}$)	41.5 ± 0.3	42.2 ± 0.4	47 ± 3	41.8 ± 0.3	6	41.8 ± 2.5
K_2 ($\mathrm{km\,s^{-1}}$)	479 ± 2	483.1 ± 1.7	484 ± 16	481.7 ± 1.4	1	482 ± 5
i (°)	85.24 ± 0.05	85.14 ± 0.07	84.4 ± 0.3	85.19 ± 0.04	< 1	85.2 ± 0.3
$\log g$	8.185 ± 0.012	8.213 ± 0.009	8.24 ± 0.08	8.203 ± 0.010	< 1	8.20 ± 0.04
T_1 (K)	–	–	–	13200 ± 700	–	13200 ± 700
d (pc)	–	–	–	220 ± 50	–	220 ± 50

Table 4.1: System parameters for PHL 1445. The errors in the combined column are returned by the model and are purely statistical. The errors in the final column take into account the systematic error due to flickering.

As stated in Section 3.7, calculation of system parameters requires a measure of the white dwarf temperature (T_1) from white dwarf atmosphere fitting (Section 3.7.1). White dwarf fluxes in u', g' and r' bands were used in the white dwarf atmosphere fit, in addition to an i'-band white dwarf flux obtained through fitting the eclipse model to the individual i'-band eclipse from the Sep 2012 observation (see section 4.3.3 for more details on this and other individual eclipse fits). The result of the white dwarf atmosphere fit is shown in the form of a colour-colour plot (Figure 4.5), with the white dwarf in PHL 1445 represented by the red data point[3]. The corresponding values for T_1 and distance (d) are shown at the bottom of column four in Table 4.1.

The system parameter errors in the first four columns of Table 4.1 are those resulting from the model fitting only, and do not account for uncertainties related to the effects of flickering. As this particular system displays strong flickering, it is clear that the errors on the system parameters from the model are underestimated, even though multiple light curves have been averaged.

To probe the effects of flickering, four additional g'-band average eclipse light curves were produced and fit with the eclipse model. Each of these new eclipse light curves contained a different combination of three of the four individual eclipses used for the original g'-band average eclipse light curve. The spread of system parameters obtained from these four model fits give a more realistic idea of the errors involved. The fifth column in Table 4.1 shows the estimated systematic error due to flickering, calculated from the weighted standard deviation of the system parameters from the four additional model fits. The values in the final column of Table 4.1 include this estimated uncertainty introduced by flickering.

---

[3] Note that the white dwarf colours shown are observed values, and have not been corrected for (low) extinction.

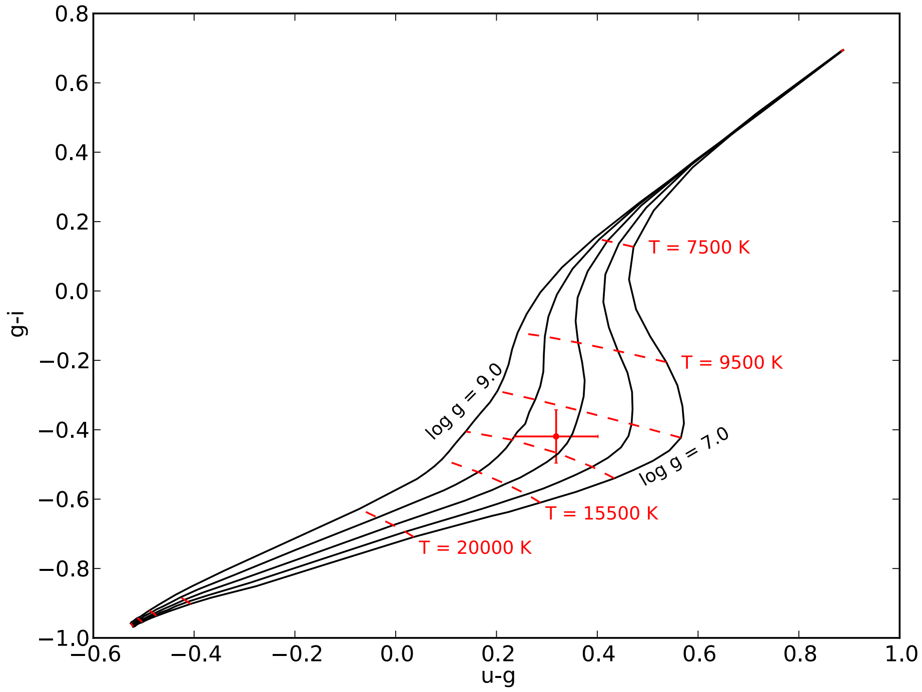

Figure 4.5: White dwarf colour-colour plot. The white dwarf in PHL 1445 is shown by the red data point and the black lines represent white dwarf models of varying $\log g$ (see Section 3.7.1).

4.3.3 Individual Eclipse Light Curve Modelling

The eclipse model was also fit to individual eclipse light curves – as long as they showed signs of a bright spot ingress – using the model parameters from the previous Section as a starting point (Table C.1). The eclipse model parameters q, $\Delta\phi$ and R_1/x_{L1} do not vary between eclipses, and so these parameter values were kept fixed for the individual fits.

In total there were 10 eclipses that showed signs of a bright spot ingress feature, and therefore qualified for individual model fitting, including the four eclipses used in the average eclipse light curve fitting. All but one of these eclipses was observed in the wavelength bands $u'g'r'$; the other in $u'g'i'$. Each individual eclipse was fit in each of the three bands, with the starting model parameters dependent on the band. The one i'-band eclipse (08 Sep 2012) was given the g'-band model parameters as a starting point. The model parameters resulting from these individual fits are found in tables C.2–C.4.

The individual g'-band eclipse light curves and corresponding eclipse model fits are shown in Figure 4.6. Through individual eclipse fitting, it is possible to study the variation of certain parameters from eclipse to eclipse, for example disc radii and component fluxes. However, due to the strong flickering present in each PHL 1445 eclipse light curve, it is important to check these fits are genuine and interpret the results with care. Looking at the individual fits in Figure 4.6, it is clear that not all achieve a true fit to the bright spot features (e.g. cycle nos. 5889, 14942 and 14945), and this will be taken into account in the following discussion.

The individual eclipse light curve fitting provided nine sets of $u'g'r'$ fluxes and one set of $u'g'i'$ fluxes for the white dwarf, accretion disc and bright spot components. A systematic error of 3% was added to all fluxes to account for uncertainties introduced during the flux calibration process (Section 2.4). There was no evidence for significant variations in white dwarf temperature across the 10 individual eclipses.

4.3.4 Accretion Disc

Individual eclipse light curve fitting produced a value of $R_{\rm disc}/x_{\rm L1}$ for all 10 eclipses. With the u'-band fits being the least reliable due to the low quality of light curves, only the the r', i'- and g'-band $R_{\rm disc}/x_{\rm L1}$ were used. For each eclipse, an average of the r', i'- and g'-band $R_{\rm disc}/x_{\rm L1}$ was plotted against $T_{\rm mid}$ in order to show how the disc varies with time. This is shown in Figure 4.7, with the plot split into two due to a sizeable time gap between observations.

The individual errors displayed in Figure 4.7 are from the model fits, and are significantly underestimated due to the effects of flickering. There is a systematic error on the disc radius of approximately 4% due to flickering, and this is represented by the bar in the bottom-left corner of Figure 4.7. Without the introduction of this systematic error, the disc changes appear to be very large, for example take the successive eclipses of 1430 and 1431 (MJD $\sim$ 55943). In the time of just one orbital period (76.3 min), $R_{\rm disc}/x_{\rm L1}$ increases from approximately 0.288 to 0.380, implying

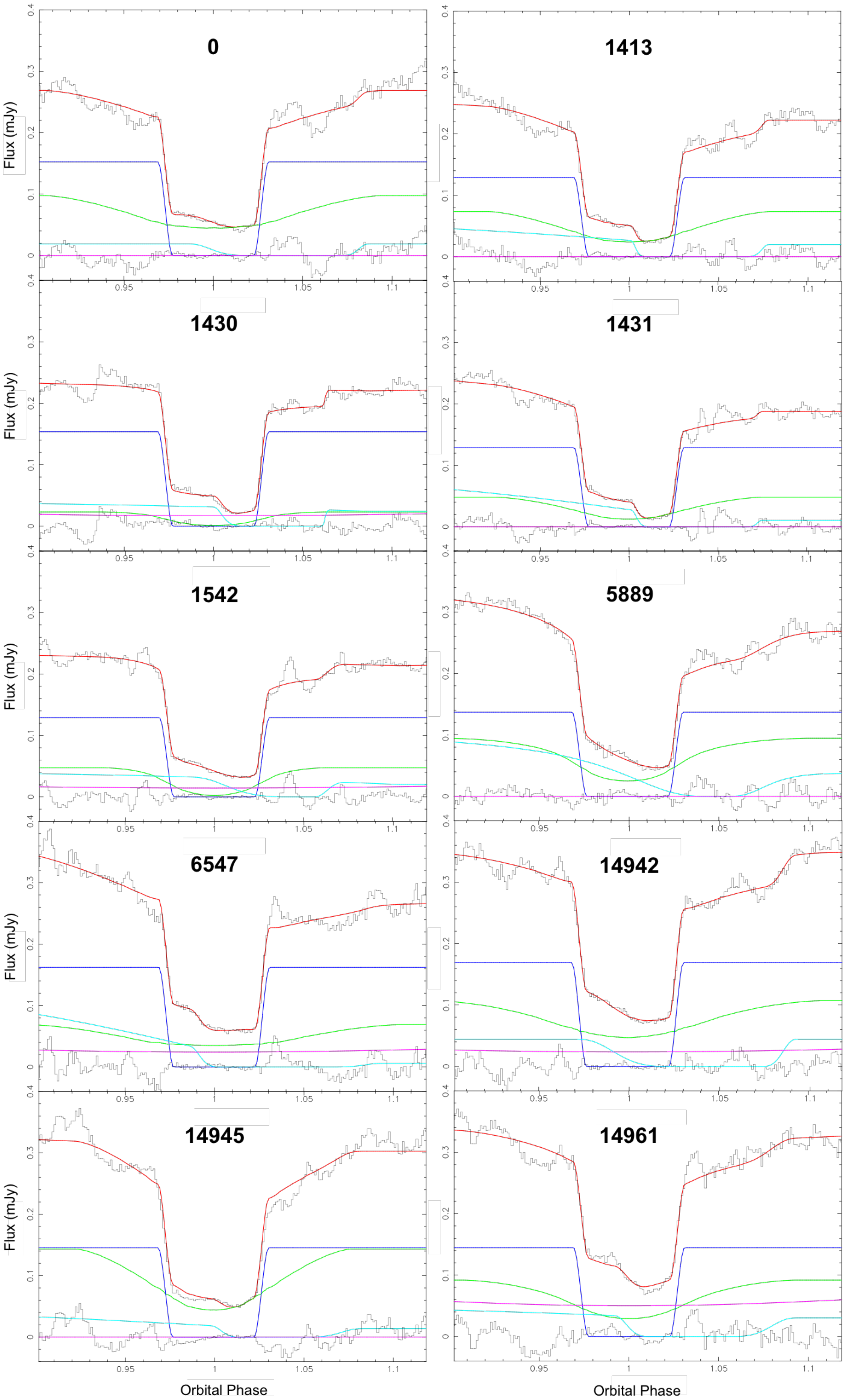

Figure 4.6: Model fits (red) to individual PHL 1445 g'-band eclipses (black). The additional coloured lines are explained in Figure 4.2. The cycle numbers of each eclipse are also displayed.

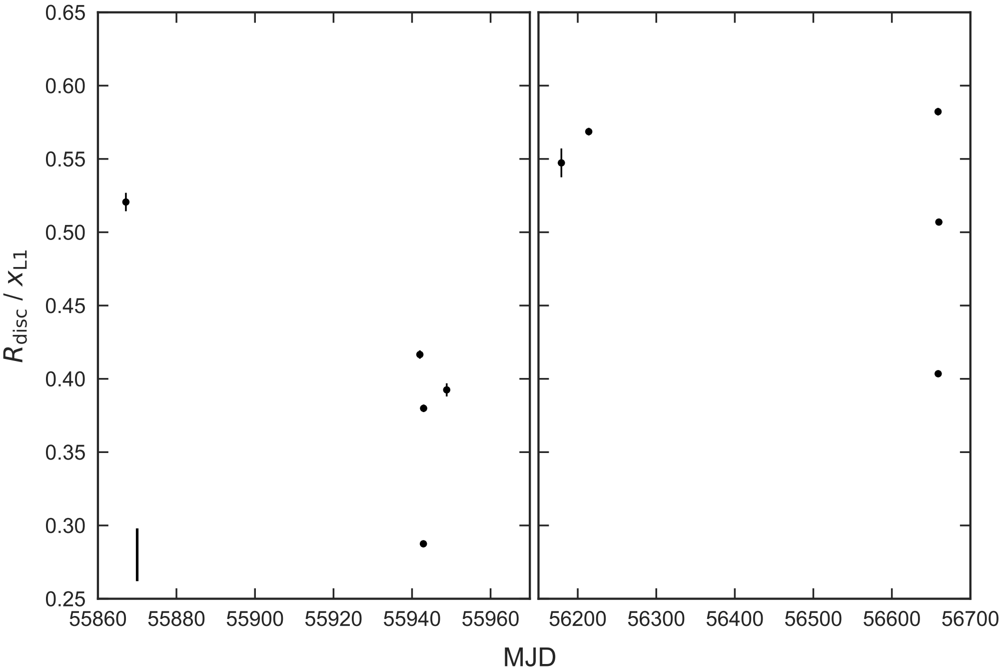

Figure 4.7: PHL 1445 accretion disc radius ($R_{\rm disc}$) as a fraction of the distance to the inner Lagrangian point ($x_{\rm L1}$) vs time (in MJD). Individual errors are purely statistical, and in most cases the error bars are smaller than the data points. The bar in the bottom-left corner gives an indication of the real error due to flickering. The figure is split into two due to a large gap in time (~ 200 days) between observations.

a disc expansion velocity of $5600\,{\rm m\,s^{-1}}$, which is significantly faster than the $2\,{\rm m\,s^{-1}}$ 'viscous velocity' of material within the disc.

As Figure 4.6 shows, both of these eclipses have clear bright spot ingress features. The fit to the bright spot ingress in the 1431 eclipse is far better than that in the 1430 eclipse, therefore the poor fitting of the 1430 eclipse may be the real reason for the large disc radius expansion observed over this orbital cycle. The poor fit to the bright spot ingress in cycle 1430 – as in many other individual eclipses (Figure 4.6) – is most likely due to the large amount of flickering present, and is addressed through the introduction of a 4% systematic error, although judging by Figure 4.7, this may be slightly underestimated. It must be noted that in some individual eclipses with weak bright spot features (e.g. cycle nos. 1542 and 5889) the bright spot ingress is hardly fit at all, resulting in much more uncertain values of $R_{\rm disc}/x_{\rm L1}$ in these cases.

The top plot in Figure 4.8 shows how the flux of the disc varies with disc radius. Again, the individual errors are underestimated, and the errors introduced by flick-

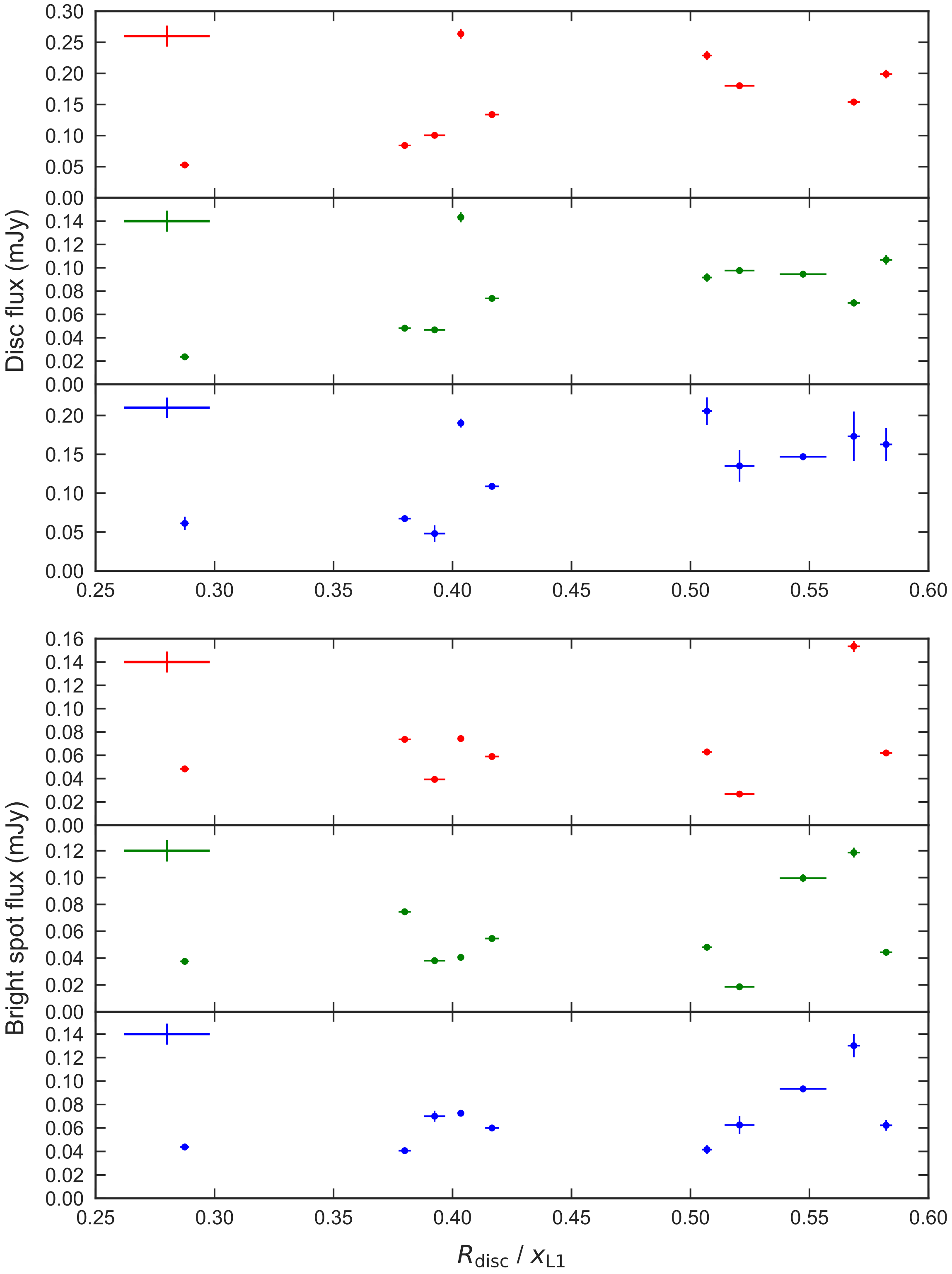

Figure 4.8: PHL 1445 accretion disc flux (top) and bright spot flux (bottom) vs accretion disc radius (R_{disc}) as a fraction of the distance to the inner Lagrangian point (x_{L1}). Red, green and blue data points represent r'-, g'- and u'-band observations, respectively. Individual errors are purely statistical, and in most cases the error bars are smaller than the data points. The bars in the top-left corners of each plot give an indication of the real error due to flickering.

ering are represented by the bars in the top-left corner of each plot. To measure the reliability of these flux changes, focus again turns to the successive eclipse cycles 1430 and 1431. In one orbital period the g'-band disc flux increases by $\sim 0.025\,\mathrm{mJy}$, but at the same time the g'-band white dwarf flux drops by the same amount. Such a change in white dwarf flux over one orbital cycle is not expected, and it is clear by looking at Figure 4.6 that a fraction of the white dwarf flux in cycle 1430 has been fit in the following cycle by the disc component instead. This may not be the case for all individual eclipse fits, but it does question the reliability of the model disc flux values. The most likely cause of this is the large amount of flickering in these individual eclipse light curves, which confirms the need for a systematic error to account for it. Even with the addition of a systematic error, there does appear to be a positive correlation between these two disc parameters in all three wavelength bands. There is no evidence for changes in disc temperature, so the trend in Figure 4.8, if real, appears to be simply due to a larger disc radius resulting in a larger disc surface area and therefore flux.

4.3.5 Bright Spot

The bright spot fluxes were also plotted against $R_{\mathrm{disc}}/x_{\mathrm{L1}}$ (see bottom plot in Figure 4.8). Unlike the disc fluxes, on the whole the bright spot fluxes appear to stay relatively constant across the different disc radii. Assuming the main contributor to bright spot flux is the relative velocity of the gas stream as it impacts with the disc, the gas stream was modelled and its velocity relative to the disc calculated for a number of disc radii across the range $0.2 < R_{\mathrm{disc}}/x_{\mathrm{L1}} < 0.6$. The relative velocity of the gas stream only increased by a factor of two across this range, which could explain why little variation in bright spot fluxes is observed.

4.4 Discussion

4.4.1 Component Masses

A white dwarf mass of $0.73 \pm 0.03\,\mathrm{M}_\odot$ is found for PHL 1445, which is much larger than the mean white dwarf mass in the field and within pre-CV systems (Zorotovic, Schreiber & Gänsicke, 2011; Tremblay et al., 2016), but is identical to the mean white dwarf mass in CV systems below the period gap ($0.73 \pm 0.05\,\mathrm{M}_\odot$) found by Knigge (2006). It is, however, lower than the mean white dwarf mass found by Savoury et al. (2011) within a group of 14 short period CVs ($0.81 \pm 0.04\,\mathrm{M}_\odot$). As for the donor in PHL 1445, it is found to have a mass of $0.064 \pm 0.005\,\mathrm{M}_\odot$. This is below the hydrogen burning mass limit of $\sim 0.075\,\mathrm{M}_\odot$ (e.g. Kumar 1963; Hayashi & Nakano 1963), which suggests it is substellar.

4.4.2 Flickering

One particular feature of all PHL 1445 eclipse light curves is high amplitude flickering. This is much larger than the flickering observed in other known CVs with substellar donors (Savoury et al., 2011), and appears to be originating from the inner accretion disc, near the white dwarf. The accretion disc and bright spot fluxes as a fraction of the white dwarf flux were calculated in u', g' and r', and compared with those from other CVs with substellar donors. PHL 1445's disc fluxes are nearly double those of the second highest disc flux system, which suggests the enhanced flickering is associated with a brighter disc.

4.4.3 Evolutionary State

It is known that PHL 1445 consists of an accreting white dwarf and a donor star, but what is not known is the nature of this donor star. It is possible that PHL 1445 lies below the period minimum because it contains an unusual donor star, one most likely off the main sequence. Having determined a mass, radius and flux for the donor star of PHL 1445, its nature can be investigated.

Halo Object

One possibility is that PHL 1445 is a Galactic halo object. A system belonging to the Galactic halo would typically have a metal-poor donor star, meaning a smaller than expected radius for its mass and therefore a higher density. Due to the inverse relation between density of a Roche lobe-filling donor star and the orbital period of a system, a metal-poor donor is one way for a CV system to have an orbital period below the period minimum (Patterson, Thorstensen & Knigge, 2008). This was found to be the case for SDSS J150722.30+52309.8 (SDSS 1507), another eclipsing CV with an orbital period (67 min) below the minimum (Patterson, Thorstensen & Knigge, 2008; Uthas et al., 2011).

SDSS 1507's halo membership is supported by both its unusually high space velocity (167 $\mathrm{km\,s^{-1}}$), calculated from its distance and proper motion by Patterson, Thorstensen & Knigge (2008), and sub-solar metallicity determined from UV spectroscopy by Uthas et al. (2011). Using the new estimate of the distance to PHL 1445 and proper motions listed in the PPMXL catalog (Roeser, Demleitner & Schilbach, 2010), a transverse velocity of $39 \pm 9\,\mathrm{km\,s^{-1}}$ was calculated. This is significantly lower than that for SDSS 1507, and is very close to the average transverse velocity of 33 $\mathrm{km\,s^{-1}}$ for CVs (Patterson, Thorstensen & Knigge, 2008), which is evidence against PHL 1445 being a member of the Galactic halo.

Evolved Donor

Another explanation for the short orbital period is a donor star that is already evolved at the start of mass transfer. One way of determining the evolutionary stage of a star is through its composition, which can be determined from its spectrum. A spectrum for PHL 1445 is shown in Wils (2009), but this is not of much use as it is dominated by the other components of the CV, not the donor. This isn't surprising, as there is a very minimal flux contribution from the donor to the overall flux of PHL 1445, even in the r' band (see Figure 4.2). An upper limit for the donor flux is acquired through model fitting, which is actually a measure of the total un-eclipsed flux from the system.

Thorstensen et al. (2002) show that an evolved donor with a central hydrogen abundance of $X_{\mathrm{c}} = 0.05$, in a system with PHL 1445's orbital period, should have a temperature in excess of 4000 K, while Podsiadlowski, Han & Rappaport (2003) show an $X_{\mathrm{c}} = 0.1$ evolved donor in a similar system to have a temperature somewhere between 1500–2000 K. Through knowledge of PHL 1445's donor angular diameter and flux from the eclipse model, a 4000 K donor can be ruled out, but there is some agreement with a 1500–2000 K donor.

$g' - r'$ colours were estimated for both a 4000 K and 1800 K donor. The colour for the 4000 K donor was found through the linear relation between T_{eff} and $g' - r'$ (Fukugita et al., 2011), but this relation doesn't extend to below $\sim$3800 K so semi-empirical model isochrones had to be used in order to obtain a colour for the 1800 K donor (Baraffe et al., 1998; Allard, Homeier & Freytag, 2011; Bell et al., 2014). From these colours, r'-band zero-magnitude angular diameters were calculated and used together with the donor angular diameter to produce an apparent r'-band donor magnitude at each temperature (Boyajian, van Belle & von Braun, 2014). It must be noted that the colour obtained for the 1800 K donor lies outside the valid range given by Boyajian, van Belle & von Braun (2014) for their magnitude-angular diameter relation.

Donor fluxes of $(15.9 \pm 1.1) \times 10^{-2}$ mJy and $(0.33 \pm 0.18) \times 10^{-2}$ mJy were calculated in the r' band for 4000 K and 1800 K, respectively. The 4000 K donor is approximately 13 times the $(1.27 \pm 0.08) \times 10^{-2}$ mJy upper limit for the r'-band donor flux from the eclipse model, while the 1800 K donor flux is approximately four times smaller. Analysis of the donor flux hence shows that a slightly evolved donor ($X_{\rm c} = 0.1$) cannot be ruled out for PHL 1445, and may be the reason for its unusually short orbital period.

Brown Dwarf Donor From Formation

PHL 1445 could also lie below the period minimum because it formed directly with a brown dwarf donor. These systems can start out with periods much shorter than the period minimum, but evolve towards longer orbital periods like post-period bounce CVs (see Section 1.4.6). The possibility of PHL 1445 forming with a brown dwarf donor is investigated by studying the relation between M_2 and $P_{\rm orb}$ (see Figure 4.9).

Figure 4.9 shows a number of different evolutionary tracks. The red track is the semi-empirical, best-fit evolutionary track for CVs with main sequence donors from Knigge, Baraffe & Patterson (2011) (see Section 1.5.4). The green track is from Thorstensen et al. (2002) and represents a system containing an evolved donor with $X_{\rm c} = 0.05$. The possibility of such a highly-evolved donor has been ruled out (see above), and this is supported by the fact that the PHL 1445 data point lies comfortably below this line. The solid blue line is from Kolb & Baraffe (1999) and represents a system that formed with a brown dwarf donor. It would appear that the PHL 1445 data point lies far from this track, but this track is computed from an old model, using a gravitational-radiation (GR) based angular momentum loss rate and ignoring deformation of the donor. Knigge, Baraffe & Patterson (2011) showed that tracks with these assumptions cannot fit the observed locus of CVs in the $M_2(P_{\rm orb})$ diagram, and that models which include deformation and an angular momentum loss rate of 2.47 × GR are required. The three additional brown dwarf donor tracks (blue: dashed, dot-dashed and dotted; Baraffe, priv. comm.) do, however, take into account both a 2.47 × GR angular momentum loss rate and deformation.

All three of these additional brown dwarf donor tracks have been calculated from a model containing a $0.75\,{\rm M}_\odot$ primary and a donor of initial mass $0.07\,{\rm M}_\odot$, with an additional variable parameter being the age of the donor at start of mass transfer

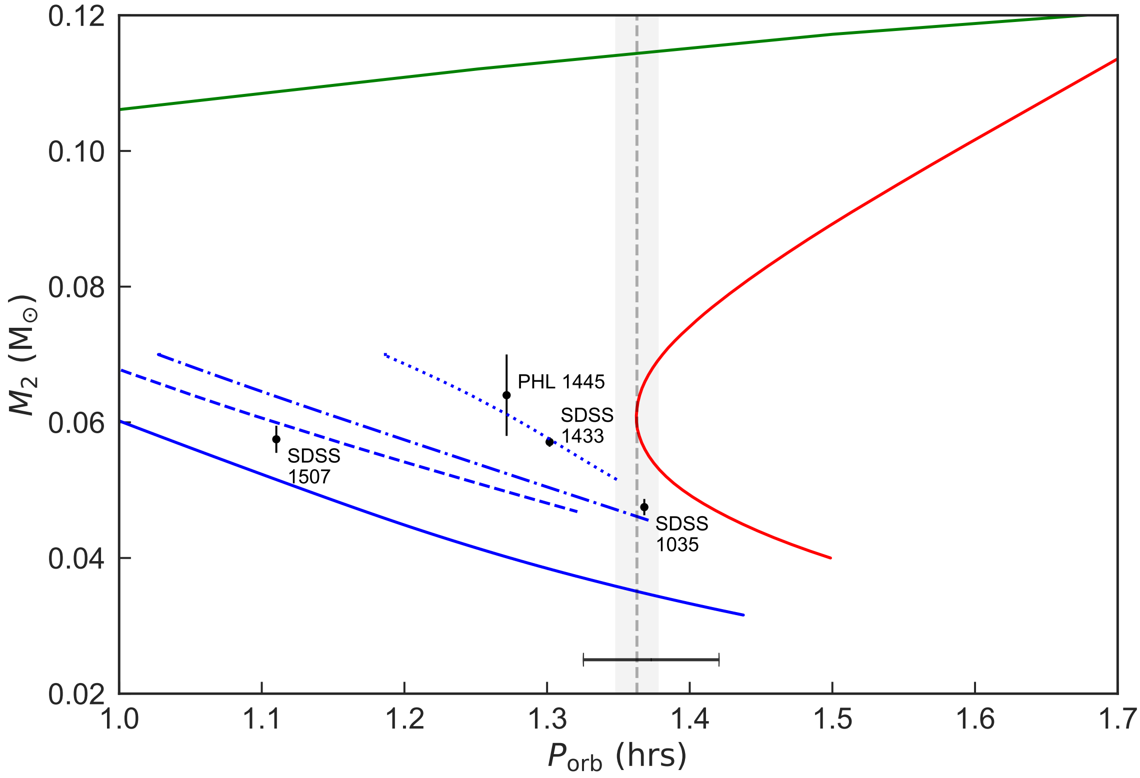

Figure 4.9: Donor mass (M_2) vs orbital period ($P_{\rm orb}$) for PHL 1445 and three other substellar donor CVs: SDSS 1433, SDSS 1035 and SDSS 1507 (Savoury et al., 2011). Also plotted are a number of evolutionary tracks: main sequence donor (red line; Knigge, Baraffe & Patterson 2011), evolved donor with $X_{\rm c} = 0.05$ (green line; Thorstensen et al. 2002) and brown dwarf donor (solid blue line; Kolb & Baraffe 1999). The three additional blue lines (Baraffe, priv. comm.) also show tracks for brown dwarf donors but with modified physics and varying donor age at start of mass transfer ($t_{\rm init}$). The dashed, dot-dashed and dotted blue lines represent $t_{\rm init}$'s of 2 Gyr, 1 Gyr and 600 Myr, respectively. The vertical dashed grey line represents the location of the CV period minimum determined by Knigge, Baraffe & Patterson (2011), with the shaded area representing the error on this value. The bar across the bottom of the plot shows the FWHM of the CV period spike observed by Gänsicke et al. (2009).

(t_{init}). This is an important parameter with regards to understanding the subsequent evolution of such a system, since a substellar object has a time-dependent radius. The dashed, dot-dashed and dotted blue lines represent t_{init}'s of 2 Gyr, 1 Gyr and 600 Myr respectively. The latter of these tracks – with a t_{init} of 600 Myr – is consistent with the PHL 1445 data point, but how feasible is such a proposed system?

In order for mass transfer to start so early in the system's lifetime, the primary star must have evolved off the main sequence very quickly to leave a white dwarf ready for mass transfer. This puts a lower limit on the initial primary mass of $2.8\,\mathrm{M}_{\odot}$ (Girardi et al., 2000). Considering the secondary has an initial mass no greater than $0.07\,\mathrm{M}_{\odot}$, this would mean an initial mass ratio of approximately 0.025 or less. This is extremely low, and main sequence star/brown dwarf binaries with extreme mass ratios are rare ('brown dwarf desert'; see Section 1.4.6), although it would seem they are able to form (Grether & Lineweaver, 2006b). Binaries with such low mass ratios have been observed, for example HIP 77900B, which has a mass ratio as low as 0.005 (Aller et al., 2013), although its separation of 3200 AU is extreme. There is also observational evidence for binaries with A-type primaries to have a bias towards low mass ratios of less than 0.1 (Kouwenhoven et al., 2005). It is therefore a possibility that PHL 1445 formed directly from a binary system with a very low mass ratio containing a $> 2.8\,\mathrm{M}_{\odot}$ primary and brown dwarf secondary.

A further two CVs found to be hosting substellar donors are SDSS J143317.78+101123.3 (SDSS 1433) and SDSS J103533.03+055158.4 (SDSS 1035) (Littlefair et al., 2008; Savoury et al., 2011). Both SDSS 1433 and SDSS 1035 were claimed to be period-bounce systems by Littlefair et al. (2008) and Savoury et al. (2011), but the generally accepted location of period minimum has since moved to a higher P_{orb} (81.8 ± 0.9 min; Knigge, Baraffe & Patterson 2011). As Figure 4.9 shows, while SDSS 1035 remains (just about) above the period minimum, SDSS 1433 is now comfortably below it, bringing its period bouncer status into question. With an orbital period below the period minimum and a substellar donor, SDSS 1433 may actually be a system that formed with a brown dwarf donor. Support for this comes from the position of SDSS 1443 in Figure 4.9, where it appears to lie on the same brown dwarf donor track as PHL 1445[4]. This suggests that the progenitor systems of both PHL 1445 and SDSS 1433 may have had extremely low mass ratios, but the chances of finding two systems with similar, extreme initial mass ratios out of such a small (four system) sample should be very low (Section 1.4.6). This finding therefore raises some suspicion.

Main Sequence Donor (Period Minimum System)

Given the low chance that both PHL 1445 and SDSS 1433 formed with a brown dwarf donor, it is possible that both may actually be CVs with main sequence donors, lying within the intrinsic scatter of the period minimum. As discussed in Section 1.5.4, the current period minimum at 81.8 ± 0.9 min (vertical dashed line in Figure 4.9) was determined by Knigge, Baraffe & Patterson (2011) through fitting a semi-empirical donor-based CV evolution track (red track in Figure 4.9) to the masses of a sample of CV donors. This sample of donors contains an intrinsic dispersion of $\sigma_{\rm int} = 0.02$ dex (Knigge, Baraffe & Patterson, 2011), introducing an intrinsic scatter around the period minimum of equal value. This is equivalent to an intrinsic dispersion of $\sigma_{\rm int} = 3.7$ min, significantly larger than the 0.9 min error on the period minimum location. Approximately one third of this intrinsic scatter is due to the $\sim 20\%$ dispersion in white dwarf masses of the sample (Knigge, 2006). The majority of the remaining error can probably be attributed to a distribution in mass-loss rates, associated with residual magnetic braking below the CV period gap. This residual magnetic braking may explain why Knigge, Baraffe & Patterson (2011) require additional angular momentum loss below the period gap in order to produce a CV evolution track that is in agreement with the donor sample.

An independent measure of the intrinsic scatter can be obtained from the pe-

---

[4] There is a case for SDSS 1035 to also lie on an extension of this line, but it is assumed that SDSS 1035 is a period-bounce system for the remainder of this analysis.

riod spike analysis of Gänsicke et al. (2009). The position of the period spike at 82.4 ± 0.7 min is a good match to the period minimum from Knigge, Baraffe & Patterson (2011), and Gänsicke et al. (2009) – assuming a Gaussian distribution – find a FWHM of 5.7 min for this feature (indicated by the black bar at bottom of Figure 4.9). The intrinsic scatter on the period spike is therefore $\sigma_{\rm int} = 2.4$ min. Using $\sigma_{\rm int}$ of the period spike from Gänsicke et al. (2009) as the dispersion of systems around the period minimum, PHL 1445 and SDSS 1433 are found to be 2.3σ and 1.5σ outliers, respectively.

In the sample of short-period eclipsing CV systems in Savoury et al. (2011), four systems have orbital periods between 80 and 86 min, making them period spike systems according to Gänsicke et al. (2009). Assuming PHL 1445 and SDSS 1433 are also period minimum systems brings the total to six. It must also be assumed that no selection biases were involved in Savoury et al. (2011)'s choice of systems for model fitting. If CVs are distributed around a period minimum of 81.8 min with an intrinsic scatter of 2.4 min, the chances of finding these two outlying systems in such a small sample are approximately 2%. This confirms the seemingly unlikely occurrence of finding two period minimum systems with orbital periods as short as SDSS 1433 and PHL 1445, if the existing estimates for the position of the period minimum and $\sigma_{\rm int}$ are correct.

It may be that the intrinsic scatter around the period minimum is underestimated, or even that the position of the period minimum is incorrect. The ability to join the three substellar donor systems, PHL 1445, SDSS 1433 and SDSS 1035 with a single main sequence evolutionary track in Figure 4.9 would provide evidence for the latter of these two possibilities, as this would suggest all three are period minimum systems that are of similar nature, just at different evolutionary stages.

Chapter 5

A Study of ASASSN-14ag

The content of Sections 5.1–5.4 in this Chapter closely resembles work published in the Monthly Notices of the Royal Astronomical Society, **464**, 1353–1364 as a paper entitled *Using Gaussian processes to model light curves in the presence of flickering: the eclipsing cataclysmic variable ASASSN-14ag*, by McAllister, Littlefair, Dhillon, Marsh, Ashley, Bours, Breedt, Hardy, Hermes, Kengkriangkrai, Kerry, Rattanasoon, Sahman (McAllister et al., 2017a). Since publication, the model fitting has been revised and it is the updated results that are included here. This revision has had no significant impact on the overall findings of the study. The following is my own work unless otherwise stated.

5.1 Introduction

After the development and implementation of the new modelling approach outlined in Section 3.6.2, the next requirement is to thoroughly test its performance. Eclipse light curves that contain high levels of flickering, but also clear bright spot eclipse features, are the most suited for this task. An eclipsing CV with available ULTRACAM/ULTRASPEC eclipse light curves that closely match this criteria is ASASSN-14ag.

ASASSN-14ag was discovered in outburst (reaching $V = 13.5$) by the All-Sky Automated Search for Supernovae (ASAS-SN; Shappee et al. 2014) on 14th March 2014. A look through existing light curve data on this system from the Catalina Real-Time Survey (CRTS; Drake et al. 2009) showed signs of eclipses, with an orbital period below the period gap[1]. Follow up photometry made in the days following the initial ASAS-SN discovery confirmed the eclipsing nature of the CV[2]. The discovery of superhumps also showed this to be a superoutburst, identifying ASASSN-14ag as a SU UMa-type dwarf nova (Kato et al., 2015).

In this Chapter, the new modelling approach is tested on ULTRASPEC eclipse light curves of ASASSN-14ag, both with and without the inclusion of the GP model. ASASSN-14ag eclipse light curves are also modelled in accordance with the existing modelling approach, providing a direct comparison of the two approaches. The final Section involves re-modelling PHL 1445 eclipse light curves (see previous Chapter) with the new modelling approach, providing yet another opportunity for comparison.

5.2 Observations and Light Curve Morphology

ASASSN-14ag was observed a total of 14 times from Nov 2014–Dec 2015 with ULTRASPEC on the TNT. Eclipses were observed in the SDSS $u'g'r'i'$ and *KG5* filters. A complete journal of observations can be found in Table A.1. Figure 5.1 shows 12 of the 14 total ASASSN-14ag eclipses, phase-folded using the ephemeris within Table 2.2. The eclipses of 03 Mar 2015 and 05 Dec 2015 were affected by poor atmospheric conditions, so were not used in this study. The eclipses in Figure 5.1 all have a clear white dwarf eclipse feature (phase -0.03 to 0.03), and the majority also have a discernible bright spot eclipse feature (phase -0.02 to 0.08). The positions of bright spot ingress and egress appear to occur at slightly different phases in each eclipse. This may be evidence for small changes in the accretion disc radius or could

---

[1] vsnet-alert 17036: http://ooruri.kusastro.kyoto-u.ac.jp/mailarchive/vsnet-alert/17036

[2] vsnet-alert 17041: http://ooruri.kusastro.kyoto-u.ac.jp/mailarchive/vsnet-alert/17041

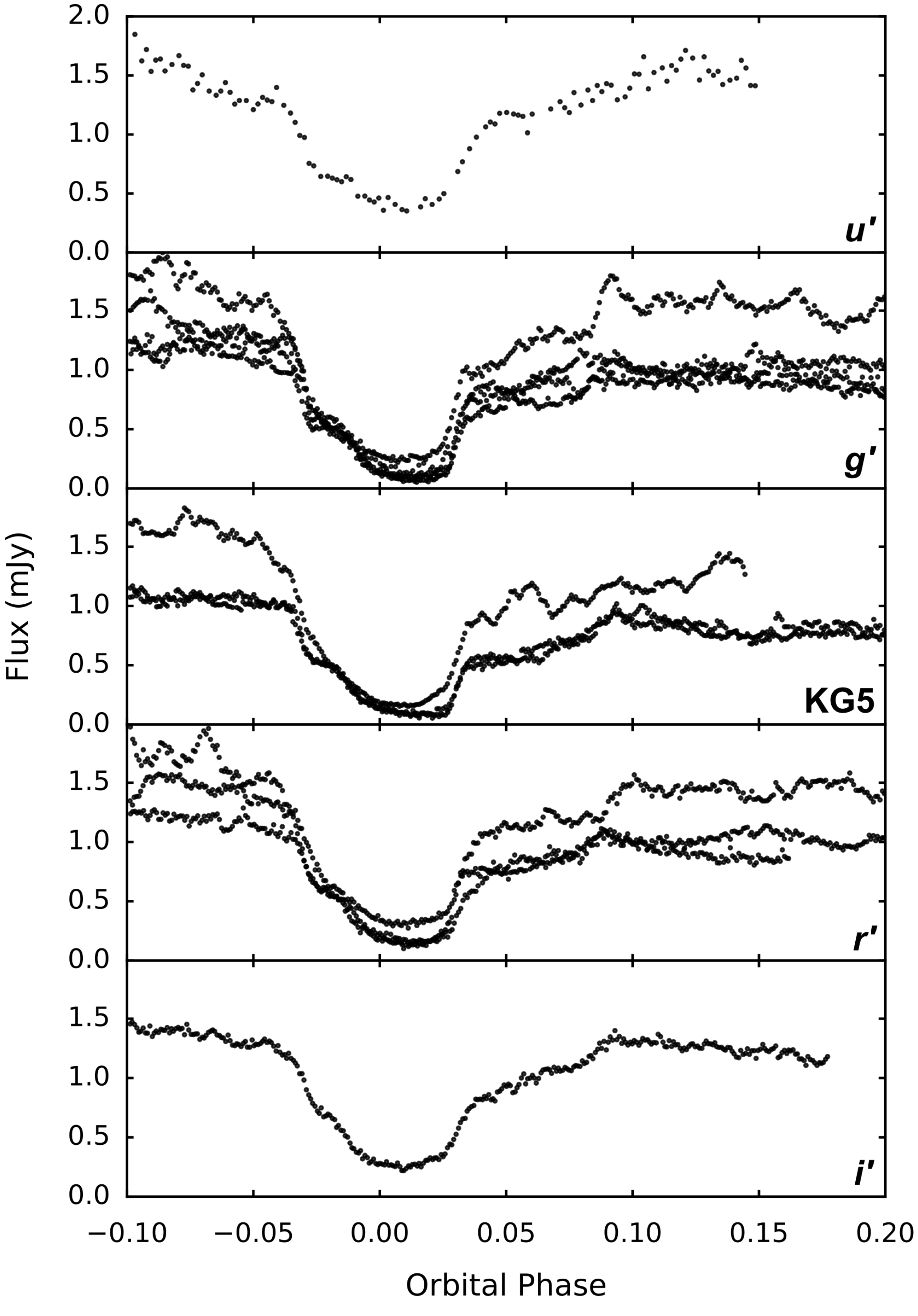

Figure 5.1: All 12 ASASSN-14ag eclipse light curves not badly affected by atmospheric conditions; phase-folded using ephemeris within Table 2.2. Each plot contains those eclipses observed in one of the five wavelength bands, with the name of each band in the bottom-right corner of each plot.

be due to flickering, which is inherent to every eclipse and of varying amplitude from one eclipse to the next.

The majority of the flickering occurs outside of white dwarf eclipse. In some cases it reappears almost immediately after white dwarf egress, implying the source of flickering to be in proximity to the white dwarf, perhaps in either the inner disc or the boundary layer. In a number of eclipses there is a small amount of flickering visible between the two ingress features. As the white dwarf is eclipsed during this period, there must be another source of flickering within the system. Flickering is greatly reduced once both the white dwarf and bright spot are eclipsed, which points to the bright spot as the secondary source of flickering.

The highest amplitude flickering is seen in the three eclipses that were observed while the system was in a slightly higher photometric state, with one such eclipse in each of the *KG5*, g' and r' bands (Figure 5.1). The higher photometric state is most likely to be the result of a more luminous disc. The high state g' and r' band eclipses do show a clear bright spot egress feature, but an ingress is not visible in any of these three eclipses and therefore none were used for the model fitting.

5.3 Results

5.3.1 Simultaneous Eclipse Light Curve Modelling

Discarding the two eclipses affected by poor atmospheric conditions and the three eclipses in the higher photometric state left a total of nine eclipses suitable for modelling. To start with, the eight suitable eclipses taken in bands other than u' were simultaneously fit with just the eclipse model (complex bright spot; Section 3.2), as outlined in Section 3.6.2. The simultaneous fit was then repeated, this time with the GP flickering model (Section 3.4.5) also included. The u'-band eclipse was not used in the simultaneous fits as a consequence of its lower signal-to-noise and time-resolution compared to other wavelength bands, although it was fit separately, both with and without the GP model (see below).

Without GP Model

The first simultaneous fit to the eight eclipse light curves, without inclusion of the GP model, is shown in Figure 5.2a. The model parameters are located in Table C.6. The most probable fit to the eight eclipses has a χ^2 of 16601 with 2598 degrees of freedom. This large value of χ^2 is due to the large amount of flickering present in each eclipse. The eclipse model appears to fit every single white dwarf eclipse reasonably well, although there are one or two cases where the depth of the white dwarf eclipse has either been slightly underestimated (e.g. cycle no. 594) or overestimated (e.g. cycle no. 1474).

In general, the bright spot eclipses have also been fit fairly well. The major exception to this is cycle no. 0. This eclipse contains low amplitude flickering until a slight brightening prior to bright spot egress and then a significant flicker just afterwards covering the orbital phases 0.08–0.13. These two features, especially the large flicker, make it impossible for the eclipse model to correctly fit the bright spot egress. An enlarged bright spot is therefore favoured, at the expense of bright spot ingress, which is free from flickering but poorly fit. Another notable bright spot ingress misfitting is in cycle no. 1455. The ingress feature is not as clear as in other eclipses, and the nature of the flickering before the eclipse results in a falsely high bright spot flux, hindering bright spot ingress fitting. Overall, every eclipse in the fit has been affected by flickering to some degree.

Also plotted in Figure 5.2a is a fill-between region representing 1σ from the mean of a random sample (size 1000) of the MCMC chain. In all but one case, this fill-between region is not visible due to it being thinner than the blue line of the most probable eclipse model fit. The exception to this is cycle no. 1441, where it is just about visible after bright spot egress (phases 0.10–0.13). The very small distribution from a sample of the chain indicates a precise solution, and this is

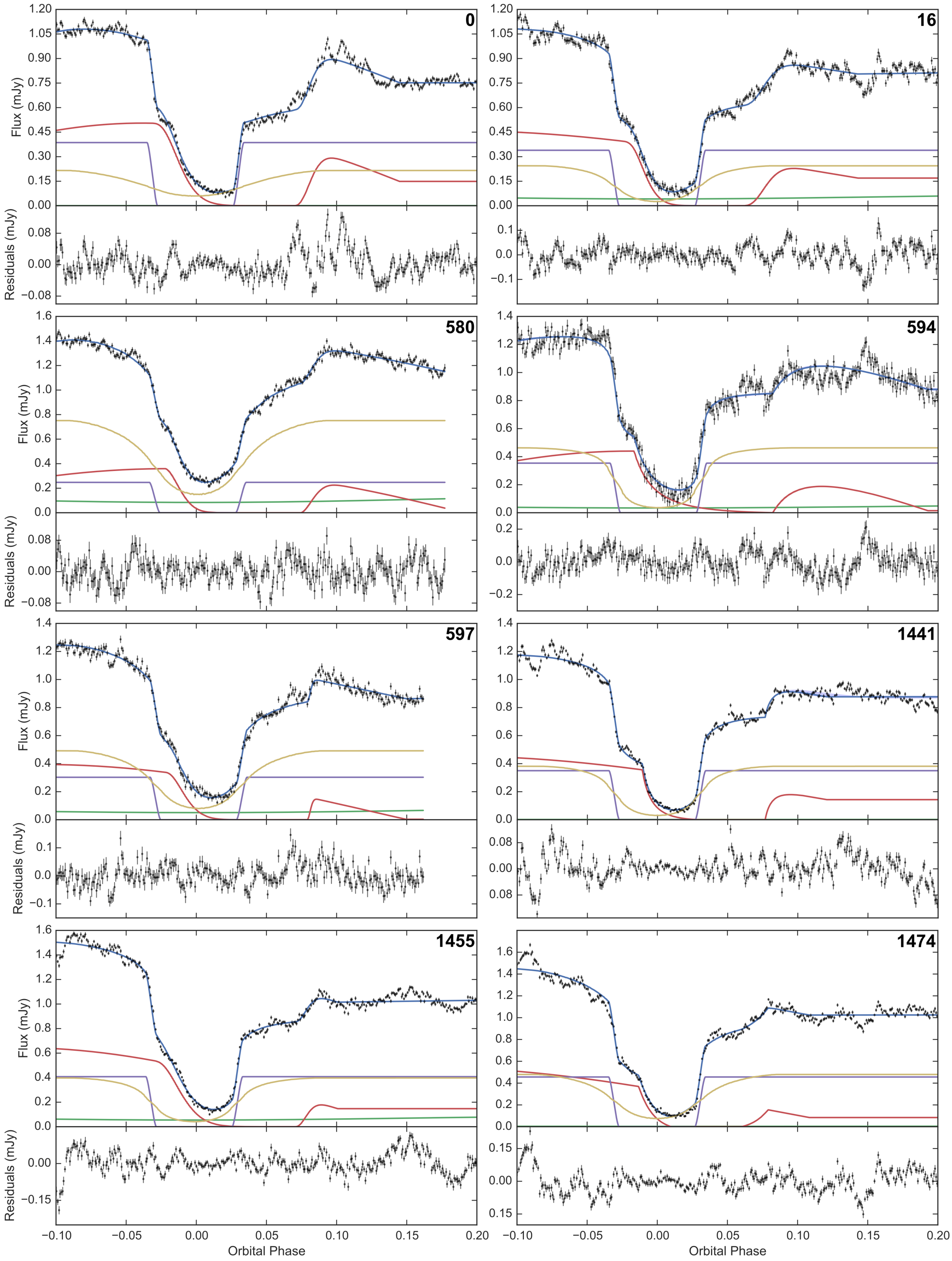

Figure 5.2a: Simultaneous eclipse model fit (blue) to eight ASASSN-14ag eclipse light curves (black) without inclusion of GP model. The blue fill-between region represents 1σ from the mean of a random sample (size 1000) of the MCMC chain, although this is thinner than the eclipse model fit line in all but one case (cycle no. 1441). Also shown are the different components to the eclipse model: white dwarf (purple), bright spot (red), accretion disc (yellow) and donor (green). The residuals are shown at the bottom of each plot. Cycle numbers are displayed at the top-right corner of each plot.

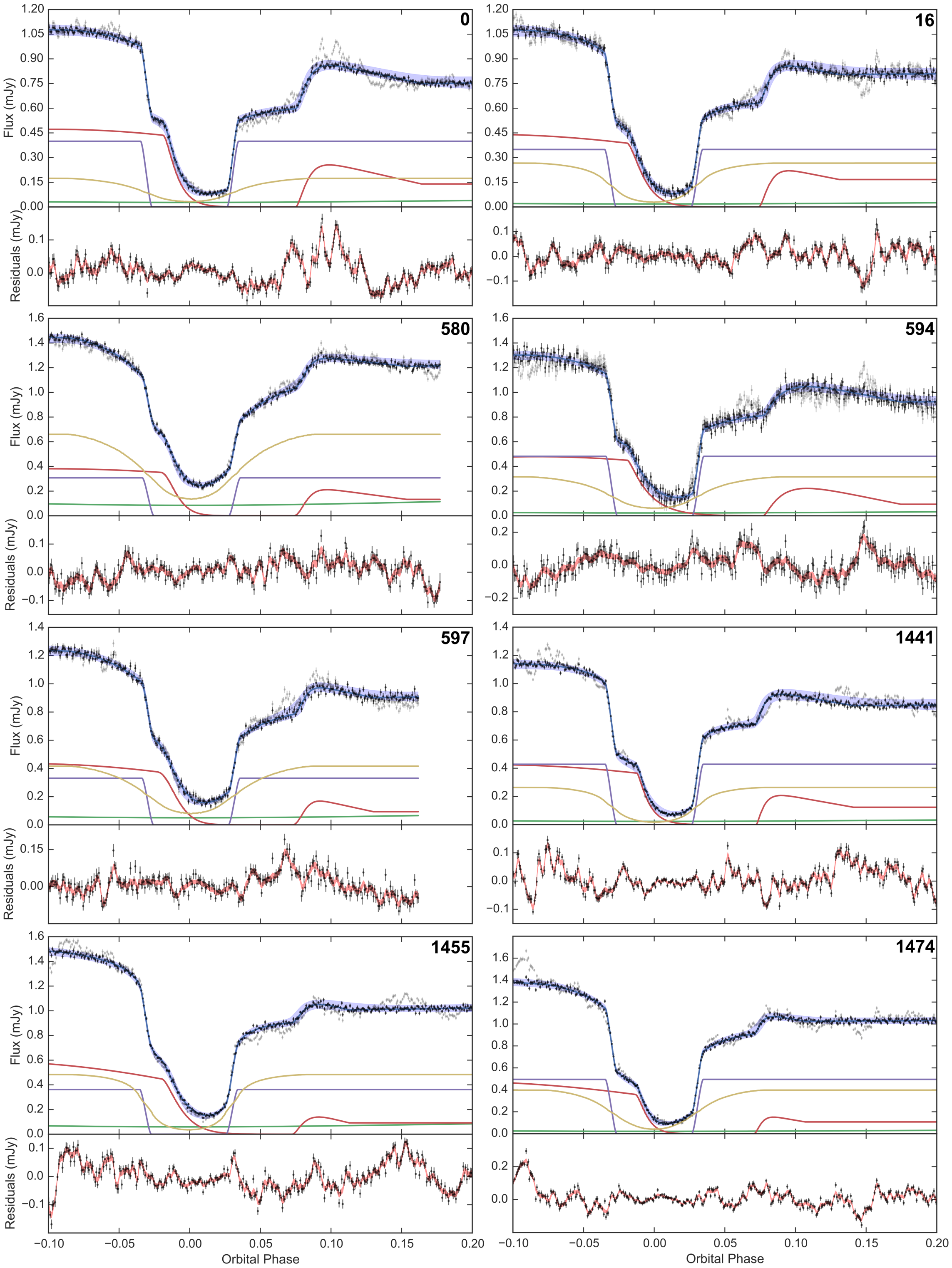

Figure 5.2b: Simultaneous eclipse model fit (blue) to eight ASASSN-14ag eclipse light curves (grey) with GP model included. The blue fill-between region represents 1σ from the mean of a random sample (size 1000) of the MCMC chain. The black points are the result of subtracting the posterior mean of the GP from the eclipse light curves. Also shown are the different components to the eclipse model: white dwarf (purple), bright spot (red), accretion disc (yellow) and donor (green). The residuals are shown at the bottom of each plot, with the red fill-between region covering 1σ from the posterior mean of the GP. Cycle numbers are displayed at the top-right corner of each plot.

reflected in the very small errors associated with the model parameters returned by the fit (Table C.6).

The post-eclipse light curve fitting procedure described in Section 3.7 was followed to produce posterior PDFs for all system parameters, shown in red within Figure 5.3. The value of each system parameter is taken as the most likely value of its PDF, with upper and lower errors derived from the 67% confidence level. System parameters and errors from the simultaneous fit without inclusion of the GP model are shown in the middle column of Table 5.1. The red probability distributions in Figure 5.3 are very narrow, which translate to small errors on the system parameters.

Also included in Table 5.1 are estimates for the temperature (T_1) and distance (d) of the white dwarf from white dwarf atmosphere fitting (Section 3.7.1), a key component of the post-eclipse light curve fitting procedure. White dwarf fluxes in u', g', r', i' and *KG5* bands were included in the white dwarf atmosphere fit, with all but the u'-band flux obtained from the MCMC chain of the simultaneous eclipse model fit. The value for the u'-band flux white dwarf flux came from a separate, individual fit to the 7th Dec 2016 u'-band eclipse, with q, R_1/x_{L1} and $\Delta\phi$ model parameters kept close to their values from the simultaneous eclipse model fit by the use of appropriate Gaussian priors. The resultant model atmosphere fit to white dwarf fluxes is shown in the left panel of Figure 5.4.

With GP Model

The second simultaneous fit to the eight eclipse light curves, this time with inclusion of the GP model, is shown in Figure 5.2b. The model parameters are located in Table C.7. The most probable fit has a much higher χ^2 of 22526 (with 2595 degrees of freedom), reflected in the greater amplitude residuals in Figure 5.2b. This is due to the additional GP component included in the fit, which models the residuals from the eclipse model fit but is not taken into account when calculating χ^2. The GP can be visualised as the red fill-between regions – representing 1σ from the GP's posterior mean – that overlay the residuals below each eclipse in Figure 5.2b. The majority of residuals are covered by this fill-between region, which indicates that the chosen Matérn-3/2 kernel provides a good description of CV flickering.

Contrary to Figure 5.2a, the black points in Figure 5.2b do not represent the real eclipse light curves, but rather how they appear after the subtraction of the posterior mean of the GP. The black points therefore resemble eclipse light curves with the model of the flickering component removed. The real eclipse light curves are shown by grey points for comparison.

An obvious consequence of including the GP model is the significant increase in size of the blue fill-between region in each eclipse. The increase reflects the much broader eclipse model parameter solution distributions, which is a consequence of fitting the eclipse model in accordance with GPs. A wider range of parameters are allowed by the data, as differences between the eclipse model and the data can be accommodated by the GP. In contrast to the non-GP fit, it is this fill-between region, not the most probable fit, that is of most importance. In most cases, this region is in agreement with both the white dwarf and bright spot eclipse features. Cycle no. 0 is a good example to show what GPs have brought to the eclipse model fitting. With just the eclipse model, the large flicker after bright spot egress created a very extended bright spot that was not able to successfully fit bright spot ingress (Figure 5.2a). When GPs are included, the flicker can be modelled, allowing a much more compact bright spot and a correctly fit ingress.

As discussed in Section 3.4.5, the GP model framework includes changepoints at the start and end of white dwarf eclipse, due to the expectation that the amplitude of flickering should differ inside and outside white dwarf eclipse. The GP amplitude inside white dwarf eclipse returned by the fit is an order of magnitude lower compared to that outside, thus validating the use of changepoints.

The posterior PDFs for each system parameter are shown in blue in Figure 5.3. The most likely parameter values and associated errors – as well as temperature

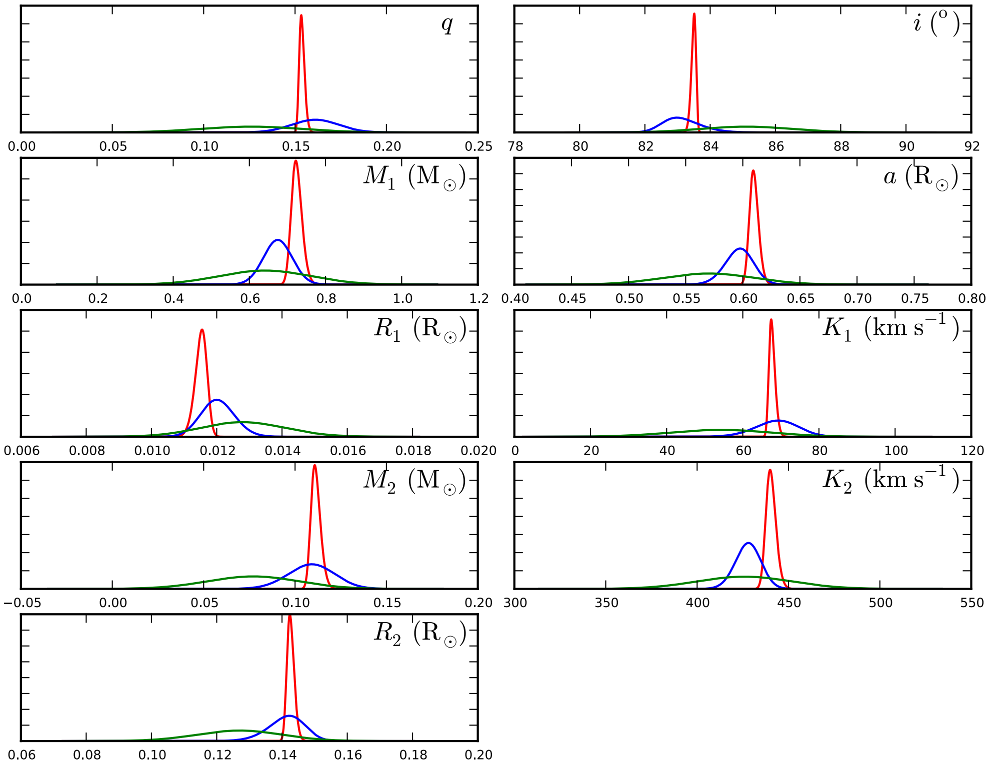

Figure 5.3: Normalised posterior probability density functions for both simultaneous eight-eclipse fits: without (red) and with (blue) GP model. Also included (green) are the parameter distributions calculated from the average eclipse fits (see Section 5.3.3).

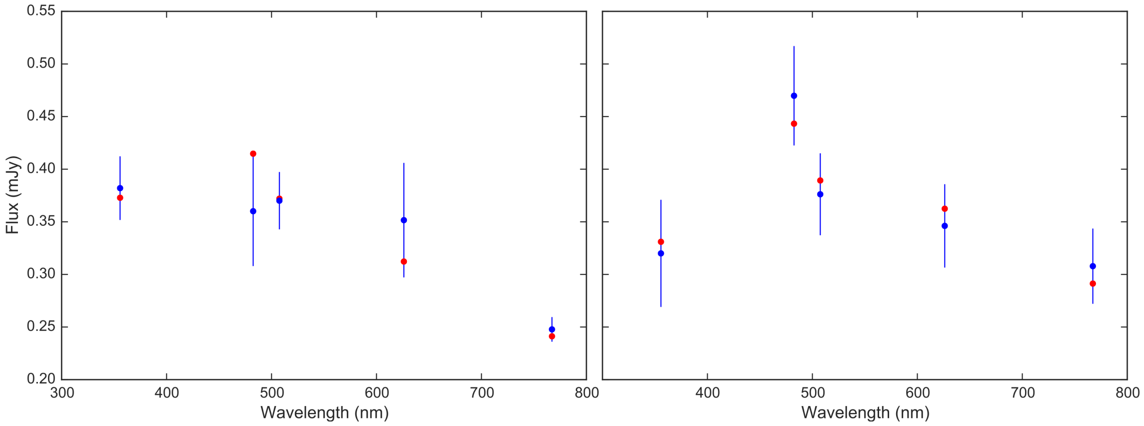

Figure 5.4: White dwarf fluxes from both simultaneous eight-eclipse and individual u'-band model fits (blue) and white dwarf atmosphere predictions (red; see Section 3.7.1), at wavelengths corresponding to (from left to right) u', g', *KG5*, r' and i' filters. *Left*: Without GP model. *Right*: With GP model.

Parameter	Without GPs	With GPs
q	$0.1534\,^{+0.0019}_{-0.0010}$	0.161 ± 0.013
M_1 ($\mathrm{M}_\odot$)	$0.722\,^{+0.017}_{-0.011}$	0.67 ± 0.04
R_1 ($\mathrm{R}_\odot$)	$0.01155\,^{+0.00014}_{-0.00022}$	0.0120 ± 0.0005
M_2 ($\mathrm{M}_\odot$)	$0.111\,^{+0.003}_{-0.002}$	0.109 ± 0.013
R_2 ($\mathrm{R}_\odot$)	$0.1424\,^{+0.0014}_{-0.0008}$	$0.142\,^{+0.004}_{-0.007}$
a ($\mathrm{R}_\odot$)	$0.609\,^{+0.005}_{-0.003}$	0.598 ± 0.012
K_1 ($\mathrm{km\,s^{-1}}$)	$67.5\,^{+1.1}_{-0.5}$	69 ± 6
K_2 ($\mathrm{km\,s^{-1}}$)	$440\,^{+3}_{-2}$	428 ± 7
i (°)	$83.51\,^{+0.05}_{-0.10}$	$83.0\,^{+0.7}_{-0.4}$
$\log g$	$8.172\,^{+0.014}_{-0.18}$	8.11 ± 0.05
T_1 (K)	17800 ± 1600	14000 ± 2000
d (pc)	$172\,^{+15}_{-12}$	$139\,^{+20}_{-16}$

Table 5.1: System parameters for ASASSN-14ag through simultaneous fitting of eight individual eclipse light curves, with and without the inclusion of GP model.

and distance estimates – are shown in the right-hand column of Table 5.1. It is very evident from Figure 5.3 that, while the probability distributions from both simultaneous fits have similar peak values, they have very contrasting values of σ. This was already apparent from the differing sizes of the blue fill-between regions in Figures 5.2a and 5.2b, and results in the errors on the system parameters from the GP model fit being significantly greater than those from the non-GP fit.

The white dwarf atmosphere model fit to white dwarf fluxes obtained with the inclusion of GPs is shown in the right-hand plot of Figure 5.4. The variation in flux across the wavelength bands is much closer to what is predicted by the atmosphere model compared to the non-GP case (left-hand side of same figure), and hence a better fit is achieved.

5.3.2 Accretion Disc

Figure 5.5 shows $R_{\mathrm{disc}}/x_{\mathrm{L1}}$ against MJD for the eight eclipses fit simultaneously, both without (top) and with the GP model (bottom). These eclipses were observed

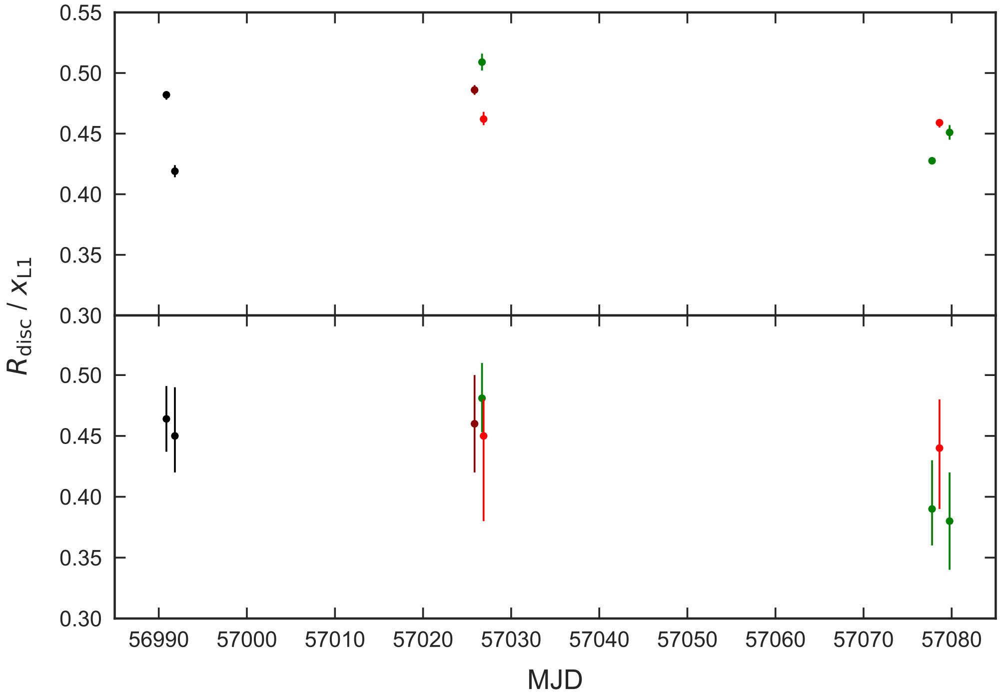

Figure 5.5: Accretion disc radius (R_{disc}) as a fraction of the distance to the inner Lagrangian point (x_{L1}) vs time (in MJD) for the eight eclipses fit simultaneously. The top panel shows radii from the non-GP fit, while the bottom panel shows radii from the GP fit. The colour of each data point shows the wavelength band its eclipse was observed in: *KG5* (black), g' (green), r' (red), i' (dark red).

during the same observing season, but over three separate observing runs, explaining the two large gaps in Figure 5.5. The errors on the disc radii from the GP fit are much larger than those from the non-GP fit, which is expected as the errors from the non-GP fit are significantly underestimated due to not taking the effects of flickering into account. Focussing on the GP fit, $R_{\mathrm{disc}}/x_{\mathrm{L1}}$ appears to be fixed at ~ 0.45 for the first two observing runs, with possibly a slight reduction to ~ 0.40 during the final run.

5.3.3 Average Eclipse Light Curve Modelling

Previous eclipse modelling studies – including the previous Chapter – have used the technique of averaging eclipses together as a way of negating flickering and/or boosting signal-to-noise (Littlefair et al., 2008; Savoury et al., 2011). To investigate how this technique compares to the new GP approach, the individual ASASSN-14ag

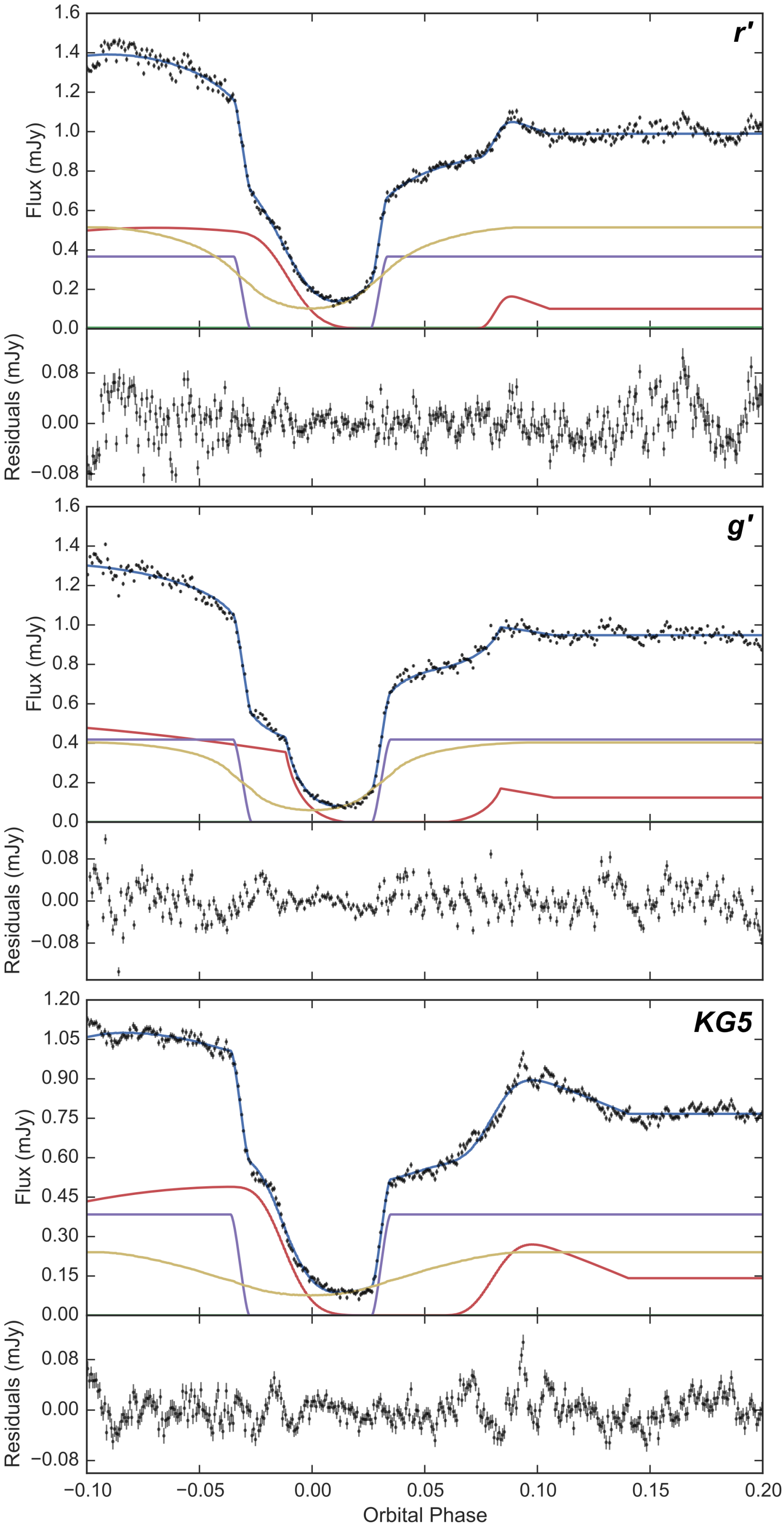

Figure 5.6: Eclipse model fits (blue) to average r', g' and *KG5* eclipses (black), without the inclusion of GPs. Also shown are the different components to the model: white dwarf (purple), bright spot (red), accretion disc (yellow) and donor (green). The residuals are shown at the bottom of each plot.

eclipses were used to create average eclipses, which were then fit separately with the eclipse model (without GPs). In addition, the eight individual eclipses used in the simultaneous fits were also fit separately[3] (again, without GPs), with their spread in system parameters providing an indication to the effects of flickering.

The two *KG5* band eclipses (cycle nos. 0 and 16) were averaged to create a *KG5* average eclipse, a process then repeated for both the g' (cycle nos. 594, 1441 and 1474) and r' (cycle nos. 597 and 1455) bands (Figure 5.6). Due to high-amplitude flickering and the small number of available eclipses, averaging is relatively ineffective in this case, with all three average eclipses containing large amounts of residual flickering. Despite this, they do all show bright spot features. The three average eclipses were individually fit with the eclipse model (without GPs) and the resulting fits are shown in Figure 5.6. The model parameters from these fits are located in Table C.9, while the system parameters for each band can be found in the first three columns of Table 5.2. The final column in Table 5.2 shows the weighted mean of the parameters from each wavelength band, with errors equal to the weighted standard deviation of the parameters resulting from fitting the eight individual eclipses separately. The system parameter distributions from the average eclipse fitting are also shown in Figure 5.3 (green PDFs). A similar – though not identical – method for estimating the error due to flickering was used in Chapter 4.

5.4 Discussion

As stated in section 5.3.3, averaging eclipses in this particular case is not an effective way of reducing flickering, as a large amount of it still remains. Obtaining many more eclipses would improve the situation, but negating the flickering would not be possible due to its high-amplitude nature. This issue – coupled with the fact that many systems show disc radius changes – shows the need for an alternative

---

[3] The model parameters for these eight individual eclipse model fits are located in Table C.8.

Parameter	g'	r'	*KG5*	Combined
q	$0.113^{+0.005}_{-0.001}$	$0.1231^{+0.0026}_{-0.0013}$	$0.1301^{+0.0022}_{-0.0007}$	0.126 ± 0.028
M_1 ($\mathrm{M}_\odot$)	0.602 ± 0.019	0.70 ± 0.04	$0.608^{+0.009}_{-0.017}$	0.64 ± 0.12
R_1 ($\mathrm{R}_\odot$)	0.01306 ± 0.00028	0.0117 ± 0.0004	$0.01296^{+0.00028}_{-0.00010}$	0.0128 ± 0.0013
M_2 ($\mathrm{M}_\odot$)	$0.068^{+0.005}_{-0.001}$	0.086 ± 0.005	$0.0794^{+0.0015}_{-0.0023}$	0.077 ± 0.025
R_2 ($\mathrm{R}_\odot$)	$0.1213^{+0.0028}_{-0.0011}$	0.1313 ± 0.0025	$0.1276^{+0.0008}_{-0.0013}$	0.127 ± 0.013
a ($\mathrm{R}_\odot$)	0.567 ± 0.006	0.597 ± 0.010	$0.571^{+0.003}_{-0.005}$	0.57 ± 0.04
K_1 ($\mathrm{km\,s^{-1}}$)	$47.8^{+2.5}_{-0.2}$	$54.8^{+1.6}_{-1.2}$	55.1 ± 0.7	54 ± 13
K_2 ($\mathrm{km\,s^{-1}}$)	426 ± 4	443 ± 7	422^{+2}_{-4}	426 ± 26
i ($^\circ$)	$86.0^{+0.1}_{-4.0}$	$84.95^{+0.09}_{-0.19}$	$85.17^{+0.06}_{-0.13}$	85.1 ± 1.4
$\log g$	7.986 ± 0.023	8.14 ± 0.04	$7.997^{+0.020}_{-0.014}$	8.01 ± 0.19

Table 5.2: System parameters for ASASSN-14ag from average eclipse light curve fitting. The parameters in the combined column are calculated from the weighted mean of the values in each of the three bands. The errors on these combined parameters come from the weighted standard deviation of the parameters from the eight individual eclipse fits.

approach to modelling CV eclipse light curves with flickering. The new approach introduced here involves modelling the flickering, while also fitting individual eclipses simultaneously.

5.4.1 Modelling of Flickering

In the previous Chapter, the effects of flickering were estimated from the spread in system parameters after fitting a further four average eclipses, each containing a different combination of three out of the four original eclipses used for the g'-band average. Here, the spread in system parameters from fitting the eight individual eclipses separately is used as an estimate the effects of flickering. The resulting system parameters are shown in Table 5.2. These individual eclipse fits show a wide spread in system parameters, which results in large errors.

Using the new approach of modelling flickering with GPs, the error associated with flickering no longer has to be estimated, as it is already included in the errors on the system parameters returned by the model. In the case of ASASSN-14ag, the contribution from flickering is seen through comparison of the errors in the last two columns of Table 5.1 and the difference in the red and blue distributions in Figure 5.3.

The size of the error associated with flickering differs depending on whether the existing or new approach is used (blue and green distributions in Figure 5.3), but which comes closest to representing the true effect? Does the existing approach of using the distribution in system parameters from individual fits overestimate the error due to flickering, or does the new approach of modelling flickering underestimate it?

Figure 5.2b shows that the GPs have done a good job of modelling the flickering, and therefore the errors on the model parameters – which are marginalised over the GP hyperparameters – are likely to be accurate. This suggests that the old approach of using the standard deviation of system parameters from additional eclipse light curve fits may overestimate the error due to flickering.

5.4.2 Component Masses

The calculated mass of the white dwarf in ASASSN-14ag from both simultaneous fits – with and without GPs – are consistent, although it is believed the errors from the GP fit are much more representative of the real uncertainty in the measurement so those system parameters are the ones adopted for the remainder of the discussion. The white dwarf mass in ASASSN-14ag is $0.67 \pm 0.04\,\mathrm{M}_\odot$, which is at the lower end for white dwarfs in CVs. ASASSN-14ag joins fellow eclipsing CVs HT Cas (Horne, Wood & Stiening, 1991) and SDSS J115207.00+404947.8 (Savoury et al., 2011) in having a white dwarf below $0.7\,\mathrm{M}_\odot$ and approaching the mean white dwarf field mass of $0.621\,\mathrm{M}_\odot$ (Tremblay et al., 2016). The corresponding donor mass of $0.109 \pm 0.013\,\mathrm{M}_\odot$ is broadly consistent with the main sequence donor evolutionary track from Knigge, Baraffe & Patterson (2011) (see Section 1.5.4), although a donor mass closer to $\sim 0.08\,\mathrm{M}_\odot$ is expected for a system with ASASSN-14ag's orbital period.

The mass ratio and donor mass of ASASSN-14ag put it within the dynamically stable region in Figure 2 of Schreiber, Zorotovic & Wijnen (2016), and is therefore in agreement with their empirical consequential angular momentum loss model that appears to solve the long-standing CV white dwarf mass problem (see Section 1.6.2).

The white dwarf temperature and mass were used to calculate a medium-term average mass transfer rate (equation 1.23) of $\dot{M} = 1.5\,^{+1.8}_{-0.9} \times 10^{-10}\,\mathrm{M_{\odot}\,yr^{-1}}$, while ASASSN-14ag's orbital period of 1.44 h was used to determine a secular mass transfer rate of $\dot{M} \sim 0.6 \times 10^{-10}\,\mathrm{M_{\odot}\,yr^{-1}}$ (Knigge, Baraffe & Patterson, 2011). Although these two values for the mass transfer rate are consistent, the slightly higher medium-term mass transfer rate indicates that the white dwarf temperature of 14000 ± 2000 K is marginally hotter than expected.

5.5 PHL 1445 – Revisited

With a new approach to eclipse modelling now developed, it was of interest to apply it to the eclipse light curves of PHL 1445; the system under study in the previous Chapter.

5.5.1 Simultaneous Eclipse Light Curve Modelling

The 10 g'-band eclipse light curves fit individually in Section 4.3.3 were the obvious choice for simultaneous eclipse light curve fitting. However, after taking another look, it became apparent that the bright spot ingress in the cycle no. 14945 eclipse was very tenuous, and may be solely a product of flickering (Figure 4.6). Furthermore, the eclipse of cycle no. 12024, with a slight but visible bright spot ingress, seemed to have been overlooked in the original fit. The solution was to replace cycle no. 14945 with cycle no. 12024, keeping the total number of eclipses at 10.

These 10 g'-band PHL 1445 eclipse light curves were simultaneously fit with both the eclipse (simple bright spot; Section 3.2) and GP flickering models (Section 3.4.5), as outlined in Section 3.6.2. Note that due to the lack of bright spot egress features in the eclipse light curves, an accurate by-eye fit of the eclipse model to obtain the starting model parameters was not possible, and so a starting position reflecting the outcome of the initial (average) PHL 1445 fit (Section 4.3.1) was used instead. The results of this new fit are shown in Figure 5.7, and the model parameters are located in Table C.5. The most probable fit has a very large χ^2 of 68795 (with 2267 degrees of freedom), a consequence of the presence of severe flickering in the majority of eclipse light curves.

PHL 1445 eclipses are a much harder test for the new modelling approach, as the amplitude of flickering is very similar to that of the bright spot eclipse in every eclipse light curve. Despite this, all 10 bright spot ingresses have been fit reasonable well, and in the majority of eclipses the model's bright spot egress appears to coincide with a reasonably convincing light curve feature. Also, as with the simultaneous ASASSN-14ag fits in Section 5.3.1, the GP appears to have successfully modelled the flickering (see eclipse model residuals below each eclipse in Figure 5.7).

The post-eclipse light curve fitting procedure (Section 3.7) was followed to produce posterior PDFs, shown in blue within Figure 5.8, and system parameter values (right-hand column in Table 5.3). Also plotted in Figure 5.8 (green) and included in Table 5.3 (middle column), for the purpose of comparison, are the PDFs and system parameter values resulting from the average PHL 1445 eclipse fits (with additional systematic errors that account for flickering, as documented in Sections 4.3.1 and 4.3.2).

It is clear from Figure 5.8 that, at least in the case of PHL 1445, both the existing and new modelling approaches produce similar results[4]. For all system parameters, the probability distributions peak at comparable values, and share approximately the same values of σ. This is in contrast to ASASSN-14ag, where values of σ

---

[4] To rule out the possibility of this being a consequence of starting the new fit from a position close to the previous solution, multiple fits were carried out from a range of starting positions. All solutions were found to be consistent.

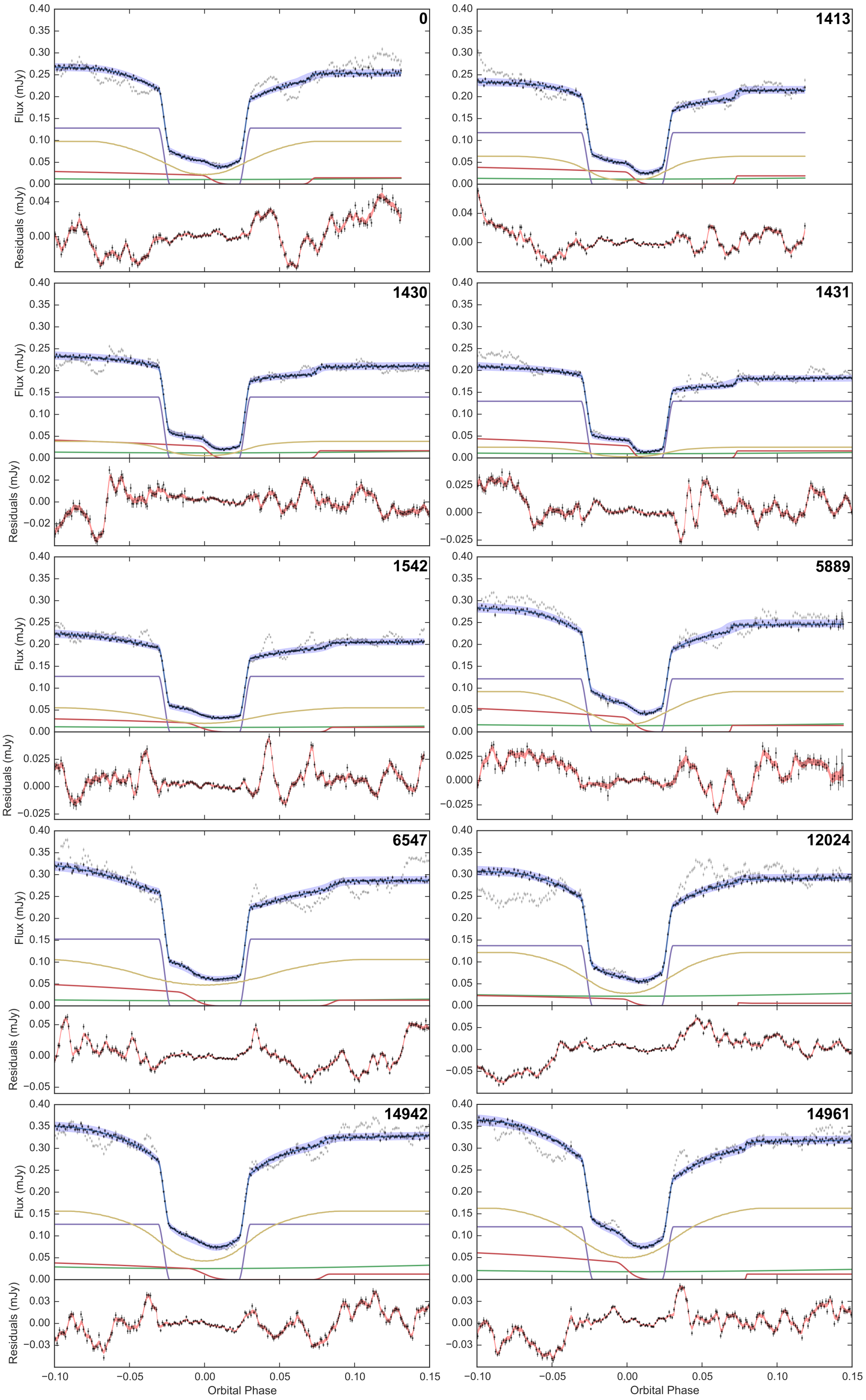

Figure 5.7: Simultaneous eclipse model fit (blue) to 10 PHL 1445 eclipse light curves (grey) with GP model included. The blue fill-between region represents 1σ from the mean of a random sample (size 1000) of the MCMC chain. The black points are the result of subtracting the posterior mean of the GP from the eclipse light curves. Also shown are the different components to the eclipse model: white dwarf (purple), bright spot (red), accretion disc (yellow) and donor (green). The residuals are shown at the bottom of each plot, with the red fill-between region covering 1σ from the posterior mean of the GP. Cycle numbers are displayed at the top-right corner of each plot.

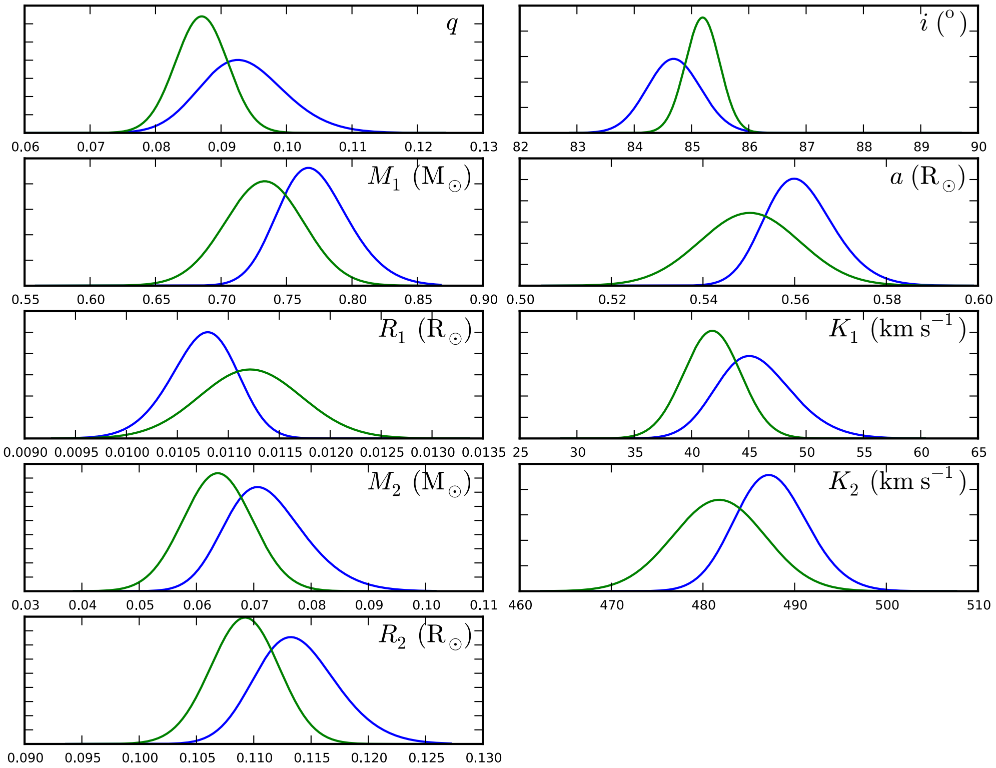

Figure 5.8: Normalised posterior probability density functions for PHL 1445. The blue PDFs are from the simultaneous 10-eclipse model fits (with GPs) and the green PDFs represent the individual average eclipse model fits with added systematic error due to flickering (from previous Chapter).

Parameter	Average eclipse fits + systematic errors	Simultaneous, individual eclipse fit + GPs
q	0.087 ± 0.004	0.093 ± 0.007
M_1 (M$_\odot$)	0.73 ± 0.03	0.77 ± 0.03
R_1 (R$_\odot$)	0.0112 ± 0.0005	0.0108 ± 0.0003
M_2 (M$_\odot$)	0.064 ± 0.006	$0.071^{+0.009}_{-0.005}$
R_2 (R$_\odot$)	0.109 ± 0.003	0.113 ± 0.004
a (R$_\odot$)	0.550 ± 0.011	$0.560^{+0.009}_{-0.006}$
K_1 (km s^{-1})	41.8 ± 2.5	45 ± 3
K_2 (km s^{-1})	482 ± 5	487 ± 4
i (°)	85.2 ± 0.3	84.7 ± 0.5
$\log g$	8.20 ± 0.04	8.26 ± 0.03

Table 5.3: System parameters for PHL 1445 from average eclipse model fits with additional systematic error to account for flickering (Sections 4.3.1 and 4.3.2) and simultaneous, individual eclipse model fit with GPs included (this Section).

notably differ due to an over-estimation of the error due to flickering obtained from the existing approach (as discussed in Section 5.4.1). This discrepancy between PHL 1445 and ASASSN-14ag is possibly a result of the difference in complexity and prominence of the bright spot within these two systems.

5.5.2 Accretion Disc

The simultaneous model fit produced 10 individual of $R_{\rm disc}/x_{\rm L1}$, giving another opportunity to look into the variation of PHL 1445's disc radius over time. This was first investigated in Section 4.3.4, using $R_{\rm disc}/x_{\rm L1}$ values returned by individual model fits to 10 PHL 1445 eclipses (Section 4.3.3). The new $R_{\rm disc}/x_{\rm L1}$ values from the simultaneous model fit to 10 g'-band eclipses were plotted against $T_{\rm mid}$ in a similar way to Figure 4.7, as shown in Figure 5.9.

Comparing Figures 4.7 and 5.9, the most obvious difference is the much larger errors from the simultaneous model fit, where flickering has been modelled with GPs. These errors are more than double the size of the 4% systematic error introduced to the radii from the individual model fits to account for flickering, although as discussed in Section 4.3.4, this systematic error is likely to be an underestimation. One of the concerns with the original analysis were apparent large changes in disc radius across very short timescales, which appeared unphysical. It was determined that these changes were not real, and instead a consequence of poor model fitting due to the presence of flickering. It is encouraging that these large changes disappear once flickering is modelled with GPs (clustered points around 55940 and 56670 MJD in Figure 5.9). All disc radii are broadly consistent with an average disc radius of $\sim 0.45\,R_{\rm disc}/x_{\rm L1}$, although there is evidence for changes in the size of the disc across the ~ 800 d observational baseline.

The variation of disc and bright spot fluxes with disc radius was also looked at in Sections 4.3.4 and 4.3.5. The new disc and bright spot fluxes from the simultaneous model fit to 10 g'-band eclipses were plotted against $R_{\rm disc}/x_{\rm L1}$ values in a similar

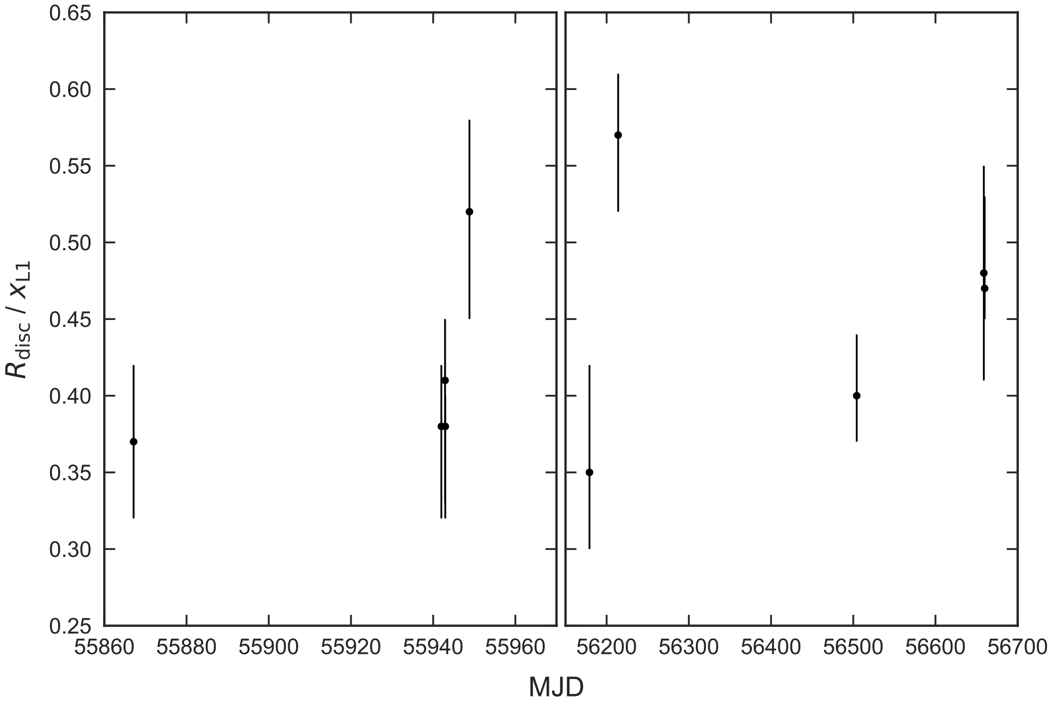

Figure 5.9: PHL 1445 accretion disc radius ($R_{\rm disc}$) as a fraction of the distance to the inner Lagrangian point ($x_{\rm L1}$) vs time (in MJD). The figure is split into two due to a large gap in time ($\sim 200\,$d) between observations. This is a revision of Figure 4.7, now with disc radii from the simultaneous model fit.

way to the middle plots within Figure 4.8, and shown in Figure 5.10. As with the disc radii discussed above, both disc and bright spot fluxes from the simultaneous model fit have much more realistic errors compared to the individual model fits from Section 4.3.3, and are comparable to, if slightly larger than the systematic error introduced to the values from the individual model fits in order to account for flickering. Looking at the top plot of Figure 5.10, there is possibly evidence for a positive correlation between disc flux and disc radii, while the bottom plot of the same Figure shows there to be no obvious correlation between bright spot flux and disc radius. These are the same findings from Sections 4.3.4 and 4.3.5.

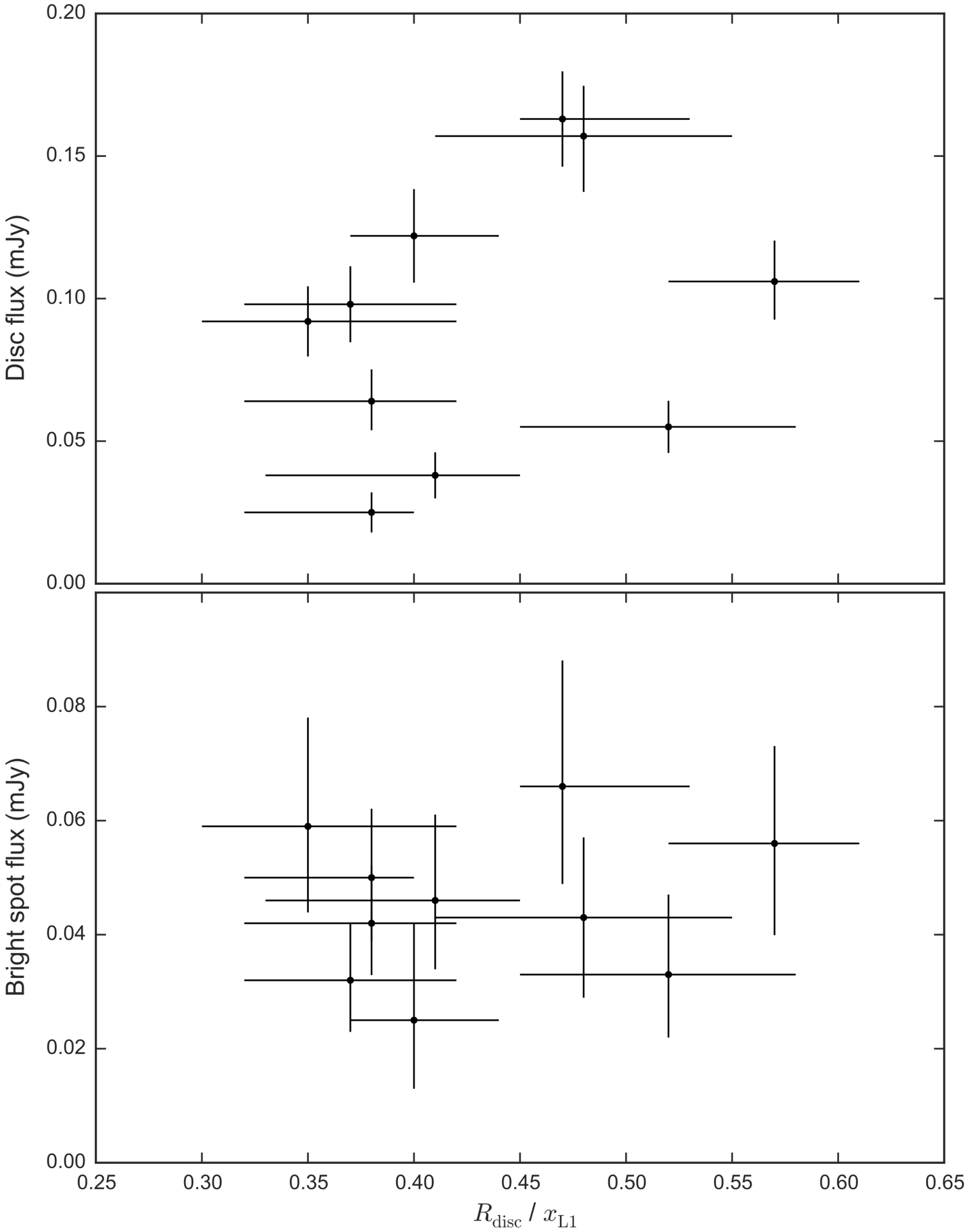

Figure 5.10: PHL 1445 accretion disc flux (top) and bright spot flux (bottom) vs accretion disc radius ($R_{\rm disc}$) as a fraction of the distance to the inner Lagrangian point ($x_{\rm L1}$). This is a revision of the middle plots within Figure 4.8, now with disc radii and fluxes the from simultaneous model fit.

Chapter 6

A Study of SDSS 1057

The contents of this Chapter have been published in the Monthly Notices of the Royal Astronomical Society, **467**, 1024–1032 as a paper entitled *SDSS J105754.25+275947.5: a period-bounce eclipsing cataclysmic variable with the lowest-mass donor yet measured*, by McAllister, Littlefair, Dhillon, Marsh, Gänsicke, Bochinski, Bours, Breedt, Hardy, Hermes, Kengkriangkrai, Kerry, Parsons, Rattanasoon (McAllister et al., 2017b). The following is my own work unless otherwise stated.

6.1 Introduction

As discussed in Section 1.4.5, period-bounce/post-period minimum CVs – systems with substellar donors evolving towards longer orbital periods – are expected to make up a significant fraction of the total CV population, however for a long time this population was missing observationally (Littlefair, Dhillon & Martín, 2003) due to being characteristically faint in quiescence and having long outburst recurrence times (Patterson, 2011). It is only during the past decade or so that the period-bounce population has finally started to be uncovered (Littlefair et al., 2008; Savoury et al., 2011), in large part thanks to the emergence of the Sloan Digital Sky Survey (SDSS; York et al. 2000). The SDSS sample contains a substantial population of period-bounce systems due to it being a reasonably deep survey ($g \sim 19$) and having candidate selection through spectral analysis, not outbursts.

One such object discovered by the SDSS is SDSS J105754.25+275947.5 (hereafter SDSS 1057). A faint system at $g' \simeq 19.5$, it was identified as a CV by Szkody et al. (2009). The SDSS spectrum for this system is dominated by the white dwarf, and also shows double-peaked Balmer emission lines, indicating a high-inclination binary. Southworth et al. (2015) confirmed SDSS 1057 to be an eclipsing CV after finding short and deep eclipses with low-time-resolution photometry. These light curves also appear flat outside of eclipse with no obvious orbital hump before eclipses, hinting at a faint bright spot feature and therefore low accretion rate. From their photometry, Southworth et al. (2015) measure SDSS 1057's orbital period to be 90.44 min. Due to a low accretion rate and no sign of a secondary star in its spectrum, Southworth et al. (2015) highlight SDSS 1057 as a good candidate for a period-bounce system.

In this Chapter, averaged ULTRACAM and ULTRASPEC eclipse light curves of SDSS 1057 are modelled using the new modelling approach to obtain precise system parameters, which are used to help clarify SDSS 1057's status as a period-bounce system.

6.2 Observations and Light Curve Morphology

SDSS 1057 was observed a total of 12 times from Apr 2012–Jun 2015, six in $u'g'r'$ filters with ULTRACAM on the WHT and another six in the *KG5* filter with ULTRASPEC on the TNT. A complete journal of observations can be found in Table A.1. A clear white dwarf eclipse is visible in all 12 eclipses, while only in a select few can a very faint bright spot eclipse also be detected. The difficulty in locating the bright spot eclipse feature in these eclipse light curves is due to the bright spot in SDSS 1057 being significantly less luminous than the white dwarf. This is made even harder due to the low signal-to-noise of each light curve – a consequence of

SDSS 1057 being a faint system ($g' \sim 19.5$).

In order to increase the signal-to-noise and strengthen the bright spot eclipse features, multiple eclipses have to be averaged. As discussed in Section 3.3.1, eclipse averaging can lead to inaccuracies if there are significant changes in disc radius. Such changes can shift the timing of the bright spot eclipse features over time and result in the broadening and weakening of these features after eclipse averaging. Not all systems exhibit significant disc radius changes, however, and visual analysis of the positions of the bright spot in individual eclipses show SDSS 1057 to have a constant disc radius – making eclipse averaging suitable in this case.

The eclipses selected to contribute to the average eclipse in each wavelength band are phase-folded using the ephemeris within Table 2.2 and plotted on top of each other in Figure 6.1. These include four out of the six ULTRACAM $u'g'r'$ eclipses and three out of the six ULTRASPEC *KG5* eclipses. The 30 Dec 2013 and 23 Jun 2015 ULTRACAM observations were not included due to being affected by transparency variations, while the first three ULTRASPEC observations were not used due to a low signal-to-noise caused by unsuitably short exposure times. As can be seen in Figure 6.1, there is no obvious flickering component in any SDSS 1057 eclipse light curve, but a large amount of white noise. Despite this, there are hints of a bright spot ingress feature around phase 0.01 and an egress at approximately phase 0.08. These features are clearest in the r' band.

The resulting average eclipses in each band are shown in Figure 6.2. All four eclipse light curves have seen an increase in signal-to-noise through averaging, and as a result the bright spot features have become clearer – sufficiently so for eclipse model fitting (see section 6.3.1). The sharp bright spot egress feature in the r' band eclipse is further evidence for no significant disc radius changes in SDSS 1057 and validates the use of eclipse averaging in this instance.

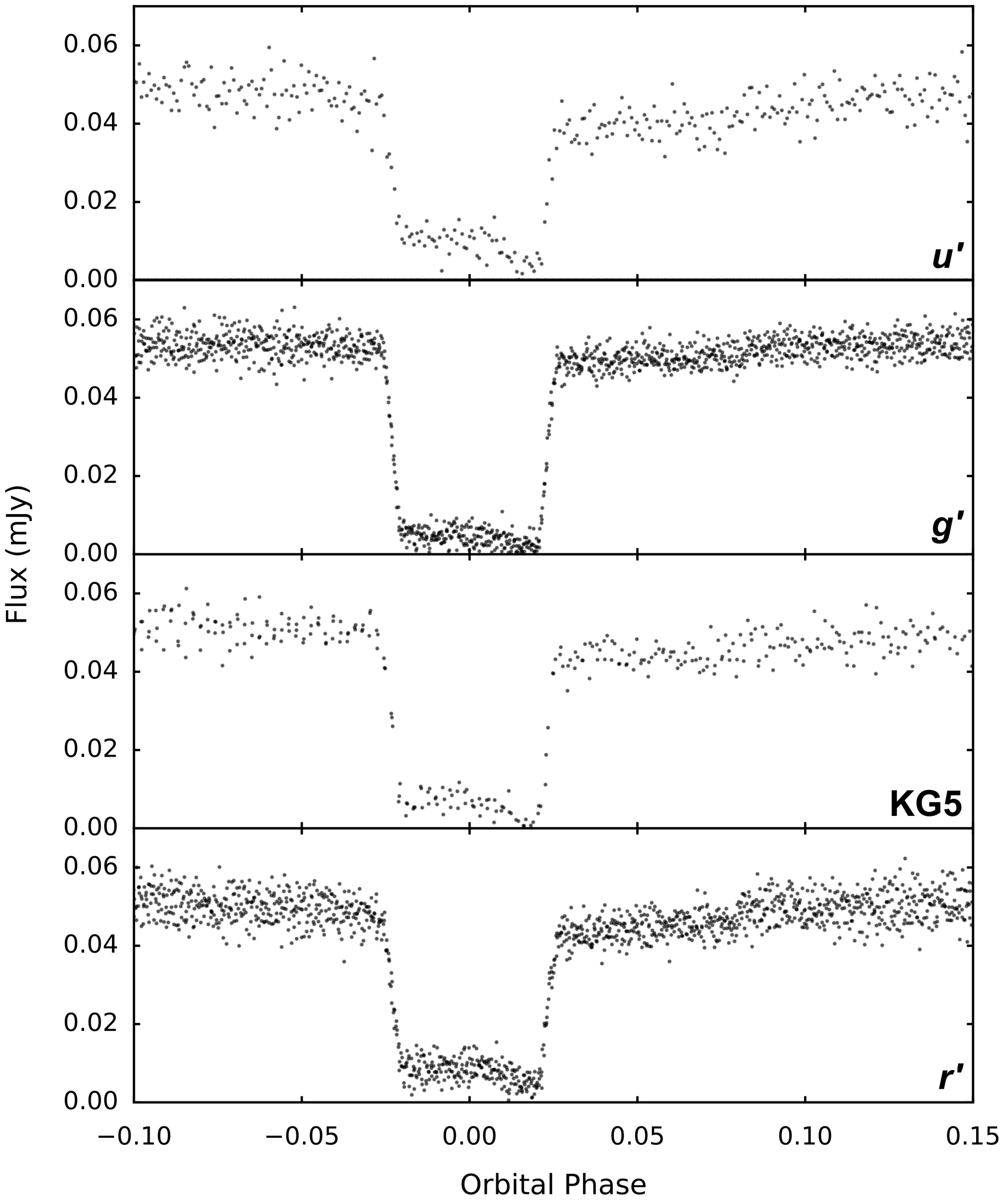

Figure 6.1: SDSS 1057 eclipse light curves (phase-folded using the ephemeris within Table 2.2 and overlaid) selected for the construction of average eclipse light curves in each of the four wavelength bands. The name of each band is shown in the bottom-right corner of each plot.

6.3 Results

6.3.1 Simultaneous Average Eclipse Light Curve Modelling

The four average eclipse light curves were then simultaneously fit with the CV eclipse model (simple bright spot; Section 3.2) alongside the GP flickering model (Section 3.4.5), as outlined in Section 3.6.2. The simple bright spot model was used in this instance due to the tenuous nature of the bright spot in SDSS 1057. The GP flickering model was included as, although the SDSS 1057 average light curves do not show any obvious signs of flickering, there is evidence for slight correlation in the residuals.

The simultaneous fit to the four average eclipse light curves is shown in Figure 6.2, while the corresponding model parameters are located in Table C.10. The blue line in Figure 6.2 represents the most probable fit, and has a χ^2 of 1561 with 966 degrees of freedom. The lines below each eclipse represent the separate components to the model: white dwarf (purple), bright spot (red), accretion disc (yellow) and donor (green). In addition to the most probable fit, a blue fill-between region can also be seen plotted on each eclipse. This represents 1σ from the mean of a random sample (size 1000) of the MCMC chain.

In all four eclipses, the model manages to fit both the white dwarf and bright spot eclipses successfully. There is no structure visible in the residuals at the phases corresponding to any of the ingresses and egresses. In general, there is some structure in the residuals, which validates the decision to include the GP model in the fit. This GP model can be visualised through the red fill-between regions overlaying each eclipse's residuals in Figure 6.2, and represents 1σ from the GP's posterior mean. The GPs appear to model the residuals successfully in the r' and g' bands, but struggle for u' and *KG5*. This may be due to differing amplitudes and timescales of the noise between eclipses, but recall that the GP model can currently only accommodate for a shared amplitude and timescale between all eclipses (Section 3.4.5).

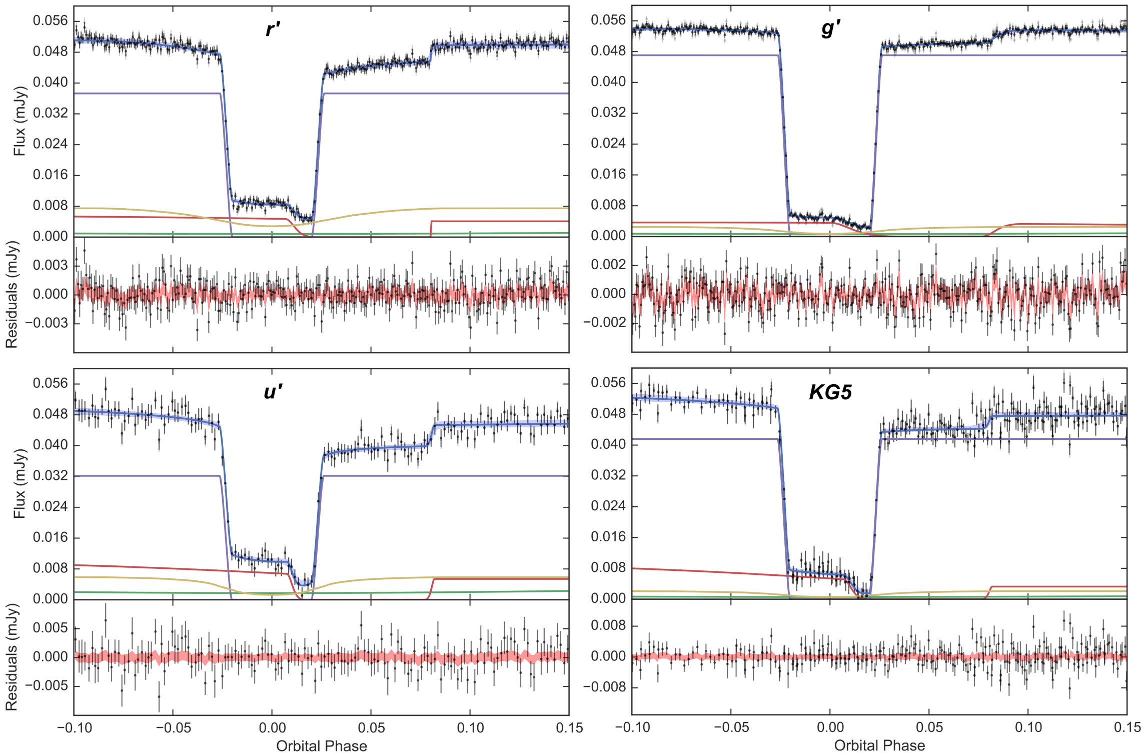

Figure 6.2: Simultaneous eclipse model fit (blue) to four average SDSS 1057 eclipse light curves (grey). The blue fill-between region represents 1σ from the mean of a random sample (size 1000) of the MCMC chain. The black points are the result of subtracting the posterior mean of the GP from the eclipse light curves. Also shown are the different components of the model: white dwarf (purple), bright spot (red), accretion disc (yellow) and donor (green). The residuals are shown at the bottom of each plot, with the red fill-between region covering 1σ from the posterior mean of the GP.

q	0.0546 ± 0.0020
M_1 ($\mathrm{M}_\odot$)	0.800 ± 0.015
R_1 ($\mathrm{R}_\odot$)	0.01040 ± 0.00017
M_2 ($\mathrm{M}_\odot$)	0.0436 ± 0.0020
R_2 ($\mathrm{R}_\odot$)	0.1086 ± 0.0017
a ($\mathrm{R}_\odot$)	0.629 ± 0.004
K_1 ($\mathrm{km\,s^{-1}}$)	$26.2\,^{+1.1}_{-0.8}$
K_2 ($\mathrm{km\,s^{-1}}$)	478 ± 3
i (°)	85.74 ± 0.21
$\log g$	8.307 ± 0.017
T_1 (K)	13300 ± 1100
d (pc)	367 ± 26

Table 6.1: System parameters for SDSS 1057.

The post-eclipse light curve fitting procedure described in Section 3.7 was followed to produce posterior PDFs for all system parameters, shown in Figure 6.3. Part of this procedure involved obtaining a temperature of the white dwarf through fitting white dwarf atmosphere predictions to multi-wavelength white dwarf fluxes from the eclipse model fit (see Section 3.7 for more details).

Figure 6.4 displays the outcome of the white dwarf flux fit, with the measured white dwarf fluxes in each band in blue and the white dwarf atmosphere model predictions in red. The model and fluxes are in good agreement in all wavelength bands, however it appears that the measured u' band flux is slightly underestimated. On close inspection of the u' band eclipse fit in Figure 6.2, there is seemingly a greater than expected contribution from both the disc and donor at this wavelength, opening up the possibility that a small fraction of the true white dwarf flux may have been mistakenly attributed to these components.

The white dwarf temperature (and distance) from the white dwarf flux fit can be found in Table 6.1, along with system parameter values obtained from the peak values of the posterior PDFs (with errors from the 67% confidence level).

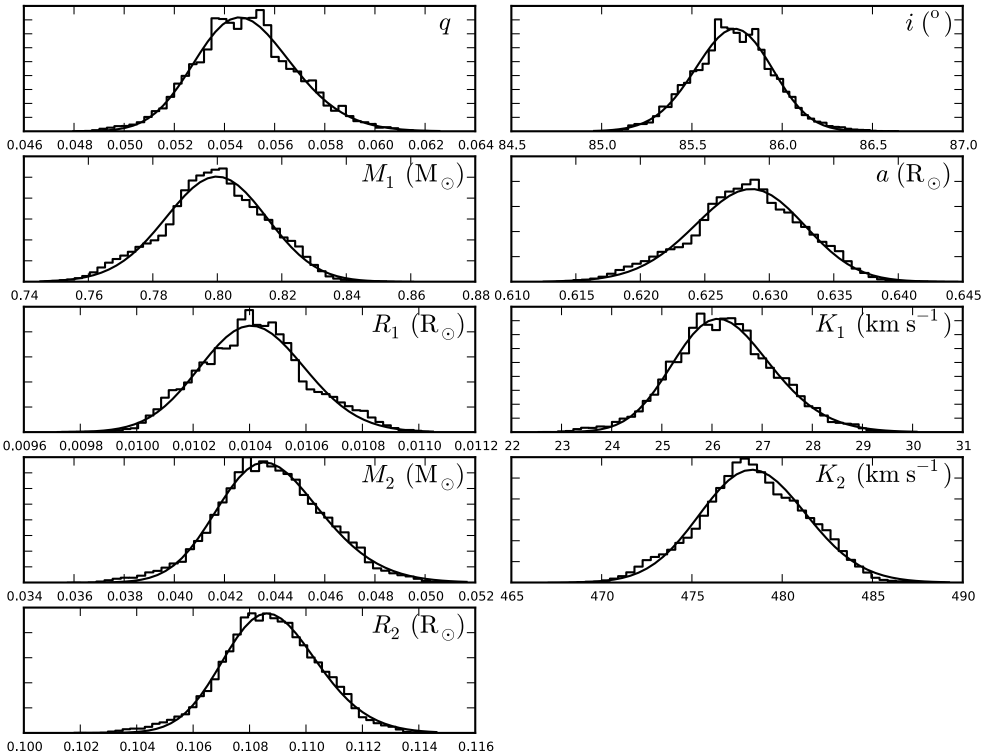

Figure 6.3: Normalised posterior probability density function for each system parameter.

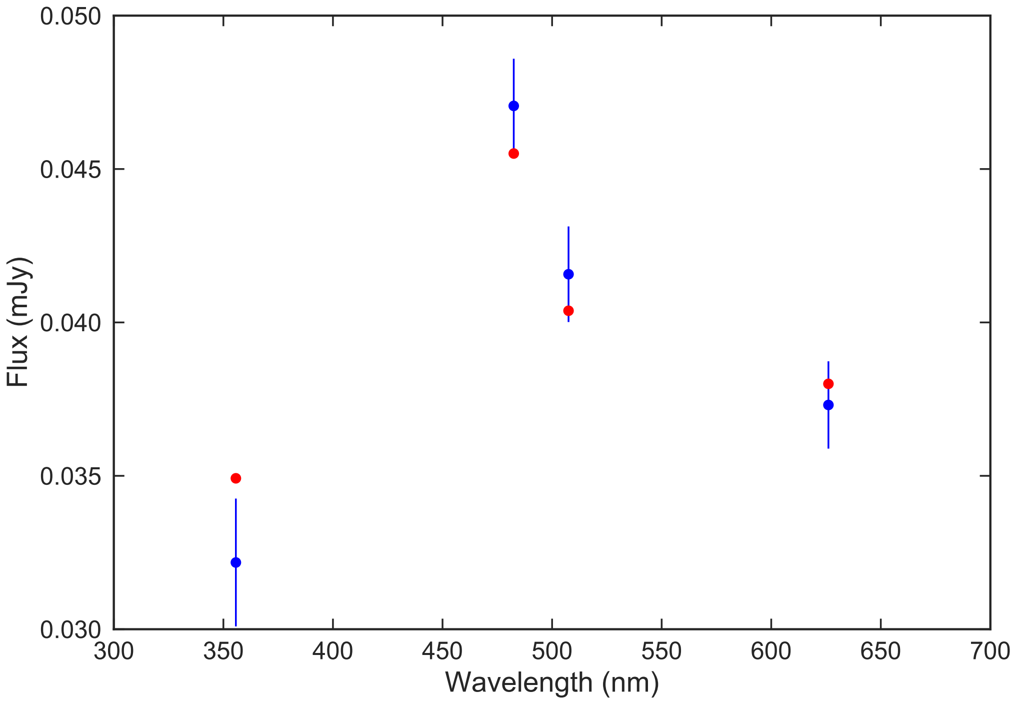

Figure 6.4: White dwarf fluxes from the simultaneous four-eclipse model fit (blue) and white dwarf atmosphere predictions (red; see Section 3.7.1), at wavelengths corresponding to (from left to right) u', g', *KG5* and r' filters.

6.3.2 Spectral Energy Distribution

Southworth et al. (2015) used both the SDSS spectrum and GALEX fluxes (Morrissey et al., 2007) to analyse the spectral energy distribution of SDSS 1507. The model of Gänsicke et al. (2006b) was able to successfully reproduce the SDSS spectrum with a white dwarf temperature of 10500 K, $\log g$ of 8.0, distance of 305 pc, accretion disc temperature of 5800 K and an L5 secondary star. However, the model does not provide a good fit to the GALEX fluxes, which Southworth et al. (2015) state could have been taken during eclipse.

As slightly different values for white dwarf temperature, $\log g$ and distance (Table 6.1) are obtained from eclipse modelling in this study, in addition to a slightly later spectral type secondary, it was investigated whether the Gänsicke et al. (2006b) model with these revised parameters is still a good fit to the SDSS spectrum (Gänsicke, priv. comm.). The resulting fit is shown in Figure 6.5. While the fit is good, the white dwarf temperature used appears to produce a slope that is slightly too blue, hinting that it might be marginally overestimated, but this may be corrected with alternate disc parameters.

As in Southworth et al. (2015), the GALEX UV fluxes (red data points) are again not fit well by the model, with both the near- and far-UV fluxes much lower than predicted by the model spectra. Using the ephemeris in Table A.1, it was possible to rule out the potential scenario of the GALEX UV fluxes having being taken during eclipse. Another reason for these low UV flux measurements could be due to absorption by an ‘accretion veil’ of hot gas positioned above the accretion disc (Horne et al., 1994; Copperwheat et al., 2012). This explanation consequently invalidates the prior assumption of an unobscured white dwarf (see Section 3.2). However, reassurance can be taken from the agreement between photometric and spectroscopic parameter estimates for two eclipsing CVs (OY Car and CTCV J1300-3052; see Chapter 7) that both show convincing evidence for an accretion veil (Copperwheat et al., 2012; Savoury et al., 2012).

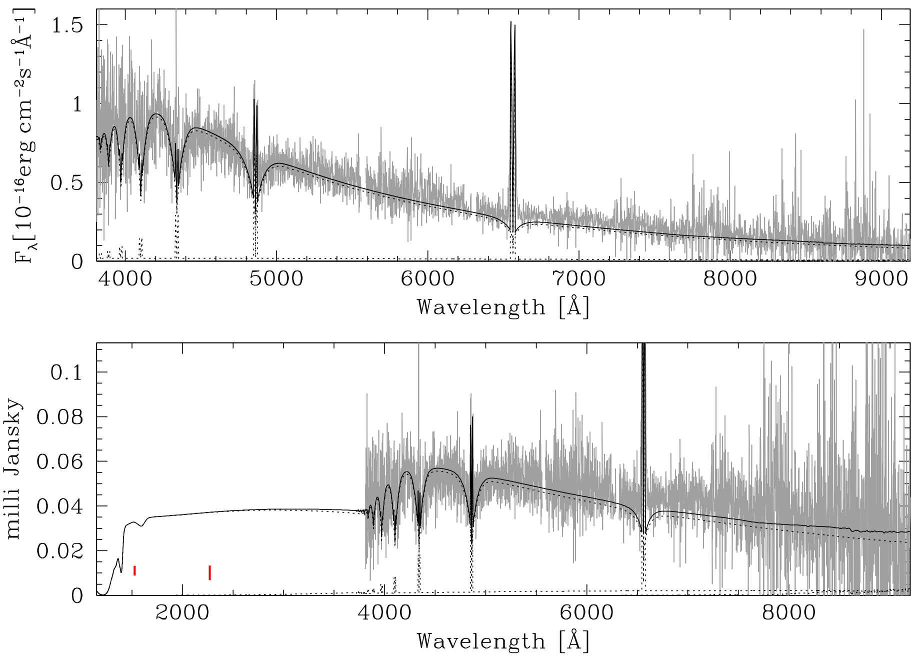

Figure 6.5: Three-component model spectra (black) overlaid on top of the SDSS spectrum of SDSS 1057 (grey), courtesy of Gänsicke (priv. comm.). The three components include a white dwarf, an isothermal and isobaric hydrogen slab and a mid-T secondary star. The two red data points represent UV flux measurements from GALEX.

6.4 Discussion

6.4.1 Component Masses

The white dwarf in SDSS 1057 is found to have a mass of $0.800 \pm 0.015\,\mathrm{M}_\odot$, which is close to the mean CV white dwarf mass of $0.81 \pm 0.04\,\mathrm{M}_\odot$ (Savoury et al., 2011) but notably higher than both the mean post-common-envelope binary (PCEB) white dwarf mass of $0.58 \pm 0.20\,\mathrm{M}_\odot$ (Zorotovic, Schreiber & Gänsicke, 2011) and mean white dwarf field mass of $0.621\,\mathrm{M}_\odot$ (Tremblay et al., 2016).

The donor has a mass of $0.0436 \pm 0.0020\,\mathrm{M}_\odot$, which makes it not only substellar – as it is well below the hydrogen burning limit of $\sim 0.075\,\mathrm{M}_\odot$ (Kumar, 1963; Hayashi & Nakano, 1963) – but also the lowest mass donor yet to be measured in an eclipsing CV.

6.4.2 Mass Transfer Rate

The white dwarf mass and temperature were used to calculate a medium-term average mass transfer rate (equation 1.23) of $\dot{M} = 6.0\,^{+2.9}_{-2.1} \times 10^{-11}\,\mathrm{M_\odot\,yr^{-1}}$. This is a number of times greater than the expected secular mass transfer rate of $\dot{M} \sim 1.5 \times 10^{-11}\,\mathrm{M_\odot\,yr^{-1}}$ for a period-bounce system at this orbital period (Knigge, Baraffe & Patterson, 2011), and is actually consistent with the secular mass transfer rate of a *pre*-bounce system of the same orbital period. This is further evidence that the white dwarf temperature derived through white dwarf atmosphere predictions may be slightly overestimated.

Recalculating the medium-term average mass transfer rate using the lower white dwarf temperature of 10500 K from Southworth et al. (2015) brings it much more in line with the expected secular mass transfer rate. Importantly, the system parameters obtained are consistent within errors, regardless of whether a white dwarf temperature of 10500 K or 13300 K is used to correct the white dwarf mass-radius relationship.

6.4.3 Evolutionary State

A substantial part of the investigation into the evolutionary state of PHL 1445 (Section 4.4.3) centred around its position on a plot of donor mass vs orbital period (Figure 4.9), in relation to a number of different evolutionary tracks. A very similar approach is used here for investigating the evolutionary state of SDSS 1057, as shown in Figure 6.6. SDSS 1057 is plotted in green, along with the four other eclipsing CVs known to harbour substellar donors (black points) that were also included in Figure 4.9, although the presence of two PHL 1445 donor masses is a new addition. The grey PHL 1445 donor mass was obtained using the old eclipse modelling approach (Chapter 4), while the black donor mass is a revised – and favoured – value from the new approach (Section 5.5). Figure 6.6 also includes the evolutionary tracks

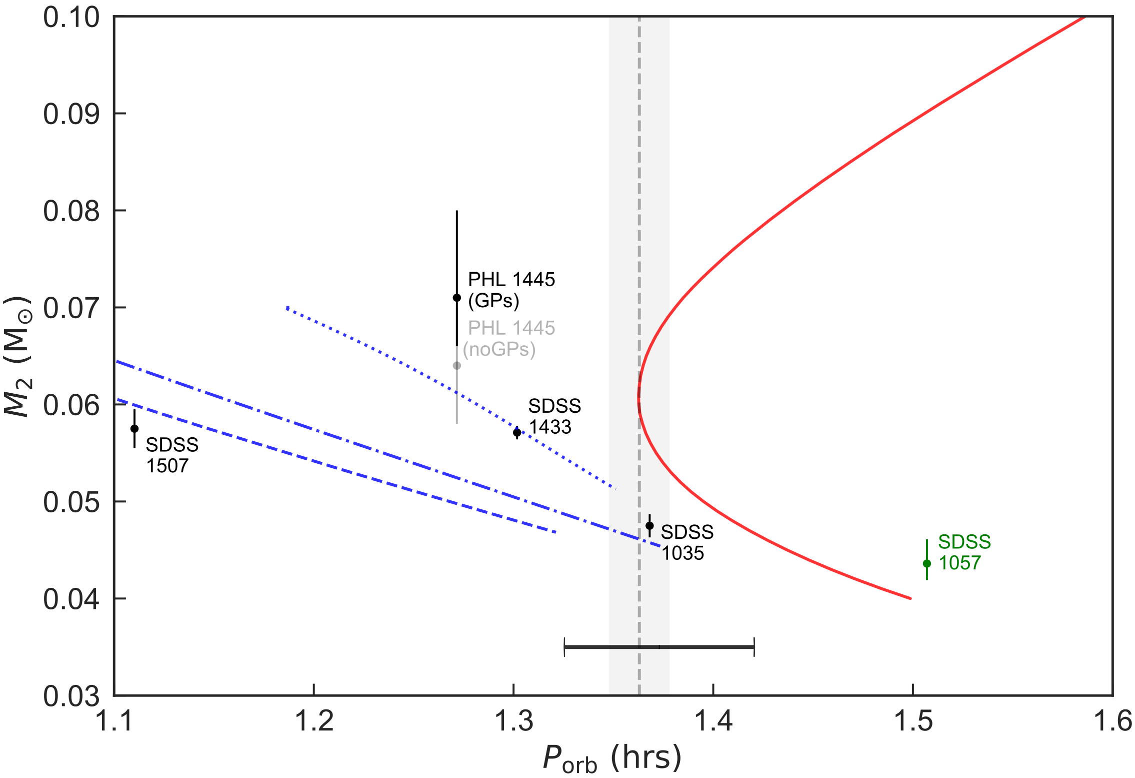

Figure 6.6: Donor mass (M_2) vs orbital period ($P_{\rm orb}$) for SDSS 1057 (green) and other substellar donor eclipsing CVs (black): SDSS 1433, SDSS 1035, SDSS 1507 (Savoury et al., 2011) and PHL 1445. The grey PHL 1445 donor mass was obtained using the old eclipse modelling approach (Chapter 4), while the black donor mass is a revised value from the new approach (Section 5.5). Also plotted are evolutionary tracks for both main sequence (red line; Knigge, Baraffe & Patterson 2011) and brown dwarf (blue lines; Baraffe, priv. comm.) donors. The three brown dwarf donor tracks vary in donor age at start of mass transfer, with the dashed, dot-dashed and dotted lines representing 2 Gyr, 1 Gyr and 600 Myr, respectively. The vertical dashed line represents the location of the CV period minimum determined by Knigge, Baraffe & Patterson (2011), with the shaded area representing the error on this value. The bar across the bottom of the plot shows the FWHM of the CV period spike observed by Gänsicke et al. (2009).

representing a main sequence donor (red; Knigge, Baraffe & Patterson 2011) and brown dwarf donors from formation (blue; Baraffe, priv. comm.). Further details on the main sequence donor track can be found in Section 1.5.4, while the brown dwarf donor tracks are discussed in Sections 1.4.6 and 4.4.3.

The evolutionary status of each of the four existing substellar systems was discussed in detail within Section 4.4.3, so only a brief summary is included here. SDSS 1507 lies significantly below the period minimum in Figure 6.6 due to being metal poor as a member of the Galactic halo, inferred from SDSS 1507's high proper motion (Patterson, Thorstensen & Knigge, 2008; Uthas et al., 2011). This is an exceptional system and therefore it is not included in the remaining discussion. From their positions in Figure 6.6, the best apparent explanation for PHL 1445 (grey) and SDSS 1433 (and arguably also SDSS 1035) is formation with a brown dwarf donor. However, due to the observation of a 'brown dwarf desert' (see Section 1.4.6) the progenitors of such systems – and therefore the systems themselves – are expected to be very rare and greatly outnumbered by those following the main sequence track. This makes it unlikely for even a single one of these systems to have formed with a brown dwarf donor, never mind the majority of this (albeit small) sample. The most likely scenario is that all three systems belong to the main sequence track, which raises concerns for the accuracy of this track (see Sections 4.4.3 and 6.4.4). This is further supported through the shift to higher masses for the revised donor mass in PHL 1445 (black), which moves it clear of all brown dwarf donor tracks.

With the lowest donor mass of all other systems discussed above, and an orbital period significantly greater than the period minimum, SDSS 1057's position in Figure 6.6 is close to the period-bounce arm of the main sequence donor track. Its 90.44 min period puts distance between it and the period minimum, giving SDSS 1057 the best case for being a true period bouncer among the other currently known eclipsing, substellar donor systems. This is backed up by SDSS 1057 possessing additional period-bouncer traits: low white dwarf temperature (although at 13300 K it is at the upper end of what's expected; Patterson 2011), faint quiescent magnitude ($g' \simeq 19.5$ at $d \simeq 367\,\mathrm{pc}$) and long outburst recurrence time (no outburst recorded in over eight years of CRTS observations; Drake et al. 2009). It must be stated that due to the merging of the brown dwarf and main sequence donor tracks post-period minimum, the scenario of SDSS 1057 directly forming with a brown dwarf donor cannot be ruled out. However, due to the lack of potential progenitors and with 80% predicted to lie below the period minimum (Politano, 2004), this seems unlikely to be the case.

6.4.4 CV Evolution at Period Minimum

This study of SDSS 1057 brings the total number of modelled eclipsing period-minimum/period-bounce systems – and therefore systems with precise system parameters – to seven. This includes the period minimum systems SDSS J150137.22+550123.3 (SDSS 1501), SDSS J090350.73+330036.1 (SDSS 0903) and SDSS J150240.98+333423.9 (SDSS 1502) from Savoury et al. (2011), which all have periods $< 86\,\mathrm{min}$ but are not included in Figure 6.6 due to having donor masses above the substellar limit.

It is evident that none of these systems – including SDSS 1057 – lie on the main sequence donor track itself, with some (namely PHL 1445 and SDSS 1433) located far from it. This raises questions about the accuracy of the donor track in the period minimum regime, but it may be evidence for a large intrinsic scatter associated with the track. It is expected for a small amount of intrinsic scatter to exist due to differences in white dwarf mass, but a significant contribution may come from variations in the additional angular momentum loss (approximately $2.5 \times \mathrm{GR}$) that is required in order for the donor track to conform with the observed period minimum (Gänsicke et al., 2009; Knigge, Baraffe & Patterson, 2011). However, recall from Section 4.4.3 that the estimated intrinsic scatter of the main sequence donor track – from the width of the observed period spike from Gänsicke et al. (2009) –

was found to be too small to account for the positions of both PHL 1445 and SDSS 1433. It is clearly evident that more precise masses from period-minimum/period-bounce systems are required, and therefore every additional eclipsing system within this regime that is suitable for modelling is of great value.

Chapter 7

Eclipse Modelling of 15 Additional Systems

7.1 Introduction

In order to secure a better understanding of CV evolution, it is imperative to obtain precise system parameters – especially component masses – for as many CVs as possible. With this in mind, the newly developed eclipse modelling approach is applied to 15 further eclipsing CV systems which have suitable eclipses in the ULTRACAM/ULTRASPEC data archive (Section 2.2). This Chapter starts with a brief introduction to these 15 additional systems, followed by the presentation of results from the eclipse modelling process.

7.2 Additional Systems for Eclipse Modelling

The 15 additional systems chosen for eclipse modelling are as follows:

- CSS080623 J140454−102702 (CSS080623)
- CSS110113 J043112−031452 (CSS110113)
- CTCV J1300−3052 (CTCV 1300; V1258 Cen)

- DV UMa
- GY Cnc
- IY UMa
- OY Car
- SDSS J090103.94+480911.0 (SDSS 0901; PU UMa)
- SDSS J100658.40+233724.4 (SDSS 1006)
- SDSS J115207.00+404947.8 (SDSS 1152)
- SDSS J150137.22+550123.4 (SDSS 1501)
- SSS100615 J200331−284941 (SSS100615)
- SSS130413 J094551−194402 (SSS130413)
- V713 Cep
- Z Cha

This list is a mix of systems that have had ULTRACAM eclipses modelled previously with the existing approach (CTCV 1300, DV UMa, SDSS 1152, SDSS 1501; Table 2.1) and those yet to have ULTRACAM/ULTRASPEC eclipses modelled (CSS080623, CSS110113, GY Cnc, IY UMa, OY Car, SDSS 0901, SDSS 1006, SSS100615, SSS130413, V713 Cep, Z Cha; Table 2.2).

7.2.1 Previously Modelled Systems

Four systems previously modelled by Savoury et al. (2011) were chosen for revision with the new eclipse modelling approach. These systems were selected primarily on their donor masses presented in Savoury et al. (2011). The donor masses of DV UMa and SDSS 1152 appear to be outliers compared to the predicted donor evolution track (see Figure 8 of Savoury et al. 2011), while the donor masses of CTCV 1300, SDSS 1152 and SDSS 1501 have notably large errors. In the case of SDSS 1152 and SDSS 1501, supplemental ULTRACAM/ULTRASPEC eclipses had since become available; obtained after the initial eclipse modelling. Revisiting these four systems also provided further opportunity to compare the new and existing approaches to eclipse modelling.

7.2.2 New Systems

The remaining 11 systems were chosen from the 24 systems observed with ULTRACAM/ULTRASPEC that are ready for modelling (Table 2.2). These 11 systems were selected primarily on the modelling potential of the available eclipse data, but also to ensure systems with a range of bright spot eclipse shapes, flickering amplitudes and orbital periods were included in the sample.

Two of the chosen systems are Z Cha and OY Car, which are both bright eclipsing CVs ($g' \sim 15.6$) and among the first eclipsing CVs to be studied in detail (e.g. Wood et al. 1986; Wade & Horne 1988; Wood & Horne 1990). These early studies produced system parameter estimates from eclipse contact phase timing and radial velocity (RV) measurements, but no eclipse modelling studies exist in the literature. The available ULTRACAM eclipses of both systems show clear white dwarf and bright spot eclipses, making Z Cha and OY Car prime candidates for eclipse modelling.

The other nine chosen systems were all discovered within the past 20 years (see Hardy et al. 2017 for more details). Of these, only three have existing system parameter estimates in the literature: IY UMa (contact phase timing; Steeghs et al. 2003), GY Cnc (RV; Thorstensen 2000) and SDSS 1006 (eclipse modelling; Southworth et al. 2009), however all have large associated errors.

7.3 Eclipse Selection

With 15 additional systems chosen, the next task involved deciding on which specific eclipses to model for each system, from the many available eclipses the ULTRACAM/ULTRASPEC data archive (see Table A.1). Indication of the eclipses selected for modelling can be found in the final column in Table A.1.

7.3.1 Average Eclipses

Eclipse averaging was used for six systems: CSS080623, CSS110113, DV UMa, SDSS 0901, SDSS 1152, SSS100615. All systems have multiple eclipse light curves observed close together in time (e.g. same observing run), and contain only low amplitude flickering. The result is multiple eclipse light curves very similar in shape, which can be averaged without encountering the issues outlined in Section 3.3.1. It was beneficial to simultaneously model a handful of average eclipses over many individual eclipses, as this kept model complexity and computational time at a minimum.

When selecting eclipses for the construction of each average eclipse, great care was taken to identify and prevent any disc radius/flux and/or bright spot shape/flux changes across individual eclipses. Firstly, only eclipses obtained during the same observing run were considered for each average eclipse. Secondly, before averaging, all eclipses were phase-folded and overlaid, with any distinct eclipses removed from consideration. An average eclipse was created for each available wavelength band, typically $u'g'r'$ or $u'g'i'$. As both CSS080623 and SDSS 0901 have multiple eclipses from two separate observing runs, two average eclipses in each wavelength band were created.

7.3.2 Individual Eclipses

The remaining nine systems were only suitable for individual eclipse model fitting. For each system, eclipses from the ULTRACAM/ULTRASPEC data archive were selected for modelling primarily on the presence of a clear bright spot ingress, with slightly less emphasis on the egress. It was also important to try and include at least one eclipse from as many different wavelength bands as possible[1], as white dwarf fluxes at a range of wavelengths are required in order to help constrain T_1 in the white dwarf atmosphere fitting procedure (see Section 7.4.2).

---

[1] Especially in the u' band, as the u' band white dwarf flux is essential for constraining T_1.

In general, the majority of eclipses showing a clear bright spot ingress feature were selected for modelling. However, for systems with many high signal-to-noise eclipses containing very clear bright spot eclipse features (e.g. OY Car and Z Cha), only six were selected. In these cases, the inclusion of additional eclipses was judged to have minimal effect on the system parameter values and errors, and did not justify the resulting increased model complexity and computational time. This approach was also taken with SSS130413 and V713 Cep, two systems with moderately clear bright spot features. The five or six eclipses with the clearest bright spot features were chosen for modelling, leaving a handful with visible bright spot ingresses surplus to requirement. While the inclusion of additional eclipses is not expected to have a significant effect on the system parameters, it may contribute to reducing errors. This should be considered if SSS130413 and V713 Cep are re-modelled in the future[2].

7.4 Results

7.4.1 Simultaneous Eclipse Light Curve Modelling

For each of the 15 additional systems, the chosen eclipses (individual or average) were simultaneously fit with the CV eclipse model (Section 3.2) alongside the GP flickering model (Section 3.4.5), as outlined in Section 3.6.2. The complex bright spot variation of the CV eclipse model was used for all but three systems (SDSS 1501, SSS100615, V713 Cep). The simple bright spot was used in these three systems due to each containing a weak bright spot component in their eclipse light curves. The typical phase range of the eclipse light curves modelled was −0.10 to 0.15, however an extended phase range was used for a number of systems. The phase range was increased for systems with a prominent bright spot (e.g. CTCV 1300, GY Cnc, SDSS 1006)[3], in addition to SDSS 1501 (tenuous bright spot component) and V713 Cep

---

[2] In the case of SSS130413, additional, high-quality eclipse light curves were obtained post-modelling, and therefore the re-modelling of this system is highly recommended.

[3] In order to obtain more accurate fits to their pronounced orbital humps.

(combination of heavy flickering post-eclipse and significant disc contribution).

The full results of the 15 simultaneous fits are shown in Figures B.1–B.15, while the corresponding model parameters are located in Table C.11. Figure 7.1 shows an example g'-band eclipse light curve fit from each of the 15 simultaneous fits. In addition to the most probable fit of the eclipse model (blue line), a blue fill-between region is plotted that covers 1σ from the mean of a random sample (size 1000) of the MCMC chain. The grey points represent the actual eclipse light curves, while the black points are the result of subtracting the GP's posterior mean (itself shown, $\pm 1\sigma$, by the red fill-between region covering the residuals below each plot). Also plotted are the separate components of the eclipse model: white dwarf (purple), bright spot (red), accretion disc (yellow) and donor (green).

7.4.2 System Parameters

The post-eclipse light curve fitting procedure described in Section 3.7 was followed to produce 15 sets of system parameter posterior PDFs. System parameter values (see Table 7.1) were then obtained from the peak of each posterior PDF, with errors from the 67% confidence level. Calculation of these PDFs relies on knowledge of T_1, which were obtained through fitting white dwarf atmosphere predictions to multi-wavelength white dwarf fluxes from the eclipse model fits (see Section 3.7 for more details). The results of these white dwarf flux fits are shown in Figure 7.2, and the resulting T_1 and d for each system are also displayed in Table 7.1. Note that the white dwarf flux fitting was not carried out for either IY UMa or SDSS 1006, due to the lack of u'-band eclipse in their eclipse model fits[4]. Thankfully, precise measurements of T_1 for both IY UMa[5] ($18000 \pm 1000\,\mathrm{K}$) and SDSS 1006 ($16000 \pm 1000\,\mathrm{K}$) from spectral fitting are given in Pala et al. (2017).

---

[4] No usable u'-band eclipse in ULTRACAM/ULTRASPEC archive for IY UMa or SDSS 1006.

[5] IY UMa entered outburst between the observations of Pala et al. (2017) and this work, so this T_1 measurement may be slightly lower than T_1 of the white dwarf in the eclipse light curves.

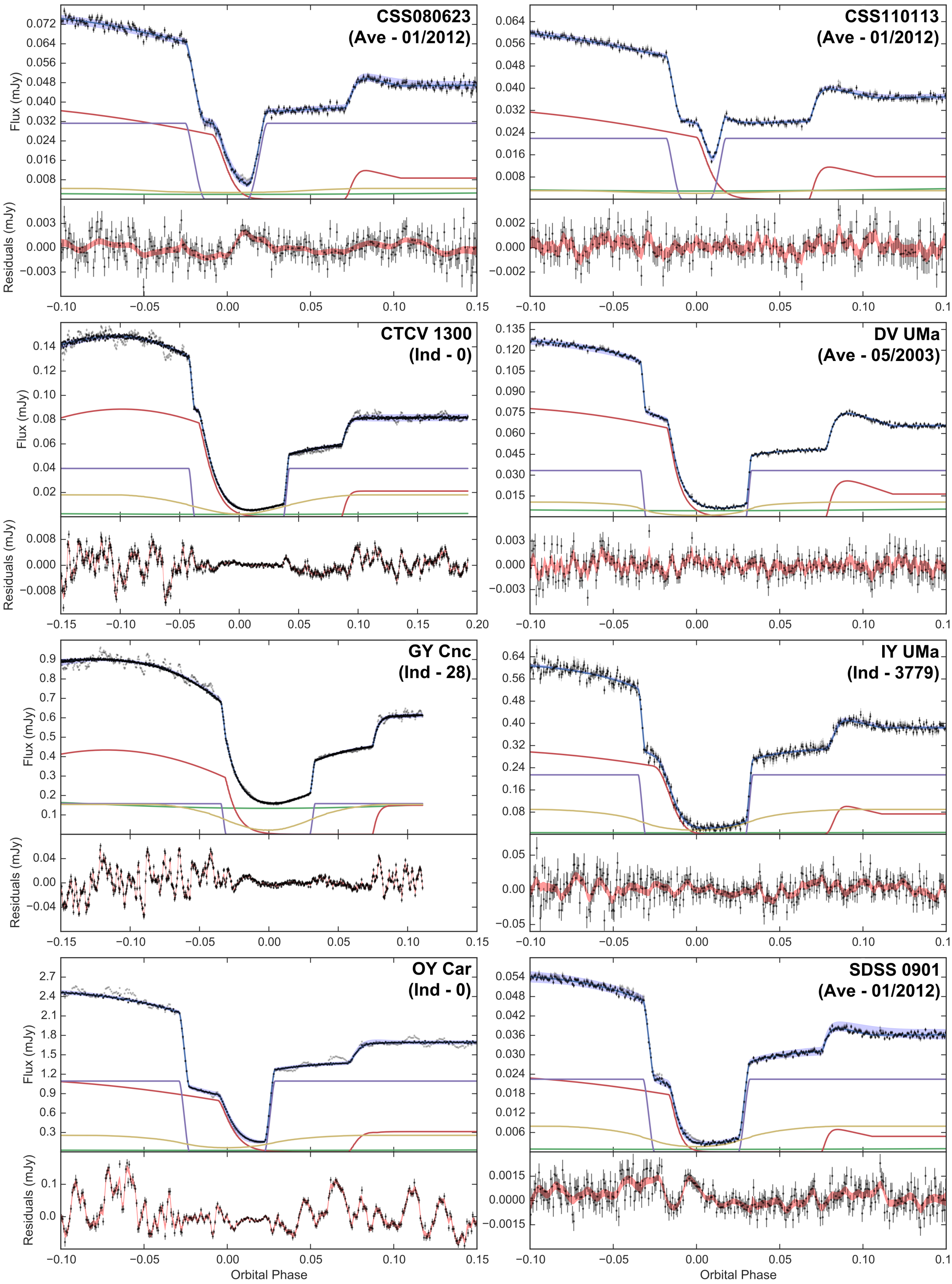

Figure 7.1: Simultaneous eclipse model fits (blue) to eclipse light curves of 15 additional systems (grey) – g'-band examples. See text for full details of what is plotted. The system name is displayed in the top-right corner of each plot, along with whether the eclipse is an individual (Ind) or average (Ave) eclipse. For individual eclipses the cycle number is shown, while for average eclipses the month associated with the constituent eclipses is otherwise shown. See Appendix B for a complete set of eclipse plots resulting from each of the 15 eclipse model fits.

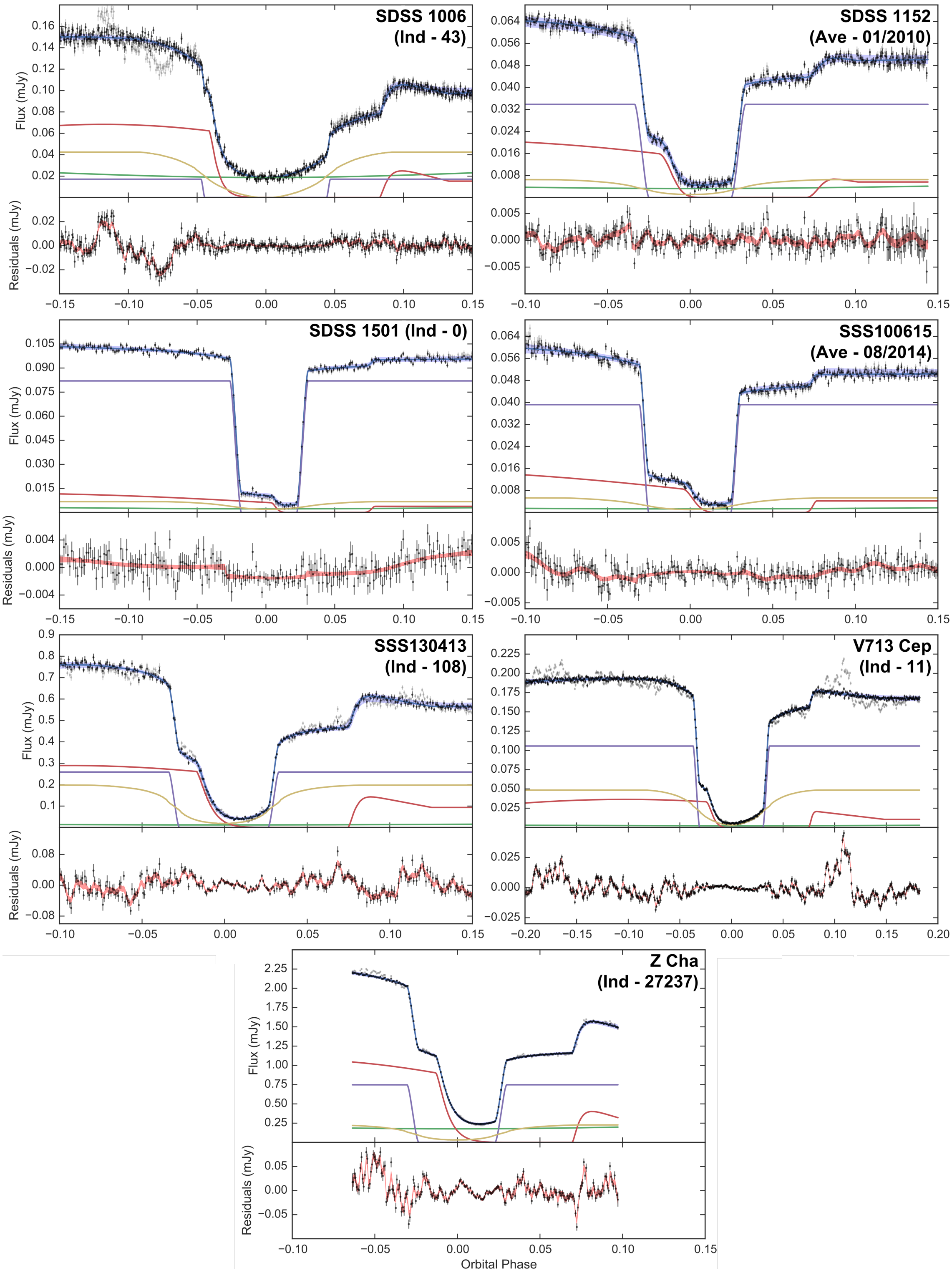

Figure 7.1: *Continued.*

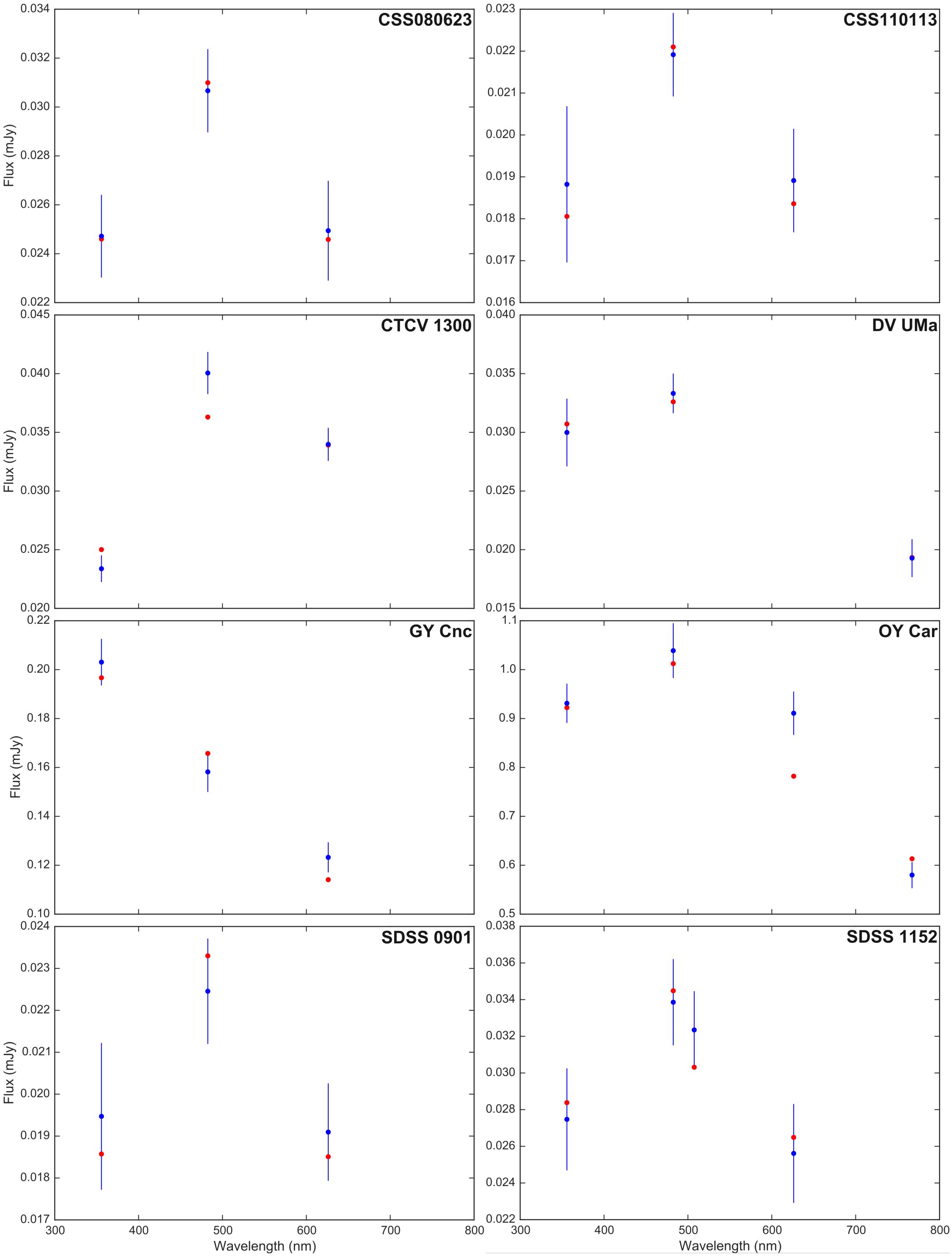

Figure 7.2: White dwarf fluxes from 13 of the additional simultaneous eclipse model fits (blue) and white dwarf atmosphere predictions (red; see Section 3.7.1), at wavelengths corresponding to u' (355.7 nm), g' (482.5 nm), *KG5* (507.5 nm), r' (626.1 nm) and i' (767.2 nm) filters. The name of each system is displayed in the top-right corner of each plot.

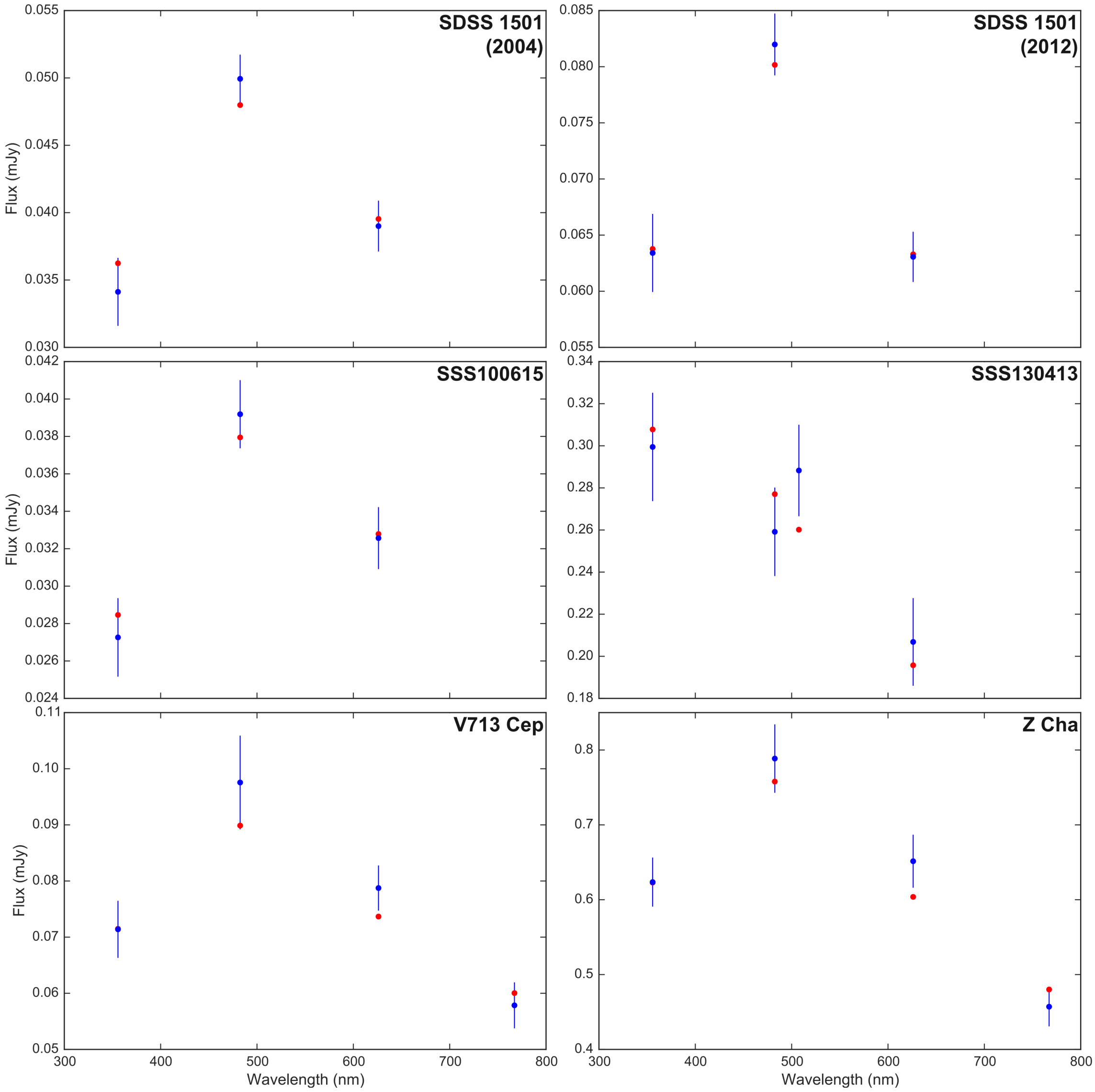

Figure 7.2: *Continued.*

Parameter	**CSS080623**	**CSS110113**	**CTCV 1300**	**DV UMa**
q	0.114 ± 0.005	0.105 ± 0.006	0.233 ± 0.004	$0.172\,^{+0.002}_{-0.007}$
M_1 ($\mathrm{M}_\odot$)	0.710 ± 0.019	$1.00\,^{+0.04}_{-0.01}$	0.717 ± 0.017	1.09 ± 0.03
R_1 ($\mathrm{R}_\odot$)	$0.0117\,^{+0.0001}_{-0.0004}$	0.0080 ± 0.0003	0.01133 ± 0.00021	0.0072 ± 0.0004
M_2 ($\mathrm{M}_\odot$)	0.081 ± 0.005	0.105 ± 0.007	$0.166\,^{+0.006}_{-0.003}$	$0.187\,^{+0.003}_{-0.012}$
R_2 ($\mathrm{R}_\odot$)	0.1275 ± 0.0024	0.149 ± 0.003	$0.2111\,^{+0.0025}_{-0.0014}$	$0.215\,^{+0.001}_{-0.005}$
a ($\mathrm{R}_\odot$)	0.593 ± 0.005	$0.711\,^{+0.009}_{-0.003}$	0.805 ± 0.007	$0.889\,^{+0.006}_{-0.012}$
K_1 ($\mathrm{km\,s^{-1}}$)	50.8 ± 2.3	$51.1\,^{+2.9}_{-2.4}$	86.4 ± 1.4	$76.1\,^{+0.9}_{-2.9}$
K_2 ($\mathrm{km\,s^{-1}}$)	$449\,^{+1}_{-6}$	487 ± 3	371 ± 3	444 ± 4
i ($^\circ$)	80.76 ± 0.19	79.94 ± 0.19	$86.9\,^{+0.5}_{-0.2}$	$83.29\,^{+0.29}_{-0.10}$
$\log g$	$8.15\,^{+0.01}_{-0.04}$	8.63 ± 0.03	8.186 ± 0.019	8.77 ± 0.04
T_1 (K)	15500 ± 1700	14500 ± 2200	11000 ± 1000	17400 ± 1900
d (pc)	550 ± 60	430 ± 60	340 ± 40	380 ± 40

Parameter	**GY Cnc**	**IY UMa**	**OY Car**	**SDSS 0901**
q	$0.448\,^{+0.014}_{-0.021}$	$0.146\,^{+0.009}_{-0.001}$	$0.1065\,^{+0.0009}_{-0.0029}$	$0.182\,^{+0.009}_{-0.004}$
M_1 ($\mathrm{M}_\odot$)	0.881 ± 0.016	$0.955\,^{+0.013}_{-0.028}$	$0.882\,^{+0.011}_{-0.015}$	$0.752\,^{+0.024}_{-0.018}$
R_1 ($\mathrm{R}_\odot$)	$0.00976\,^{+0.00021}_{-0.00018}$	$0.0087\,^{+0.0003}_{-0.0001}$	$0.00957\,^{+0.00018}_{-0.00012}$	$0.01105\,^{+0.00022}_{-0.00029}$
M_2 ($\mathrm{M}_\odot$)	$0.394\,^{+0.016}_{-0.022}$	0.141 ± 0.007	$0.093\,^{+0.004}_{-0.001}$	0.138 ± 0.007
R_2 ($\mathrm{R}_\odot$)	$0.446\,^{+0.006}_{-0.009}$	0.1770 ± 0.0028	$0.1388\,^{+0.0018}_{-0.0003}$	0.182 ± 0.003
a ($\mathrm{R}_\odot$)	1.429 ± 0.012	$0.765\,^{+0.004}_{-0.009}$	0.662 ± 0.003	0.739 ± 0.007
K_1 ($\mathrm{km\,s^{-1}}$)	125 ± 4	$66\,^{+4}_{-1}$	50.4 ± 0.9	73 ± 3
K_2 ($\mathrm{km\,s^{-1}}$)	278.0 ± 2.4	453 ± 3	475.9 ± 2.1	401 ± 3
i ($^\circ$)	$77.06\,^{+0.29}_{-0.18}$	$84.9\,^{+0.1}_{-0.5}$	$83.27\,^{+0.10}_{-0.13}$	$81.4\,^{+0.1}_{-0.3}$
$\log g$	8.40 ± 0.019	8.54 ± 0.03	$8.422\,^{+0.017}_{-0.013}$	$8.228\,^{+0.022}_{-0.025}$
T_1 (K)	25900 ± 2300	–	$18600\,^{+2800}_{-1600}$	14900 ± 2000
d (pc)	320 ± 30	–	90 ± 5	600 ± 70

Table 7.1: System parameters for 15 additional eclipsing systems.

Parameter	**SDSS 1006**	**SDSS 1152**	**SDSS 1501**	**SSS100615**
q	0.46 ± 0.03	$0.153\,^{+0.015}_{-0.011}$	0.084 ± 0.004	0.095 ± 0.004
M_1 ($\mathrm{M}_\odot$)	0.82 ± 0.11	0.62 ± 0.04	$0.723\,^{+0.017}_{-0.013}$	0.88 ± 0.03
R_1 ($\mathrm{R}_\odot$)	0.0102 ± 0.0013	0.0129 ± 0.0006	$0.01142\,^{+0.00016}_{-0.00022}$	0.0095 ± 0.0003
M_2 ($\mathrm{M}_\odot$)	0.37 ± 0.06	$0.094\,^{+0.016}_{-0.009}$	0.061 ± 0.004	0.083 ± 0.005
R_2 ($\mathrm{R}_\odot$)	$0.457\,^{+0.022}_{-0.026}$	0.147 ± 0.006	$0.1129\,^{+0.0025}_{-0.0016}$	$0.1276\,^{+0.0028}_{-0.0024}$
a ($\mathrm{R}_\odot$)	1.46 ± 0.07	0.627 ± 0.014	0.574 ± 0.004	0.628 ± 0.007
K_1 ($\mathrm{km\,s^{-1}}$)	124 ± 9	62 ± 5	$39.5\,^{+2.2}_{-1.3}$	$46.5\,^{+2.2}_{-1.7}$
K_2 ($\mathrm{km\,s^{-1}}$)	270 ± 13	402 ± 7	468 ± 3	493 ± 5
i ($^\circ$)	$83.1\,^{+1.2}_{-0.7}$	82.6 ± 0.5	$83.89\,^{+0.20}_{-0.27}$	85.1 ± 0.3
$\log g$	8.33 ± 0.13	8.01 ± 0.05	$8.182\,^{+0.016}_{-0.019}$	8.43 ± 0.03
T_1 (K)	–	15900 ± 2000	13400 ± 1100 (2004) 14900 ± 1000 (2012)	13600 ± 1500
d (pc)	–	610 ± 80	400 ± 30 (2004) 338 ± 21 (2012)	350 ± 30

Parameter	**SSS130413**	**V713 Cep**	**Z Cha**
q	$0.169\,^{+0.011}_{-0.006}$	$0.246\,^{+0.006}_{-0.014}$	0.189 ± 0.004
M_1 ($\mathrm{M}_\odot$)	0.84 ± 0.03	$0.703\,^{+0.012}_{-0.015}$	0.803 ± 0.014
R_1 ($\mathrm{R}_\odot$)	$0.0102\,^{+0.0006}_{-0.0002}$	$0.01173\,^{+0.00020}_{-0.00015}$	0.01046 ± 0.00017
M_2 ($\mathrm{M}_\odot$)	$0.140\,^{+0.012}_{-0.008}$	$0.176\,^{+0.007}_{-0.018}$	0.152 ± 0.005
R_2 ($\mathrm{R}_\odot$)	0.163 ± 0.004	$0.208\,^{+0.002}_{-0.005}$	0.1820 ± 0.0020
a ($\mathrm{R}_\odot$)	$0.680\,^{+0.007}_{-0.011}$	0.781 ± 0.006	0.734 ± 0.005
K_1 ($\mathrm{km\,s^{-1}}$)	75 ± 4	$91\,^{+2}_{-5}$	$78.4\,^{+1.4}_{-1.8}$
K_2 ($\mathrm{km\,s^{-1}}$)	$443\,^{+3}_{-7}$	$367.6\,^{+2.6}_{-2.3}$	$413.2\,^{+2.5}_{-2.0}$
i ($^\circ$)	82.5 ± 0.3	81.7 ± 0.3	80.44 ± 0.11
$\log g$	8.35 ± 0.04	$8.147\,^{+0.017}_{-0.014}$	8.304 ± 0.016
T_1 (K)	24000 ± 3000	$17000\,^{+6000}_{-3000}$	16300 ± 1400
d (pc)	240 ± 40	320 ± 30	103 ± 6

Table 7.1: *Continued.*

7.4.3 White Dwarf Flux and Orbital Period Variations in SDSS 1501

The eclipses of SDSS 1501 are white dwarf dominated, but some show faint BS features – similar to the eclipses of SDSS 1057 (Chapter 6). There are a total of 15 available ULTRACAM eclipses of SDSS 1501, obtained during observing runs in 2004 (one eclipse), 2006 (eight), 2010 (two) and 2012 (one) (see Table A.1 for further details). However, only the single eclipses from 2004 and 2012 show signs of a bright spot eclipse, so both[6] were chosen for simultaneous eclipse modelling described above.

It became apparent that there was an appreciable increase in white dwarf flux across all three ($u'g'r'$) bands between the 2004 and 2012 eclipses. For this reason, white dwarf flux fitting to atmosphere predictions was carried out separately for each eclipse, as shown in Figure 7.2. The resulting d and T_1 for each eclipse are shown in Table 7.1. The white dwarf in 2012 appears marginally hotter, but note the 1.6σ discrepancy in d, which should of course remain constant. The white dwarf flux fitting was repeated for both eclipses, but this time with d held fixed at 360 pc. This now gives $T_1(2004) = 12100 \pm 300\,\mathrm{K}$ and $T_1(2012) = 15800 \pm 300\,\mathrm{K}$, a much larger increase of 3700 K.

Such a large discrepancy in T_1 indicates that the white dwarf in SDSS 1501 underwent a period of enhanced accretion between 2004 and 2012, most likely a superoutburst. The possible window for the event can be constrained further to between Jan 2010 and Mar 2011, as the white dwarf fluxes in the 2006 and 2010 eclipses are consistent with those in the 2004 eclipse, in addition to SDSS 1501's CRTS (Drake et al., 2009) long-term light curve showing a notable increase in overall brightness post-Mar 2011. According to vsnet-alert 12169[7], the superoutburst

---

[6] Each ULTRACAM eclipse is in three bands ($u'g'r'$), giving six individual eclipses for modelling.

[7] http://ooruri.kusastro.kyoto-u.ac.jp/mailarchive/vsnet-alert/12169

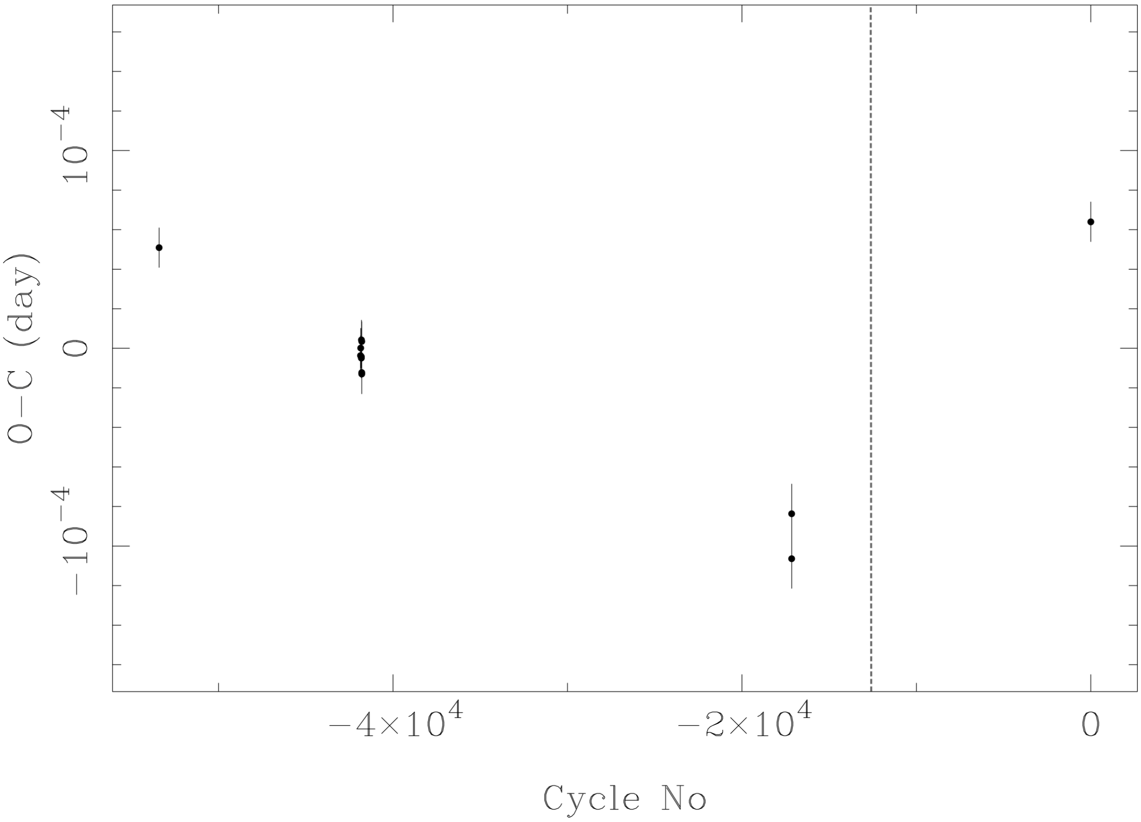

Figure 7.3: O − C diagram for all 12 available ULTRACAM eclipses of SDSS 1501, spanning ∼ 8 yrs. The vertical dashed line corresponds to Sep 2010, when SDSS 1501 was reportedly observed in superoutburst. The y-axis covers ±15 s.

occurred in Sep 2010, with the observer claiming to have observed SDSS 1501 in outburst in addition to obtaining part of a superhump. Unfortunately, this is the only available documentation of this rare[8] superoutburst. With a precise value of q obtained in this work, a measured superhump period would have allowed SDSS 1501 to be used as a calibrator of the $\epsilon(q)$ relation (see Sections 1.5.2 and 8.4).

In addition to white dwarf flux variations, SDSS 1501 also exhibits small orbital period variations. The white dwarf-dominated SDSS 1501 eclipses enable very precise mid-eclipse times to be obtained (see Section 3.1). It is these mid-eclipse times – after the subtraction of a linear ephemeris – that are shown in Figure 7.3. The orbital period of SDSS 1501 appears to depart from linearity by approximately ±7 s over the ∼ 8 yr ULTRACAM observational baseline. Such variations are not uncom-

---

[8] Supercycles of period minimum systems are typically decades in length (Hellier, 2001).

mon in CVs, and are thought to be caused by a magnetically-driven process within the donor (Section 3.1). However, they are not observed in CVs with donors of spectral type later than M6 (Bours et al., 2016), due to magnetic activity in the donor decreasing with later spectral types. SDSS 1501's donor mass obtained through eclipse modelling (see Section 7.4.1) is substellar ($0.061 \pm 0.004\,\mathrm{M_\odot}$), strongly indicating a spectral type later than M6, and so the observation of period variations is surprising.

A logical deduction from looking at Figure 7.3 is that the superoutburst from Sep 2010 (dashed line) may have caused the observed change in orbital period, as the ephemeris appears approximately linear up until this point. In this scenario, the 2012 eclipse occurs $\sim$21 s later than expected, implying an increase in SDSS 1501's orbital period of 0.0016 s ($\Delta P_{\mathrm{orb}}/P_{\mathrm{orb}} = 3.2 \times 10^{-7}$), but can the accretion of the disc's contents onto the white dwarf during superoutburst account for an increase in period of this size? Assuming that mass is conserved within the system ($\Delta M_1 = -\Delta M_2$), equation 1.12 indicates that the white dwarf must have increased in mass by $7.1 \times 10^{-9}\,\mathrm{M_\odot}$ during superoutburst, and therefore the accretion disc must have contained the same amount of mass at the start of superoutburst. With SDSS 1501's system parameters known (Table 7.1), equation 1.23 can be used to determine a medium-term average mass transfer rate[9] for SDSS 1501 of $\dot{M} = 9.3 \times 10^{-11}\,\mathrm{M_\odot\,yr^{-1}}$. At this mass transfer rate, it would take approximately 76 yrs to produce an accretion disc of mass $7.1 \times 10^{-9}\,\mathrm{M_\odot}$, however period minimum systems are observed to have superoutburst cycles much shorter than this (20–30 yrs). It therefore appears that the Sep 2010 superoutburst is not (at least not fully) responsible for the period variations exhibited by SDSS 1501. Another possible cause of the period variations is the presence of a third body within the system, however additional precise mid-eclipse timings are required in order to investigate this further.

---

[9] Using value of T_{eff} obtained from the 2004 (pre-superoutburst) data.

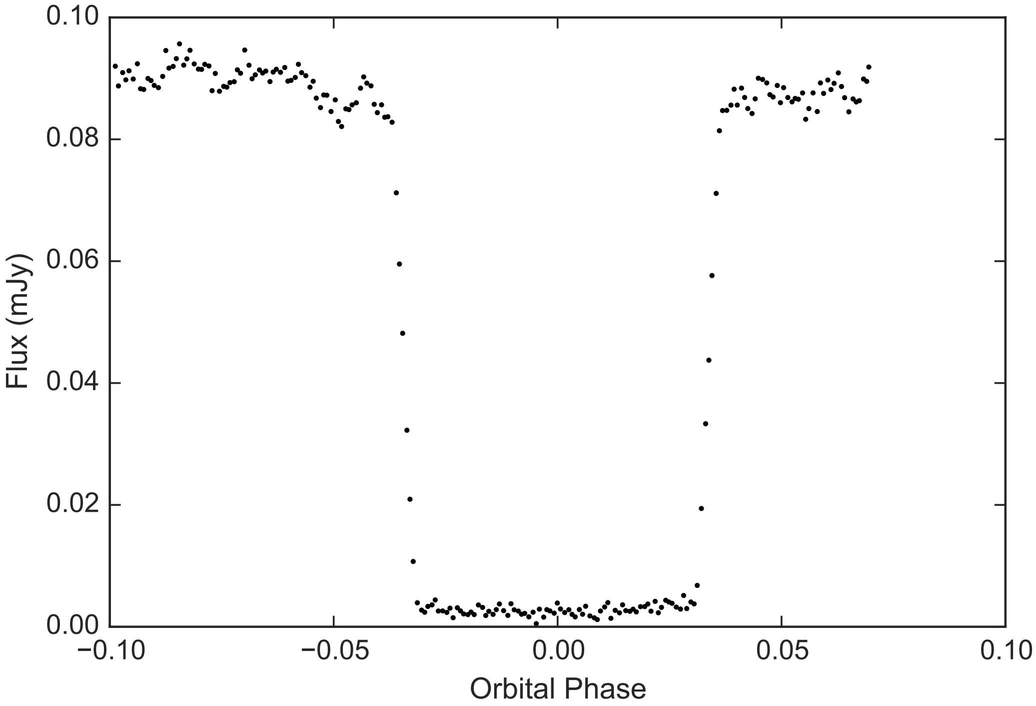

Figure 7.4: g'-band eclipse light curve (24 Jun 2015, cycle no. 11955) of V713 Cep during a low state.

7.4.4 Observed Low State of V713 Cep

The ULTRACAM/ULTRASPEC data archive contains a total of 15 V713 Cep eclipses, with two ULTRACAM eclipses (cycle nos. 11 [$u'g'r'$] and 3655 [$u'g'i'$]) showing clear bright spot features selected for eclipse modelling (see Section 7.4.1). A feature of these two eclipses is a notable disc contribution (see Figure B.14), which is seen in all other V713 Cep eclipses in the archive, with the exception of one. The ULTRACAM $u'g'r'$ eclipse of 24 Jun 2015 (cycle no. 11955, g'-band eclipse shown in Figure 7.4) contains no obvious signs of either a disc or bright spot eclipse, and at first glance resembles an eclipse of a detached, non-accreting binary. However, on closer inspection there are signs of flickering outside of white dwarf eclipse, as well as a very slight curvature inside eclipse. These two features are both evidence for the presence of an – albeit considerably diminished – accretion disc. A dwindling accretion disc and no sign of a bright spot indicates that the secondary has stopped supplying the disc with material and the system is in what is known as a ‘low state’.

As discussed in Section 1.2.4, low states are relatively common phenomena for both magnetic CVs and a subgroup of novalike (NL) CVs called VY Scl stars, however they appear to be very rare (and unexpected) for DN below the period gap. In fact, there is only one existing documentation of such an occurrence in the literature – an extended ($>2\,$yrs) low state of IR Com (Manser & Gänsicke, 2014). With only one eclipse of V713 Cep obtained during its low state, it is not known exactly how long this low state lasted. An upper limit of 403 days can be estimated based on the timings of other ULTRACAM eclipses, and therefore it was significantly shorter than the low state of IR Com.

Chapter 8

Discussion

8.1 Introduction

With new or revised precise system parameter determinations for 18 CV systems obtained through this work (Chapters 4–7), attention now turns towards what impact these results may have on the current understanding of CVs and their evolution.

8.2 CV White Dwarf Masses

As discussed in Section 1.6, there has been shown to be a significant discrepancy between the mean white dwarf mass in the field and that within CVs (e.g. Zorotovic, Schreiber & Gänsicke 2011). This is illustrated by the top panel of Figure 8.1, which shows measured CV white dwarf masses published pre-2014[1] (the start of this work) plotted against the orbital period of the CV; the vast majority of which lie above the mean white dwarf field mass of $0.621\,\mathrm{M}_{\odot}$ from Tremblay et al. (2016) (grey dotted line). This sample of measured CV white dwarf masses is very similar to the 'fiducial' sample used by Zorotovic, Schreiber & Gänsicke (2011) to obtain a mean CV white dwarf mass of 0.82 ± 0.03[2] $\mathrm{M}_{\odot}$ ($\sigma = 0.15$[3] $\mathrm{M}_{\odot}$), shown with a black line

---

[1] See Table D.1 for further details and references.

[2] Uncertainty shown represents 1σ error of the mean.

[3] Standard deviation of the mass distribution.

in Figure 8.1 (error represented by shaded region).

This work has produced nine new and nine revised white dwarf masses through eclipse modelling. An updated CV white dwarf mass plot with these 18 new and revised masses (green) included – along with a handful of masses published post-2014 from other sources (see Table D.1) – is shown in the bottom plot of Figure 8.1. An updated estimate for the mean CV white dwarf mass is $0.812 \pm 0.020\,\mathrm{M_\odot}$ ($\sigma = 0.13\,\mathrm{M_\odot}$), obtained using the χ^2 metric, as detailed in Appendix B of Knigge (2006). The updated mean CV white dwarf mass and error are plotted as a red line and shaded region, respectively. While the additional masses have little effect on the value of $\langle M_1 \rangle$, the sizes of both the error and σ have been reduced.

One way to explain the presence of high white dwarf masses in CVs is through white dwarf mass growth through steady accretion across the lifetime of a CV, but this requires the observation of higher white dwarf masses in systems with lower orbital periods (see Section 1.6.1 for further details). To test this, $\langle M_1 \rangle$ was re-calculated for only systems below the period gap ($P_{\mathrm{orb}} \sim 2.15\,\mathrm{hrs}$), giving $\langle M_1 \rangle(\text{below gap}) = 0.802 \pm 0.020\,\mathrm{M_\odot}$ ($\sigma = 0.10\,\mathrm{M_\odot}$). This is in fact lower than when systems at all orbital periods are taken into account, and therefore evidence against significant white dwarf mass growth in CVs. While white dwarf mass growth in CVs appears doubtful, further precise white dwarf masses from systems at long period ($> 3\,\mathrm{hrs}$) are required until it can be entirely dismissed.

8.2.1 Testing the Validity of the Empirical CAML Model

The focus of Section 1.6.3 was an empirical consequential angular momentum loss (eCAML) model from Schreiber, Zorotovic & Wijnen (2016). The model produces a low dynamical stability limit on q, causing systems with low-mass white dwarfs to become unstable to mass transfer. These systems consequently merge, removing them from the CV population, and enables the observed CV white dwarf mass distribution to be reproduced (see Figure 2 in Schreiber, Zorotovic & Wijnen 2016).

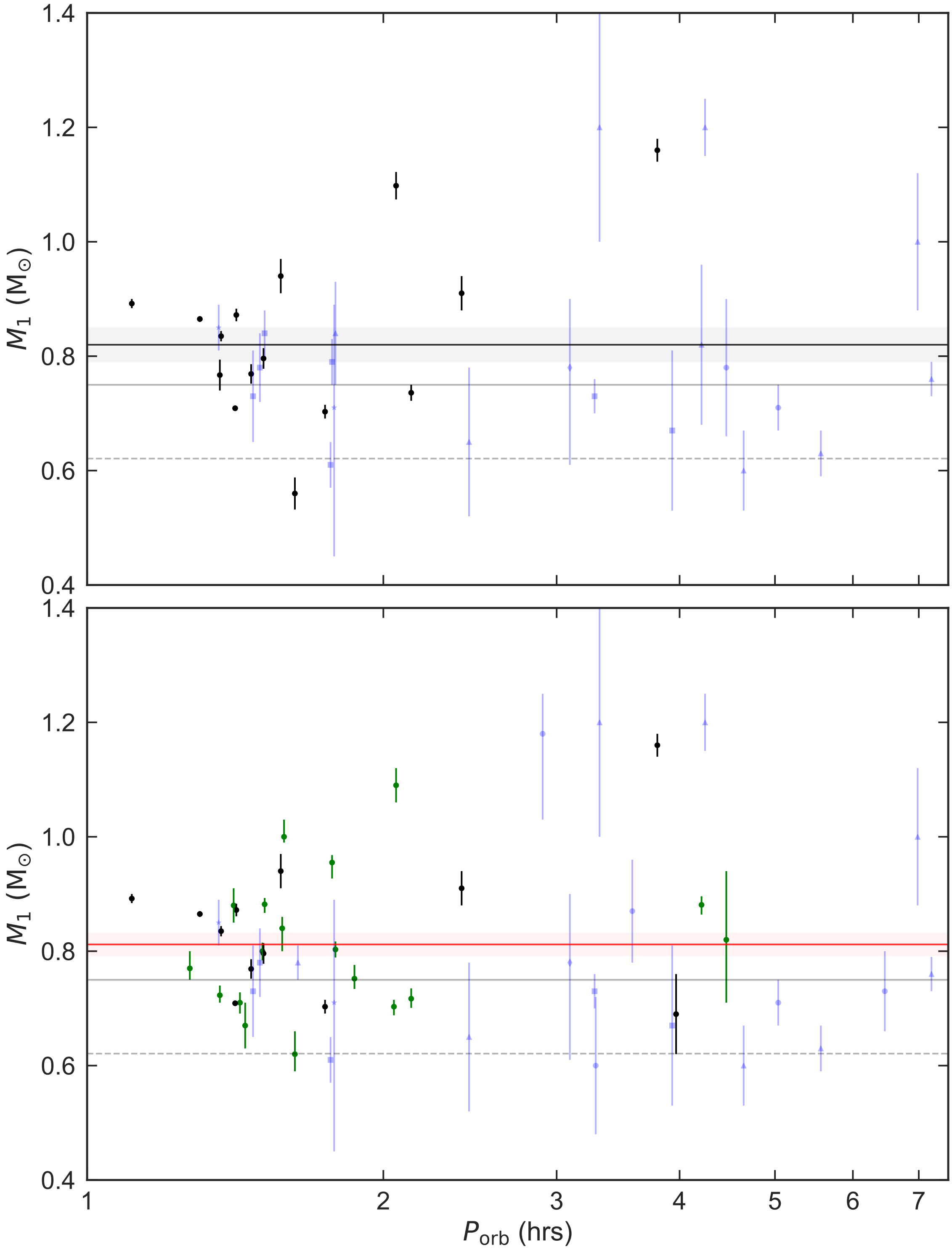

Figure 8.1: Measured CV white dwarf masses (M_1) as a function of orbital period ($P_{\rm orb}$), both before (top) and after (bottom) the start of this work. The green and black points represent masses obtained from eclipse modelling of ULTRACAM/ULTRASPEC data, either from this work (green) or otherwise (black). The faint blue points represent measured CV masses from other methods: eclipse modelling of other data (circles), contact phase timing (squares), radial velocity (triangles), gravitational redshift (stars) and spectrophotometric modelling (diamonds). Also shown is the mean field white dwarf mass from Tremblay et al. (2016) (dashed grey lines), as well as mean CV white dwarf masses from: Knigge (2006) (solid grey lines), Zorotovic, Schreiber & Gänsicke (2011) (black line in top plot), and this work (red line in bottom plot). The shaded regions represent 1σ errors.

The top-left plot of Figure 2 in Schreiber, Zorotovic & Wijnen (2016) was updated to take into account the results of this work (Figure 8.2). This plot is in M_2 vs q parameter space, with regions (grey) that are theoretically prohibited due to constraints put on M_1. The dark grey prohibited region in the bottom right of Figure 8.2 is an upper mass limit on M_1, resulting from the Chandrasekhar mass limit of a white dwarf ($1.44\,\mathrm{M}_\odot$). The light grey prohibited region is a lower mass limit on M_1 and is a consequence of the dynamical stability limit on q supplied by the eCAML model. Also plotted in Figure 8.2 are systems with measured M_2 and q, either from this work (green points) or elsewhere (black/blue points; see Table D.1). These systems with measured system parameters provide a test of the eCAML model, as all should lie within the valid region (white). Any systems lying inside the prohibited dynamically unstable region would compromise the credibility of the model.

All systems modelled in this work lie comfortably within the valid region of Figure 8.2, along with the vast majority of other systems. Two appear to (just) violate the dynamical instability constraint, namely SDSS 0756+0858 (Tovmassian et al., 2014) and DQ Her (Horne, Welsh & Wade, 1993), however both systems could feasibly be valid taking into account their errors. This outcome offers support to the validity of the eCAML model as a solution to the CV white dwarf mass problem, however a much larger sample of systems with precise system parameters is necessary in order to provide a more stringent test of the model.

8.3 Reviewing the Properties of the Period Spike

The period spike (Section 1.4.5) was discovered by Gänsicke et al. (2009) through analysing the orbital period distribution of newly identified CVs from SDSS (York et al., 2000). These systems were all identified spectroscopically (e.g. Szkody et al. 2002), and therefore not affected by the same biases/limitations as systems discov-

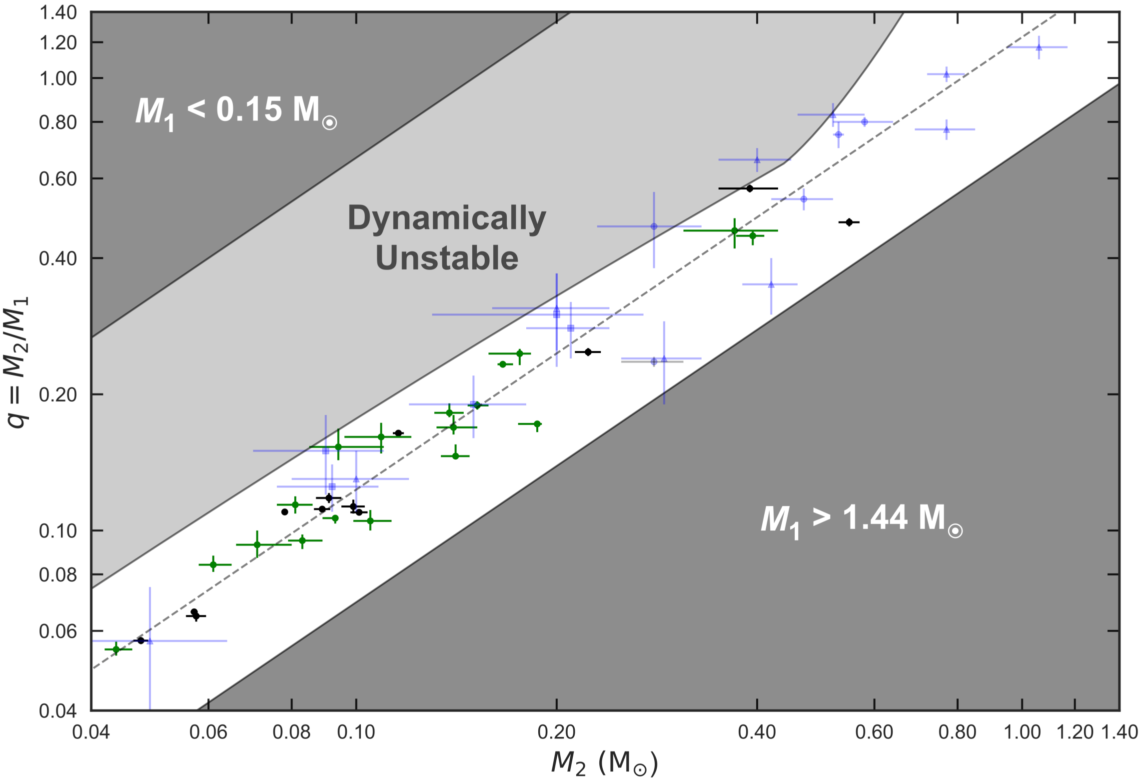

Figure 8.2: q vs M_2 plot for CVs. The grey regions are theoretically prohibited due to constraints put on M_1. The dark grey regions cover unrealistically low white dwarf masses ($\lesssim 0.15\,\mathrm{M}_\odot$) and masses greater than the Chandrasekhar mass limit ($1.44\,\mathrm{M}_\odot$), while the light grey region is forbidden by the empirical consequential angular momentum loss (eCAML) model of Schreiber, Zorotovic & Wijnen (2016). The dashed grey line represents the mean value of M_1 from this work (see Section 8.2). The data point colour/shape scheme is the same as in Figure 8.1.

ered through other means, e.g. DN outbursts and X-ray emission (see Gänsicke et al. 2009 for more details). Spectroscopic identification, coupled with a survey depth of $g' \sim 19.5$, gives this particular sample the ability to provide the closest representation of the true orbital period distribution of CVs to date, a claim supported by the emergence of the long predicted-but-elusive period spike at the period minimum. Gänsicke et al. (2009) produced estimates for the location (82.4 ± 0.7 min) and width (FWHM = 5.7 min) of the period spike, however the findings of Section 4.4.3 provide possible evidence that these estimates may be incorrect. Eight years on, the sample has increased and more $P_{\rm orb}$ measurements have become available, enabling the orbital period distribution – and in particular the properties of the period spike – to be reviewed.

The Gänsicke et al. (2009) sample consisted of 49 spectroscopically-identified SDSS CVs below the period gap ($P_{\rm orb} \lesssim 129$ min; Knigge 2006) with precise $P_{\rm orb}$ measurements (errors < 30 s). Precise $P_{\rm orb}$ measurements for an additional 23 systems (and updated measurements for a handful from the original sample) have since become available, increasing the sample to 72 systems[4]. Of the new systems, six are eclipsing systems with observations in the ULTRACAM/ULTRASPEC data archive[5], 10 are from Thorstensen et al. (2015, 2017) and the remaining seven are from the Ritter & Kolb (2003) catalogue (v7.24) (see references within). All systems were discovered by the SDSS (e.g. Szkody et al. 2011) except two, PHL 1445 (Chapter 4) and CSS110113[6] (Chapter 7), which were discovered by the 6dF Galaxy Survey (6dFGS; Jones et al. 2004).

Figure 8.3 shows the orbital period distribution of all 72 spectroscopically-identified CVs in the form of both a histogram (red) and cumulative plot (blue). As with the Gänsicke et al. (2009) sample (dark red histogram), the new sample shows a clear accumulation of systems centred around ~ 82 min, which is clearly

---

[4] As with Gänsicke et al. (2009), known AM CVn systems were not considered.

[5] Including PHL 1445 (Chapter 4) and SDSS 1057 (Chapter 6).

[6] System re-discovered by CTRS (Drake et al., 2009) at a later date.

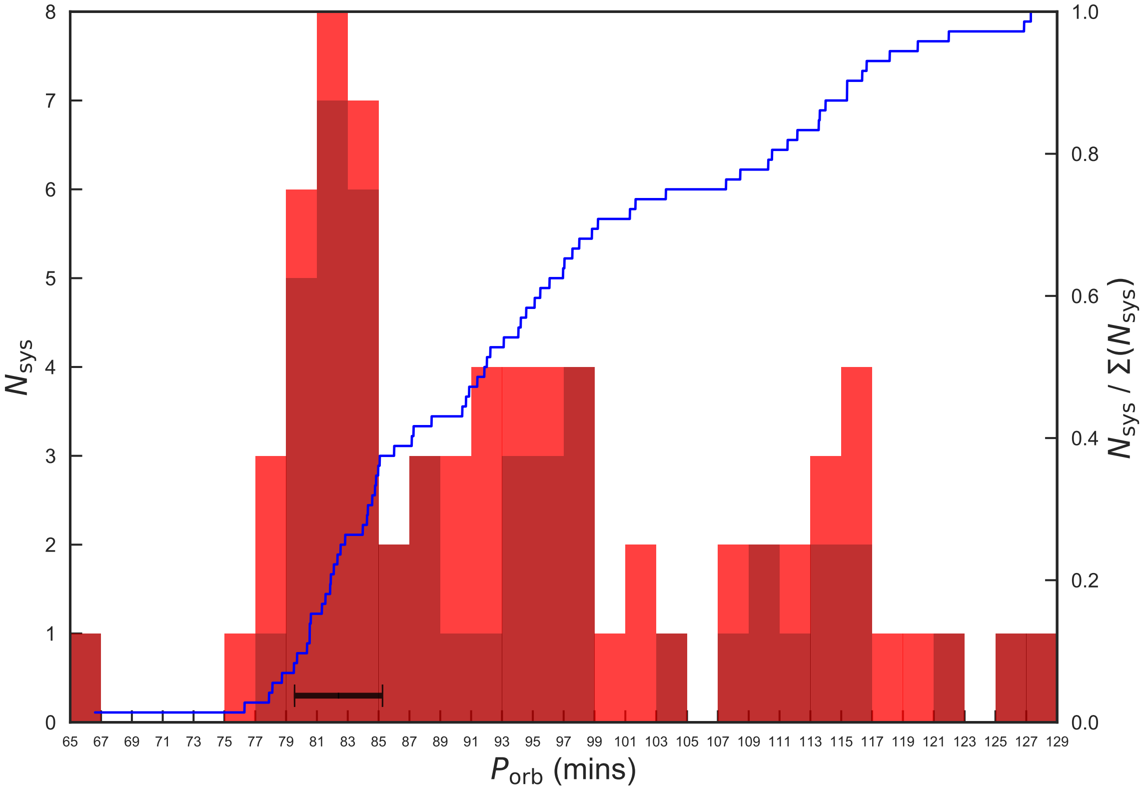

Figure 8.3: Histogram (red) and cumulative plot (blue) for 72 spectroscopically-identified (from SDSS and 6dFGS) CVs below the period gap with precise $P_{\rm orb}$ measurements (sub-30 s errors). For comparison, the existing sample of Gänsicke et al. (2009) is also shown (dark red histogram), in addition to the position and FWHM of an existing estimate of the period spike from the same study (black bar).

identifiable as the period spike. Estimating $P_{\rm spike}$ involved the fitting of a Gaussian distribution[7] to the orbital period distribution between 77 and 87 min. An estimate of $P_{\rm spike} = 82.7 \pm 0.4\,{\rm min}$ ($\sigma = 2.35\,{\rm min}$, FWHM $= 5.53\,{\rm min}$) was obtained, which is largely unchanged from the Gänsicke et al. (2009) sample. This is not surprising, as the majority ($\sim 75\%$) of additional systems have $P_{\rm orb} > 89\,{\rm min}$, and therefore do not belong to the period spike.

While it is reasonably clear that the period spike peaks between 82–83 min, a larger sample is required in order to further probe its structure. There are approximately 100 additional below-gap systems discovered by SDSS that have yet to have their orbital periods precisely measured (Szkody et al., 2011), and therefore obtaining $P_{\rm orb}$ for these systems should be a high priority. Also, a large number of CVs are expected to be discovered spectroscopically by Gaia (Gilmore et al., 2012) over the next few years, which will expand the available sample. Further discussion of the period spike and period minimum can be found in Section 8.7.1.

8.4 Updating the Calibration of the $\epsilon(q)$ Relation

The $\epsilon(q)$ relation for CVs was introduced in Section 1.5.2, along with an existing calibration from Knigge (2006) (equation 1.27, Figure 1.5). From this current work and the work of others (e.g. Savoury et al. 2011), new potential calibration systems have emerged, in addition to revised q values for existing calibration systems. Revised superhump periods ($P_{\rm sh}$) – required for calculating ϵ (equation 1.26) – have also been measured, courtesy of the SU UMa-type DNe survey of Kato et al. (2009, 2010, 2012, 2013, 2014b,a, 2015, 2016, 2017). With all of these new measurements becoming available since the work of Knigge (2006), it was appropriate to update the calibration of the $\epsilon(q)$ relation.

---

[7] Assuming the period spike has a Gaussian distribution, which may not be the case.

System	$P_{\rm orb}$ (d)	$P_{\rm sh}^{\rm B}$ (d)	$P_{\rm sh}^{\rm C}$ (d)	Ref.(s)
SDSS 1507	0.04625828(4)	0.046825(4)	–	1,2
SSS100615*	0.0587045(4)§	0.05972(9)	–	3
SDSS 1502	0.05890961(5)	0.060463(13)	0.060145(19)	1,4
SDSS 0903	0.059073543(9)	0.06036(5)	0.06007(5)	1,4
ASASSN-14ag*	0.060310665(9)§	0.06206(6)	–	5
XZ Eri	0.061159491(5)	0.062807(18)	0.06265(12)	1,6
SDSS 1227	0.062959041(7)	0.064604(29)	0.06440(5)	1,7
OY Car*	0.06312092545(24)§	0.064653(28)	0.06444(5)	8
SSS130413*	0.0657692903(12)§	–	0.06751(24)	5
CSS110113*	0.0660508707(18)§	0.067583(26)	0.06731(4)	7
SDSS 1152*	0.0677497026(3)§	0.07036(4)	0.069914(19)	8
OU Vir	0.072706113(5)	0.074912(17)	–	1,6
IY UMa*	0.07390892818(21)§	0.076210(25)	0.075729(19)	4
Z Cha*	0.0744992631(3)§	0.07736(8)	0.076948(23)	5
SDSS 0901*	0.0778805321(5)§	0.08109(5)	0.08072(10)	9
DV UMa*	0.0858526308(7)§	0.08880(3)	0.08841(3)	6
SDSS 1702	0.10008209(9)	0.10507(8)	–	1,6
WZ Sge	0.0566878460(3)	0.057204(5)	–	6,10
V2051 Oph	0.06242785751(8)§	0.06471(9)	0.06414(4)	5,11
HT Cas	0.0736471745(5)§	0.076333(5)	0.075886(5)	3,12
V4140 Sgr	0.0614296779(9)	0.06351(4)	0.06309(7)	6,11
V348 Pup	0.101838931(14)	0.108567(2)†	–	13
V603 Aql	0.13820103(8)	0.14686(7)†	–	14,15
DW UMa	0.136606499(3)	0.14539(13)†	–	16,17
UU Aqr	0.1638049430	0.17510(18)†	–	18,19

Table 8.1: Orbital ($P_{\rm orb}$) and superhump ($P_{\rm sh}$) periods of the systems used to calibrate the $\epsilon(q)$ relation. The majority of systems are SU UMa-type DNe, however the bottom four are CNe/NLs. $P_{\rm sh}^{\rm B}$ and $P_{\rm sh}^{\rm C}$ are the periods for stage B and C superhumps, respectively. See Tables 5.1, 7.1 and D.1 for q values. References: (1) Savoury et al. (2011), (2) Patterson et al. (2017), (3) Kato et al. (2016), (4) Kato et al. (2010), (5) Kato et al. (2015), (6) Kato et al. (2009), (7) Kato et al. (2012), (8) Kato et al. (2017), (9) Kato et al. (2013), (10) Patterson (1998), (11) Baptista et al. (2003), (12) Horne, Wood & Stiening (1991), (13) Rolfe, Haswell & Patterson (2000), (14) Peters & Thorstensen (2006), (15) Patterson et al. (1997), (16) Araujo-Betancor et al. (2003), (17) Patterson et al. (2002), (18) Baptista & Bortoletto (2008), (19) Patterson et al. (2005).

*Updated q value produced in this work (Tables 5.1 and 7.1), †Superhump period from permanent superhumps, $^§P_{\rm orb}$ from this work

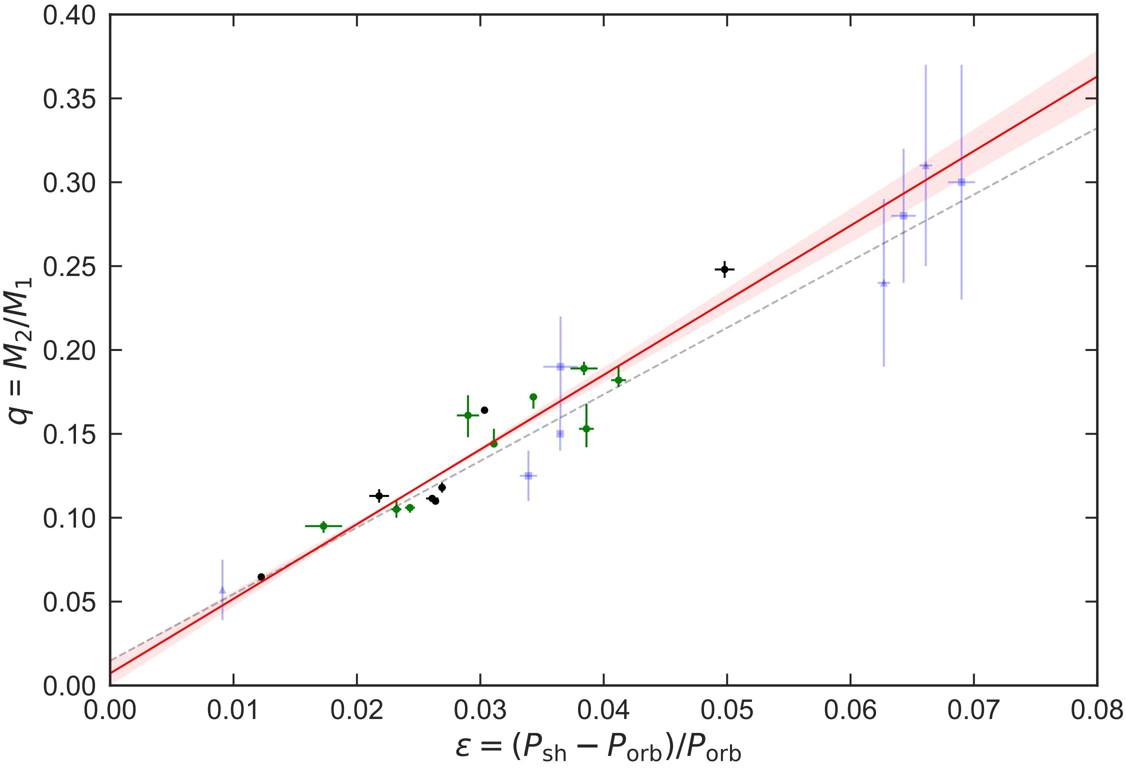

Figure 8.4: Measured $\epsilon_{\rm B}$ and q values of superhumping and eclipsing[9] CVs, with the same data point colour/shape scheme as Figure 8.1. The dashed grey line shows the existing linear calibration of the $\epsilon(q)$ relation for superhumping CVs from Knigge (2006) (see Figure 1.5), while the red line shows an updated calibration for stage B superhumps from this work. The red shaded region represents 1σ errors.

Table 8.1 contains all of the calibrating systems currently available[8], along with their orbital and superhump periods (and references). The two superhump period columns, $P_{\rm sh}^{\rm B}$ and $P_{\rm sh}^{\rm C}$, represent the superhump periods during stage B and stage C of superoutburst, respectively (see Section 1.5.2 for more details). All but the final four systems in Table 8.1 are SU UMa-type DNe that undergo superoutbursts. The other four systems are either CNe or NLs that display permanent superhumps, and it is assumed these superhump periods resemble those of $P_{\rm sh}^{\rm B}$ for SU UMa-type DNe.

For each system, the periods listed in Table 8.1 were input into equation 1.26 to produce values of $\epsilon_{\rm B}$ and $\epsilon_{\rm C}$ (depending on $P_{\rm sh}^{\rm B}/P_{\rm sh}^{\rm C}$ availability). Figure 8.4 shows $\epsilon_{\rm B}$ plotted against q (see Tables 5.1, 7.1 and D.1) for the 24 calibration systems from Table 8.1 with available $P_{\rm sh}^{\rm B}$ measurements. The dashed grey line shows the existing

---

[8] The calibration system KV UMa used by Knigge (2006) was not included on the basis of it being a low-mass X-ray binary, rather than a CV.

[9] With the exception of V603 Aql.

calibration from Knigge (2006), while the red line represents the following, updated linear calibration:

$$q(\epsilon_{\rm B}) = (0.118 \pm 0.003) + (4.45 \pm 0.28) \times (\epsilon_{\rm B} - 0.025). \tag{8.1}$$

This updated calibration was obtained through the same χ^2 minimisation technique employed by Knigge (2006) (see Appendix A of reference), and infers an intrinsic dispersion (σ) of 0.012. While there is good coverage for systems with $0.1 < q < 0.2$, more calibration systems with q outside this range are required in order to further constrain the gradient. For example, due to its position in Figure 8.4, SDSS 1702 ($q \approx 0.25$) has a rather large influence on the gradient, so therefore more systems with precisely measured values of q greater than 0.2 are highly coveted. Unfortunately, this includes period gap systems, which are rare, and systems above the gap, for which precise measurements of q are hard to obtain. It is clear from Figure 8.4 that the new calibration has a steeper gradient that the existing one from Knigge (2006). A possible reason for this is the variation in measurement of $P_{\rm sh}$ between Patterson et al. (2005) and Kato et al. (2009); the sources of $P_{\rm sh}$ for both the existing and new calibration, respectively. As mentioned in Section 1.5.2, Patterson et al. (2005) measures $P_{\rm sh}$ from 'common' superhumps, which typically cover stage B, but can also cover only a fraction of this stage or spread into stages A and C.

The same treatment was given to the 15 calibration systems in Table 8.1 with available $P_{\rm sh}^{\rm C}$ measurements, producing the following linear relation (with $\sigma = 0.012$ again inferred):

$$q(\epsilon_{\rm C}) = (0.135 \pm 0.004) + (5.0 \pm 0.7) \times (\epsilon_{\rm C} - 0.025). \tag{8.2}$$

8.5 Donor Masses and Radii of Superhumping CVs

Section 1.5.3 began with an explanation of how the parameters of the donor within a superhumping system can be inferred, just from knowledge of the system's $P_{\rm sh}$ and $P_{\rm orb}$. Donor properties were derived for each system in a sample of superhumping CVs by Patterson et al. (2005), and subsequently revised by Knigge (2006) and Knigge, Baraffe & Patterson (2011). This work has produced an updated $\epsilon(q)$ calibration (Section 8.4) and $\langle M_1 \rangle$ (Section 8.2), making it possible to further refine the donor parameters for each of the 78 systems in the Patterson et al. (2005) superhumper sample.

Firstly, $P_{\rm sh}$ values for all SU UMa-type DNe in the Patterson et al. (2005) sample (70 systems) were replaced by $P_{\rm sh}^{\rm B}$ measurements from the SU UMa-type DNe survey of Kato et al. (2009, 2010, 2012, 2013, 2014b,a, 2015, 2016, 2017). For a number of systems, $P_{\rm orb}$ was also updated, either from measurements made by Kato et al., or additional studies (see references within Kato et al.). Values of $\epsilon_{\rm B}$ were obtained from $P_{\rm sh}^{\rm B}$ and $P_{\rm orb}$ through equation 1.26, then subsequently converted into q via the newly calibrated $\epsilon_{\rm B}(q)$ relation (equation 8.1)[10]. Assuming a constant white dwarf mass of $\langle M_1 \rangle = 0.812\,{\rm M}_\odot$, donor mass estimates were obtained for all systems in the superhumper sample.

As the donor fills its Roche lobe, the Eggleton (1983) approximation for the volume-averaged Roche lobe size (equation 1.3) – combined with Kepler's 3rd law (equation 1.1) – can be used to obtain estimates for donor radii from q, M_2 and $P_{\rm orb}$:

$$\frac{R_2}{{\rm R}_\odot} = 0.2478 \left(\frac{M_2}{{\rm M}_\odot}\right)^{1/3} P_{\rm orb}^{2/3} \left[\frac{q^{1/3}(1+q)^{1/3}}{0.6q^{2/3} + \ln(1+q^{1/3})}\right], \tag{8.3}$$

where $P_{\rm orb}$ is in units of hrs. The Eggleton (1983) approximation for the volume-

---

[10] Equation 8.1 was also used to determine q for the eight systems displaying permanent superhumps.

averaged Roche lobe size is the same one used to determine R_2 for systems that have been eclipse modelled (see Section 3.7.2), establishing consistency between the superhumper and eclipsing samples (important for following Section). It is important to note that Knigge, Baraffe & Patterson (2011) use a more complex, accurate approximation for the volume-averaged size of the Roche lobe based on the results of Sirotkin & Kim (2009), which represents the donor as a polytrope, rather than a point source. However, the advantage of using the Sirotkin & Kim (2009) approximation is minimal, with only a $\sim 1\%$ difference between the two approximations (Figure 3 of Knigge, Baraffe & Patterson 2011).

In addition to the 78 superhumper sample from Patterson et al. (2005), Kato et al. provide $P_{\rm sh}^{\rm B,C}$ and $P_{\rm orb}$ values for a further 147 systems. These systems were given the same treatment as the Patterson et al. (2005) sample (outlined above)[11], bringing the total number of superhumping systems with inferred donor properties to 225.

8.6 Updating the Semi-Empirical Mass-Radius Relation for CV Donor Stars

With donor masses and radii for 18 eclipsing systems obtained from this work, a further 31 (mostly) eclipsing systems from the literature (see Table D.1) and 225 superhumpers, it was possible to update the mass-radius relation for CV donor stars from Knigge (2006) (revised in Knigge, Baraffe & Patterson 2011) that was introduced in Section 1.5.3. As shown by equation 1.28 and Figure 1.6, the donor mass-radius relation is in the form of a broken-power-law split covering three separate regions: long period (above period gap) systems, short period (below period gap) systems and period-bouncers. The same fitting procedure used by Knigge, Baraffe & Patterson (2011) (outlined in detail within Appendix C of Knigge 2006) was followed

---

[11] A handful of systems only have available $P_{\rm sh}^{\rm C}$ values, in which case equation 8.2 was used.

to update the mass-radius relation. Assumptions for the donor mass within the period gap $M_{\rm conv}$, and upper $P_{\rm gap,+}$ and lower $P_{\rm gap,-}$ bounds of the period gap from Knigge, Baraffe & Patterson (2011) remained unchanged, although an alternative value for $P_{\rm min}$ was chosen:

$$\begin{array}{lll} M_{\rm bounce} = 0.063\,^{+0.005}_{-0.002}\,{\rm M}_{\odot}, & M_{\rm conv} = 0.20 \pm 0.02\,{\rm M}_{\odot}, & M_{\rm evol} \simeq 0.6{-}0.8\,{\rm M}_{\odot}. \\ P_{\rm min} = 76.3 \pm 1.0\,{\rm min}, & P_{\rm gap,-} = 2.15 \pm 0.03\,{\rm hrs}, & P_{\rm gap,+} = 3.18 \pm 0.04\,{\rm hrs}. \end{array}$$

Knigge, Baraffe & Patterson (2011) used the location of the period spike from Gänsicke et al. (2009) for $P_{\rm min}$, claiming it to be the best available estimate. Here, however, the absolute minimum period possible for a main sequence CV is considered to be a more suitable option. The rationale behind this choice is linked to the fact that the continuous period bounce feature in the evolutionary donor sequence is fit with just two separate power laws. The intersection between the two power laws should, as a consequence, occur at an M_2-R_2 pairing that corresponds to an orbital period slightly shorter than the real $P_{\rm min}$. PHL 1445 (Chapter 4) is expected to be close to the absolute minimum period for main sequence CVs, and so its orbital period of 76.3 min is used for $P_{\rm min}$ here. The value of $M_{\rm bounce}$ shown above was determined from the optimal short-period fit[12].

The short- and long-period optimal power law fits were carried out through the minimisation of the χ^2 statistic shown in equation C9 of Knigge (2006), which takes into account both the intrinsic dispersion in radii ($\sigma_{\rm int}$) and systematic errors. The systematic error term was removed for the period-bouncer fit, following the warning of Knigge, Baraffe & Patterson (2011) that its inclusion may produce unphysical results. The donor masses and radii for all but 12 systems were included in the fits. The majority of these systems were excluded due to being period gap systems (see grey box in bottom plot of Figure 8.5), while SDSS 1507 (outlying black data point in period bouncer regime) was excluded as it is known to be a Galactic halo object

---

[12] The value of $M_{\rm bounce}$ determines the number of data points included in the short-period fit.

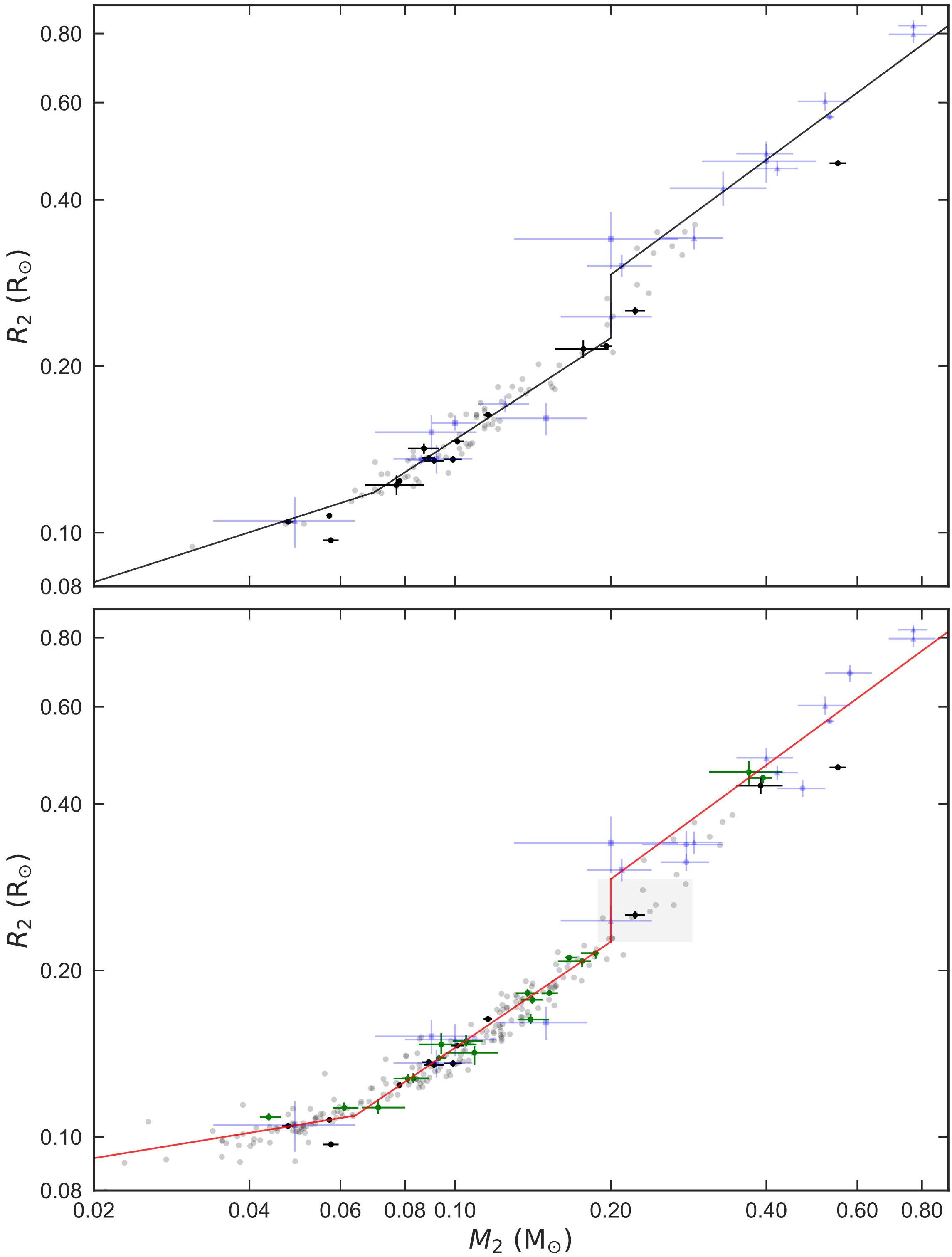

Figure 8.5: Measured CV donor masses (M_2) and radii (R_2), both before (top) and after (bottom) this work. The data point colour/shape scheme is the same as in Figure 8.1, but with additional superhumping systems (grey points), for which error bars have been omitted for clarity. The black line in the top plot is the optimal mass-radius relation (broken-power-law fit) from Knigge, Baraffe & Patterson (2011) (see Figure 1.6, equation 1.28). The red line in the bottom plot is an updated version of the mass-radius relation from this work (equation 8.4). The grey shaded region contains systems assumed to lie within the period gap, and are therefore not included in the updated broken-power-law fit.

(Patterson, Thorstensen & Knigge, 2008; Uthas et al., 2011). The results from the three power law fits are shown in the bottom plot of Figure 8.5 (red line), and take the following form:

$$\frac{R_2}{\mathrm{R}_\odot} = \begin{cases} 0.109 \pm 0.003 \left(\frac{M_2}{M_{\mathrm{bounce}}}\right)^{0.152\pm0.018} & M_2 < M_{\mathrm{bounce}} \\ 0.225 \pm 0.008 \left(\frac{M_2}{M_{\mathrm{conv}}}\right)^{0.636\pm0.012} & M_{\mathrm{bounce}} < M_2 < M_{\mathrm{conv}} \\ 0.293 \pm 0.010 \left(\frac{M_2}{M_{\mathrm{conv}}}\right)^{0.69\pm0.05} & M_{\mathrm{conv}} < M_2 < M_{\mathrm{evol}}. \end{cases} \quad (8.4)$$

Comparing these results with those of Knigge, Baraffe & Patterson (2011) (top plot in Figure 8.5 and equation 1.28), it is apparent that there is little change in the exponents of the mass-radius relation in both the long- and short-period regimes. One notable difference, however, is the amount of σ_{int} required for the short-period systems, reduced from approximately $0.02\,\mathrm{R}_\odot$ to $0.005\,\mathrm{R}_\odot$. The minimal scatter is further evidence for a very constrained evolutionary path followed by non-evolved CV donors. The scatter within the long-period regime, at $0.04\,\mathrm{R}_\odot$, is almost a factor of 10 larger than that at short periods, but this is still relatively constrained. The bottom plot of Figure 8.5 shows two outlying long-period systems with $R_2 \simeq 0.40\,\mathrm{R}_\odot$, namely IP Peg (Copperwheat et al., 2010) and HS 0220+0603 (Rodríguez-Gil et al., 2015). The donors within these two systems are undersized for their masses, and may even be in thermal equilibrium, which is unexpected for a CV donor. It is possible that both IP Peg and HS 0220+0603 have donors in thermal equilibrium due to recently starting mass transfer.

The mass-radius relation for period-bouncers, on the other hand, has changed significantly. The new power law exponent of 0.152 ± 0.018 is much smaller than that of Knigge, Baraffe & Patterson (2011), a consequence of using lower values for both M_{bounce} and P_{min}, in addition to the inclusion of many more period-bouncers in the new donor sample, which enables a better constraint of the power law in this regime.

8.7 Semi-Empirical Donor-Based CV Evolution Tracks

In addition to a broken-power-law mass-radius relation for CV donors, Knigge, Baraffe & Patterson (2011) present a semi-empirical evolutionary track, produced with the aim of quantifying the secular mass transfer rate in CVs (see Section 1.5.4). The track resulting from a fit to their donor sample requires reduced magnetic braking above the gap ($f_{\rm MB} = 0.66 \pm 0.05$), but additional angular momentum loss below the gap that gravitational radiation alone cannot account for ($f_{\rm GR} = 2.47 \pm 0.22$). The best-fit track in the M_2-R_2 and $P_{\rm orb}$-M_2 planes is shown by the red lines in Figures 8.6 and 8.7, respectively. Also shown for comparison is the 'standard' track (black lines), which has values of $f_{\rm GR} = f_{\rm MB} = 1$. Updating the existing best-fit track to accommodate the new data available is beyond the scope of this work, however it is of interest to see if the existing track still provides a good fit to the current donor sample.

Focussing firstly on the M_2-R_2 plane, the bottom plot in Figure 8.6 shows both the best-fit and standard tracks overlaid onto the current donor sample. With only minor changes to the donor sample above the period gap, it is no surprise that the best-fit track continues to provide a good representation of the data. Below the gap, where the donor sample has increased substantially, the best-fit track appears to slightly overestimate the donor radius for a given mass. This is particularly evident for donor masses in the range 0.10–0.20 $\rm M_{\odot}$, and implies a lower amount of additional angular momentum loss is required than the 2.47 × GR originally suggested by Knigge, Baraffe & Patterson (2011).

Inconsistencies between the evolutionary tracks and the current donor sample below the period gap are more apparent in the $P_{\rm orb}$-M_2 plane, which is shown in the bottom plot in Figure 8.7. It is clear that the best-fit track (red line) slightly under predicts the donor mass at all orbital periods below the period gap, and

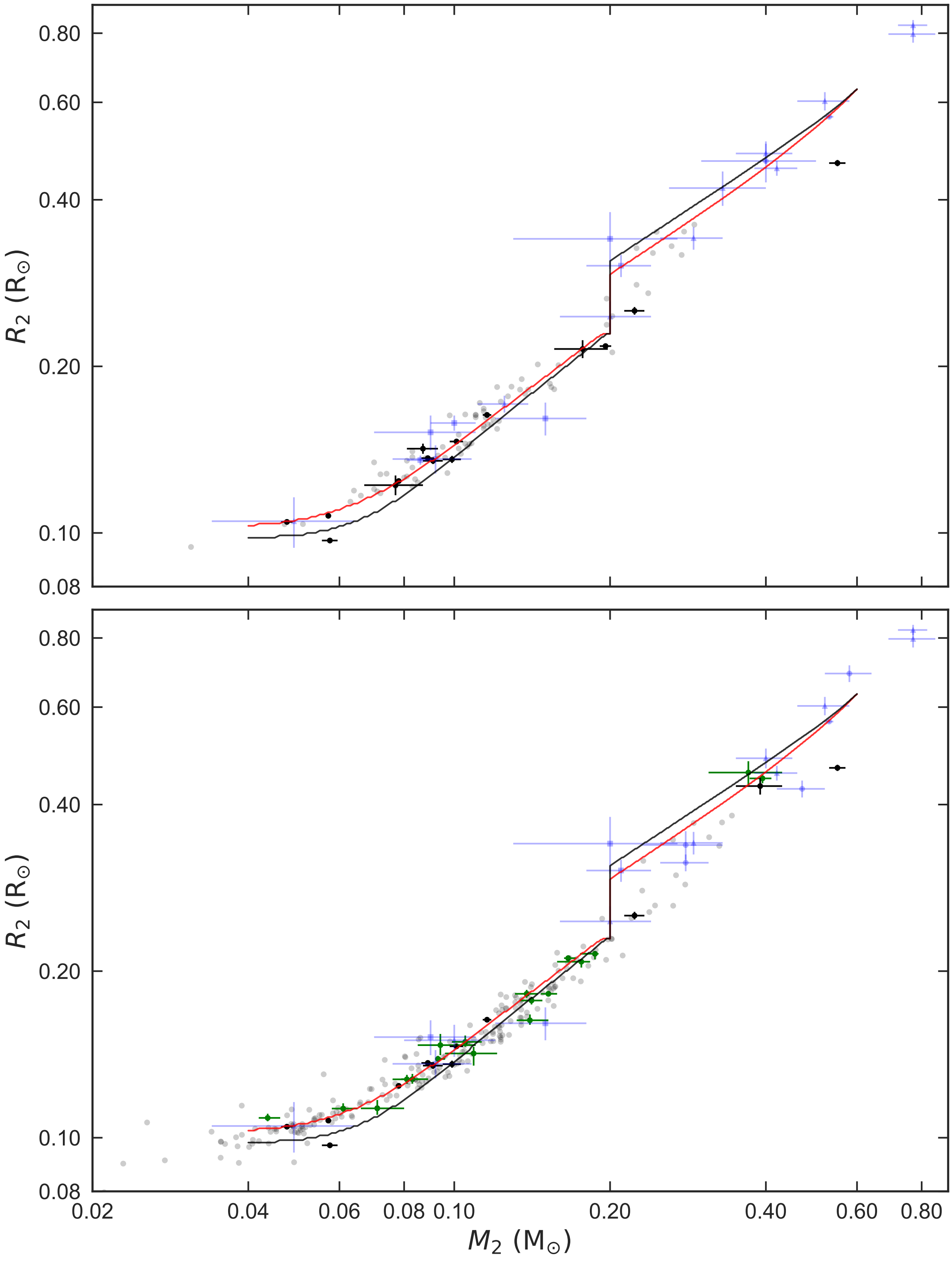

Figure 8.6: Measured CV donor masses (M_2) and radii (R_2), both before (top) and after (bottom) this work. The data point colour/shape scheme is the same as in Figure 8.5. The red and black lines represent the best-fit ($f_{\mathrm{GR}} = 2.47 \pm 0.22$, $f_{\mathrm{MB}} = 0.66 \pm 0.05$) and 'standard' ($f_{\mathrm{GR}} = f_{\mathrm{MB}} = 1$) evolutionary tracks from Knigge, Baraffe & Patterson (2011), respectively.

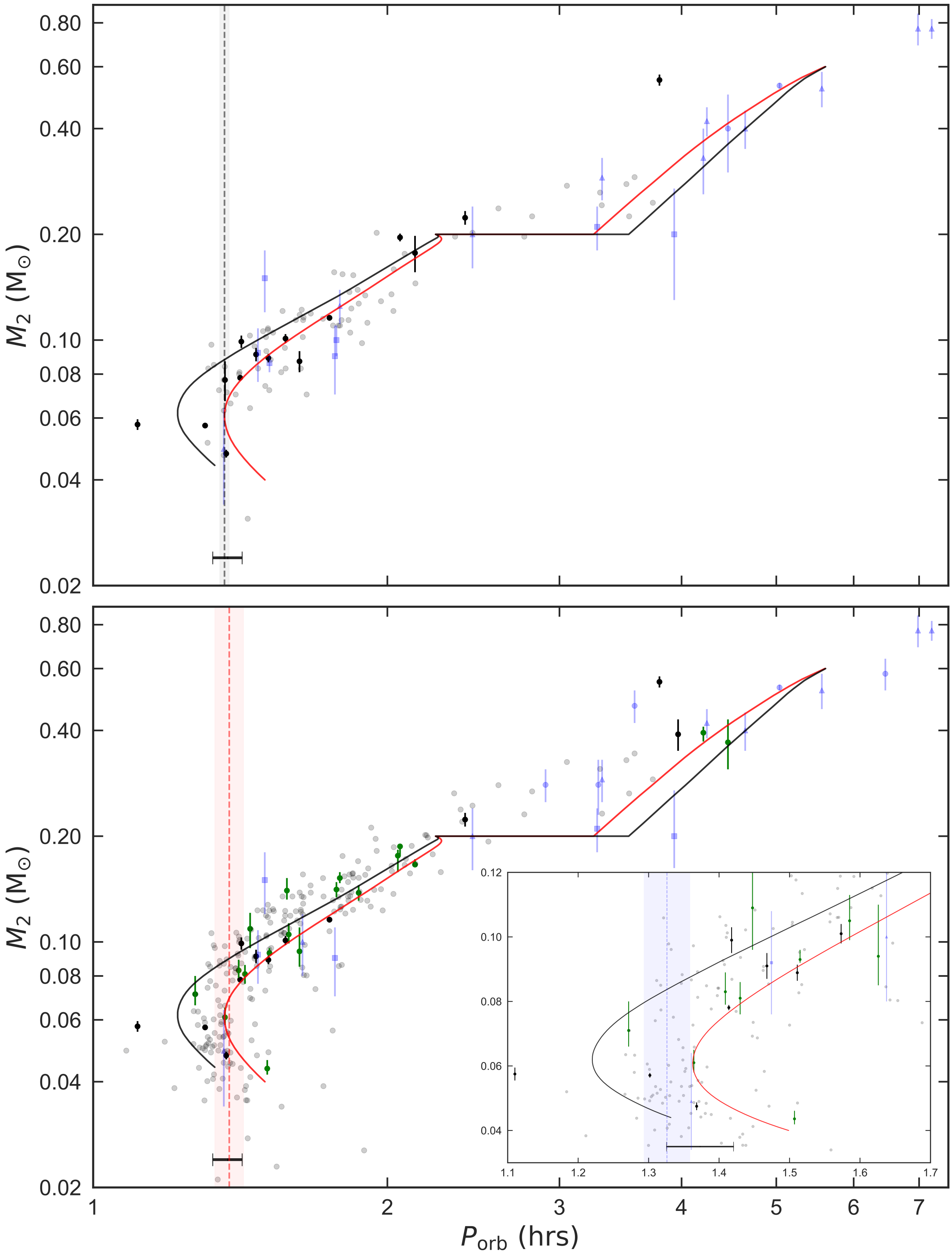

Figure 8.7: Measured CV donor masses (M_2) as a function of orbital period ($P_{\rm orb}$), both before (top) and after (bottom) this work. The data point colour/shape scheme is the same as in Figure 8.5. The red and black lines represent the best-fit ($f_{\rm GR} = 2.47 \pm 0.22$, $f_{\rm MB} = 0.66 \pm 0.05$) and 'standard' ($f_{\rm GR} = f_{\rm MB} = 1$) evolutionary tracks from Knigge, Baraffe & Patterson (2011), respectively. The vertical dashed black line and shaded region in the top plot show the inferred location of $P_{\rm min}$ (and error) from the best-fit track. The vertical dashed red line and shaded region in the bottom plot show the location of $P_{\rm spike}$ (and FWHM) from Section 8.3. The bar across the bottom of each plot shows the location and FWHM of $P_{\rm spike}$ determined by Gänsicke et al. (2009). *Inset:* Close-up of short period region. The vertical dashed blue line and shaded region is an estimate of the true $P_{\rm min}$ (see text for details).

appears to project a period minimum that is longer than observed (see Section 8.7.1 for further discussion about the period minimum). This again implies that less additional angular momentum loss is needed below the period gap than originally anticipated by Knigge, Baraffe & Patterson (2011).

Interestingly, the standard track (black line), which represents solely GR-driven evolution below the gap ($f_{\mathrm{GR}} = 1$), provides a seemingly good fit to the data for masses between 0.10–0.20 $\mathrm{M}_{\odot}$, before diverging and predicting a period minimum well below what is observed. This is possible evidence for limited residual magnetic braking below the period gap, but with the existence an additional source of angular momentum loss that only comes into effect when the donor's mass falls below $\simeq 0.10\,\mathrm{M}_{\odot}$. Alternatively, it may be the case that the assumed mass of a donor at the lower edge of the period gap ($M_{\mathrm{conv}} = 0.20 \pm 0.02\,\mathrm{M}_{\odot}$; Knigge 2006) is too low, and a larger M_{conv} is required to shift the evolutionary tracks below the gap to higher masses and into better agreement with the data. However, this would also have the effect of shifting the location of the predicted lower edge of the period gap towards longer periods, and further away from the observed lower edge of the period gap (2.15 hrs; Knigge 2006). It is evident that further precise donor masses for CVs across the entire short-period regime are needed to gain a better comprehension of the angular momentum loss mechanisms that drive CV evolution below the period gap.

8.7.1 The Period Minimum

It is apparent from the bottom plot and inset of Figure 8.7 that the current donor sample contains a sufficiently large number of systems at the shortest orbital periods to finally begin to reveal the configuration of the period minimum regime. The period minimum feature of the current donor sample appears to cover an approximate period range of 76–82 min (1.27–1.37 hrs). Fitting a Gaussian distribution to the donor sample within this period range returned the following estimates for both the period minimum ($P_{\rm min} = 79.57 \pm 0.22\,{\rm min}$) and its width (FWHM $= 3.90\,{\rm min}$). These estimates for $P_{\rm min}$ and its width are shown by the blue vertical dashed line and shaded area within the inset of the bottom plot of Figure 8.7, respectively.

It was briefly mentioned in the previous Section that the observed location of the period minimum appears to be slightly lower than predicted by the best-fit track of Knigge, Baraffe & Patterson (2011) ($P_{\rm min} = 81.8 \pm 0.9\,{\rm min}$). The new measurement of $P_{\rm min}$ from the donor sample confirms this, with the two $P_{\rm min}$ estimates differing by approximately 2.4σ. Recall that a lower value of $P_{\rm min}$ than the existing estimate of Knigge, Baraffe & Patterson (2011) was previously hinted at in Section 4.4.3. The inset of Figure 8.7 shows that with the new estimate for $P_{\rm min}$, PHL 1445 ($P_{\rm orb} = 1.27\,{\rm hrs}$) and SDSS 1433 ($P_{\rm orb} = 1.30\,{\rm hrs}$) are no longer troublesome outliers.

Interestingly, the period minimum of the donor sample does not appear to exactly coincide with the (slightly longer) estimated locations of the period spike from both Gänsicke et al. (2009) ($82.4 \pm 0.7\,{\rm min}$; black bar) and Section 8.3 of this work ($82.7 \pm 0.4\,{\rm min}$; red dotted line). One potential explanation for this relates to the curved shape/structure of the CV evolutionary track arising from period bounce. This particular morphology may cause the density of systems in the short-period regime to peak at an orbital period slightly longer than the period minimum. Alternatively, it may be the case that the predominantly-SDSS CV sample used to measure the period spike is not able to fully sample the period minimum population of CVs, a consequence of the SDSS only being reasonably complete down to a magnitude of $g \sim 19$. The majority of the period minimum systems in the current donor sample are superhumping systems, discovered during superoutburst by transient surveys such as ASAS-SN. The quiescent magnitudes of these systems are typically $g \sim 20$–22 (Kato et al., 2016, 2017), which is within the magnitude limit of the SDSS ($g \sim 22.5$), but a magnitude range where the SDSS is far from complete.

Chapter 9

Conclusions and Future Work

9.1 Conclusions

This thesis has presented a new approach to modelling CV eclipse light curves, which for the first time enables multiple eclipses of the same system to be modelled simultaneously (whilst sharing intrinsic model parameters, e.g. q), and attempts to model flickering – rather than reduce it through eclipse averaging – with the help of Gaussian processes (GPs).

The new model fitting approach was used on 18 eclipsing CV systems in total. All eclipse light curves used for model fitting were acquired with the high-speed imaging cameras ULTRACAM and ULTRASPEC. Both cameras provide sufficient high-time-resolution for resolving the separate white dwarf and bright spot components of an eclipse, which is an essential requirement for eclipse modelling.

PHL 1445, an eclipsing CV with an orbital period approximately ~ 5 min below the current estimate for the period minimum (81.8 ± 0.9 min; Knigge, Baraffe & Patterson 2011), initially had its eclipse light curves modelled using the existing approach, prior to the development of the new approach. From the resulting system parameters, specifically the donor mass, it was determined that PHL 1445 is most likely a main sequence CV at its period minimum, although an evolved donor or brown dwarf donor from formation cannot be completely ruled out. If PHL 1445 is in fact a main sequence CV, this is possible evidence for the current estimate of the period minimum being incorrect. PHL 1445's individual eclipse light curves, all containing large amounts of flickering, were later re-modelled, this time using the newly developed modelling approach. The results from both approaches are found to produce similar system parameter values and errors.

The new modelling approach was given its first full test on eclipse light curves of the short-period CV ASASSN-14ag, which include a prominent bright spot, coupled with heavy flickering. As part of the testing procedure, the eclipse light curves were also modelled in accordance with the existing modelling approach, thereby providing the opportunity to compare the two approaches. The error associated with flickering determined from the existing approach is notably over-estimated compared to the errors from new approach. This is in contrast to the findings from the modelling of PHL 1445, where the existing and new approaches produce consistent results. One potential reason for this discrepancy is the sizeable difference in prominence and complexity of the bright spot within these two systems.

SDSS 1057, an eclipsing candidate period-bounce system with orbital period $\sim 90\,\mathrm{min}$, was also modelled using the new approach. The donor mass obtained from eclipse modelling, $M_2 = 0.0436 \pm 0.0020\,\mathrm{M}_{\odot}$, is the lowest yet measured in an eclipsing CV, and strongly suggests that SDSS 1057's is in fact a period-bounce CV. Interestingly, the temperature of the white dwarf, $T_1 = 13300 \pm 1100\,\mathrm{K}$, obtained through fitting white dwarf atmosphere predictions to multi-colour white dwarf fluxes, is marginally higher than expected for a system in this evolutionary phase ($T_1 < 10\,000\,\mathrm{K}$).

The other 15 eclipsing systems include four already modelled with the existing approach (CTCV 1300, DV UMa, SDSS 1152, SDSS 1501; Savoury et al. 2011) and 11 that are newly modelled (CSS080623, CSS110113, GY Cnc, IY UMa, OY Car, SDSS 0901, SDSS 1006, SSS100615, SSS130413, V713 Cep, Z Cha). Eclipse light curves of the short-period, white dwarf-dominated CV SDSS 1501 show a significant increase in white dwarf flux, and therefore T_1, between Jan 2010 and Sep 2012; thought to be the result of a poorly observed superoutburst in Sep 2010. The same system also shows $\pm 7\,\mathrm{s}$ departures from a linear ephemeris over $\sim 8\,\mathrm{yrs}$, which is unexpected for CV with a substellar donor ($M_2 = 0.061 \pm 0.004\,\mathrm{M}_\odot$) and warrants further investigation. An eclipse light curve of V713 Cep from Jun 2015 appears to show a considerably diminished accretion disc, which is indicative of a 'low state'; only the second to be observed in a short-period ($P_\mathrm{orb} \lesssim 2\,\mathrm{hrs}$) system to date.

The final portion of this work involves using the 18 new/revised sets of precise system parameters, together with system parameters for 30+ (mostly) eclipsing CV systems from the literature, to try and improve the current understanding of CVs and their evolution. A mean CV white dwarf mass of $0.812 \pm 0.020\,\mathrm{M}_\odot$ ($\sigma = 0.13\,\mathrm{M}_\odot$) was determined from the new sample, in agreement with the previous estimate of $0.82 \pm 0.03\,\mathrm{M}_\odot$ ($\sigma = 0.15\,\mathrm{M}_\odot$) from Zorotovic, Schreiber & Gänsicke (2011), and significantly greater than the mean white dwarf mass in the field of $0.621\,\mathrm{M}_\odot$ from Tremblay et al. (2016). No evidence for significant white dwarf mass growth in CVs was found, although further precise white dwarf masses are required before this can be completely discounted. None of the 18 systems modelled in this work were found to invalidate the empirical consequential angular momentum loss (eCAML) model developed by Schreiber, Zorotovic & Wijnen (2016) to try and explain the observed high white dwarf masses in CVs compared to in the field, thus giving further support to the model.

The method of using spectroscopically-identified CVs from the SDSS by Gänsicke et al. (2009) to uncover and quantify the period spike was repeated, in light of additional orbital period measurements now being available. The period spike remained largely unchanged following the new analysis, and found to be $P_\mathrm{spike} = 82.7 \pm 0.4\,\mathrm{min}$ (FWHM $= 5.53\,\mathrm{min}$).

The $\epsilon(q)$ relation for superhumping systems from Knigge (2006) was recalibrated, following an increase in the number of available calibrator systems. The $\epsilon(q)$ relation is well constrained for $q \simeq 0.1$–0.2 ($\epsilon \simeq 0.01$–0.04), but less so outside of this range due to a lack of calibrator systems. The new $\epsilon(q)$ calibration and mean CV white dwarf mass, were used to infer the donor masses and radii of 225 superhumping systems, which were then added to the 49 measured donor masses and radii from this work and literature to form the most comprehensive donor sample to date.

The new donor sample was used to update the semi-empirical mass-radius relation for CV donors from Knigge, Baraffe & Patterson (2011). The long- and short-period regimes remained largely unchanged, however the exponent of the relation in the period bouncer regime was significantly reduced. Standard and best-fit donor-based evolutionary tracks from Knigge, Baraffe & Patterson (2011) were then compared with the new donor sample in both R_2-M_2 and M_2-$P_{\rm orb}$ planes. It is apparent that less additional angular momentum loss is required in the short-period regime than the $2.47 \times$ GR prescribed by Knigge, Baraffe & Patterson (2011). However, further precise donor masses for CVs across the entire short-period regime are needed before the angular momentum loss mechanisms at work below the period gap can be fully understood.

The large number of period minimum systems – mostly superhumpers – in the new donor sample has finally began to reveal the structure of the period minimum. The period minimum is measured to be 79.57 ± 0.22 min (FWHM $= 3.90$ min), which is over 2 min shorter than the period minimum estimate of Knigge, Baraffe & Patterson (2011) (81.8 ± 0.9 min; obtained from their best-fit evolutionary track) and over 3 min shorter than the estimate of the period spike from this work (see above). The period spike may occur at a slightly longer orbital period than the period minimum due to the morphology of the CV evolutionary track. Alternatively, the SDSS sample used to measure the period spike may not be able to fully sample the period minimum population, due to magnitude limitations.

9.2 Future Work

The obvious continuation to this work is the application of the new modelling approach to many further eclipsing CVs. Firstly, there are the additional 12 eclipsing CVs observed with ULTRACAM/ULTRASPEC that have been modelled using the existing approach (Table 2.1). There are also the 10 systems with ULTRACAM/ULTRASPEC observations that currently have sufficient and suitable data available for modelling (Table 2.2). It is possible for the number of systems ready for modelling to significantly increase with future observations of the 30+ previously observed systems with modelling potential (Tables 2.3 and 2.4). Furthermore, there are another ~ 30 identified eclipsers that have yet to be observed at high-time-resolution, which also require future observation. In addition, it is important to keep track of new eclipsing CV discoveries, both in the short-term from surveys such as CRTS, ASAS-SN, Gaia, and in the longer-term from the Large Synoptic Survey Telescope (LSST).

It is important to mention here what a significant contribution the second Gaia data release (DR2), expected in Apr 2018 and set to contain over one billion precise parallaxes, will have on the field. These parallaxes will yield precise distances to the majority of known CVs, which will greatly improve current estimates of CV white dwarf temperatures (Section 3.7.1), amongst many other notable advancements.

Four known eclipsing systems yet to be observed at high-time-resolution, all of which are faint ($g \sim 20$–22) and discovered through superoutburst (Kato et al., 2013, 2016), are planned for observation with HiPERCAM (successor to ULTRACAM; Dhillon et al. 2016) on the Gran Telescopio Canarias (GTC) in Jan 2018. Each system's value of $\epsilon_{\rm B}$ is known, with all happening to fall within one of the two regions ($\epsilon_{\rm B} \simeq 0.015$ and $\epsilon_{\rm B} \simeq 0.05$) which are lacking calibrators for the $\epsilon_{\rm B}(q)$ relation (Section 8.4). Obtaining precise values of q through eclipse modelling will enable these systems to be used as calibrators, and help further constrain the calibration of the $\epsilon_{\mathrm{B}}(q)$ relation.

As far as further improvements to the modelling approach are concerned, it would be advantageous to somehow introduce a time-dependent constraint on the variation of model parameters between the individual eclipses in the fit. For example, consider the disc radii of two individual eclipses from the same system. If the eclipses are separated by just a single orbital cycle, the two disc radii should be very similar. However, if the eclipses are instead separated by 1000 orbital cycles, then the radii may well be very different. One potential way to implement this would be through the utilisation of hierarchical Bayesian modelling (Gelman & Hill, 2006).

Bibliography

Abramowitz M., Stegun I. A., 1964, Handbook of Mathematical Functions with Formulas, Graphs, and Mathematical Tables. Dover, New York

Allard F., Homeier D., Freytag B., 2011, in Astronomical Society of the Pacific Conference Series, Vol. 448, 16th Cambridge Workshop on Cool Stars, Stellar Systems, and the Sun, Johns-Krull C., Browning M. K., West A. A., eds., p. 91

Aller K. M. et al., 2013, Astrophysical Journal, 773, 63

Ambikasaran S., Foreman-Mackey D., Greengard L., Hogg D. W., O'Neil M., 2016, IEEE Trans. Pattern Anal. Mach. Intell., 38, 252

Andronov N., Pinsonneault M., Sills A., 2003, Astrophysical Journal, 582, 358

Angus R., Morton T., Aigrain S., Foreman-Mackey D., Rajpaul V., 2018, Monthly Notices of the Royal Astronomical Society, 474, 2094

Applegate J. H., 1992, Astrophysical Journal, 385, 621

Araujo-Betancor S. et al., 2003, Astrophysical Journal, 583, 437

Arenas J., Catalán M. S., Augusteijn T., Retter A., 2000, Monthly Notices of the Royal Astronomical Society, 311, 135

Arnold S., Berg R. A., Duthie J. G., 1976, Astrophysical Journal, 206, 790

Augusteijn T., van der Hooft F., de Jong J. A., van Paradijs J., 1996, Astronomy and Astrophysics, 311, 889

Bailey J., 1979, Monthly Notices of the Royal Astronomical Society, 187, 645

Balbus S. A., Hawley J. F., 1991, Astrophysical Journal, 376, 214

Balbus S. A., Hawley J. F., 1992a, Astrophysical Journal, 400, 610

Balbus S. A., Hawley J. F., 1992b, Astrophysical Journal, 392, 662

Balbus S. A., Hawley J. F., 1994, Monthly Notices of the Royal Astronomical Society, 266, 769

Baptista R., Borges B. W., Bond H. E., Jablonski F., Steiner J. E., Grauer A. D., 2003, Monthly Notices of the Royal Astronomical Society, 345, 889

Baptista R., Bortoletto A., 2004, Astronomical Journal, 128, 411

Baptista R., Bortoletto A., 2008, Astrophysical Journal, 676, 1240

Baptista R., Steiner J. E., Cieslinski D., 1994, Astrophysical Journal, 433, 332

Baraffe I., Chabrier G., Allard F., Hauschildt P. H., 1998, Astronomy and Astrophysics, 337, 403

Basri G., 2009, in American Institute of Physics Conference Series, Vol. 1094, 15th Cambridge Workshop on Cool Stars, Stellar Systems, and the Sun, Stempels E., ed., pp. 206–215

Bell C. P. M., Naylor T., Mayne N. J., Jeffries R. D., Littlefair S. P., 2012, Monthly Notices of the Royal Astronomical Society, 424, 3178

Bell C. P. M., Rees J. M., Naylor T., Mayne N. J., Jeffries R. D., Mamajek E. E., Rowe J., 2014, Monthly Notices of the Royal Astronomical Society, 445, 3496

Berger J., Fringant A.-M., 1984, Astronomy and Astrophysics Supplements, 58, 565

Bergeron P., Leggett S. K., Ruiz M. T., 2001, Astrophysical Journal Supplements, 133, 413

Bergeron P., Wesemael F., Beauchamp A., 1995, Publications of the Astronomical Society of the Pacific, 107, 1047

Bishop C. M., 2006, Pattern Recognition and Machine Learning. Springer-Verlag, New York

Borges B. W., Baptista R., 2005, Astronomy and Astrophysics, 437, 235

Bours M. C. P. et al., 2014, Monthly Notices of the Royal Astronomical Society, 445, 1924

Bours M. C. P. et al., 2016, Monthly Notices of the Royal Astronomical Society, 460, 3873

Boyajian T. S., van Belle G., von Braun K., 2014, Astronomical Journal, 147, 47

Boyd D., Oksanen A., Henden A., 2006, Journal of the British Astronomical Association, 116, 187

Breedt E., Gänsicke B. T., Marsh T. R., Steeghs D., Drake A. J., Copperwheat C. M., 2012, Monthly Notices of the Royal Astronomical Society, 425, 2548

Brinkworth C. S., Marsh T. R., Dhillon V. S., Knigge C., 2006, Monthly Notices of the Royal Astronomical Society, 365, 287

Bruch A., 1992, Astronomy and Astrophysics, 266, 237

Bruch A., 2000, Astronomy and Astrophysics, 359, 998

Bruch A., 2015, Astronomy and Astrophysics, 579, A50

Büning A., Ritter H., 2004, Astronomy and Astrophysics, 423, 281

Cannizzo J. K., 1993, The Limit Cycle Instability in Dwarf Nova Accretion Disks, World Scientific Publishing Co, pp. 6–40

Castelli F., Kurucz R. L., 2004, ArXiv Astrophysics e-prints

Charbonneau P., MacGregor K. B., 1997, Astrophysical Journal, 486, 502

Cook M. C., 1985, Monthly Notices of the Royal Astronomical Society, 215, 211

Cook M. C., Warner B., 1984, Monthly Notices of the Royal Astronomical Society, 207, 705

Copperwheat C. M., Marsh T. R., Dhillon V. S., Littlefair S. P., Hickman R., Gänsicke B. T., Southworth J., 2010, Monthly Notices of the Royal Astronomical Society, 402, 1824

Copperwheat C. M. et al., 2012, Monthly Notices of the Royal Astronomical Society, 421, 149

Dhillon V. S. et al., 2014, Monthly Notices of the Royal Astronomical Society, 444, 4009

Dhillon V. S. et al., 2016, in Proceedings of the International Society for Optical Engineering, Vol. 9908, Ground-based and Airborne Instrumentation for Astronomy VI, p. 99080Y

Dhillon V. S. et al., 2007, Monthly Notices of the Royal Astronomical Society, 378, 825

Dillon M. et al., 2008, Monthly Notices of the Royal Astronomical Society, 386, 1568

Donati J.-F., Landstreet J. D., 2009, Annual Review of Astronomy and Astrophysics, 47, 333

Dotter A., Chaboyer B., Jevremović D., Kostov V., Baron E., Ferguson J. W., 2008, Astrophysical Journal Supplements, 178, 89

Drake A. J. et al., 2009, Astrophysical Journal, 696, 870

Duchêne G., Kraus A., 2013, Annual Review of Astronomy and Astrophysics, 51, 269

Duquennoy A., Mayor M., 1991, Astronomy and Astrophysics, 248, 485

Echevarría J., de la Fuente E., Costero R., 2007, Astronomical Journal, 134, 262

Echevarría J., Ramírez-Torres A., Michel R., Hernández Santisteban J. V., 2016, Monthly Notices of the Royal Astronomical Society, 461, 1576

Eggleton P. P., 1983, Astrophysical Journal, 268, 368

Epelstain N., Yaron O., Kovetz A., Prialnik D., 2007, Monthly Notices of the Royal Astronomical Society, 374, 1449

Evans T. M., Aigrain S., Gibson N., Barstow J. K., Amundsen D. S., Tremblin P., Mourier P., 2015, Monthly Notices of the Royal Astronomical Society, 451, 680

Faulkner J., 1971, Astrophysical Journal Letters, 170, L99

Feline W. J., Dhillon V. S., Marsh T. R., Brinkworth C. S., 2004a, Monthly Notices of the Royal Astronomical Society, 355, 1

Feline W. J., Dhillon V. S., Marsh T. R., Stevenson M. J., Watson C. A., Brinkworth C. S., 2004b, Monthly Notices of the Royal Astronomical Society, 347, 1173

Feline W. J., Dhillon V. S., Marsh T. R., Watson C. A., Littlefair S. P., 2005, Monthly Notices of the Royal Astronomical Society, 364, 1158

Ford E. B., 2005, Astronomical Journal, 129, 1706

Foreman-Mackey D., Hogg D. W., Lang D., Goodman J., 2013, Publications of the Astronomical Society of the Pacific, 125, 306

Fukugita M., Ichikawa T., Gunn J. E., Doi M., Shimasaku K., Schneider D. P., 1996, Astronomical Journal, 111, 1748

Fukugita M., Yasuda N., Doi M., Gunn J. E., York D. G., 2011, Astronomical Journal, 141, 47

Gänsicke B. T. et al., 2009, Monthly Notices of the Royal Astronomical Society, 397, 2170

Gänsicke B. T., Long K. S., Barstow M. A., Hubeny I., 2006a, Astrophysical Journal, 639, 1039

Gänsicke B. T. et al., 2006b, Monthly Notices of the Royal Astronomical Society, 365, 969

Garnett R., Osborne M., Reece S., Rogers A., Roberts S., 2010, The Computer Journal, 53, 1430

Gelman A., Hill J., 2006, Data Analysis Using Regression and Multilevel/Hierarchical Models, Analytical Methods for Social Research. Cambridge University Press

Gianninas A., Strickland B. D., Kilic M., Bergeron P., 2013, Astrophysical Journal, 766, 3

Gibson N. P., Aigrain S., Roberts S., Evans T. M., Osborne M., Pont F., 2012, Monthly Notices of the Royal Astronomical Society, 419, 2683

Gilmore G. et al., 2012, The Messenger, 147, 25

Girardi L., Bressan A., Bertelli G., Chiosi C., 2000, Astronomy and Astrophysics Supplements, 141, 371

Goliasch J., Nelson L., 2015, Astrophysical Journal, 809, 80

Goodman J., Weare J., 2010, Comm. App. Math. Comp. Sci., 5, 65

Goranskii V. P., Lyutyi V. M., Shugarov S. Y., 1985, Soviet Astronomy Letters, 11, 293

Gregory P. C., 2005, Bayesian Logical Data Analysis for the Physical Sciences: A Comparative Approach with ‘Mathematica’ Support. Cambridge University Press

Grether D., Lineweaver C. H., 2006a, Astrophysical Journal, 640, 1051

Grether D., Lineweaver C. H., 2006b, Astrophysical Journal, 640, 1051

Hamada T., Salpeter E. E., 1961, Astrophysical Journal, 134, 683

Han Z.-T., Qian S.-B., Voloshina I., Metlov V. G., Zhu L.-Y., Li L.-J., 2016, Research in Astronomy and Astrophysics, 16, 156

Hardy L. K. et al., 2017, Monthly Notices of the Royal Astronomical Society, 465, 4968

Haro G., Luyten W. J., 1962, Boletin de los Observatorios Tonantzintla y Tacubaya, 3, 37

Hastings W. K., 1970, Biometrika, 57, 97

Hayashi C., Nakano T., 1963, Progress of Theoretical Physics, 30, 460

Hellier C., 2001, Cataclysmic Variable Stars: How and Why they Vary. Springer-Praxis, New York

Hernandez M. S., Zharikov S., Neustroev V., Tovmassian G., 2017, Monthly Notices of the Royal Astronomical Society, 470, 1960

Hjellming M. S., 1989, PhD thesis, Illinois Univ. at Urbana-Champaign, Savoy.

Holberg J. B., Bergeron P., 2006, Astronomical Journal, 132, 1221

Horne K., Cook M. C., 1985, Monthly Notices of the Royal Astronomical Society, 214, 307

Horne K., Marsh T. R., Cheng F. H., Hubeny I., Lanz T., 1994, Astrophysical Journal, 426, 294

Horne K., Welsh W. F., Wade R. A., 1993, Astrophysical Journal, 410, 357

Horne K., Wood J. H., Stiening R. F., 1991, Astrophysical Journal, 378, 271

Howell S. B., Nelson L. A., Rappaport S., 2001, Astrophysical Journal, 550, 897

Howell S. B., Warnock A., Mason K. O., Reichert G. A., Kreidl T. J., 1988, Monthly Notices of the Royal Astronomical Society, 233, 79

Iben, Jr. I., Livio M., 1993, Publications of the Astronomical Society of the Pacific, 105, 1373

Idan I., Shaviv N. J., Shaviv G., 2013, Monthly Notices of the Royal Astronomical Society, 433, 2884

Ivanova N., Taam R. E., 2003, Astrophysical Journal, 599, 516

Jones D. H. et al., 2004, Monthly Notices of the Royal Astronomical Society, 355, 747

Kato T. et al., 2014a, Publications of the Astronomical Society of Japan, 66, 90

Kato T. et al., 2015, Publications of the Astronomical Society of Japan, 67, 105

Kato T. et al., 2013, Publications of the Astronomical Society of Japan, 65, 23

Kato T. et al., 2014b, Publications of the Astronomical Society of Japan, 66, 30

Kato T. et al., 2016, Publications of the Astronomical Society of Japan, 68, 65

Kato T. et al., 2009, Publications of the Astronomical Society of Japan, 61, S395

Kato T. et al., 2017, Publications of the Astronomical Society of Japan, 69, 75

Kato T. et al., 2012, Publications of the Astronomical Society of Japan, 64, 21

Kato T. et al., 2010, Publications of the Astronomical Society of Japan, 62, 1525

Kawaler S. D., 1988, Astrophysical Journal, 333, 236

Kazarovets E. V., Samus N. N., Durlevich O. V., Kireeva N. N., Pastukhova E. N., 2015, Information Bulletin on Variable Stars, 6151

Kennedy M. R. et al., 2016, Astronomical Journal, 152, 27

Khruslov A. V., Kusakin A. V., Barsukova E. A., Goranskij V. P., Valeev A. F., Samus N. N., 2015, Research in Astronomy and Astrophysics, 15, 1005

King A. R., Frank J., Kolb U., Ritter H., 1995, Astrophysical Journal Letters, 444, L37

King A. R., Frank J., Kolb U., Ritter H., 1996, Astrophysical Journal, 467, 761

King A. R., Kolb U., 1995, Astrophysical Journal, 439, 330

Knigge C., 2006, Monthly Notices of the Royal Astronomical Society, 373, 484

Knigge C., Baraffe I., Patterson J., 2011, Astrophysical Journal Supplements, 194, 28

Knigge C., King A. R., Patterson J., 2000, Astronomy and Astrophysics, 364, L75

Kolb U., 1993, Astronomy and Astrophysics, 271, 149

Kolb U., Baraffe I., 1999, Monthly Notices of the Royal Astronomical Society, 309, 1034

Kolb U., Rappaport S., Schenker K., Howell S., 2001, Astrophysical Journal, 563, 958

Kouwenhoven M. B. N., Brown A. G. A., Zinnecker H., Kaper L., Portegies Zwart S. F., 2005, Astronomy and Astrophysics, 430, 137

Kowalski P. M., Saumon D., 2006, Astrophysical Journal Letters, 651, L137

Kumar S. S., 1963, Astrophysical Journal, 137, 1121

Lasota J.-P., 2001, New Astronomy Reviews, 45, 449

Levenberg K., 1944, Quaterly Journal on Applied Mathematics, 164

Littlefair S. P., Burningham B., Helling C., 2017, Monthly Notices of the Royal Astronomical Society, 466, 4250

Littlefair S. P., Dhillon V. S., Gänsicke B. T., Bours M. C. P., Copperwheat C. M., Marsh T. R., 2014, Monthly Notices of the Royal Astronomical Society, 443, 718

Littlefair S. P., Dhillon V. S., Marsh T. R., Gänsicke B. T., 2006a, Monthly Notices of the Royal Astronomical Society, 371, 1435

Littlefair S. P., Dhillon V. S., Marsh T. R., Gänsicke B. T., Baraffe I., Watson C. A., 2007, Monthly Notices of the Royal Astronomical Society, 381, 827

Littlefair S. P., Dhillon V. S., Marsh T. R., Gänsicke B. T., Southworth J., Baraffe I., Watson C. A., Copperwheat C., 2008, Monthly Notices of the Royal Astronomical Society, 388, 1582

Littlefair S. P., Dhillon V. S., Marsh T. R., Gänsicke B. T., Southworth J., Watson C. A., 2006b, Science, 314, 1578

Littlefair S. P., Dhillon V. S., Martín E. L., 2003, Monthly Notices of the Royal Astronomical Society, 340, 264

Littlefair S. P. et al., 2013, Monthly Notices of the Royal Astronomical Society, 431, 2820

Livio M., Govarie A., Ritter H., 1991, Astronomy and Astrophysics, 246, 84

Livio M., Pringle J. E., 1994, Astrophysical Journal, 427, 956

Livio M., Shara M. M., 1987, Astrophysical Journal, 319, 819

Lubow S. H., Shu F. H., 1975, Astrophysical Journal, 198, 383

MacDonald J., 1986, Astrophysical Journal, 305, 251

MacGregor K. B., Charbonneau P., 1997, Astrophysical Journal, 486, 484

Manser C. J., Gänsicke B. T., 2014, Monthly Notices of the Royal Astronomical Society, 442, L23

Maoz D., Mannucci F., Nelemans G., 2014, Annual Review of Astronomy and Astrophysics, 52, 107

Marcy G. W., Butler R. P., 2000, Publications of the Astronomical Society of the Pacific, 112, 137

Marquardt D. W., 1963, SIAM Journal on Applied Mathematics, 11, 431

Matérn B., 1960, Spatial variation: stochastic models and their application to some problems in forest surveys and other sampling investigations, Meddelanden från Statens skogsforskningsinstitut. Stockholm

Matt S. P., MacGregor K. B., Pinsonneault M. H., Greene T. P., 2012, Astrophysical Journal Letters, 754, L26

McAllister M. J. et al., 2015, Monthly Notices of the Royal Astronomical Society, 451, 114

McAllister M. J. et al., 2017a, Monthly Notices of the Royal Astronomical Society, 464, 1353

McAllister M. J. et al., 2017b, Monthly Notices of the Royal Astronomical Society, 467, 1024

Mestel L., Spruit H. C., 1987, Monthly Notices of the Royal Astronomical Society, 226, 57

Metropolis N., Rosenbluth A. W., Rosenbluth M. N., Teller A. H., Teller E., 1953, Journal of Chemical Physics, 21, 1087

Miszalski B. et al., 2016, Monthly Notices of the Royal Astronomical Society, 456, 633

Moffat A. F. J., 1969, Astronomy and Astrophysics, 3, 455

Morin J., Donati J.-F., Petit P., Delfosse X., Forveille T., Jardine M. M., 2010, Monthly Notices of the Royal Astronomical Society, 407, 2269

Morrissey P. et al., 2007, Astrophysical Journal Supplements, 173, 682

Murray J. R., 2000, Monthly Notices of the Royal Astronomical Society, 314, L1

Naylor T., 1998, Monthly Notices of the Royal Astronomical Society, 296, 339

Nelemans G., Siess L., Repetto S., Toonen S., Phinney E. S., 2016, Astrophysical Journal, 817, 69

Nogami D., Kato T., Baba H., Novák R., Lockley J. J., Somers M., 2001, Monthly Notices of the Royal Astronomical Society, 322, 79

O'Donoghue D., 1990, Monthly Notices of the Royal Astronomical Society, 246, 29

Oke J. B., Gunn J. E., 1983, Astrophysical Journal, 266, 713

Olech A., Schwarzenberg-Czerny A., Kedzierski P., Zloczewski K., Mularczyk K., Wisniewski M., 2003, Acta Astronomica, 53, 175

Osaki Y., 1974, Publications of the Astronomical Society of Japan, 26, 429

Osaki Y., 1989, Publications of the Astronomical Society of Japan, 41, 1005

Osaki Y., 1996, Publications of the Astronomical Society of the Pacific, 108, 39

Paczyński B., 1965, Acta Astronomica, 15, 89

Paczyński B., 1967, Acta Astronomica, 17, 287

Paczyński B., 1971, Annual Review of Astronomy and Astrophysics, 9, 183

Paczynski B., 1976, in IAU Symposium, Vol. 73, Structure and Evolution of Close Binary Systems, Eggleton P., Mitton S., Whelan J., eds., p. 75

Pala A. F. et al., 2017, Monthly Notices of the Royal Astronomical Society, 466, 2855

Panei J. A., Althaus L. G., Benvenuto O. G., 2000, Astronomy and Astrophysics, 353, 970

Patterson J., 1984, Astrophysical Journal Supplements, 54, 443

Patterson J., 1998, Publications of the Astronomical Society of the Pacific, 110, 1132

Patterson J., 2001, Publications of the Astronomical Society of the Pacific, 113, 736

Patterson J., 2011, Monthly Notices of the Royal Astronomical Society, 411, 2695

Patterson J. et al., 2017, Society for Astronomical Sciences Annual Symposium, 37, 1

Patterson J. et al., 2002, Publications of the Astronomical Society of the Pacific, 114, 1364

Patterson J. et al., 2005, Publications of the Astronomical Society of the Pacific, 117, 1204

Patterson J., Kemp J., Saad J., Skillman D. R., Harvey D., Fried R., Thorstensen J. R., Ashley R., 1997, Publications of the Astronomical Society of the Pacific, 109, 468

Patterson J., Thorstensen J. R., Knigge C., 2008, Publications of the Astronomical Society of the Pacific, 120, 510

Patterson J. et al., 2000, Publications of the Astronomical Society of the Pacific, 112, 1584

Peters C. S., Thorstensen J. R., 2006, Publications of the Astronomical Society of the Pacific, 118, 687

Podsiadlowski P., Han Z., Rappaport S., 2003, Monthly Notices of the Royal Astronomical Society, 340, 1214

Politano M., 1996, Astrophysical Journal, 465, 338

Politano M., 2004, Astrophysical Journal, 604, 817

Prialnik D., Kovetz A., 1995, Astrophysical Journal, 445, 789

Pyrzas S. et al., 2012, Publications of the Astronomical Society of the Pacific, 124, 204

Qian S. B., Han Z. T., Fernández Lajús E., Zhu L. Y., Li L. J., Liao W. P., Zhao E. G., 2015, Astrophysical Journal Supplements, 221, 17

Rajpaul V., Aigrain S., Osborne M. A., Reece S., Roberts S., 2015, Monthly Notices of the Royal Astronomical Society, 452, 2269

Rajpaul V., Aigrain S., Roberts S., 2016, Monthly Notices of the Royal Astronomical Society, 456, L6

Rappaport S., Joss P. C., Webbink R. F., 1982, Astrophysical Journal, 254, 616

Rappaport S., Verbunt F., Joss P. C., 1983, Astrophysical Journal, 275, 713

Rasmussen C. E., Williams C. K. I., 2006, Gaussian Processes for Machine Learning. The MIT Press, Cambridge, MA

Rebassa-Mansergas A., Gänsicke B. T., Schreiber M. R., Koester D., Rodríguez-Gil P., 2010, Monthly Notices of the Royal Astronomical Society, 402, 620

Rebassa-Mansergas A., Nebot Gómez-Morán A., Schreiber M. R., Gänsicke B. T., Schwope A., Gallardo J., Koester D., 2012, Monthly Notices of the Royal Astronomical Society, 419, 806

Reiners A., 2011, in Astronomical Society of the Pacific Conference Series, Vol. 448, 16th Cambridge Workshop on Cool Stars, Stellar Systems, and the Sun, Johns-Krull C., Browning M. K., West A. A., eds., p. 255

Reiners A., Basri G., 2008, Astrophysical Journal, 684, 1390

Reiners A., Basri G., 2009, Astronomy and Astrophysics, 496, 787

Reiners A., Basri G., 2010, Astrophysical Journal, 710, 924

Reiners A., Joshi N., Goldman B., 2012, Astronomical Journal, 143, 93

Renvoizé V., Baraffe I., Kolb U., Ritter H., 2002, Astronomy and Astrophysics, 389, 485

Ritter H., Burkert A., 1986, Astronomy and Astrophysics, 158, 161

Ritter H., Kolb U., 2003, Astronomy and Astrophysics, 404, 301

Ritter H., Zhang Z.-Y., Kolb U., 2000, Astronomy and Astrophysics, 360, 959

Roberts G. O., 1996, Markov Chain Concepts Related to Sampling Algorithms. Chapman and Hall, pp. 45–57

Roberts S., Osborne M., Ebden M., Reece S., Gibson N., Aigrain S., 2013, Phil. Trans. R. Soc. A, 371, 20110550

Robinson E. L., 1974, Astrophysical Journal, 193, 191

Rodríguez-Gil P. et al., 2007, Monthly Notices of the Royal Astronomical Society, 377, 1747

Rodríguez-Gil P., Martínez-Pais I. G., Casares J., Villada M., van Zyl L., 2001, Monthly Notices of the Royal Astronomical Society, 328, 903

Rodríguez-Gil P., Schmidtobreick L., Gänsicke B. T., 2007, Monthly Notices of the Royal Astronomical Society, 374, 1359

Rodríguez-Gil P. et al., 2015, Monthly Notices of the Royal Astronomical Society, 452, 146

Roeser S., Demleitner M., Schilbach E., 2010, Astronomical Journal, 139, 2440

Rolfe D. J., Haswell C. A., Patterson J., 2000, Monthly Notices of the Royal Astronomical Society, 317, 759

Savoury C. D. J. et al., 2011, Monthly Notices of the Royal Astronomical Society, 415, 2025

Savoury C. D. J., Littlefair S. P., Marsh T. R., Dhillon V. S., Parsons S. G., Copperwheat C. M., Steeghs D., 2012, Monthly Notices of the Royal Astronomical Society, 422, 469

Scaringi S., 2014, Monthly Notices of the Royal Astronomical Society, 438, 1233

Scaringi S., Groot P. J., Still M., 2013, Monthly Notices of the Royal Astronomical Society, 435, L68

Scaringi S., Körding E., Uttley P., Knigge C., Groot P. J., Still M., 2012, Monthly Notices of the Royal Astronomical Society, 421, 2854

Schaefer B. E., 1990, Astrophysical Journal Letters, 355, L39

Schaefer B. E., 2010, Astrophysical Journal Supplements, 187, 275

Schaefer B. E., Pagnotta A., Shara M. M., 2010, Astrophysical Journal, 708, 381

Schaefer B. E., Ringwald F. A., 1995, Astrophysical Journal Letters, 447, L45

Schenker K., Kolb U., Ritter H., 1998, Monthly Notices of the Royal Astronomical Society, 297, 633

Schlafly E. F., Finkbeiner D. P., 2011, Astrophysical Journal, 737, 103

Schreiber M. R., Zorotovic M., Wijnen T. P. G., 2016, Monthly Notices of the Royal Astronomical Society, 455, L16

Shafter A. W., 2017, Astrophysical Journal, 834, 196

Shafter A. W., Holland J. N., 2003, Publications of the Astronomical Society of the Pacific, 115, 1105

Shakura N. I., Sunyaev R. A., 1973, Astronomy and Astrophysics, 24, 337

Shappee B. J. et al., 2014, Astrophysical Journal, 788, 48

Shara M. M., Livio M., Moffat A. F. J., Orio M., 1986, Astrophysical Journal, 311, 163

Shears J., Brady S., Foote J., Starkey D., Vanmunster T., 2008, Journal of the British Astronomical Association, 118, 288

Shen K. J., 2015, Astrophysical Journal Letters, 805, L6

Sing D. K., Green E. M., Howell S. B., Holberg J. B., Lopez-Morales M., Shaw J. S., Schmidt G. D., 2007, Astronomy and Astrophysics, 474, 951

Sirotkin F. V., Kim W.-T., 2009, Astrophysical Journal, 698, 715

Smak J., 1979, Acta Astronomica, 29, 309

Smith A. J., Haswell C. A., Hynes R. I., 2006, Monthly Notices of the Royal Astronomical Society, 369, 1537

Smith D. A., Dhillon V. S., 1998, Monthly Notices of the Royal Astronomical Society, 301, 767

Smith J. A. et al., 2002, Astronomical Journal, 123, 2121

Solheim J.-E., 2010, Publications of the Astronomical Society of the Pacific, 122, 1133

Soszyński I. et al., 2016, Acta Astronomica, 66, 405

Soszyński I. et al., 2015, Acta Astronomica, 65, 39

Southworth J., Copperwheat C. M., Gänsicke B. T., Pyrzas S., 2010, Astronomy and Astrophysics, 510, A100

Southworth J., Hickman R. D. G., Marsh T. R., Rebassa-Mansergas A., Gänsicke B. T., Copperwheat C. M., Rodríguez-Gil P., 2009, Astronomy and Astrophysics, 507, 929

Southworth J., Marsh T. R., Gänsicke B. T., Aungwerojwit A., Hakala P., de Martino D., Lehto H., 2007, Monthly Notices of the Royal Astronomical Society, 382, 1145

Southworth J., Tappert C., Gänsicke B. T., Copperwheat C. M., 2015, Astronomy and Astrophysics, 573, A61

Spark M. K., O'Donoghue D., 2015, Monthly Notices of the Royal Astronomical Society, 449, 175

Steeghs D., Howell S. B., Knigge C., Gänsicke B. T., Sion E. M., Welsh W. F., 2007, Astrophysical Journal, 667, 442

Steeghs D., Marsh T., Knigge C., Maxted P. F. L., Kuulkers E., Skidmore W., 2001, Astrophysical Journal Letters, 562, L145

Steeghs D., Perryman M. A. C., Reynolds A., de Bruijne J. H. J., Marsh T., Dhillon V. S., Peacock A., 2003, Monthly Notices of the Royal Astronomical Society, 339, 810

Stehle R., Ritter H., Kolb U., 1996, Monthly Notices of the Royal Astronomical Society, 279, 581

Stein M. L., 1999, Interpolation of spatial data, Springer Series in Statistics. Springer-Verlag, New York, pp. xviii+247

Szkody P. et al., 2002, Astronomical Journal, 123, 430

Szkody P. et al., 2011, Astronomical Journal, 142, 181

Szkody P. et al., 2009, Astronomical Journal, 137, 4011

Szkody P., Brownlee D. E., 1977, Astrophysical Journal Letters, 212, L113

Szkody P. et al., 2007, Astronomical Journal, 134, 185

Taam R. E., Sandquist E. L., 2000, Annual Review of Astronomy and Astrophysics, 38, 113

Tappert C., Augusteijn T., Maza J., 2004, Monthly Notices of the Royal Astronomical Society, 354, 321

Thoroughgood T. D. et al., 2005, Monthly Notices of the Royal Astronomical Society, 357, 881

Thoroughgood T. D., Dhillon V. S., Watson C. A., Buckley D. A. H., Steeghs D., Stevenson M. J., 2004, Monthly Notices of the Royal Astronomical Society, 353, 1135

Thorstensen J. R., 2000, Publications of the Astronomical Society of the Pacific, 112, 1269

Thorstensen J. R., Alper E. H., Weil K. E., 2016, Astronomical Journal, 152, 226

Thorstensen J. R., Fenton W. H., Patterson J. O., Kemp J., Krajci T., Baraffe I., 2002, Astrophysical Journal Letters, 567, L49

Thorstensen J. R., Ringwald F. A., Taylor C. J., Sheets H. A., Peters C. S., Skinner J. N., Alper E. H., Weil K. E., 2017, Research Notes of the American Astronomical Society, 1, 29

Thorstensen J. R., Ringwald F. A., Wade R. A., Schmidt G. D., Norsworthy J. E., 1991, Astronomical Journal, 102, 272

Thorstensen J. R., Taylor C. J., Peters C. S., Skinner J. N., Southworth J., Gänsicke B. T., 2015, Astronomical Journal, 149, 128

Tovmassian G., Stephania Hernandez M., González-Buitrago D., Zharikov S., García-Díaz M. T., 2014, Astronomical Journal, 147, 68

Townsley D. M., Bildsten L., 2003, Astrophysical Journal Letters, 596, L227

Townsley D. M., Bildsten L., 2004, Astrophysical Journal, 600, 390

Townsley D. M., Gänsicke B. T., 2009, Astrophysical Journal, 693, 1007

Tremblay P.-E., Bergeron P., Gianninas A., 2011, Astrophysical Journal, 730, 128

Tremblay P.-E., Cummings J., Kalirai J. S., Gänsicke B. T., Gentile-Fusillo N., Raddi R., 2016, Monthly Notices of the Royal Astronomical Society, 461, 2100

Tulloch S. M., Rodríguez-Gil P., Dhillon V. S., 2009, Monthly Notices of the Royal Astronomical Society, 397, L82

Uemura M. et al., 2004, Publications of the Astronomical Society of Japan, 56, S141

Uhlenbeck G. E., Ornstein L. S., 1930, Phys. Rev., 36, 823

Uthas H., Knigge C., Long K. S., Patterson J., Thorstensen J., 2011, Monthly Notices of the Royal Astronomical Society, 414, L85

van Amerongen S., Damen E., Groot M., Kraakman H., van Paradijs J., 1987, Monthly Notices of the Royal Astronomical Society, 225, 93

Van de Sande M., Scaringi S., Knigge C., 2015, Monthly Notices of the Royal Astronomical Society, 448, 2430

Verbunt F., Zwaan C., 1981, Astronomy and Astrophysics, 100, L7

Vogt N., Schoembs R., Krzeminski W., Pedersen H., 1981, Astronomy and Astrophysics, 94, L29

Vrielmann S., Stiening R. F., Offutt W., 2002, Monthly Notices of the Royal Astronomical Society, 334, 608

Wade R. A., Horne K., 1988, Astrophysical Journal, 324, 411

Warner B., 1995, Cataclysmic Variable Stars. Cambridge Univ. Press, Cambridge

Warner B., O'Donoghue D., 1988, Monthly Notices of the Royal Astronomical Society, 233, 705

Way M. J., Foster L. V., Gazis P. R., Srivastava A. N., 2009, Astrophysical Journal, 706, 623

Way M. J., Srivastava A. N., 2006, Astrophysical Journal, 647, 102

Webbink R. F., 1976, Astrophysical Journal, 209, 829

Welsh W. F., Froning C. S., Marsh T. R., Reimer T. W., Robinson E. L., Wood P. R., 2007, in Astronomical Society of the Pacific Conference Series, Vol. 362, The Seventh Pacific Rim Conference on Stellar Astrophysics, Kang Y. W., Lee H.-W., Leung K.-C., Cheng K.-S., eds., p. 241

Wijnen T. P. G., Zorotovic M., Schreiber M. R., 2015, Astronomy and Astrophysics, 577, A143

Willems B., Kolb U., 2004, Astronomy and Astrophysics, 419, 1057

Willems B., Kolb U., Sandquist E. L., Taam R. E., Dubus G., 2005, Astrophysical Journal, 635, 1263

Wils P., 2009, Information Bulletin on Variable Stars, 5916, 1

Wils P., Krajci T., Hambsch F.-J., Muyllaert E., 2011, Information Bulletin on Variable Stars, 5982

Wolf S., Mantel K. H., Horne K., Barwig H., Schoembs R., Baernbantner O., 1993, Astronomy and Astrophysics, 273, 160

Wood J., Horne K., Berriman G., Wade R., O'Donoghue D., Warner B., 1986, Monthly Notices of the Royal Astronomical Society, 219, 629

Wood J. H., Horne K., 1990, Monthly Notices of the Royal Astronomical Society, 242, 606

Wood J. H., Horne K., Berriman G., Wade R. A., 1989a, Astrophysical Journal, 341, 974

Wood J. H., Irwin M. J., Pringle J. E., 1985, Monthly Notices of the Royal Astronomical Society, 214, 475

Wood J. H. et al., 1989b, Monthly Notices of the Royal Astronomical Society, 239, 809

Wood M. A., 1995, in Lecture Notes in Physics, Berlin Springer Verlag, Vol. 443, White Dwarfs, Koester D., Werner K., eds., p. 41

Woudt P. A., Warner B., 2001, Monthly Notices of the Royal Astronomical Society, 328, 159

Yaron O., Prialnik D., Shara M. M., Kovetz A., 2005, Astrophysical Journal, 623, 398

York D. G. et al., 2000, Astronomical Journal, 120, 1579

Zorotovic M., Schreiber M. R., Gänsicke B. T., 2011, Astronomy and Astrophysics, 536, A42

Appendix A

Journal of Observations

The following table contains details on all ULTRACAM/ULTRASPEC eclipse observations – up to Feb 2017 – of the 18 systems that are modelled across Chapters 4, 5, 6 and 7.

Date	Object	Instrument Setup	Filter(s)	T_{mid} (MJD)	Cycle No.	Phase Coverage	T_{exp} (s)	$N_{u'}$	N_{exp}	Seeing ($''$)	Flag
2014 Nov 27	ASASSN-14ag	TNT+USPEC	*KG5*	56988.75612(3)^h	−35	−0.304–0.146	1.964	–	1186	1.8–2.1	6
2014 Nov 29	ASASSN-14ag	TNT+USPEC	*KG5*	56990.86702(3)^h	0	−0.107–0.321	1.964	–	1124	1.0–1.4	1,2
2014 Nov 30	ASASSN-14ag	TNT+USPEC	*KG5*	56991.83195(3)^h	16	−0.207–0.244	1.964	–	1188	1.3–2.5	1,2
2015 Jan 01	ASASSN-14ag	TNT+USPEC	g'	57023.73631(4)^h	545	−0.245–0.201	1.964	–	1177	1.2–2.1	6
2015 Jan 02	ASASSN-14ag	TNT+USPEC	r'	57024.64101(4)^h	560	−0.133–0.202	1.964	–	883	1.2–2.0	6
2015 Jan 03	ASASSN-14ag	TNT+USPEC	i'	57025.84724(4)^h	580	−0.122–0.177	1.964	–	789	0.9–1.2	1
2015 Jan 04	ASASSN-14ag	TNT+USPEC	g'	57026.69153(4)^h	594	−0.135–0.267	1.964	–	1061	1.5–2.3	1,2
2015 Jan 04	ASASSN-14ag	TNT+USPEC	r'	57026.87251(4)^h	597	−0.134–0.163	2.964	–	521	1.1–1.7	1,2
2015 Feb 24	ASASSN-14ag	TNT+USPEC	g'	57077.77465(3)^h	1441	−0.355–0.253	3.964	–	795	1.7–3.2	1,2
2015 Feb 25	ASASSN-14ag	TNT+USPEC	r'	57078.61896(3)^h	1455	−0.293–0.215	3.352	–	787	1.2–2.0	1,2
2015 Feb 26	ASASSN-14ag	TNT+USPEC	g'	57079.76494(3)^h	1474	−0.109–0.343	3.964	–	594	1.8–2.4	1,2
2015 Mar 03	ASASSN-14ag	TNT+USPEC	i'	57084.65017(8)^h	1555	−0.258–0.271	4.852	–	569	1.2–2.3	7
2015 Dec 05	ASASSN-14ag	TNT+USPEC	u'	57361.77768(8)^h	6150	−0.151–0.155	9.564	–	169	2.3–2.7	7
2015 Dec 07	ASASSN-14ag	TNT+USPEC	u'	57363.76780(8)^h	6183	−0.299–0.148	9.564	–	246	2.0–2.7	1
2010 May 12	CSS080623	NTT+UCAM	$u'\,g'\,r'$	55329.23459(3)^h	0	−0.110–0.177	3.301	3	504	1.2–1.4	2
2010 May 17	CSS080623	NTT+UCAM	$u'\,g'\,r'$	55334.12012(3)^h	82	−0.318–0.363	4.920	3	712	0.9–1.8	2
2010 May 17	CSS080623	NTT+UCAM	$u'\,g'\,r'$	55334.17971(3)^h	83	−0.244–0.451	3.923	4	909	1.1–1.4	2

Table A.1: Journal of observations for systems modelled in this thesis. The instrument setup column shows both the telescope and instrument (UCAM and USPEC refer to ULTRACAM and ULTRASPEC, respectively) used for each eclipse observation. T_{mid} represents the mid-eclipse time (taken to be that of the white dwarf, when visible), T_{exp} the exposure time and N_{exp} the number of exposures. $N_{u'}$ indicates the number of u' band frames which were co-added on-chip to reduce the impact of readout noise. The final column is a flag for eclipse status: (1) modelled individually, (2) modelled as constituent of average eclipse, (3) usable for individual modelling but not chosen, (4) obtained post-modelling but usable, (5) clear bright spot features but not included in average eclipse due to significant change in disc radius/contribution, (6) lack of bright spot ingress/merged ingresses, (7) poor SNR, (8) in outburst.
^{h}Heliocentric (HMJD), ^{b}Barycentric (BMJD)

Date	Object	Instrument Setup	Filter(s)	$T_{\rm mid}$ (MJD)	Cycle No.	Phase Coverage	$T_{\rm exp}$ (s)	$N_{u'}$	$N_{\rm exp}$	Seeing ($''$)	Flag
2010 May 17	CSS080623	NTT+UCAM	$u'\,g'\,r'$	55334.23925(3)^h	84	−0.512–0.269	3.923	3	1021	1.2–1.6	2
2010 Jun 07	CSS080623	NTT+UCAM	$u'\,g'\,r'$	55355.03231(3)^h	433	−0.254–0.226	3.818	2	644	1.0–1.1	2
2010 Jun 07	CSS080623	NTT+UCAM	$u'\,g'\,r'$	55355.15152(3)^h	435	−0.318–0.250	3.818	2	764	1.0–1.8	2
2011 May 27	CSS080623	NTT+UCAM	$u'\,g'\,r'$	55709.05056(3)^h	6375	−0.100–0.141	2.890	2	427	0.9–1.1	2
2011 May 30	CSS080623	NTT+UCAM	$u'\,g'\,r'$	55711.96995(3)^h	6424	−0.192–0.146	3.941	3	440	1.1–1.3	2
2011 May 30	CSS080623	NTT+UCAM	$u'\,g'\,r'$	55712.02952(3)^h	6425	−0.479–0.136	3.941	3	798	1.1–1.5	2
2011 May 30	CSS080623	NTT+UCAM	$u'\,g'\,r'$	55712.14867(3)^h	6427	−0.505–0.279	3.941	3	1023	1.0–1.2	2
2011 Jan 18	CSS110113	NTT+UCAM	$u'\,g'\,i'$	55580.12190(10)^h	−5479	−0.332–0.159	2.376	3	1168	0.9–1.0	8
2012 Jan 14	CSS110113	WHT+UCAM	$u'\,g'\,r'$	55940.95783(3)^h	−16	−0.215–0.178	3.985	3	563	1.0–1.6	2
2012 Jan 15	CSS110113	WHT+UCAM	$u'\,g'\,r'$	55942.01465(3)^h	0	−0.167–0.175	4.980	4	393	1.2–1.8	2
2012 Jan 16	CSS110113	WHT+UCAM	$u'\,g'\,r'$	55942.87330(3)^h	13	−0.237–0.117	3.985	3	507	1.4–2.1	2
2012 Sep 09	CSS110113	WHT+UCAM	$u'\,g'\,r'$	56180.12801(3)^h	3605	−0.197–0.114	3.987	3	448	1.4–1.8	5
2012 Oct 13	CSS110113	WHT+UCAM	$u'\,g'\,r'$	56214.07819(3)^h	4119	−0.232–0.140	2.989	3	711	1.2–1.4	5
2014 Jan 02	CSS110113	WHT+UCAM	$u'\,g'\,r'$	56659.92157(3)^h	10869	−0.194–0.091	3.980	3	408	0.9–1.4	5
2014 Jan 28	CSS110113	TNT+USPEC	*KG5*	56685.54929(3)^h	11257	−0.030–0.174	9.352	–	126	1.3–2.0	7
2014 Jan 28	CSS110113	TNT+USPEC	*KG5*	56685.61535(3)^h	11258	−0.186–0.185	9.352	–	227	1.4–1.7	7
2014 Jan 29	CSS110113	TNT+USPEC	g'	56686.54005(3)^h	11272	−0.533–0.324	9.352	–	523	1.4–3.0	7
2014 Feb 01	CSS110113	TNT+USPEC	g'	56689.57840(3)^h	11318	−0.106–0.358	8.958	–	296	1.9–2.1	7
2014 Mar 14	CSS110113	WHT+UCAM	$u'\,g'\,r'$	56730.86018(3)^h	11943	−0.205–0.240	2.627	3	957	1.2–1.8	7
2007 Jun 10	CTCV 1300	VLT+UCAM	$u'\,g'\,r'$	54262.09916(3)^h	0	−0.270–0.193	1.002	4	3463	1.2–2.3	1
2007 Jun 13	CTCV 1300	VLT+UCAM	$u'\,g'\,i'$	54265.12310(3)^h	34	−0.261–0.144	1.952	3	1574	1.4–2.1	1
2010 Jun 07	CTCV 1300	NTT+UCAM	$u'\,g'\,r'$	55355.00260(5)^h	12288	−0.142–0.120	3.938	3	511	0.9–1.1	6
2011 May 30	CTCV 1300	NTT+UCAM	$u'\,g'\,r'$	55712.18836(5)^h	16304	−0.175–0.149	2.895	3	852	0.9–1.7	1

Table A.1: *Continued.*

Date	Object	Instrument Setup	Filter(s)	T_{mid} (MJD)	Cycle No.	Phase Coverage	T_{exp} (s)	$N_{u'}$	N_{exp}	Seeing (″)	Flag
2003 May 20	DV UMa	WHT+UCAM	$u'\,g'\,i'$	52779.969152(20)^{h}	−35	−0.092–0.177	5.921	1	339	1.2–2.7	2
2003 May 22	DV UMa	WHT+UCAM	$u'\,g'\,i'$	52781.943747(20)^{h}	−12	−0.126–0.104	4.921	1	345	0.9–1.1	2
2003 May 23	DV UMa	WHT+UCAM	$u'\,g'\,i'$	52782.974025(20)^{h}	0	−0.135–0.151	3.921	1	540	0.9–1.1	5
2007 Oct 19	DV UMa	WHT+UCAM	$u'\,g'\,r'$	54393.225867(10)^{h}	18756	−0.172–0.180	2.754	2	940	1.2–2.4	2
2003 May 23	GY Cnc	WHT+UCAM	$u'\,g'\,i'$	52782.93530(10)^{b}	−17985	−0.085–0.128	1.628	1	1945	0.9–1.1	8
2012 Jan 11	GY Cnc	WHT+UCAM	$u'\,g'\,r'$	55938.26366(5)^{b}	0	−0.082–0.140	3.974	3	842	1.0–1.2	6
2012 Jan 14	GY Cnc	WHT+UCAM	$u'\,g'\,r'$	55941.24626(5)^{b}	17	−0.077–0.128	3.077	2	1005	1.2–1.8	6
2012 Jan 16	GY Cnc	WHT+UCAM	$u'\,g'\,r'$	55943.00068(5)^{b}	27	−0.066–0.115	2.480	3	1096	0.9–1.6	6
2012 Jan 16	GY Cnc	WHT+UCAM	$u'\,g'\,r'$	55943.17605(5)^{b}	28	−0.168–0.112	2.480	3	1692	1.1–1.5	1
2012 Jan 20	GY Cnc	WHT+UCAM	$u'\,g'\,r'$	55947.21130(5)^{b}	51	−0.109–0.093	3.879	3	784	2.1–2.7	6
2013 Dec 30	GY Cnc	WHT+UCAM	$u'\,g'\,r'$	56657.22682(5)^{b}	4098	−0.180–0.115	3.974	3	1120	0.9–1.2	6
2014 Jan 26	GY Cnc	TNT+USPEC	*KG5*	56683.71865(5)^{b}	4249	−0.112–0.098	1.273	–	2462	1.0–1.6	1
2015 Feb 27	GY Cnc	TNT+USPEC	*KG5*	57080.56902(10)^{b}	6511	−0.059–0.138	2.473	–	1200	1.6–2.2	6
2015 Dec 11	GY Cnc	TNT+USPEC	*KG5*	57367.76812(10)^{b}	8148	−0.146–0.213	3.967	–	1370	1.3–1.6	6
2016 Mar 13	GY Cnc	TNT+USPEC	g'	57460.57718(10)^{b}	8677	−0.111–0.123	3.926	–	898	1.1–1.6	6
2017 Feb 13	GY Cnc	TNT+USPEC	g'	57797.60241(15)^{b}	10598	−0.185–0.161	1.766	–	2944	1.3–1.8	6
2014 Mar 30	IY UMa	TNT+USPEC	*KG5*	56746.639516(20)^{h}	0	−0.102–0.325	2.190	–	1243	1.5–2.9	1
2014 Mar 30	IY UMa	TNT+USPEC	*KG5*	56746.713426(20)^{h}	1	−0.060–0.201	2.190	–	763	1.6–2.0	1
2014 Mar 30	IY UMa	TNT+USPEC	*KG5*	56746.787335(20)^{h}	2	−0.066–0.249	2.190	–	913	1.8–2.5	1
2014 Nov 30	IY UMa	TNT+USPEC	*KG5*	56991.94334(10)^{h}	3319	−0.090–0.174	3.352	–	502	1.6–1.9	8
2015 Jan 03	IY UMa	TNT+USPEC	g'	57025.94133(3)^{h}	3779	−0.203–0.176	3.352	–	713	1.1–1.4	1
2015 Jan 06	IY UMa	TNT+USPEC	r'	57028.89764(5)^{h}	3819	−0.159–0.125	3.952	–	458	1.2–1.5	3
2015 Feb 23	IY UMa	TNT+USPEC	r'	57076.86456(3)^{h}	4468	−0.130–0.249	3.852	–	632	1.9–2.3	1

Table A.1: *Continued.*

Date	Object	Instrument Setup	Filter(s)	$T_{\rm mid}$ (MJD)	Cycle No.	Phase Coverage	$T_{\rm exp}$ (s)	$N_{u'}$	$N_{\rm exp}$	Seeing ($''$)	Flag
2016 Mar 11	IY UMa	TNT+USPEC	u'	$57458.67790(10)^h$	9634	-0.185–0.269	29.78	–	99	1.7–2.3	6
2016 Mar 13	IY UMa	TNT+USPEC	u'	$57460.67369(10)^h$	9661	-0.195–0.287	25.35	–	122	1.5–2.0	3
2016 Mar 13	IY UMa	TNT+USPEC	i'	$57460.74748(5)^h$	9662	-0.363–0.320	7.852	–	655	1.1–1.5	1
2010 Apr 27	OY Car	NTT+UCAM	$u'\,g'\,r'$	$55314.104056(8)^h$	-632	-0.103–0.140	1.760	3	747	1.7–2.7	3
2010 Jun 06	OY Car	NTT+UCAM	$u'\,g'\,r'$	$55353.996480(8)^h$	0	-0.119–0.170	1.424	3	3116	1.3–1.4	1
2010 Jun 07	OY Car	NTT+UCAM	$u'\,g'\,r'$	$55355.069543(8)^h$	17	-0.293–0.249	1.369	3	2120	1.1–1.8	3
2010 Nov 18	OY Car	NTT+UCAM	$u'\,g'\,i'$	$55519.310181(8)^h$	2619	-0.206–0.487	1.329	4	3894	1.3–2.7	1
2010 Dec 17	OY Car	NTT+UCAM	$u'\,g'\,i'$	$55548.282678(8)^h$	3078	-0.189–0.126	2.814	2	606	0.8–1.0	1
2011 May 24	OY Car	NTT+UCAM	$u'\,g'\,r'$	$55706.084989(8)^h$	5578	-0.368–0.180	1.329	1	2205	1.3–2.0	3
2016 Nov 10	OY Car	NTT+UCAM	$u'\,g'\,r'$	$57703.294204(8)^h$	37219	-0.141–0.202	1.979	2	931	0.9–1.4	4
2011 Aug 26	PHL 1445	WHT+UCAM	$u'\,g'\,i'$	$55800.15107(10)^h$	-1264	-0.338–0.902	2.685	2	2098	0.9–1.3	8
2011 Nov 01	PHL 1445	WHT+UCAM	$u'\,g'\,r'$	$55867.12400(3)^h$	0	-0.604–0.131	2.137	2	1119	1.0–2.4	1,2
2012 Jan 14	PHL 1445	WHT+UCAM	$u'\,g'\,r'$	$55940.87898(3)^h$	1392	-0.144–0.217	1.979	3	827	1.4–2.1	6
2012 Jan 14	PHL 1445	WHT+UCAM	$u'\,g'\,r'$	$55940.98490(3)^h$	1394	-0.304–0.177	1.979	3	1102	1.5–2.4	7
2012 Jan 15	PHL 1445	WHT+UCAM	$u'\,g'\,r'$	$55941.99163(3)^h$	1413	-0.322–0.119	1.979	3	1008	1.2–1.7	1,2
2012 Jan 16	PHL 1445	WHT+UCAM	$u'\,g'\,r'$	$55942.89237(3)^h$	1430	-0.208–0.500	1.979	3	1619	1.5–2.7	1,2
2012 Jan 16	PHL 1445	WHT+UCAM	$u'\,g'\,r'$	$55942.94534(3)^h$	1431	-0.500–0.183	1.979	3	1561	1.5–2.1	1,2
2012 Jan 22	PHL 1445	WHT+UCAM	$u'\,g'\,r'$	$55948.82668(3)^h$	1542	-0.275–0.147	1.979	3	966	1.1–1.9	1
2012 Sep 08	PHL 1445	WHT+UCAM	$u'\,g'\,i'$	$56179.15198(3)^h$	5889	-0.322–0.173	2.982	3	754	1.0–1.8	1
2012 Oct 13	PHL 1445	WHT+UCAM	$u'\,g'\,r'$	$56214.01605(3)^h$	6547	-0.260–0.175	3.480	3	571	1.5–2.4	1
2013 Jul 30	PHL 1445	WHT+UCAM	$u'\,g'\,i'$	$56504.21431(3)^h$	12024	-0.294–0.176	3.852	3	557	1.5–2.5	1
2013 Nov 10	PHL 1445	TNT+USPEC	*KG5*	$56606.63413(3)^h$	13957	-0.498–0.158	4.850	–	618	1.2–1.9	7
2013 Dec 31	PHL 1445	WHT+UCAM	$u'\,g'\,r'$	$56657.97642(3)^h$	14926	-0.121–0.216	3.922	3	394	1.5–2.5	6

Table A.1: *Continued.*

Date	Object	Instrument Setup	Filter(s)	T_{mid} (MJD)	Cycle No.	Phase Coverage	T_{exp} (s)	$N_{u'}$	N_{exp}	Seeing ($''$)	Flag
2014 Jan 01	PHL 1445	WHT+UCAM	$u'\,g'\,r'$	56658.82417(3)^h	14942	−0.204–0.260	3.628	3	584	1.0–1.9	1
2014 Jan 01	PHL 1445	WHT+UCAM	$u'\,g'\,r'$	56658.98310(3)^h	14945	−0.343–0.127	3.628	3	591	1.0–1.9	1
2014 Jan 02	PHL 1445	WHT+UCAM	$u'\,g'\,r'$	56659.83095(3)^h	14961	−0.219–0.153	3.628	3	467	0.9-1.3	1
2014 Jan 25	PHL 1445	TNT+USPEC	*KG5*	56682.50845(3)^h	15389	−0.145–0.139	4.947	–	263	1.0–1.2	7
2014 Jan 26	PHL 1445	TNT+USPEC	*KG5*	56683.56814(3)^h	15409	−0.210–0.127	4.947	–	312	1.6–2.3	6
2014 Feb 01	PHL 1445	TNT+USPEC	g'	56689.55548(10)^h	15522	−0.110–0.083	4.850	–	184	1.4–2.3	8
2006 Mar 09	SDSS 0901	WHT+UCAM	$u'\,g'\,r'$	53803.906350(20)^h	−27455	−0.763–0.259	4.972	1	1374	1.2–2.0	2
2006 Mar 10	SDSS 0901	WHT+UCAM	$u'\,g'\,r'$	53804.996665(20)^h	−27441	−0.135–0.092	4.972	1	307	1.1–1.4	2
2006 Mar 10	SDSS 0901	WHT+UCAM	$u'\,g'\,r'$	53805.152456(20)^h	−27439	−0.258–0.178	4.972	1	590	1.2–1.7	2
2010 Jan 07	SDSS 0901	WHT+UCAM	$u'\,g'\,r'$	55203.96452(5)^h	−9478	−0.289–0.137	1.677	4	1685	1.7–3.0	6
2012 Jan 15	SDSS 0901	WHT+UCAM	$u'\,g'\,r'$	55942.116352(20)^h	0	−0.350–0.152	4.480	3	752	0.8–1.0	2
2012 Jan 15	SDSS 0901	WHT+UCAM	$u'\,g'\,r'$	55942.194233(20)^h	1	−0.416–0.240	4.480	3	987	0.9–1.4	2
2012 Jan 16	SDSS 0901	WHT+UCAM	$u'\,g'\,r'$	55942.973064(20)^h	11	−0.132–0.146	4.480	3	417	1.1–1.6	2
2012 Jan 16	SDSS 0901	WHT+UCAM	$u'\,g'\,r'$	55943.050921(20)^h	12	−0.373–0.128	4.480	3	752	1.0–1.9	2
2012 Jan 16	SDSS 0901	WHT+UCAM	$u'\,g'\,r'$	55943.206687(20)^h	14	−0.125–0.179	4.480	3	456	1.1–1.7	2
2012 Jan 16	SDSS 0901	WHT+UCAM	$u'\,g'\,r'$	55943.284578(20)^h	15	−0.235–0.219	4.480	3	678	1.1–2.1	2
2012 Jan 15	SDSS 1006	WHT+UCAM	$u'\,g'\,r'$	55942.05221(10)^h	−3984	−0.116–0.180	3.980	3	1187	0.8–1.7	6
2014 Jan 25	SDSS 1006	TNT+USPEC	*KG5*	56682.72940(20)^h	0	−0.114–0.129	3.352	–	1165	1.6–2.3	1
2014 Jan 25	SDSS 1006	TNT+USPEC	*KG5*	56682.91552(20)^h	1	−0.190–0.127	3.352	–	1514	1.6–2.0	6
2014 Jan 26	SDSS 1006	TNT+USPEC	*KG5*	56683.84494(20)^h	6	−0.127–0.155	3.352	–	1342	1.2–1.4	3
2014 Jan 28	SDSS 1006	TNT+USPEC	*KG5*	56685.88995(20)^h	17	−0.171–0.131	3.352	–	1446	1.2–1.4	1
2014 Feb 02	SDSS 1006	TNT+USPEC	g'	56690.72366(20)^h	43	−0.267–0.176	5.892	–	1204	1.4–2.0	1
2014 Feb 02	SDSS 1006	TNT+USPEC	r'	56690.90953(20)^h	44	−0.143–0.117	3.352	–	1244	1.3–2.1	1

Table A.1: *Continued.*

Date	Object	Instrument Setup	Filter(s)	T_{mid} (MJD)	Cycle No.	Phase Coverage	T_{exp} (s)	$N_{u'}$	N_{exp}	Seeing ($''$)	Flag
2015 Dec 06	SDSS 1006	TNT+USPEC	g'	57362.79981(20)^h	3658	−0.144–0.138	4.946	–	974	2.2–3.6	7
2016 Mar 14	SDSS 1006	TNT+USPEC	g'	57461.70591(20)^h	4190	−0.266–0.202	9.640	–	783	1.0–3.1	7
2017 Feb 20	SDSS 1006	TNT+USPEC	*KG5*	57804.71547(20)^h	6035	−0.239–0.208	4.970	–	1437	1.4–3.4	6
2017 Feb 21	SDSS 1006	TNT+USPEC	g'	57805.64520(20)^h	6040	−0.198–0.152	5.470	–	1024	2.0–2.7	7
2012 Apr 28	SDSS 1057	WHT+UCAM	$u'\,g'\,r'$	56046.002399(12)^h	0	−0.581–0.149	4.021	3	981	1.2–2.7	2
2012 Apr 29	SDSS 1057	WHT+UCAM	$u'\,g'\,r'$	56046.944270(12)^h	15	−0.239–0.228	4.021	3	628	1.1–2.0	2
2013 Dec 30	SDSS 1057	WHT+UCAM	$u'\,g'\,r'$	56657.28205(3)^h	9735	−0.558–0.320	4.021	3	1178	1.0–1.6	7
2014 Jan 25	SDSS 1057	TNT+USPEC	*KG5*	56682.775595(12)^h	10141	−0.316–0.064	4.877	–	422	1.4–2.7	7
2014 Nov 28	SDSS 1057	TNT+USPEC	*KG5*	56989.82829(3)^h	15031	−0.225–0.138	3.945	–	498	1.3–2.5	7
2014 Nov 29	SDSS 1057	TNT+USPEC	*KG5*	56990.89570(3)^h	15048	−0.158–0.143	4.945	–	331	0.9–1.4	7
2015 Feb 24	SDSS 1057	TNT+USPEC	*KG5*	57077.862577(12)^h	16433	−0.219–0.281	11.852	–	230	1.4–2.1	2
2015 Feb 25	SDSS 1057	TNT+USPEC	*KG5*	57078.867265(12)^h	16449	−0.207–0.169	11.946	–	172	2.0–2.4	2
2015 Mar 01	SDSS 1057	TNT+USPEC	*KG5*	57082.885950(12)^h	16513	−0.101–0.138	11.852	–	111	1.4–1.8	2
2015 Jun 21	SDSS 1057	WHT+UCAM	$u'\,g'\,r'$	57194.906824(12)^h	18297	−0.390–0.182	4.021	3	769	1.2–2.1	2
2015 Jun 22	SDSS 1057	WHT+UCAM	$u'\,g'\,r'$	57195.911476(12)^h	18313	−0.170–0.171	4.021	3	460	1.2–2.3	2
2015 Jun 23	SDSS 1057	WHT+UCAM	$u'\,g'\,r'$	57196.916157(12)^h	18329	−0.179–0.130	4.021	3	416	1.1–2.0	5
2010 Jan 07	SDSS 1152	WHT+UCAM	$u'\,g'\,r'$	55204.101280(10)^h	0	−0.840–0.137	3.800	3	1492	2.4–4.0	2
2010 Jan 07	SDSS 1152	WHT+UCAM	$u'\,g'\,r'$	55204.169035(10)^h	1	−0.274–0.116	3.800	3	600	1.2–2.6	2
2010 Jan 07	SDSS 1152	WHT+UCAM	$u'\,g'\,r'$	55204.236772(10)^h	2	−0.151–0.119	3.800	3	415	1.5–3.0	2
2014 Mar 14	SDSS 1152	WHT+UCAM	$u'\,g'\,r'$	56730.908566(10)^h	22536	−0.265–0.195	4.029	3	668	1.2–1.7	7
2014 Mar 30	SDSS 1152	TNT+USPEC	*KG5*	56746.694264(10)^h	22769	−0.385–0.195	5.352	–	634	1.3–1.6	2
2014 Mar 30	SDSS 1152	TNT+USPEC	*KG5*	56746.762006(10)^h	22770	−0.322–0.259	5.352	–	634	1.2–1.7	2
2014 Mar 30	SDSS 1152	TNT+USPEC	*KG5*	56746.829759(10)^h	22771	−0.290–0.285	5.352	–	628	1.4–1.9	2

Table A.1: *Continued.*

Date	Object	Instrument Setup	Filter(s)	T_{mid} (MJD)	Cycle No.	Phase Coverage	T_{exp} (s)	$N_{u'}$	N_{exp}	Seeing ($''$)	Flag
2004 May 17	SDSS 1501	WHT+UCAM	$u'\,g'\,r'$	53142.921635(10)^h	−53411	−0.198–0.218	6.115	1	335	0.9–1.4	1
2006 Mar 04	SDSS 1501	WHT+UCAM	$u'\,g'\,r'$	53799.210838(10)^h	−41865	−0.663–0.165	4.971	1	813	1.4–2.4	6
2006 Mar 05	SDSS 1501	WHT+UCAM	$u'\,g'\,r'$	53800.120302(10)^h	−41849	−0.845–0.195	5.971	1	853	2.1–3.9	6
2006 Mar 07	SDSS 1501	WHT+UCAM	$u'\,g'\,r'$	53802.052900(10)^h	−41815	−0.294–0.192	4.971	1	480	1.0–1.5	6
2006 Mar 07	SDSS 1501	WHT+UCAM	$u'\,g'\,r'$	53802.109742(10)^h	−41814	−0.316–0.217	4.971	1	525	1.1–1.4	6
2006 Mar 07	SDSS 1501	WHT+UCAM	$u'\,g'\,r'$	53802.223433(10)^h	−41812	−0.189–0.214	4.971	1	397	1.0–1.3	6
2006 Mar 08	SDSS 1501	WHT+UCAM	$u'\,g'\,r'$	53803.132876(10)^h	−41796	−0.175–0.143	4.971	1	315	1.1–1.6	6
2006 Mar 08	SDSS 1501	WHT+UCAM	$u'\,g'\,r'$	53803.189718(10)^h	−41795	−0.057–0.141	4.971	1	197	1.1–1.5	6
2006 Mar 08	SDSS 1501	WHT+UCAM	$u'\,g'\,r'$	53803.246575(10)^h	−41794	−0.088–0.139	4.971	1	227	0.9–1.1	6
2010 Jan 07	SDSS 1501	WHT+UCAM	$u'\,g'\,r'$	55204.213149(15)^h	−17147	−0.217–0.120	3.800	3	435	1.4–3.9	7
2010 Jan 07	SDSS 1501	WHT+UCAM	$u'\,g'\,r'$	55204.270013(15)^h	−17146	−0.119–0.129	3.800	3	321	1.2–2.7	7
2012 Sep 08	SDSS 1501	WHT+UCAM	$u'\,g'\,r'$	56178.870508(10)^h	0	−0.158–0.165	3.475	3	455	1.0–1.5	1
2014 Aug 03	SSS100615	WHT+UCAM	$u'\,g'\,r'$	56873.023626(5)^h	0	−0.764–0.157	3.005	4	1538	1.0–1.2	2
2014 Aug 04	SSS100615	WHT+UCAM	$u'\,g'\,r'$	56874.021600(5)^h	17	−0.084–0.162	3.005	3	416	1.0–1.1	2
2014 Aug 05	SSS100615	WHT+UCAM	$u'\,g'\,i'$	56874.960873(5)^h	33	−0.114–0.103	5.056	3	219	1.7–2.3	2
2014 Jan 26	SSS130413	TNT+USPEC	*KG5*	56683.67392(5)^h	0	−0.175–0.195	5.804	–	362	1.6–2.2	3
2014 Jan 26	SSS130413	TNT+USPEC	*KG5*	56683.73977(5)^h	1	−0.085–0.141	5.804	–	222	1.5–2.0	1
2014 Jan 26	SSS130413	TNT+USPEC	*KG5*	56683.80551(5)^h	2	−0.230–0.194	5.804	–	415	1.3–1.5	1
2014 Jan 27	SSS130413	TNT+USPEC	*KG5*	56684.72635(5)^h	16	−0.602–0.349	5.804	–	928	1.8–2.9	3
2014 Jan 28	SSS130413	TNT+USPEC	*KG5*	56685.71280(5)^h	31	−0.209–0.181	2.934	–	752	1.4–1.7	3
2014 Feb 01	SSS130413	TNT+USPEC	*KG5*	56689.65905(5)^h	91	−0.291–0.191	2.934	–	931	1.9–2.2	3
2014 Feb 01	SSS130413	TNT+USPEC	*KG5*	56689.85631(5)^h	94	−0.148–0.176	2.934	–	627	1.5–2.0	1
2014 Feb 02	SSS130413	TNT+USPEC	g'	56690.77702(5)^h	108	−0.304–0.215	2.934	–	998	1.5–1.7	1

Table A.1: *Continued.*

Date	Object	Instrument Setup	Filter(s)	T_{mid} (MJD)	Cycle No.	Phase Coverage	T_{exp} (s)	$N_{u'}$	N_{exp}	Seeing ($''$)	Flag
2014 Feb 02	SSS130413	TNT+USPEC	r'	56690.84278(5)^h	109	−0.223–0.126	2.934	–	673	1.3–1.5	1
2014 Mar 23	SSS130413	TNT+USPEC	*KG5*	56739.64406(8)^h	851	−0.177–0.149	2.934	–	628	1.3–1.6	7
2015 Jan 01	SSS130413	TNT+USPEC	i'	57023.76697(3)^h	5171	−0.120–0.190	2.939	–	595	1.0–1.4	7
2016 Jan 29	SSS130413	TNT+USPEC	u'	57416.73848(5)^h	11146	−0.388–0.161	9.252	–	338	2.7–3.6	7
2016 Jan 31	SSS130413	TNT+USPEC	u'	57418.71160(5)^h	11176	−0.228–0.167	8.052	–	280	2.0–2.7	1
2017 Feb 12	SSS130413	TNT+USPEC	r'	57796.75351(10)^h	16924	−0.656–0.244	8.052	–	670	1.8–2.7	7
2017 Feb 20	SSS130413	TNT+USPEC	g'	57804.77728(3)^h	17046	−0.210–0.147	3.951	–	511	2.1–3.1	4
2017 Feb 21	SSS130413	TNT+USPEC	*KG5*	57805.69806(3)^h	17060	−0.284–0.285	3.951	–	815	1.4–2.7	4
2017 Feb 24	SSS130413	TNT+USPEC	r'	57808.78922(3)^h	17107	−0.305–0.186	3.952	–	705	1.2–1.6	4
2011 Aug 27	V713 Cep	WHT+UCAM	$u'\,g'\,i'$	55801.180379(20)^h	−4399	−0.383–0.136	2.185	2	1737	1.2–1.6	6
2012 Sep 06	V713 Cep	WHT+UCAM	$u'\,g'\,r'$	56176.936374(20)^h	0	−0.373–0.127	3.445	3	1065	1.0–1.2	3
2012 Sep 07	V713 Cep	WHT+UCAM	$u'\,g'\,r'$	56177.875986(20)^h	11	−0.346–0.184	3.445	3	1126	1.0–1.2	1
2012 Sep 09	V713 Cep	WHT+UCAM	$u'\,g'\,r'$	56180.011450(20)^h	36	−0.212–0.169	3.445	3	811	0.9–1.4	6
2013 Jul 14	V713 Cep	WHT+UCAM	$u'\,g'\,z'$	56488.201454(20)^h	3644	−0.309–0.291	3.445	3	1277	1.0–1.2	3
2013 Jul 15	V713 Cep	WHT+UCAM	$u'\,g'\,i'$	56489.055641(20)^h	3654	−0.124–0.162	3.445	3	609	1.1–1.3	3
2013 Jul 15	V713 Cep	WHT+UCAM	$u'\,g'\,i'$	56489.141063(20)^h	3655	−0.105–0.111	3.445	3	460	0.9–4.5	1
2013 Jul 15	V713 Cep	WHT+UCAM	$u'\,g'\,i'$	56489.226484(20)^h	3656	−0.429–0.110	3.445	3	1150	0.9–1.1	7
2013 Jul 25	V713 Cep	WHT+UCAM	$u'\,g'\,z'$	56499.220435(20)^h	3773	−0.275–0.205	3.445	3	1022	1.1–1.3	6
2013 Aug 04	V713 Cep	WHT+UCAM	$u'\,g'\,r'$	56509.214395(20)^h	3890	−0.323–0.308	3.445	3	1342	1.1–1.7	3
2013 Aug 05	V713 Cep	WHT+UCAM	$u'\,g'\,r'$	56510.154021(20)^h	3901	−0.288–0.168	3.445	3	971	0.9–1.4	6
2014 Aug 02	V713 Cep	WHT+UCAM	$u'\,g'\,r'$	56872.07224(3)^h	8138	−0.388–0.216	1.983	3	2224	1.4–3.0	6
2014 Aug 10	V713 Cep	WHT+UCAM	$u'\,g'\,i'$	56880.18702(3)^h	8233	−0.182–0.155	3.445	3	719	1.1–2.4	7

Table A.1: *Continued.*

Date	Object	Instrument Setup	Filter(s)	T_{mid} (MJD)	Cycle No.	Phase Coverage	T_{exp} (s)	$N_{u'}$	N_{exp}	Seeing (″)	Flag
2015 Jun 24	V713 Cep	WHT+UCAM	$u'\,g'\,r'$	57198.114652(20)^h	11955	−0.213–0.070	3.445	3	603	0.8–1.0	6
2015 Sep 17	V713 Cep	WHT+UCAM	$u'\,g'\,r'$	57282.849778(20)^h	12947	−0.047–0.118	4.985	3	245	1.1–1.5	6
2005 May 07	Z Cha	VLT+UCAM	$u'\,g'\,r'$	53498.011478(10)^h	0	−0.147–0.142	0.476	1	4300	1.7–2.3	3
2005 May 10	Z Cha	VLT+UCAM	$u'\,g'\,r'$	53500.991449(10)^h	40	−0.373–0.175	0.476	1	7632	1.3–4.8	6
2005 May 12	Z Cha	VLT+UCAM	$u'\,g'\,r'$	53503.002929(10)^h	67	−0.071–0.113	0.476	1	10070	2.1–8.1	3
2005 May 15	Z Cha	VLT+UCAM	$u'\,g'\,r'$	53505.982900(10)^h	107	−0.108–0.204	0.476	1	7007	1.7–2.7	3
2005 May 17	Z Cha	VLT+UCAM	$u'\,g'\,r'$	53507.994355(10)^h	134	−0.586–0.176	0.476	1	9769	2.1–3.9	3
2005 May 21	Z Cha	VLT+UCAM	$u'\,g'\,r'$	53512.017323(10)^h	188	−0.113–0.161	0.476	1	6674	1.8–3.6	3
2010 Apr 26	Z Cha	NTT+UCAM	$u'\,g'\,r'$	55313.03694(3)^h	24363	−0.056–0.119	1.517	4	731	2.6–3.6	6
2010 Jun 06	Z Cha	NTT+UCAM	$u'\,g'\,r'$	55354.08603(10)^h	24914	−0.337–0.090	1.331	3	2024	1.1–1.8	8
2010 Nov 26	Z Cha	NTT+UCAM	$u'\,g'\,i'$	55527.147891(20)^h	27237	−0.063–0.097	1.381	3	1636	0.8–1.1	1
2010 Dec 02	Z Cha	NTT+UCAM	$u'\,g'\,r'$	55533.33134(10)^h	27320	−0.153–0.265	1.324	3	1996	1.1–1.7	8
2010 Dec 11	Z Cha	NTT+UCAM	$u'\,g'\,i'$	55542.345728(20)^h	27441	−0.169–0.171	1.331	3	1775	1.1–1.6	6
2010 Dec 17	Z Cha	NTT+UCAM	$u'\,g'\,i'$	55548.082204(20)^h	27518	−0.136–0.128	2.874	2	589	1.1–2.0	1
2010 Dec 17	Z Cha	NTT+UCAM	$u'\,g'\,i'$	55548.305686(20)^h	27521	−0.124–0.134	2.874	2	576	0.8–1.0	3
2011 May 19	Z Cha	NTT+UCAM	$u'\,g'\,r'$	55701.029233(20)^h	29571	−0.295–0.202	2.855	2	1108	1.8–3.6	1

Table A.1: *Continued.*

Appendix B

Model Fits

The following figures show the full sets of eclipse model fits for the 15 additional systems from Section 7.4.1.

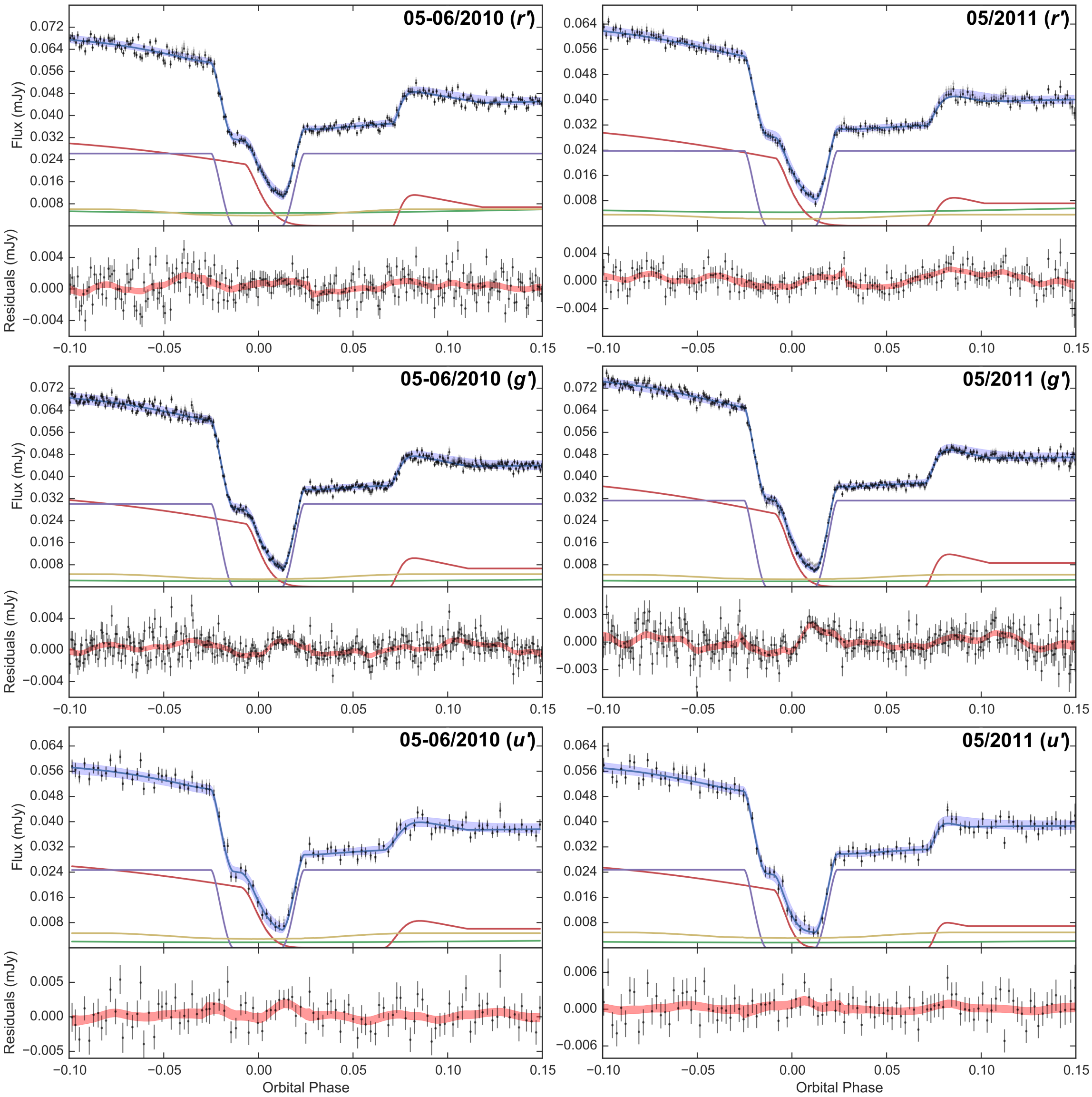

Figure B.1: Simultaneous eclipse model fit to six average CSS080623 eclipse light curves. See Section 7.4.1 for full details of what is plotted. Displayed in the top-right corner of each average eclipse plot is the month(s) and wavelength band each of the constituent eclipses were observed in.

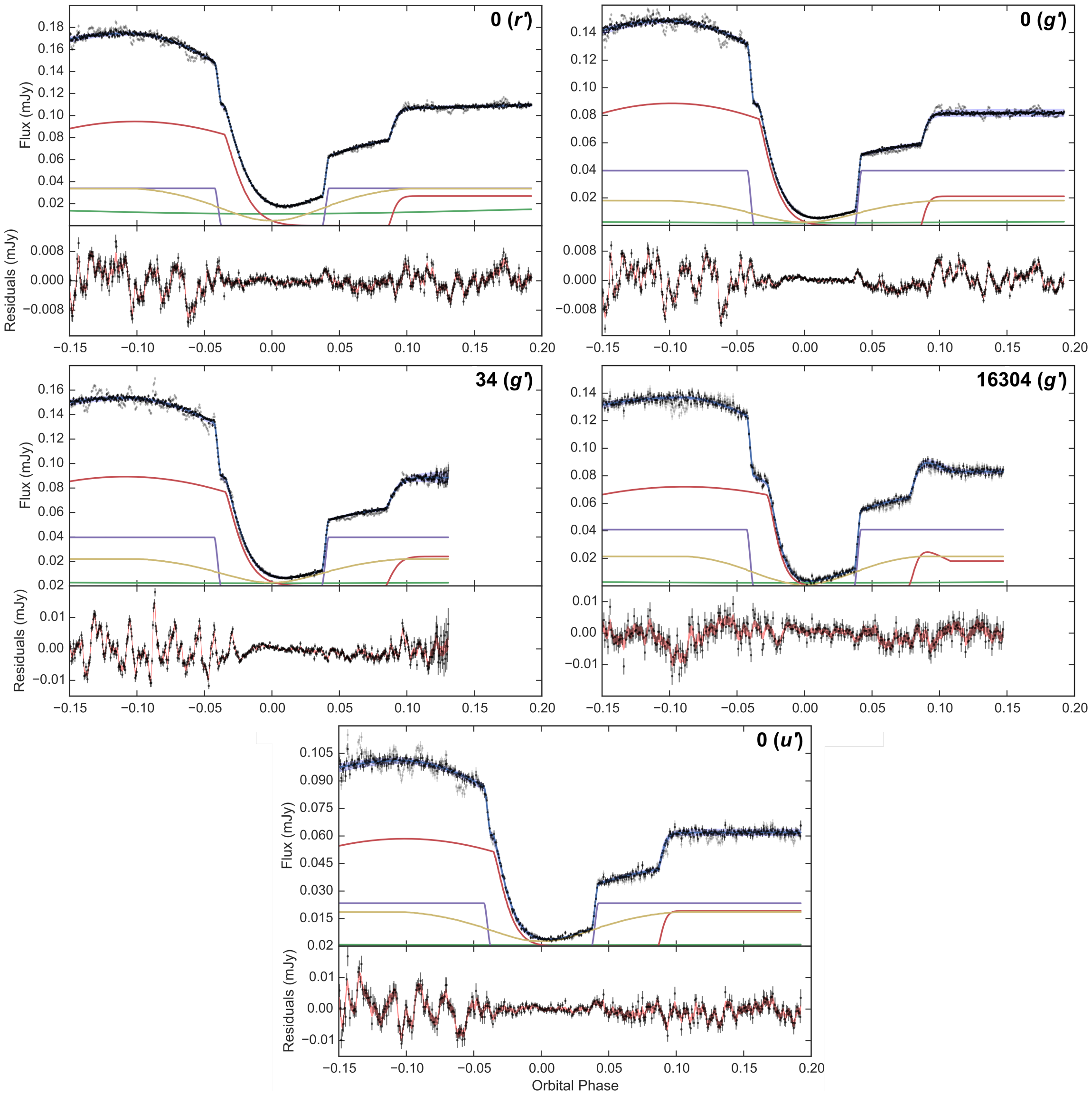

Figure B.2: Simultaneous eclipse model fit to five CTCV 1300 eclipse light curves. See Section 7.4.1 for full details of what is plotted. Displayed in the top-right corner of each eclipse plot is the cycle no. of the eclipse and the wavelength band it was observed in.

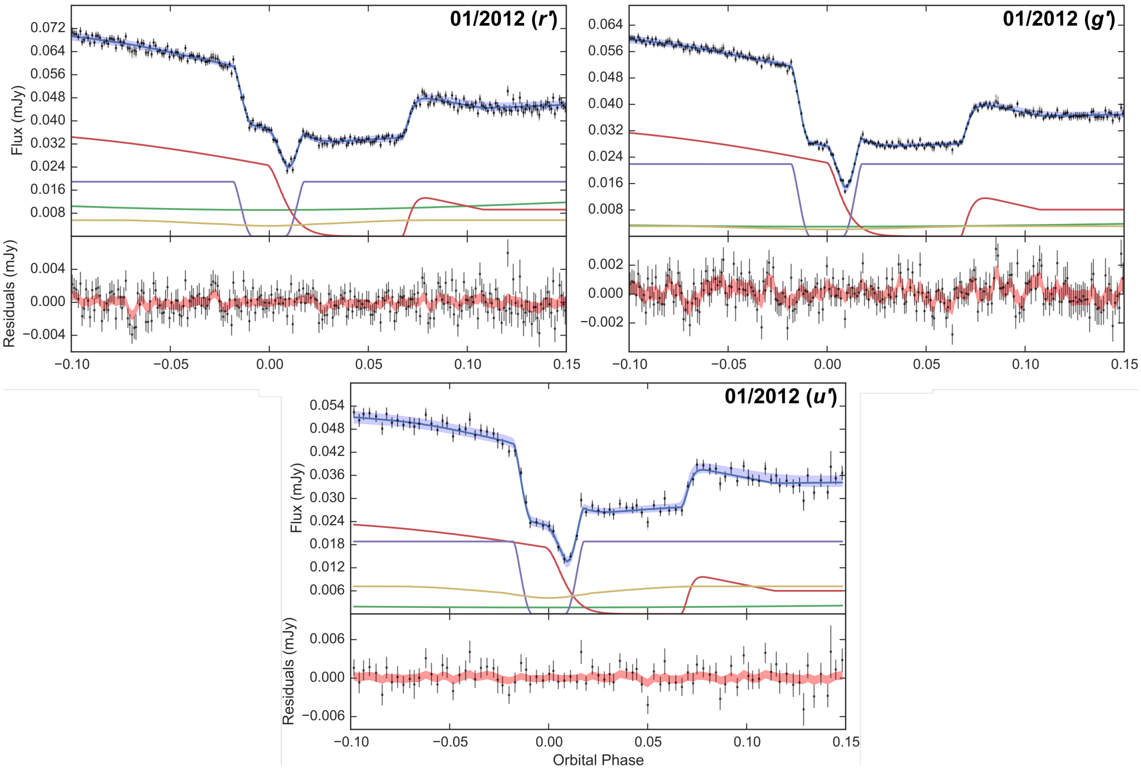

Figure B.3: Simultaneous eclipse model fit to three average CSS110113 eclipse light curves. See Section 7.4.1 for full details of what is plotted. Displayed in the top-right corner of each average eclipse plot is the month and wavelength band each of the constituent eclipses were observed in.

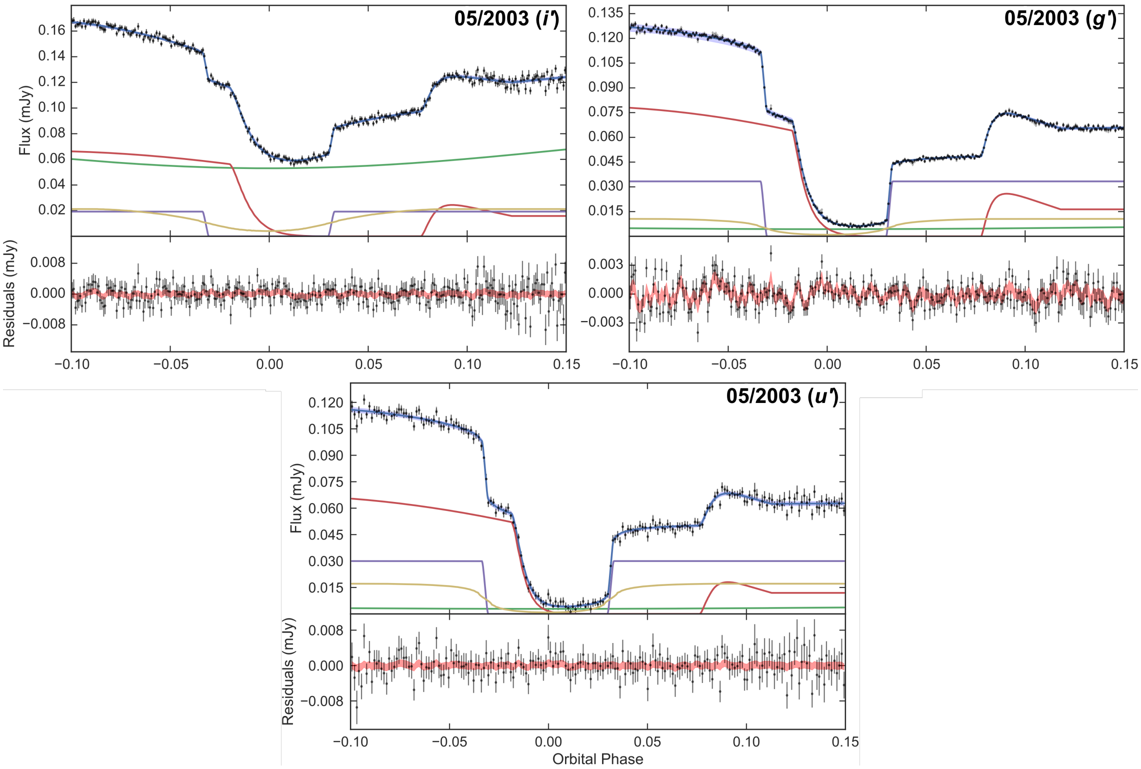

Figure B.4: Simultaneous eclipse model fit to three average DV UMa eclipse light curves. See Section 7.4.1 for full details of what is plotted. Displayed in the top-right corner of each average eclipse plot is the month and wavelength band each of the constituent eclipses were observed in.

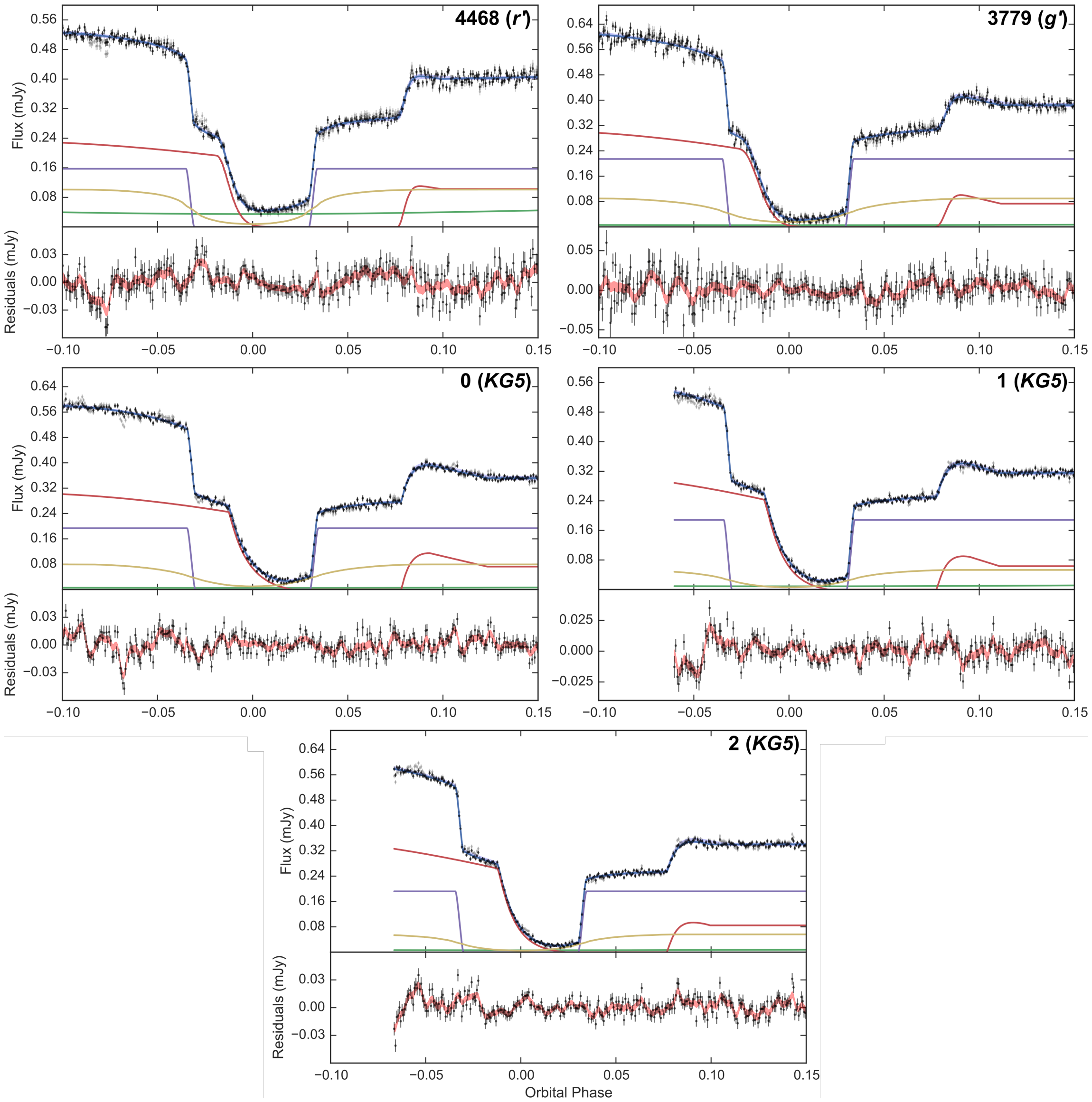

Figure B.5: Simultaneous eclipse model fit to five IY UMa eclipse light curves. See Section 7.4.1 for full details of what is plotted. Displayed in the top-right corner of each eclipse plot is the cycle no. of the eclipse and the wavelength band it was observed in.

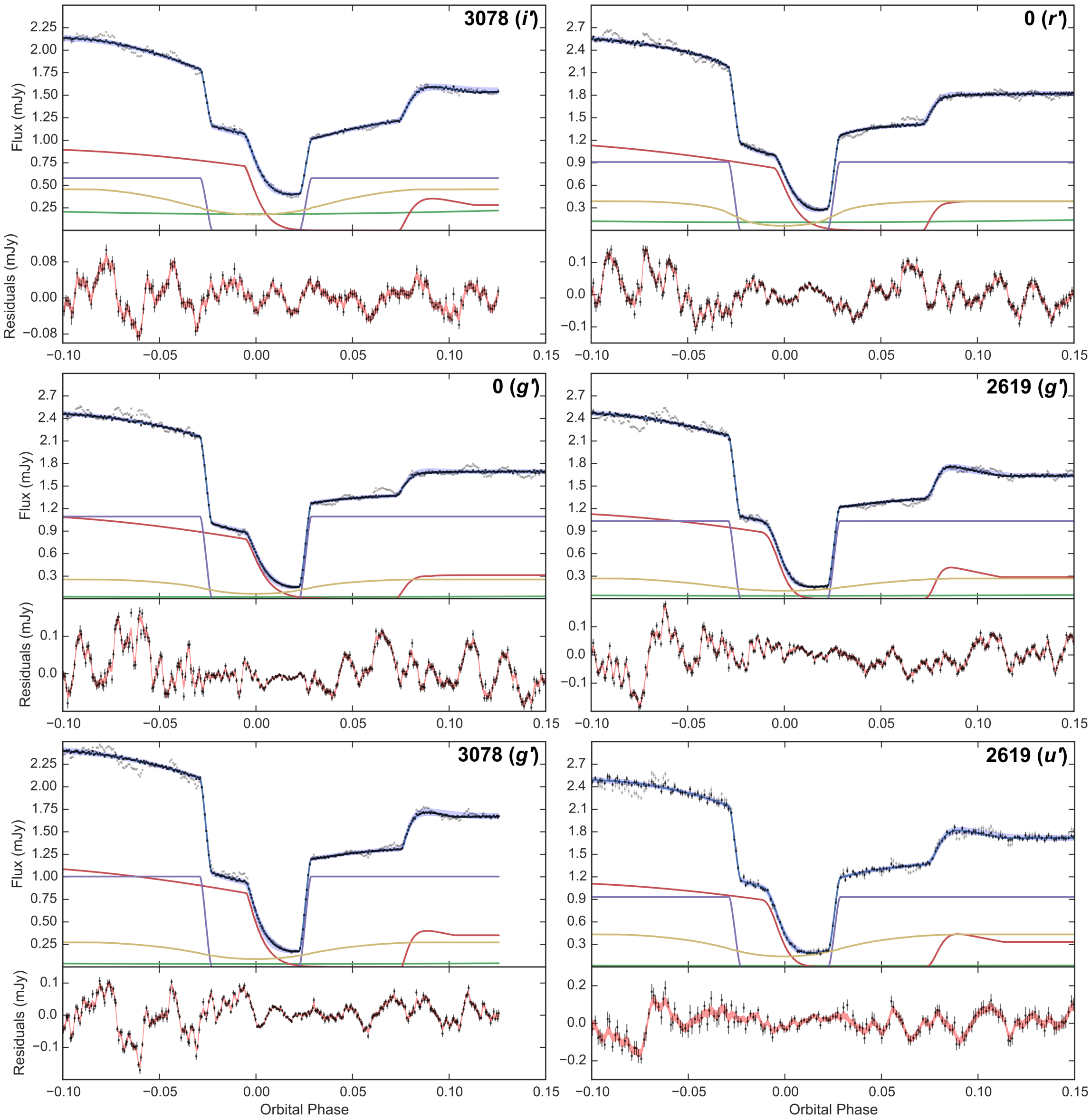

Figure B.6: Simultaneous eclipse model fit to six OY Car eclipse light curves. See Section 7.4.1 for full details of what is plotted. Displayed in the top-right corner of each eclipse plot is the cycle no. of the eclipse and the wavelength band it was observed in.

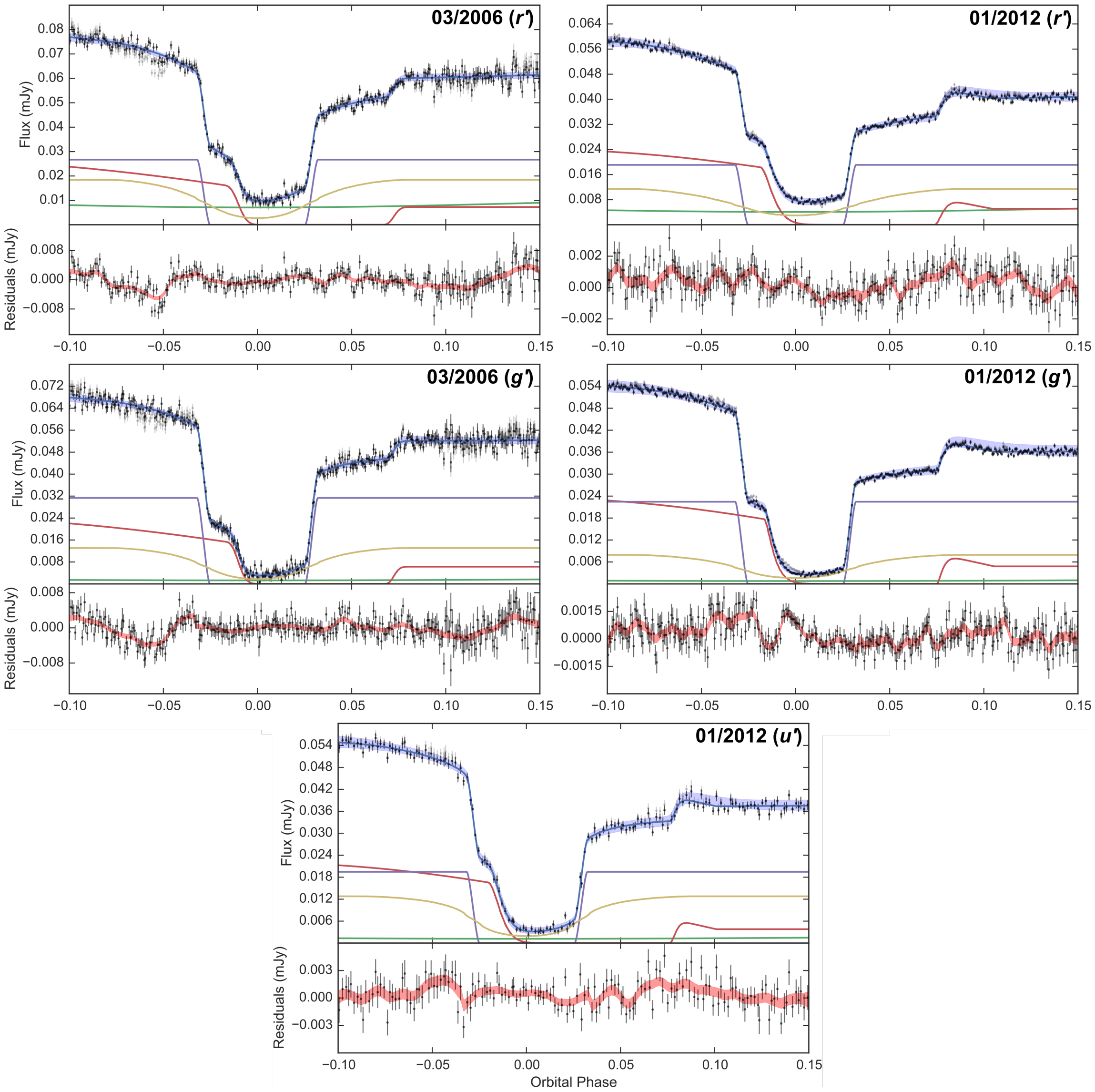

Figure B.7: Simultaneous eclipse model fit to five average SDSS 0901 eclipse light curves. See Section 7.4.1 for full details of what is plotted. Displayed in the top-right corner of each average eclipse plot is the month and wavelength band each of the constituent eclipses were observed in.

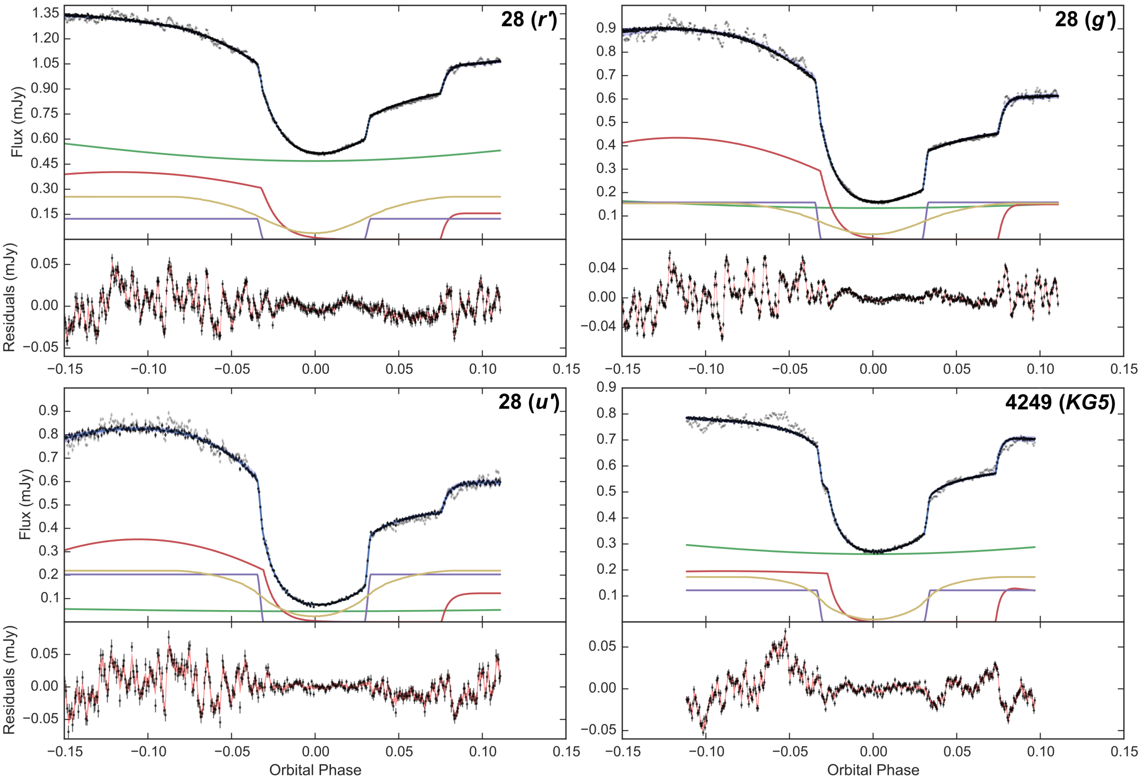

Figure B.8: Simultaneous eclipse model fit to four GY Cnc eclipse light curves. See Section 7.4.1 for full details of what is plotted. Displayed in the top-right corner of each eclipse plot is the cycle no. of the eclipse and the wavelength band it was observed in.

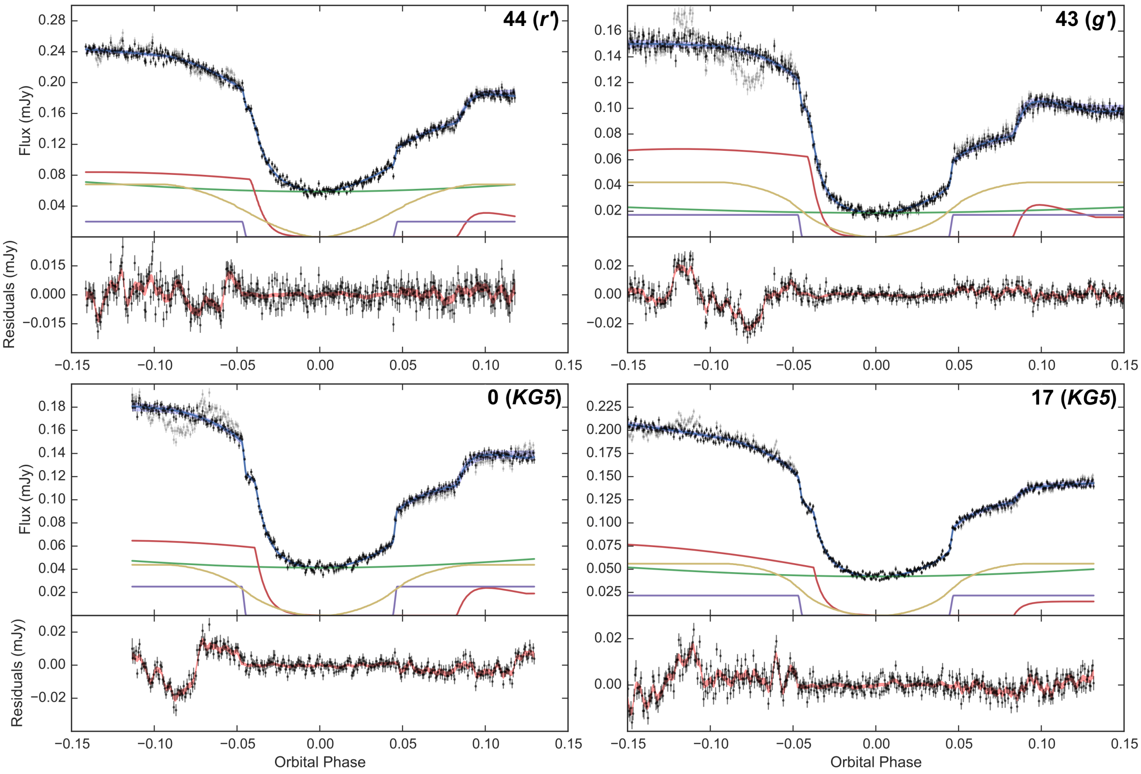

Figure B.9: Simultaneous eclipse model fit to four SDSS 1006 eclipse light curves. See Section 7.4.1 for full details of what is plotted. Displayed in the top-right corner of each eclipse plot is the cycle no. of the eclipse and the wavelength band it was observed in.

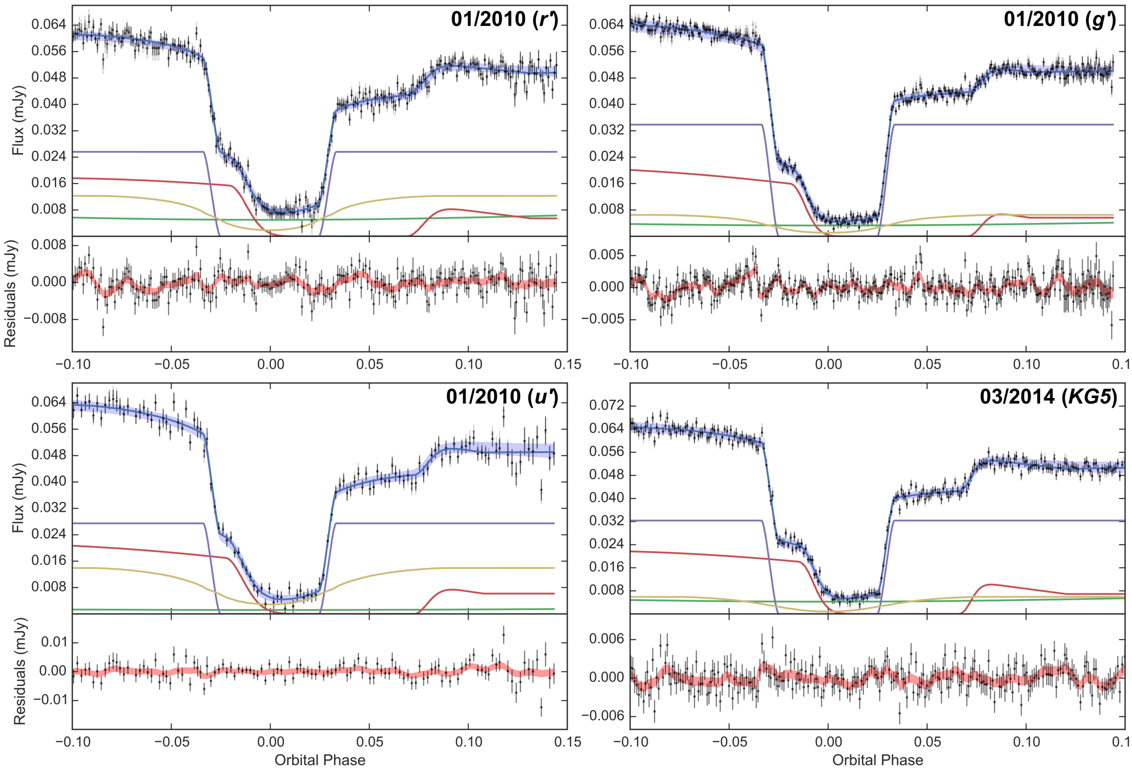

Figure B.10: Simultaneous eclipse model fit to four average SDSS 1152 eclipse light curves. See Section 7.4.1 for full details of what is plotted. Displayed in the top-right corner of each average eclipse plot is the month and wavelength band each of the constituent eclipses were observed in.

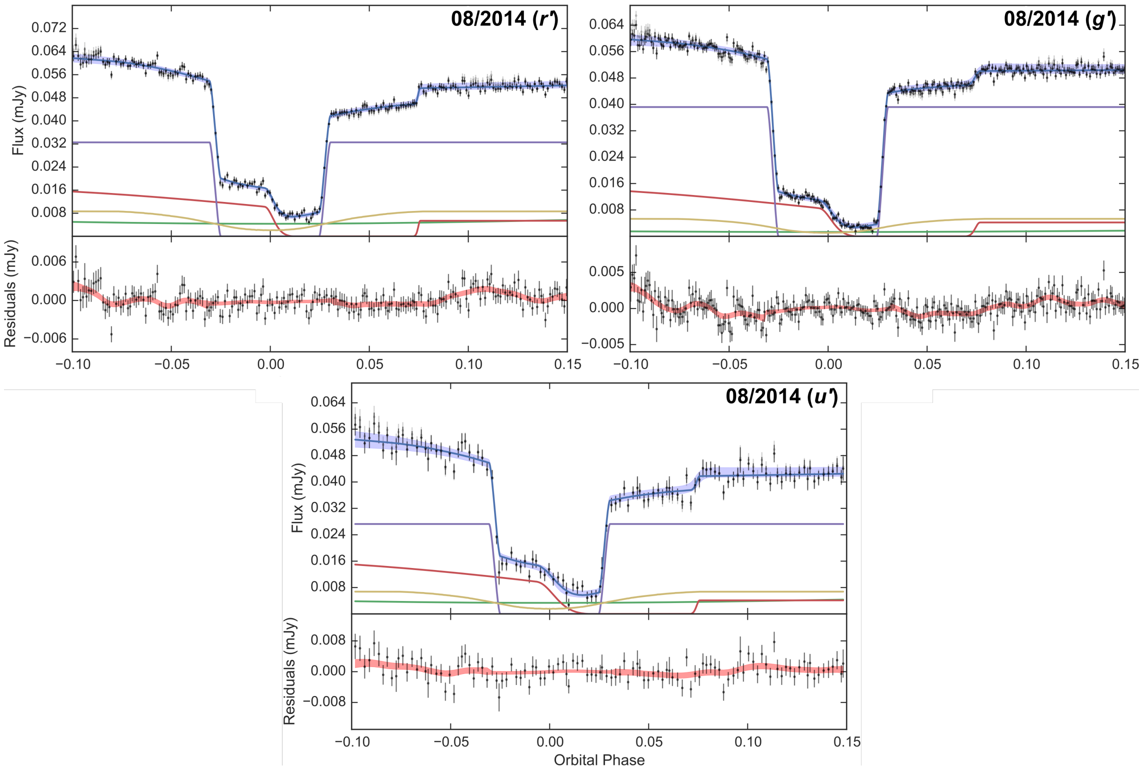

Figure B.11: Simultaneous eclipse model fit to three average SSS100615 eclipse light curves. See Section 7.4.1 for full details of what is plotted. Displayed in the top-right corner of each average eclipse plot is the month and wavelength band each of the constituent eclipses were observed in.

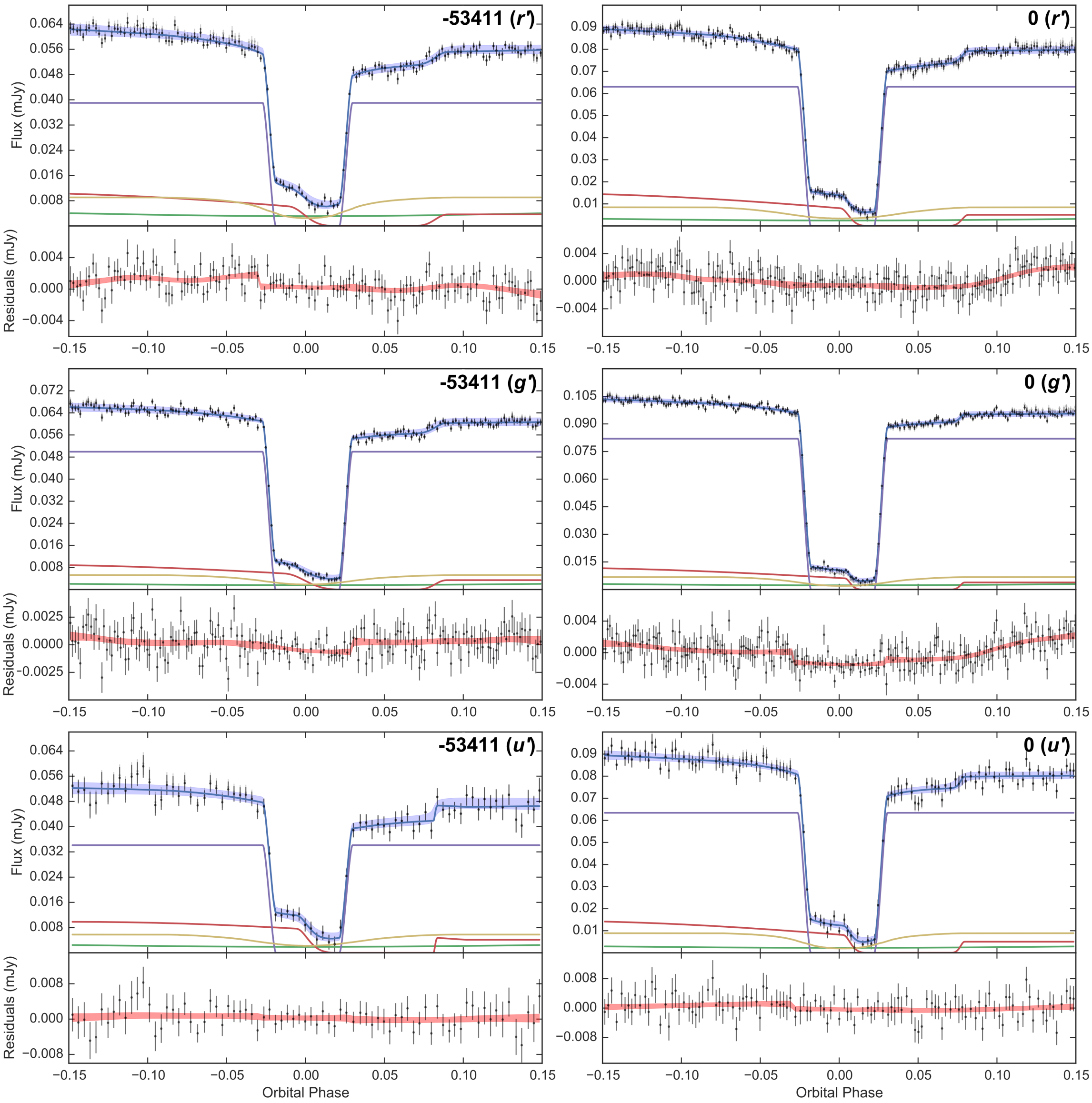

Figure B.12: Simultaneous eclipse model fit to six SDSS 1501 eclipse light curves. See Section 7.4.1 for full details of what is plotted. Displayed in the top-right corner of each eclipse plot is the cycle no. of the eclipse and the wavelength band it was observed in.

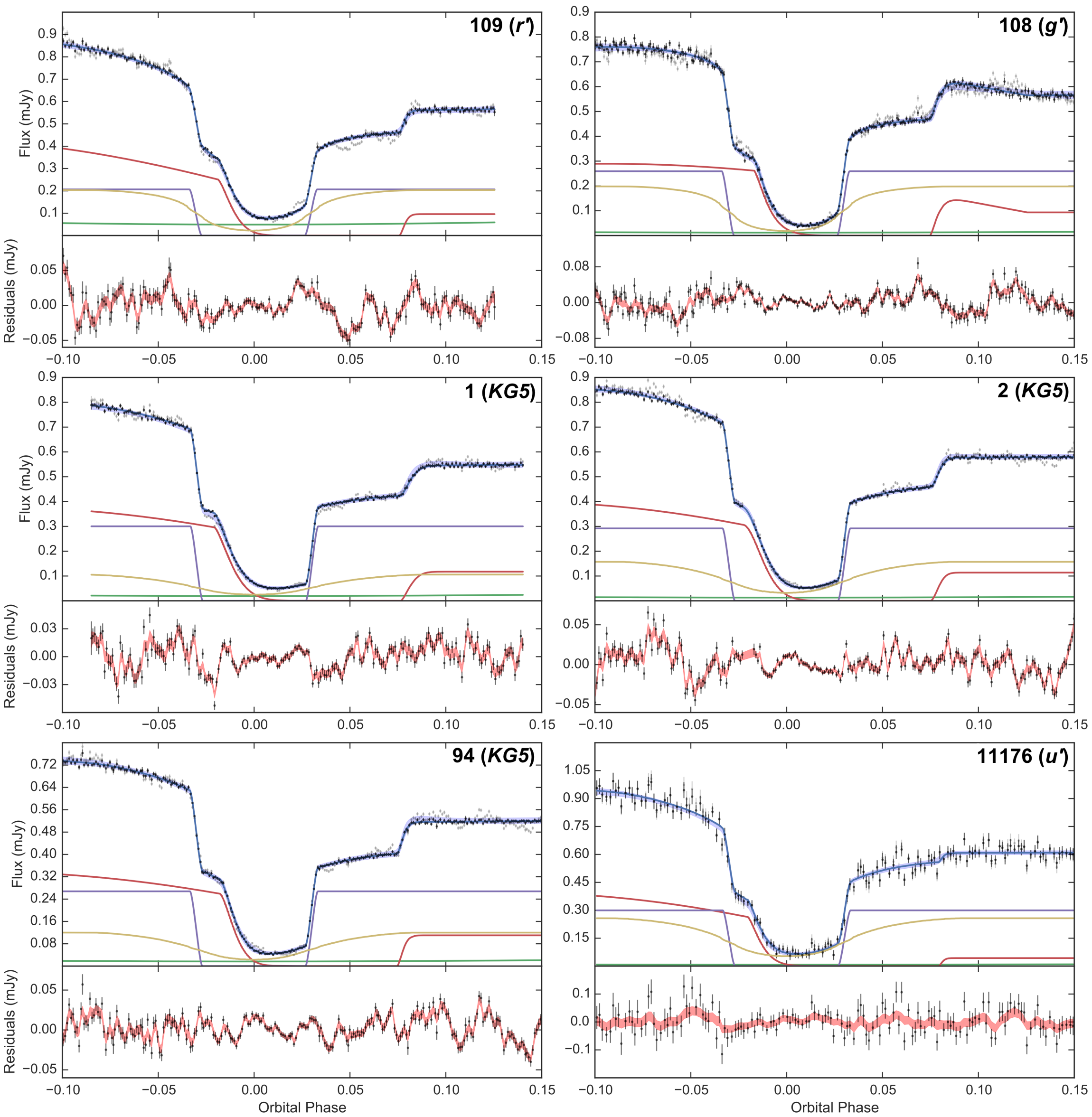

Figure B.13: Simultaneous eclipse model fit to six SSS130413 eclipse light curves. See Section 7.4.1 for full details of what is plotted. Displayed in the top-right corner of each eclipse plot is the cycle no. of the eclipse and the wavelength band it was observed in.

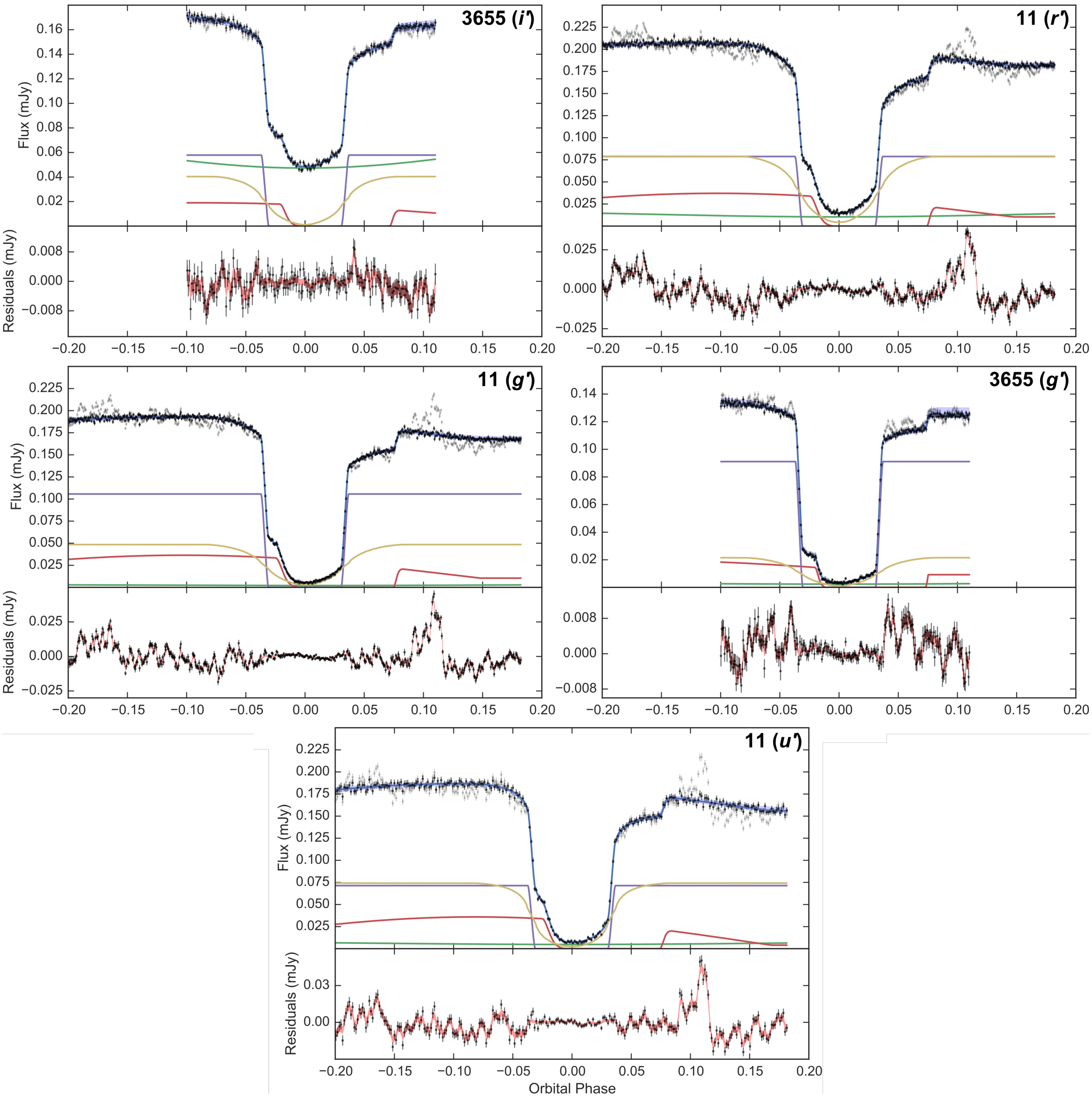

Figure B.14: Simultaneous eclipse model fit to five V713 Cep eclipse light curves. See Section 7.4.1 for full details of what is plotted. Displayed in the top-right corner of each eclipse plot is the cycle no. of the eclipse and the wavelength band it was observed in.

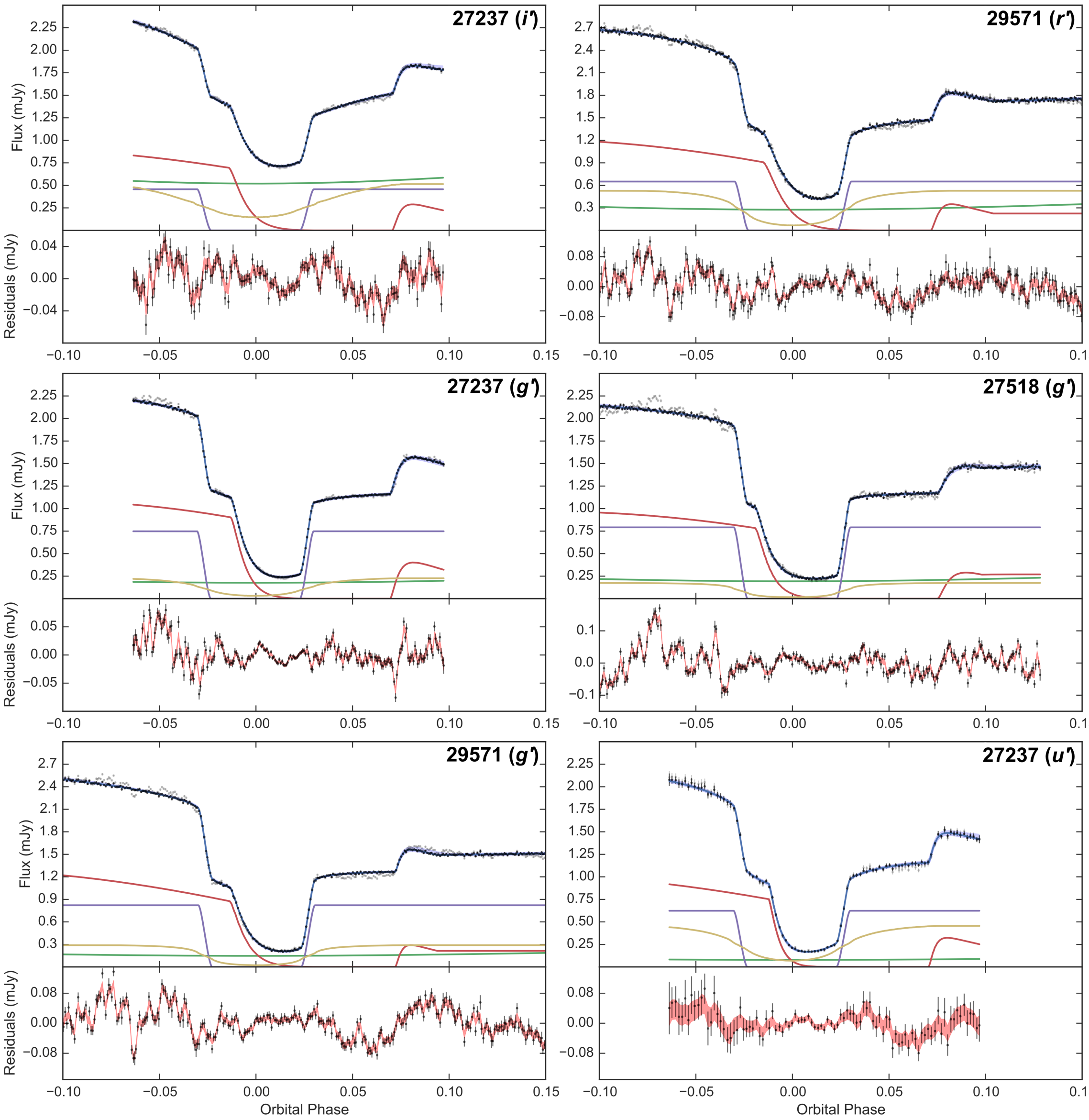

Figure B.15: Simultaneous eclipse model fit to six Z Cha eclipse light curves. See Section 7.4.1 for full details of what is plotted. Displayed in the top-right corner of each eclipse plot is the cycle no. of the eclipse and the wavelength band it was observed in.

Appendix C

Model Parameters

The following tables include the model parameters for the numerous eclipse model fits performed across Chapters 4, 5, 6 and 7 of this work.

PHL 1445 – Average eclipse fits			
Cycle no.	–	–	–
Band	r'	g'	u'
q	0.0868 ± 0.0006	0.0870 ± 0.0009	0.097 ± 0.004
$\Delta\phi$	0.05399 ± 0.00009	0.05384 ± 0.00006	0.0535 ± 0.0005
R_1/x_{L1}	0.0282 ± 0.0006	0.0275 ± 0.0004	0.027 ± 0.003
$R_{\mathrm{disc}}/x_{\mathrm{L1}}$	0.4139 ± 0.0017	0.405 ± 0.005	0.395 ± 0.013
S/x_{L1}	0.0170 ± 0.0013	0.033 ± 0.003	0.015 ± 0.005
θ_{az}	150.8 ± 1.2	165.1 ± 1.4	125 ± 12
f_{iso}	0.416 ± 0.011	0.414 ± 0.014	0.06 ± 0.18
b	0.006 ± 0.019	0.29 ± 0.11	0.04 ± 0.22
ϕ_0 ($\times 10^{-5}$)	-6 ± 4	-3.0 ± 1.7	-1 ± 15
Y	–	–	–
Z	–	–	–
θ_{tilt}	–	–	–
θ_{yaw}	–	–	–
F_1 (mJy)	0.1284 ± 0.0006	0.1393 ± 0.0005	0.104 ± 0.003
F_{disc} (mJy)	0.1081 ± 0.0012	0.0586 ± 0.0009	0.088 ± 0.006
F_{bs} (mJy)	0.0493 ± 0.0003	0.04783 ± 0.00029	0.0390 ± 0.0012
F_2 (mJy)	0.0127 ± 0.0008	0.0058 ± 0.0004	0.0004 ± 0.0027
U_1	0.340	0.390	0.469

Table C.1: Model parameters for the average PHL 1445 eclipse light curve fits in Section 4.3.1.

PHL 1445 – Individual r'-band eclipse fits					
q	0.0868*				
$\Delta\phi$	0.05399*				
R_1/x_{L1}	0.0282*				
Cycle no.	0	1413	1430	1431	1542
Band	r'	r'	r'	r'	r'
R_{disc}/x_{L1}	0.533 ± 0.005	0.430 ± 0.004	0.290 ± 0.003	0.381 ± 0.004	0.498 ± 0.008
S/x_{L1}	0.050 ± 0.007	0.028 ± 0.006	0.0208 ± 0.0019	0.023 ± 0.004	0.0234 ± 0.0025
θ_{az}	159.9 ± 2.5	162.6 ± 2.0	104 ± 4	160.7 ± 1.4	109 ± 5
f_{iso}	0.999 ± 0.004	0.446 ± 0.023	0.15 ± 0.11	0.169 ± 0.011	0.00 ± 0.12
b	0.003 ± 0.020	0.001 ± 0.008	1.50 ± 0.08	0.01 ± 0.05	1.23 ± 0.18
ϕ_0 ($\times 10^{-5}$)	-4 ± 7	-32 ± 8	-6 ± 8	-15 ± 6	6 ± 6
Y	–	–	–	–	–
Z	–	–	–	–	–
θ_{tilt}	–	–	–	–	–
θ_{yaw}	–	–	–	–	–
F_1 (mJy)	0.1420 ± 0.0005	0.1194 ± 0.0007	0.1374 ± 0.0019	0.1175 ± 0.0007	0.1172 ± 0.0014
F_{disc} (mJy)	0.1802 ± 0.0008	0.1338 ± 0.0011	0.0528 ± 0.0025	0.0842 ± 0.0009	0.1005 ± 0.0024
F_{bs} (mJy)	0.0267 ± 0.0008	0.0589 ± 0.0006	0.0483 ± 0.0006	0.0736 ± 0.0006	0.0393 ± 0.0006
F_2 (mJy)	0 ± 0	0 ± 0	0.0372 ± 0.0010	0 ± 0	0.0362 ± 0.0014
U_1	0.340	0.340	0.340	0.340	0.340
Cycle no.	5889	6547	14942	14945	14961
Band	i'	r'	r'	r'	r'
R_{disc}/x_{L1}	0.545 ± 0.014	0.570 ± 0.004	0.575 ± 0.004	0.4178 ± 0.0020	0.5171 ± 0.0023
S/x_{L1}	0.186 ± 0.011	0.046 ± 0.007	0.0581 ± 0.0028	0.076 ± 0.010	0.0111 ± 0.0009
θ_{az}	160.2 ± 0.8	168.94 ± 0.06	159.4 ± 0.8	168.93 ± 0.08	131.1 ± 1.6
f_{iso}	0.49 ± 0.03	0.056 ± 0.009	1.0000 ± 0.0027	0.291 ± 0.027	0.003 ± 0.021
b	1.11 ± 0.16	0.002 ± 0.009	0.70 ± 0.08	0.001 ± 0.007	0.01 ± 0.03
ϕ_0 ($\times 10^{-5}$)	-87 ± 13	-11 ± 6	-79 ± 6	-89 ± 6	4 ± 7
Y	–	–	–	–	–
Z	–	–	–	–	–
θ_{tilt}	–	–	–	–	–
θ_{yaw}	–	–	–	–	–
F_1 (mJy)	0.0946 ± 0.0025	0.1578 ± 0.0010	0.1798 ± 0.0013	0.1331 ± 0.0010	0.1550 ± 0.0011
F_{disc} (mJy)	0.1749 ± 0.0004	0.154 ± 0.003	0.199 ± 0.003	0.2637 ± 0.0015	0.2288 ± 0.0029
F_{bs} (mJy)	0.1168 ± 0.0015	0.1534 ± 0.0013	0.0620 ± 0.0007	0.0743 ± 0.0012	0.0628 ± 0.0007
F_2 (mJy)	0 ± 0	0.0569 ± 0.0025	0.0900 ± 0.0024	0 ± 0	0.0759 ± 0.0023
U_1	0.301	0.340	0.340	0.340	0.340

Table C.2: Model parameters for the individual PHL 1445 r'-band eclipse light curve fits in Section 4.3.3.

*Parameter not included in fit (held fixed at displayed value)

PHL 1445 – Individual g'-band eclipse fits					
q	0.0870*				
$\Delta\phi$	0.05384*				
R_1/x_{L1}	0.0275*				
Cycle no.	0	1413	1430	1431	1542
Band	g'	g'	g'	g'	g'
$R_{\mathrm{disc}}/x_{\mathrm{L1}}$	0.508 ± 0.011	0.403 ± 0.004	0.2850 ± 0.0016	0.379 ± 0.003	0.287 ± 0.003
S/x_{L1}	0.047 ± 0.016	0.025 ± 0.003	0.0231 ± 0.0026	0.0232 ± 0.0025	0.072 ± 0.007
θ_{az}	159 ± 5	168.8 ± 1.1	148.4 ± 1.9	164.2 ± 1.1	143 ± 3
f_{iso}	0.9991 ± 0.0021	0.359 ± 0.017	0.651 ± 0.021	0.139 ± 0.010	0.531 ± 0.026
b	0.002 ± 0.019	0.001 ± 0.014	1.50 ± 0.04	0.35 ± 0.15	1.494 ± 0.020
ϕ_0 ($\times 10^{-5}$)	-5 ± 4	-8 ± 6	-2 ± 4	-8 ± 3	-2 ± 4
Y	–	–	–	–	–
Z	–	–	–	–	–
θ_{tilt}	–	–	–	–	–
θ_{yaw}	–	–	–	–	–
F_1 (mJy)	0.15240 ± 0.00025	0.1288 ± 0.0003	0.1536 ± 0.0014	0.1286 ± 0.0003	0.1295 ± 0.0013
F_{disc} (mJy)	0.0976 ± 0.0004	0.0737 ± 0.0005	0.0236 ± 0.0017	0.0482 ± 0.0004	0.0468 ± 0.0016
F_{bs} (mJy)	0.01866 ± 0.00018	0.0546 ± 0.0004	0.0376 ± 0.0005	0.0745 ± 0.0004	0.03810 ± 0.0005
F_2 (mJy)	0 ± 0	0 ± 0	0.0255 ± 0.0006	0 ± 0	0.0221 ± 0.0007
U_1	0.390	0.390	0.390	0.390	0.390
Cycle no.	5889	6547	14942	14945	14961
Band	g'	g'	g'	g'	g'
$R_{\mathrm{disc}}/x_{\mathrm{L1}}$	0.550 ± 0.014	0.5669 ± 0.0028	0.589 ± 0.003	0.3892 ± 0.0019	0.497 ± 0.004
S/x_{L1}	0.190 ± 0.009	0.036 ± 0.005	0.056 ± 0.003	0.066 ± 0.012	0.057 ± 0.004
θ_{az}	159.9 ± 0.5	170.39 ± 0.05	157.0 ± 0.8	170.38 ± 0.11	170.38 ± 0.24
f_{iso}	0.380 ± 0.016	0.050 ± 0.007	1.0000 ± 0.0027	0.341 ± 0.025	0.628 ± 0.026
b	1.48 ± 0.06	0.005 ± 0.020	0.66 ± 0.12	0.005 ± 0.007	0.946 ± 0.085
ϕ_0 ($\times 10^{-5}$)	-85 ± 5	-17 ± 4	-82 ± 4	-77 ± 5	15 ± 6
Y	–	–	–	–	–
Z	–	–	–	–	–
θ_{tilt}	–	–	–	–	–
θ_{yaw}	–	–	–	–	–
F_1 (mJy)	0.1369 ± 0.0012	0.1620 ± 0.0007	0.1691 ± 0.0009	0.1454 ± 0.0005	0.1448 ± 0.0011
F_{disc} (mJy)	0.0945 ± 0.0018	0.0699 ± 0.0023	0.1068 ± 0.0026	0.1433 ± 0.0008	0.0916 ± 0.0023
F_{bs} (mJy)	0.0996 ± 0.0008	0.1186 ± 0.0010	0.0444 ± 0.0005	0.0406 ± 0.0006	0.0481 ± 0.0006
F_2 (mJy)	0 ± 0	0.0358 ± 0.0019	0.0357 ± 0.0018	0 ± 0	0.0757 ± 0.0013
U_1	0.390	0.390	0.390	0.390	0.390

Table C.3: Model parameters for the individual PHL 1445 g'-band eclipse light curve fits in Section 4.3.3.

*Parameter not included in fit (held fixed at displayed value)

PHL 1445 – Individual u'-band eclipse fits					
q	0.097*				
$\Delta\phi$	0.0535*				
R_1/x_{L1}	0.027*				
Cycle no.	0	1413	1430	1431	1542
Band	u'	u'	u'	u'	u'
$R_{\mathrm{disc}}/x_{\mathrm{L1}}$	0.54 ± 0.14	0.400 ± 0.025	0.27 ± 0.13	0.394 ± 0.019	0.228 ± 0.005
S/x_{L1}	0.07 ± 0.11	0.033 ± 0.026	0.02 ± 0.03	0.016 ± 0.007	0.084 ± 0.018
θ_{az}	170 ± 7	171 ± 10	95 ± 5	139 ± 10	130 ± 16
f_{iso}	0.2 ± 0.3	0.29 ± 0.15	0.31 ± 0.06	0.12 ± 0.11	0.92 ± 0.13
b	0.3 ± 0.5	0.04 ± 0.21	1.48 ± 0.18	0.0 ± 0.3	1.3 ± 0.5
ϕ_0 ($\times10^{-5}$)	30 ± 40	10 ± 40	−20 ± 100	25 ± 24	−100 ± 60
Y	–	–	–	–	–
Z	–	–	–	–	–
θ_{tilt}	–	–	–	–	–
θ_{yaw}	–	–	–	–	–
F_1 (mJy)	0.126 ± 0.007	0.0863 ± 0.0014	0.101 ± 0.007	0.0945 ± 0.0008	0.065 ± 0.009
F_{disc} (mJy)	0.135 ± 0.020	0.1088 ± 0.0017	0.061 ± 0.008	0.0673 ± 0.0009	0.048 ± 0.011
F_{bs} (mJy)	0.063 ± 0.007	0.0600 ± 0.0021	0.0438 ± 0.0023	0.0407 ± 0.0005	0.070 ± 0.004
F_2 (mJy)	0.023 ± 0.014	0 ± 0	0.018 ± 0.003	0 ± 0	0.022 ± 0.004
U_1	0.469	0.469	0.469	0.469	0.469
Cycle no.	5889	6547	14942	14945	14961
Band	u'	u'	u'	u'	u'
$R_{\mathrm{disc}}/x_{\mathrm{L1}}$	0.56 ± 0.09	0.89 ± 0.05	0.547 ± 0.022	0.407 ± 0.022	0.457 ± 0.028
S/x_{L1}	0.14 ± 0.12	0.067 ± 0.025	0.026 ± 0.011	0.21 ± 0.07	0.009 ± 0.012
θ_{az}	148 ± 8	141 ± 24	107 ± 20	163 ± 3	108 ± 29
f_{iso}	0.50 ± 0.13	0.5 ± 0.3	1.00 ± 0.14	0.71 ± 0.15	0.07 ± 0.3
b	1.24 ± 0.27	1.21 ± 0.17	1.0 ± 0.4	0.28 ± 0.26	0.3 ± 0.3
ϕ_0 ($\times10^{-5}$)	−60 ± 50	−10 ± 40	−90 ± 50	−160 ± 40	−70 ± 40
Y	–	–	–	–	–
Z	–	–	–	–	–
θ_{tilt}	–	–	–	–	–
θ_{yaw}	–	–	–	–	–
F_1 (mJy)	0.1119 ± 0.0004	0.110 ± 0.009	0.138 ± 0.009	0.1005 ± 0.0003	0.091 ± 0.008
F_{disc} (mJy)	0.1469 ± 0.0007	0.17 ± 0.03	0.163 ± 0.021	0.1902 ± 0.0007	0.206 ± 0.017
F_{bs} (mJy)	0.0933 ± 0.0004	0.130 ± 0.009	0.062 ± 0.004	0.07256 ± 0.00026	0.042 ± 0.004
F_2 (mJy)	0 ± 0	0.016 ± 0.025	0.107 ± 0.012	0 ± 0	0.089 ± 0.010
U_1	0.469	0.469	0.469	0.469	0.469

Table C.4: Model parameters for the individual PHL 1445 u'-band eclipse light curve fits in Section 4.3.3.

*Parameter not included in fit (held fixed at displayed value)

PHL 1445 – Simultaneous individual eclipse fit										
q	0.092 ± 0.007									
$\Delta\phi$	0.05391 ± 0.00017									
R_1/x_{L1}	0.0266 ± 0.0010									
$\log h_1$	-7.72 ± 0.16									
$\log h_2$	-9.58 ± 0.25									
$\log \lambda$	-10.07 ± 0.16									
Eclipse no.	1/10	2/10	3/10	4/10	5/10	6/10	7/10	8/10	9/10	10/10
Cycle no.	0	1413	1430	1431	1542	5889	6547	12024	14942	14961
Band	g'	g'	g'	g'	g'	g'	g'	g'	g'	g'
$R_{\mathrm{disc}}/x_{\mathrm{L1}}$	0.37 ± 0.05	0.38 ± 0.05	$0.41^{+0.04}_{-0.08}$	$0.38^{+0.02}_{-0.06}$	0.52 ± 0.07	0.35 ± 0.06	0.57 ± 0.05	0.40 ± 0.04	0.48 ± 0.07	$0.47^{+0.06}_{-0.02}$
S/x_{L1}	0.042 ± 0.016	0.030 ± 0.012	0.030 ± 0.011	0.022 ± 0.006	0.039 ± 0.018	0.041 ± 0.013	0.038 ± 0.014	0.027 ± 0.013	0.048 ± 0.017	0.030 ± 0.011
θ_{az}	161^{+9}_{-19}	157^{+11}_{-24}	160^{+8}_{-12}	160^{+8}_{-13}	156^{+13}_{-20}	155^{+11}_{-23}	160^{+11}_{-14}	150^{+19}_{-23}	158^{+11}_{-18}	152 ± 13
f_{iso}	0.46 ± 0.19	0.46 ± 0.19	0.37 ± 0.15	0.33 ± 0.13	0.3 ± 0.12	0.25 ± 0.09	0.23 ± 0.09	0.22 ± 0.09	0.30 ± 0.11	0.18 ± 0.07
b	0.47 ± 0.19	1.5 ± 0.5	1.6 ± 0.5	1.7 ± 0.6	0.8 ± 0.3	0.64 ± 0.29	0.47 ± 0.16	0.8 ± 0.3	1.1 ± 0.3	0.84 ± 0.29
ϕ_0 ($\times 10^{-5}$)	1 ± 20	3 ± 22	-8 ± 20	-3 ± 20	15 ± 19	-42 ± 24	26 ± 19	-1^{+27}_{-19}	-14 ± 21	27^{+24}_{-21}
Y	–	–	–	–	–	–	–	–	–	–
Z	–	–	–	–	–	–	–	–	–	–
θ_{tilt}	–	–	–	–	–	–	–	–	–	–
θ_{yaw}	–	–	–	–	–	–	–	–	–	–
F_1 (mJy)	0.128 ± 0.009	0.118 ± 0.009	0.140 ± 0.008	0.130 ± 0.008	0.127 ± 0.008	0.121 ± 0.009	0.153 ± 0.009	0.137 ± 0.011	0.127 ± 0.011	0.120 ± 0.010
F_{disc} (mJy)	0.098 ± 0.013	0.064 ± 0.011	0.038 ± 0.008	0.025 ± 0.007	0.055 ± 0.009	0.092 ± 0.012	0.106 ± 0.014	0.122 ± 0.016	0.157 ± 0.018	0.163 ± 0.016
F_{bs} (mJy)	0.032 ± 0.010	0.042 ± 0.010	$0.046^{+0.015}_{-0.012}$	0.050 ± 0.012	$0.033^{+0.014}_{-0.011}$	$0.059^{+0.019}_{-0.015}$	0.056 ± 0.017	$0.025^{+0.017}_{-0.012}$	0.043 ± 0.014	$0.066^{+0.022}_{-0.017}$
F_2 (mJy)	0.016 ± 0.006	0.018 ± 0.007	0.019 ± 0.006	0.015 ± 0.006	0.016 ± 0.008	0.022 ± 0.008	0.018 ± 0.009	0.033 ± 0.011	0.039 ± 0.013	0.027 ± 0.010
U_1	0.390	0.390	0.390	0.390	0.390	0.390	0.390	0.390	0.390	0.390

Table C.5: Model parameters for the simultaneous PHL 1445 g'-band eclipse light curve fit in Section 5.5.1.

ASASSN-14ag – Simultaneous individual eclipse fit – without GPs

q	0.1536 ± 0.0015							
$\Delta\phi$	0.06162 ± 0.00006							
R_1/x_{L1}	0.0277 ± 0.0006							
$\log h_1$	–							
$\log h_2$	–							
$\log \lambda$	–							
Eclipse no.	1/8	2/8	3/8	4/8	5/8	6/8	7/8	8/8
Cycle no.	0	16	580	594	597	1441	1455	1474
Band	*KG5*	*KG5*	i'	g'	r'	g'	r'	g'
$R_{\mathrm{disc}}/x_{\mathrm{L1}}$	0.482 ± 0.004	0.419 ± 0.005	0.486 ± 0.004	0.509 ± 0.007	0.462 ± 0.006	$0.4276^{+0.0024}_{-0.0029}$	0.459 ± 0.004	0.451 ± 0.006
S/x_{L1}	0.0144 ± 0.0014	0.044 ± 0.005	0.061 ± 0.003	0.022 ± 0.003	0.033 ± 0.003	$0.0104^{+0.0018}_{-0.0010}$	0.025 ± 0.004	0.0204 ± 0.0014
θ_{az}	112.0 ± 2.6	74 ± 6	92 ± 7	54^{+6}_{-3}	141.8 ± 2.0	107^{+7}_{-18}	126.6 ± 2.3	165.7 ± 1.0
f_{iso}	0.295 ± 0.006	0.369 ± 0.010	0.08 ± 0.04	0.034 ± 0.020	$0.008^{+0.008}_{-0.005}$	$0.315^{+0.007}_{-0.029}$	0.228 ± 0.005	0.154 ± 0.006
b	0.45 ± 0.09	1.48 ± 0.11	1.13 ± 0.04	2.27 ± 0.10	1.25 ± 0.06	1.85 ± 0.08	1.80 ± 0.07	1.23 ± 0.05
ϕ_0 $(\times 10^{-5})$	-60 ± 7	-29 ± 15	107 ± 15	59 ± 19	163 ± 11	-15 ± 6	-146 ± 7	-22 ± 8
Y	$3.85^{+0.12}_{-0.16}$	$3.06^{+0.28}_{-0.25}$	$0.70^{+0.22}_{-0.19}$	$0.23^{+0.10}_{-0.13}$	1.8 ± 0.5	0.08 ± 0.05	2.45 ± 0.26	0.41 ± 0.14
Z	0.881 ± 0.028	1.38 ± 0.08	1.79 ± 0.10	0.58 ± 0.04	0.95 ± 0.05	0.57 ± 0.04	0.90 ± 0.05	0.525 ± 0.026
θ_{tilt}	$164.4^{+0.8}_{-1.1}$	26 ± 4	159 ± 3	154 ± 4	60 ± 8	41^{+5}_{-22}	137 ± 5	30^{+6}_{-3}
θ_{yaw}	-8.4 ± 2.6	68 ± 6	6 ± 7	44 ± 4	-11.2 ± 2.2	37^{+18}_{-6}	9.6 ± 2.4	-13.4 ± 1.4
F_1 (mJy)	0.386 ± 0.005	0.339 ± 0.010	0.248 ± 0.009	0.354 ± 0.020	0.303 ± 0.010	0.350 ± 0.009	0.408 ± 0.010	0.456 ± 0.008
F_{disc} (mJy)	0.216 ± 0.007	0.245 ± 0.013	0.751 ± 0.015	0.463 ± 0.018	0.492 ± 0.013	0.381 ± 0.009	0.398 ± 0.013	0.480 ± 0.010
F_{bs} (mJy)	0.505 ± 0.004	0.459 ± 0.007	0.359 ± 0.006	0.440 ± 0.009	0.394 ± 0.004	0.455 ± 0.009	0.646 ± 0.005	0.549 ± 0.008
F_2 (mJy)	$0.0010^{+0.0014}_{-0.0007}$	0.063 ± 0.006	0.126 ± 0.009	0.051 ± 0.006	0.076 ± 0.008	$0.0025^{+0.0024}_{-0.0017}$	0.082 ± 0.007	0.005 ± 0.004
U_1	0.360	0.360	0.272	0.369	0.317	0.369	0.317	0.369

Table C.6: Model parameters for the simultaneous ASASSN-14ag eclipse light curve fit – without GPs – in Section 5.3.1.

ASASSN-14ag – Simultaneous individual eclipse fit – with GPs								
q	0.162 ± 0.013							
$\Delta\phi$	0.0614 ± 0.0004							
R_1/x_{L1}	0.0296 ± 0.0017							
$\log h_1$	-5.72 ± 0.17							
$\log h_2$	-6.68 ± 0.27							
$\log \lambda$	-10.75 ± 0.19							
Eclipse no.	1/8	2/8	3/8	4/8	5/8	6/8	7/8	8/8
Cycle no.	0	16	580	594	597	1441	1455	1474
Band	*KG5*	*KG5*	i'	g'	r'	g'	r'	g'
$R_{\mathrm{disc}}/x_{\mathrm{L1}}$	0.464 ± 0.027	0.45 ± 0.03	0.46 ± 0.04	0.481 ± 0.029	$0.45^{+0.03}_{-0.07}$	0.39 ± 0.04	0.44 ± 0.05	0.38 ± 0.04
S/x_{L1}	0.015 ± 0.004	0.020 ± 0.008	0.020 ± 0.007	0.023 ± 0.006	0.020 ± 0.007	0.014 ± 0.004	0.025 ± 0.012	0.019 ± 0.006
θ_{az}	95 ± 20	115^{+14}_{-17}	102 ± 22	93 ± 20	117^{+14}_{-17}	112^{+16}_{-19}	116^{+16}_{-19}	116 ± 17
f_{iso}	0.30 ± 0.10	0.38 ± 0.09	0.35 ± 0.12	0.20 ± 0.09	0.22 ± 0.08	0.29 ± 0.09	0.16 ± 0.05	0.23 ± 0.09
b	1.08 ± 0.22	1.67 ± 0.25	0.86 ± 0.14	1.14 ± 0.15	0.88 ± 0.15	1.8 ± 0.3	2.04 ± 0.22	1.11 ± 0.20
ϕ_0 $(\times 10^{-5})$	-10 ± 28	-40 ± 50	120 ± 70	40 ± 40	90 ± 70	0 ± 18	-70 ± 50	5 ± 24
Y	1.1 ± 0.5	1.1 ± 0.6	1.7 ± 0.7	0.6 ± 0.4	2.3 ± 1.1	0.7 ± 0.3	1.0 ± 0.5	$0.89^{+0.25}_{-0.17}$
Z	$0.82^{+0.16}_{-0.11}$	$0.82^{+0.20}_{-0.15}$	1.0 ± 0.3	$0.73^{+0.14}_{-0.10}$	$0.94^{+0.26}_{-0.15}$	$0.73^{+0.15}_{-0.11}$	$0.81^{+0.22}_{-0.15}$	$0.89^{+0.25}_{-0.17}$
θ_{tilt}	63 ± 29	86 ± 22	82 ± 27	70^{+28}_{-25}	102 ± 27	68 ± 29	63^{+28}_{-23}	82 ± 28
θ_{yaw}	29 ± 19	18 ± 14	24 ± 21	27 ± 20	15 ± 14	20^{+19}_{-16}	27 ± 16	27 ± 17
F_1 (mJy)	0.399 ± 0.025	0.350 ± 0.029	0.31 ± 0.03	0.48 ± 0.04	0.33 ± 0.03	0.428 ± 0.028	0.36 ± 0.04	0.50 ± 0.03
F_{disc} (mJy)	0.174 ± 0.022	0.27 ± 0.03	0.66 ± 0.06	0.32 ± 0.04	0.42 ± 0.04	0.26 ± 0.03	0.48 ± 0.05	0.40 ± 0.04
F_{bs} (mJy)	0.47 ± 0.04	0.44 ± 0.04	0.38 ± 0.04	0.48 ± 0.04	0.43 ± 0.04	0.43 ± 0.04	0.59 ± 0.05	0.48 ± 0.04
F_2 (mJy)	0.041 ± 0.010	0.027 ± 0.010	0.13 ± 0.03	0.034 ± 0.011	0.075 ± 0.018	0.035 ± 0.010	0.089 ± 0.028	0.033 ± 0.011
U_1	0.360	0.360	0.272	0.369	0.317	0.369	0.317	0.369

Table C.7: Model parameters for the simultaneous ASASSN-14ag eclipse light curve fit – with GPs – in Section 5.3.1.

ASASSN-14ag – Individual eclipse fits

Cycle no.	0	16	580	594	597	1441	1455	1474
Band	*KG5*	*KG5*	i'	g'	r'	g'	r'	g'
q	0.1401 ± 0.0025	0.156 ± 0.005	$0.148^{+0.021}_{-0.009}$	0.129 ± 0.016	0.197 ± 0.006	0.188 ± 0.004	0.1246 ± 0.0024	$0.204^{+0.011}_{-0.007}$
$\Delta\phi$	0.06244 ± 0.00013	0.06311 ± 0.00021	0.06099 ± 0.00027	0.0599 ± 0.0004	0.06139 ± 0.00022	0.06197 ± 0.00013	0.06060 ± 0.00011	0.06144 ± 0.00013
R_1/x_{L1}	$0.0299^{+0.0010}_{-0.0006}$	0.0411 ± 0.0019	0.043 ± 0.005	0.046 ± 0.004	0.030 ± 0.003	0.0261 ± 0.0013	$0.0275^{+0.0016}_{-0.0011}$	$0.0253^{+0.0015}_{-0.0020}$
$\log h_1$	–	–	–	–	–	–	–	–
$\log h_2$	–	–	–	–	–	–	–	–
$\log \lambda$	–	–	–	–	–	–	–	–
$R_{\mathrm{disc}}/x_{\mathrm{L1}}$	$0.487^{+0.006}_{-0.002}$	$0.408^{+0.008}_{-0.005}$	$0.496^{+0.006}_{-0.012}$	0.529 ± 0.013	0.469 ± 0.004	0.385 ± 0.006	0.491 ± 0.003	0.270 ± 0.003
S/x_{L1}	0.0870 ± 0.0006	0.118 ± 0.006	$0.024^{+0.016}_{-0.007}$	$0.026^{+0.022}_{-0.008}$	0.0130 ± 0.0009	$0.0556^{+0.0011}_{-0.0016}$	0.0758 ± 0.0014	$0.065^{+0.005}_{-0.008}$
θ_{az}	108.6 ± 0.6	54 ± 4	97 ± 9	120^{+9}_{-14}	137.6 ± 1.3	$51.0^{+1.4}_{-0.8}$	134.7 ± 1.2	102 ± 7
f_{iso}	0.287 ± 0.006	0.390 ± 0.010	0.05 ± 0.04	0.163 ± 0.022	$0.0029^{+0.0029}_{-0.0014}$	$0.16^{+0.04}_{-0.09}$	0.213 ± 0.005	0.187 ± 0.003
b	0.35 ± 0.15	0.3 ± 0.3	0.85 ± 0.12	1.05 ± 0.5	1.18 ± 0.12	1.90 ± 0.07	1.37 ± 0.08	1.87 ± 0.22
ϕ_0 ($\times 10^{-5}$)	-72 ± 8	-51 ± 12	114 ± 11	5 ± 17	136 ± 12	-28 ± 6	-141 ± 0.00005	-1 ± 6
Y	3.81 ± 0.12	$3.4^{+0.4}_{-0.7}$	$1.5^{+1.2}_{-0.8}$	$0.6^{+0.8}_{-0.4}$	$0.05^{+0.07}_{-0.03}$	$0.030^{+0.015}_{-0.019}$	$3.89^{+0.08}_{-0.18}$	$0.23^{+0.13}_{-0.09}$
Z	1.81 ± 0.03	$2.35^{+0.15}_{-0.12}$	1.1 ± 0.3	$0.90^{+0.27}_{-0.17}$	$0.435^{+0.028}_{-0.024}$	$0.934^{+0.026}_{-0.016}$	1.405 ± 0.021	$1.77^{+0.24}_{-0.20}$
θ_{tilt}	169.0 ± 0.3	55^{+27}_{-18}	159 ± 3	$172.1^{+1.6}_{-1.3}$	161.3 ± 1.0	11.4 ± 2.0	167.9 ± 0.8	53 ± 4
θ_{yaw}	-9.7 ± 0.7	79 ± 5	2 ± 8	-24^{+13}_{-9}	-30.8 ± 1.6	$89.6^{+0.3}_{-0.8}$	$-15.9^{+2.4}_{-2.0}$	78 ± 7
F_1 (mJy)	0.369 ± 0.006	0.419 ± 0.010	0.332 ± 0.023	0.55 ± 0.04	$0.282^{+0.022}_{-0.026}$	0.334 ± 0.016	0.410 ± 0.013	0.40 ± 0.03
F_{disc} (mJy)	0.230 ± 0.007	0.123 ± 0.019	0.705 ± 0.025	0.33 ± 0.03	$0.581^{+0.026}_{-0.022}$	0.388 ± 0.016	0.478 ± 0.013	0.34 ± 0.03
F_{bs} (mJy)	$0.534^{+0.012}_{-0.016}$	0.464 ± 0.008	0.348 ± 0.005	0.41 ± 0.05	0.376 ± 0.004	0.446 ± 0.004	0.599 ± 0.004	0.925 ± 0.013
F_2 (mJy)	$0.0006^{+0.0010}_{-0.0004}$	0.096 ± 0.010	0.092 ± 0.014	$0.006^{+0.010}_{-0.005}$	0.003 ± 0.004	$0.0006^{+0.0012}_{-0.0004}$	$0.006^{+0.007}_{-0.005}$	0.140 ± 0.007
U_1	0.360	0.360	0.272	0.369	0.317	0.369	0.317	0.369

Table C.8: Model parameters for the individual ASASSN-14ag eclipse light curve fits in Section 5.3.3.

ASASSN-14ag – Average eclipse fits			
Cycle no.	–	–	–
Band	r'	g'	*KG5*
q	$0.1238^{+0.0026}_{-0.0017}$	$0.1144^{+0.0025}_{-0.0020}$	$0.1308^{+0.0018}_{-0.0013}$
$\Delta\phi$	0.06082 ± 0.00010	0.06165 ± 0.00009	0.06268 ± 0.00012
R_1/x_{L1}	0.0282 ± 0.0015	0.0327 ± 0.0010	0.0327 ± 0.0007
$\log h_1$	–	–	–
$\log h_2$	–	–	–
$\log \lambda$	–	–	–
$R_{\mathrm{disc}}/x_{\mathrm{L1}}$	$0.489^{+0.002}_{-0.006}$	0.514 ± 0.004	$0.4825^{+0.0013}_{-0.0018}$
S/x_{L1}	0.0672 ± 0.0019	0.031 ± 0.004	0.0959 ± 0.00005
θ_{az}	133.3 ± 1.7	165.8 ± 0.6	85.1 ± 0.6
f_{iso}	0.198 ± 0.006	0.241 ± 0.005	0.290 ± 0.004
b	1.25 ± 0.07	1.76 ± 0.05	$0.02^{+0.05}_{-0.02}$
ϕ_0 ($\times 10^{-5}$)	-69 ± 5	-12 ± 6	-65 ± 5
Y	3.7 ± 0.3	0.05 ± 0.05	$3.86^{+0.09}_{-0.12}$
Z	1.423 ± 0.028	0.55 ± 0.03	2.22 ± 0.03
θ_{tilt}	168.9 ± 0.6	17 ± 4	169.5 ± 0.4
θ_{yaw}	$-18.6^{+2.5}_{-2.2}$	-11.1 ± 2.8	16.7 ± 0.8
F_1 (mJy)	0.366 ± 0.011	0.419 ± 0.009	0.384 ± 0.004
F_{disc} (mJy)	0.515 ± 0.012	0.404 ± 0.009	0.240 ± 0.004
F_{bs} (mJy)	0.5125 ± 0.0026	0.517 ± 0.010	$0.4894^{+0.0025}_{-0.0028}$
F_2 (mJy)	$0.008^{+0.008}_{-0.005}$	$0.0007^{+0.0012}_{-0.0005}$	$0.0006^{+0.0009}_{-0.0004}$
U_1	0.317	0.369	0.360

Table C.9: Model parameters for the average ASASSN-14ag eclipse light curve fits in Section 5.3.3.

SDSS 1057 – Simultaneous average eclipse fit				
q	0.0546 ± 0.0020			
$\Delta\phi$	0.04645 ± 0.00006			
R_1/x_{L1}	0.0218 ± 0.0005			
$\log h_1$	-14.17 ± 0.16			
$\log h_2$	-14.7 ± 0.3			
$\log \lambda$	-20 ± 4			
Eclipse no.	1/4	2/4	3/4	4/4
Cycle no.	–	–	–	–
Band	r'	g'	u'	*KG5*
$R_{\mathrm{disc}}/x_{\mathrm{L1}}$	$0.478^{+0.012}_{-0.008}$	0.506 ± 0.012	0.488 ± 0.016	0.483 ± 0.025
S/x_{L1}	$0.019^{+0.011}_{-0.008}$	$0.023^{+0.011}_{-0.007}$	$0.016^{+0.013}_{-0.007}$	$0.022^{+0.020}_{-0.011}$
θ_{az}	150^{+8}_{-18}	120 ± 30	159^{+9}_{-14}	158 ± 10
f_{iso}	0.75 ± 0.07	$0.82^{+0.09}_{-0.18}$	0.56 ± 0.09	0.37 ± 0.07
b	1.0 ± 0.5	1.6 ± 0.7	$1.8^{+0.5}_{-0.8}$	$1.6^{+0.7}_{-1.0}$
ϕ_0 ($\times 10^{-5}$)	7 ± 6	4 ± 3	-12 ± 17	-13 ± 11
Y	–	–	–	–
Z	–	–	–	–
θ_{tilt}	–	–	–	–
θ_{yaw}	–	–	–	–
F_1 (mJy)	0.0373 ± 0.0009	0.0471 ± 0.0006	$0.0322^{+0.0016}_{-0.0020}$	0.0416 ± 0.0009
F_{disc} (mJy)	0.0075 ± 0.0011	0.0025 ± 0.0008	0.0059 ± 0.0025	$0.0021^{+0.0012}_{-0.0008}$
F_{bs} (mJy)	0.0055 ± 0.0004	$0.00366^{+0.00024}_{-0.00021}$	0.0097 ± 0.0012	0.0088 ± 0.0013
F_2 (mJy)	0.0013 ± 0.0009	0.0010 ± 0.0006	0.0027 ± 0.0016	$0.0009^{+0.0009}_{-0.0006}$
U_1	0.328	0.392	0.427	0.374

Table C.10: Model parameters for the simultaneous average SDSS 1057 eclipse light curve fit in Section 6.3.1.

Model fit	**CSS080623** – Simultaneous average eclipse fit						**GY Cnc** – Simultaneous individual eclipse fit			
q	0.116 ± 0.005						$0.446^{+0.016}_{-0.019}$			
$\Delta\phi$	0.03865 ± 0.00022						$0.06422^{+0.00017}_{-0.00014}$			
$R_1/x_{\rm L1}$	0.0273 ± 0.0008						0.0117 ± 0.0003			
$\log h_1$	$-14.0^{+1.1}_{-0.5}$						-7.59 ± 0.14			
$\log h_2$	$-12.9^{+1.2}_{-0.8}$						-9.81 ± 0.21			
$\log \lambda$	$-9.0^{+1.8}_{-1.2}$						-12.71 ± 0.15			
Eclipse no.	1/6	2/6	3/6	4/6	5/6	6/6	1/4	2/4	3/4	4/4
Cycle no.	–	–	–	–	–	–	28	28	28	4249
Band	r'	r'	g'	g'	u'	u'	r'	g'	u'	*KG5*
$R_{\rm disc}/x_{\rm L1}$	0.468 ± 0.007	0.485 ± 0.009	0.460 ± 0.008	0.478 ± 0.007	0.462 ± 0.016	0.493 ± 0.013	0.440 ± 0.008	0.437 ± 0.007	$0.442^{+0.007}_{-0.010}$	$0.403^{+0.005}_{-0.009}$
$S/x_{\rm L1}$	0.045 ± 0.020	$0.041^{+0.019}_{-0.022}$	0.040 ± 0.019	0.040 ± 0.016	$0.052^{+0.019}_{-0.022}$	0.040 ± 0.019	0.0180 ± 0.0015	$0.0166^{+0.0011}_{-0.0022}$	$0.0155^{+0.0019}_{-0.0021}$	0.0063 ± 0.0006
$\theta_{\rm az}$	125^{+6}_{-12}	115^{+10}_{-16}	117^{+9}_{-15}	116 ± 9	95^{+29}_{-23}	116^{+18}_{-22}	126 ± 4	122 ± 4	116 ± 5	117 ± 6
$f_{\rm iso}$	0.22 ± 0.04	0.23 ± 0.05	0.20 ± 0.04	0.22 ± 0.03	0.22 ± 0.05	0.25 ± 0.05	0.387 ± 0.026	0.344 ± 0.026	0.35 ± 0.04	0.29 ± 0.05
b	$0.13^{+0.12}_{-0.09}$	0.18 ± 0.12	$0.16^{+0.13}_{-0.10}$	0.14 ± 0.11	0.18 ± 0.12	$0.15^{+0.13}_{-0.10}$	0.66 ± 0.07	0.67 ± 0.09	1.11 ± 0.15	1.41 ± 0.17
ϕ_0 $(\times 10^{-5})$	-36 ± 25	-50 ± 30	-36 ± 19	-60 ± 22	-50 ± 40	-70 ± 40	-76 ± 15	-66 ± 13	-66 ± 13	28^{+16}_{-13}
Y	0.6 ± 0.4	0.6 ± 0.4	0.8 ± 0.4	0.9 ± 0.4	0.8 ± 0.4	0.7 ± 0.5	0.46 ± 0.08	0.41 ± 0.09	0.23 ± 0.05	$0.52^{+0.17}_{-0.20}$
Z	1.3 ± 0.4	1.2 ± 0.5	1.3 ± 0.5	1.4 ± 0.5	1.7 ± 0.7	1.8 ± 0.7	0.73 ± 0.04	0.75 ± 0.04	0.70 ± 0.06	0.63 ± 0.05
$\theta_{\rm tilt}$	40^{+17}_{-14}	52^{+29}_{-23}	45 ± 17	47^{+28}_{-19}	44 ± 17	56^{+28}_{-25}	160^{+2}_{-5}	162.2 ± 2.0	$164.2^{+0.6}_{-1.1}$	63 ± 3
$\theta_{\rm yaw}$	23^{+15}_{-10}	36^{+16}_{-13}	32^{+16}_{-11}	35 ± 12	55^{+22}_{-28}	37 ± 22	6 ± 3	10 ± 3	12 ± 5	5.1 ± 2.9
F_1 (mJy)	0.0262 ± 0.0014	0.0238 ± 0.0014	0.0301 ± 0.0013	0.0313 ± 0.0012	0.0247 ± 0.0015	0.0248 ± 0.0015	0.123 ± 0.005	0.158 ± 0.007	0.203 ± 0.007	0.122 ± 0.004
$F_{\rm disc}$ (mJy)	$0.0061^{+0.0027}_{-0.0024}$	0.0036 ± 0.0015	0.0046 ± 0.0016	0.0044 ± 0.0017	0.0047 ± 0.0020	0.0049 ± 0.0017	0.255 ± 0.010	0.154 ± 0.009	0.219 ± 0.007	0.173 ± 0.006
$F_{\rm bs}$ (mJy)	$0.0315^{+0.0021}_{-0.0017}$	$0.0315^{+0.0027}_{-0.0020}$	0.0334 ± 0.0021	0.0390 ± 0.0026	0.0275 ± 0.0024	0.027 ± 0.003	0.403 ± 0.010	0.434 ± 0.009	0.353 ± 0.010	0.196 ± 0.007
F_2 (mJy)	0.0070 ± 0.0029	0.0065 ± 0.0027	0.0031 ± 0.0018	0.0030 ± 0.0017	0.0026 ± 0.0012	0.0025 ± 0.0013	0.663 ± 0.008	0.189 ± 0.005	$0.0642^{+0.0029}_{-0.0025}$	0.369 ± 0.006
U_1	0.323	0.323	0.367	0.367	0.423	0.423	264	302	370	300

Table C.11: Model parameters for the eclipse light curve fits of additional systems in Section 7.4.1.

Model fit	**OY Car** – Simultaneous individual eclipse fit						**SDSS 1006** – Simultaneous individual eclipse fit			
q	$0.1057^{+0.0026}_{-0.0023}$						0.46 ± 0.04			
$\Delta\phi$	0.05150 ± 0.00015						0.09123 ± 0.00018			
$R_1/x_{\rm L1}$	0.0204 ± 0.0005						0.0122 ± 0.0021			
$\log h_1$	-5.73 ± 0.16						-10.04 ± 0.14			
$\log h_2$	-6.03 ± 0.23						-13.2 ± 0.4			
$\log \lambda$	-11.36 ± 0.17						-11.08 ± 0.24			
Eclipse no.	1/6	2/6	3/6	4/6	5/6	6/6	1/4	2/4	3/4	4/4
Cycle no.	3078	0	0	2619	3078	2619	44	43	0	17
Band	i'	r'	g'	g'	g'	u'	r'	g'	*KG5*	*KG5*
$R_{\rm disc}/x_{\rm L1}$	0.457 ± 0.013	$0.426^{+0.012}_{-0.017}$	0.438 ± 0.011	0.467 ± 0.011	0.456 ± 0.009	0.480 ± 0.010	0.443 ± 0.014	$0.437^{+0.015}_{-0.011}$	0.423 ± 0.017	$0.415^{+0.020}_{-0.014}$
$S/x_{\rm L1}$	0.036 ± 0.004	$0.0185^{+0.0022}_{-0.0019}$	0.021 ± 0.004	0.033 ± 0.004	0.025 ± 0.004	0.025 ± 0.004	$0.015^{+0.011}_{-0.007}$	$0.013^{+0.009}_{-0.005}$	$0.012^{+0.011}_{-0.006}$	$0.011^{+0.009}_{-0.005}$
$\theta_{\rm az}$	100 ± 8	117 ± 8	109 ± 8	114 ± 9	120 ± 6	102 ± 8	92 ± 19	87^{+28}_{-23}	78^{+25}_{-18}	100^{+24}_{-21}
$f_{\rm iso}$	0.31 ± 0.04	0.33 ± 0.03	0.278 ± 0.028	0.249 ± 0.025	0.31 ± 0.03	0.29 ± 0.03	$0.32^{+0.09}_{-0.14}$	0.22 ± 0.08	$0.29^{+0.09}_{-0.14}$	0.19 ± 0.05
b	0.34 ± 0.05	1.67 ± 0.22	1.11 ± 0.19	0.36 ± 0.06	0.78 ± 0.14	0.92 ± 0.11	$0.44^{+0.29}_{-0.26}$	1.0 ± 0.4	0.9 ± 0.3	$1.10^{+0.23}_{-0.28}$
ϕ_0 $(\times 10^{-5})$	0 ± 30	-14^{+21}_{-18}	-13 ± 13	10 ± 17	23 ± 16	-12 ± 21	1^{+23}_{-18}	-15 ± 21	-21 ± 16	-2 ± 17
Y	0.46 ± 0.12	1.04 ± 0.20	0.84 ± 0.18	2.2 ± 0.4	0.46 ± 0.09	1.9 ± 0.4	0.9 ± 0.5	0.8 ± 0.5	0.5 ± 0.4	$0.21^{+0.22}_{-0.15}$
Z	$1.23^{+0.19}_{-0.15}$	0.84 ± 0.08	$0.89^{+0.10}_{-0.07}$	$1.49^{+0.21}_{-0.18}$	$0.92^{+0.17}_{-0.11}$	1.29 ± 0.16	$0.87^{+0.24}_{-0.16}$	$0.84^{+0.24}_{-0.15}$	$0.74^{+0.20}_{-0.15}$	$0.66^{+0.17}_{-0.12}$
$\theta_{\rm tilt}$	103 ± 10	99 ± 10	120 ± 10	77 ± 8	60 ± 7	86 ± 9	80 ± 50	90 ± 50	110 ± 50	100 ± 50
$\theta_{\rm yaw}$	38 ± 7	99 ± 10	35 ± 8	27 ± 9	27 ± 6	37 ± 7	47^{+19}_{-22}	$46^{+22}_{-0.26}$	56^{+19}_{-26}	57^{+22}_{-25}
F_1 (mJy)	0.580 ± 0.019	0.91 ± 0.04	1.09 ± 0.03	$1.034^{+0.024}_{-0.027}$	$1.004^{+0.028}_{-0.024}$	$0.931^{+0.026}_{-0.029}$	0.020 ± 0.004	0.017 ± 0.004	0.025 ± 0.004	0.022 ± 0.004
$F_{\rm disc}$ (mJy)	0.46 ± 0.03	0.39 ± 0.04	0.256 ± 0.024	0.268 ± 0.023	$0.273^{+0.020}_{-0.023}$	0.43 ± 0.03	0.068 ± 0.005	0.042 ± 0.005	0.044 ± 0.005	0.056 ± 0.005
$F_{\rm bs}$ (mJy)	0.91 ± 0.04	1.19 ± 0.06	1.13 ± 0.05	1.16 ± 0.05	1.14 ± 0.06	1.13 ± 0.05	0.084 ± 0.004	0.068 ± 0.003	0.065 ± 0.004	0.078 ± 0.006
F_2 (mJy)	0.276 ± 0.023	0.163 ± 0.015	0.036 ± 0.005	0.058 ± 0.004	0.051 ± 0.005	0.0238 ± 0.0021	0.0841 ± 0.0017	0.0268 ± 0.0013	0.0592 ± 0.0014	0.0604 ± 0.0013
U_1	0.247	0.285	0.327	0.327	0.327	0.396	0.311	0.354	0.352	0.352

Table C.11: *Continued.*

Model fit	**SDSS 1501** – Simultaneous individual eclipse fit						**SDSS 1152** – Simultaneous average eclipse fit			
q	0.085 ± 0.004						$0.156^{+0.015}_{-0.012}$			
$\Delta\phi$	0.04877 ± 0.00008						0.05867 ± 0.00026			
R_1/x_{L1}	0.0272 ± 0.0006						$0.0302^{+0.0021}_{-0.0018}$			
$\log h_1$	-13.1 ± 0.8						-13.3 ± 0.4			
$\log h_2$	$-13.3^{+1.2}_{-1.8}$						-13.2 ± 0.6			
$\log \lambda$	-5.2 ± 1.2						$-11.0^{+1.2}_{-0.8}$			
Eclipse no.	1/6	2/6	3/6	4/6	5/6	6/6	1/4	2/4	3/4	4/4
Cycle no.	-53411	0	-53411	0	-53411	0	–	–	–	–
Band	r'	r'	g'	g'	u'	u'	r'	g'	u'	*KG5*
$R_{\mathrm{disc}}/x_{\mathrm{L1}}$	0.530 ± 0.029	0.445 ± 0.016	0.53 ± 0.03	$0.427^{+0.017}_{-0.011}$	$0.505^{+0.028}_{-0.025}$	0.43 ± 0.04	0.45 ± 0.03	0.45 ± 0.03	0.481 ± 0.026	0.380 ± 0.014
S/x_{L1}	$0.048^{+0.020}_{-0.023}$	$0.034^{+0.029}_{-0.014}$	$0.055^{+0.016}_{-0.020}$	$0.023^{+0.014}_{-0.008}$	$0.022^{+0.019}_{-0.010}$	$0.027^{+0.027}_{-0.014}$	$0.050^{+0.023}_{-0.027}$	0.046 ± 0.019	0.048 ± 0.024	0.036 ± 0.018
θ_{az}	160^{+10}_{-40}	163 ± 9	160^{+6}_{-12}	164 ± 8	144^{+14}_{-27}	161^{+10}_{-14}	90 ± 30	88^{+25}_{-21}	100 ± 28	101^{+23}_{-26}
f_{iso}	0.35 ± 0.16	0.34 ± 0.08	0.38 ± 0.13	0.32 ± 0.08	0.42 ± 0.20	0.35 ± 0.10	$0.31^{+0.09}_{-0.13}$	$0.27^{+0.05}_{-0.08}$	$0.29^{+0.07}_{-0.10}$	0.31 ± 0.07
b	1.6 ± 0.7	0.4 ± 0.4	1.2 ± 0.7	1.1 ± 0.7	$0.9^{+0.9}_{-0.6}$	1.5 ± 0.8	1.5 ± 0.8	1.4 ± 0.8	1.2 ± 0.7	0.9 ± 0.7
ϕ_0 $(\times 10^{-5})$	134 ± 12	211 ± 8	121 ± 7	223 ± 5	140 ± 34	217 ± 16	-30 ± 40	-2 ± 20	-30 ± 40	-5 ± 22
Y	–	–	–	–	–	–	$1.3^{+1.2}_{-0.8}$	1.2 ± 0.8	$1.0^{+1.0}_{-0.6}$	2.1 ± 1.2
Z	–	–	–	–	–	–	1.8 ± 0.7	2.0 ± 0.7	1.7 ± 0.7	$1.6^{+0.8}_{-0.5}$
θ_{tilt}	–	–	–	–	–	–	90 ± 50	70 ± 50	70 ± 50	90 ± 50
θ_{yaw}	–	–	–	–	–	–	50 ± 30	57^{+21}_{-25}	43 ± 27	37^{+27}_{-24}
F_1 (mJy)	0.0390 ± 0.0015	0.0631 ± 0.0012	0.0499 ± 0.0010	0.0820 ± 0.0012	$0.0341^{+0.0021}_{-0.0024}$	0.063 ± 0.003	$0.0256^{+0.0024}_{-0.0029}$	$0.0339^{+0.0019}_{-0.0022}$	$0.0275^{+0.0024}_{-0.0029}$	0.0323 ± 0.0018
F_{disc} (mJy)	0.009 ± 0.003	0.008 ± 0.003	0.0053 ± 0.0022	$0.0068^{+0.0022}_{-0.0025}$	0.006 ± 0.003	0.009 ± 0.004	0.012 ± 0.004	0.0065 ± 0.0028	0.014 ± 0.003	0.006 ± 0.003
F_{bs} (mJy)	$0.0106^{+0.0024}_{-0.0021}$	0.0149 ± 0.0025	$0.0090^{+0.0016}_{-0.0019}$	0.0120 ± 0.0022	0.0098 ± 0.0022	0.0146 ± 0.0028	$0.0177^{+0.0023}_{-0.0013}$	$0.0210^{+0.0021}_{-0.0017}$	$0.0214^{+0.0029}_{-0.0019}$	$0.0220^{+0.0019}_{-0.0014}$
F_2 (mJy)	0.0048 ± 0.0027	$0.0038^{+0.0028}_{-0.0023}$	$0.0024^{+0.0023}_{-0.0017}$	0.004 ± 0.003	$0.0029^{+0.0027}_{-0.0019}$	0.003 ± 0.003	$0.0075^{+0.0021}_{-0.0024}$	0.0049 ± 0.0017	0.0018 ± 0.0012	0.0064 ± 0.0018
U_1	0.326	0.312	0.376	0.363	0.441	0.423	0.327	0.381	0.436	0.370

Table C.11: *Continued.*

Model fit	**CTCV 1300** – Simultaneous individual eclipse fit					**IY UMa** – Simultaneous individual eclipse fit				
q	0.233 ± 0.004					0.148 ± 0.004				
$\Delta\phi$	0.07972 ± 0.00014					0.06460 ± 0.00008				
R_1/x_{L1}	0.0219 ± 0.0006					0.0168 ± 0.0006				
$\log h_1$	-11.10 ± 0.15					-9.18 ± 0.15				
$\log h_2$	-12.66 ± 0.20					-9.71 ± 0.24				
$\log \lambda$	-11.89 ± 0.17					-11.69 ± 0.26				
Eclipse no.	1/5	2/5	3/5	4/5	5/5	1/5	2/5	3/5	4/5	5/5
Cycle no.	0	0	34	16304	0	4468	3779	0	1	2
Band	r'	g'	g'	g'	u'	r'	g'	*KG5*	*KG5*	*KG5*
$R_{\mathrm{disc}}/x_{\mathrm{L1}}$	$0.521^{+0.010}_{-0.007}$	0.515 ± 0.007	0.507 ± 0.009	0.407 ± 0.008	$0.525^{+0.013}_{-0.010}$	0.452 ± 0.007	0.495 ± 0.007	0.434 ± 0.004	0.431 ± 0.008	0.421 ± 0.007
S/x_{L1}	0.049 ± 0.004	0.047 ± 0.004	0.042 ± 0.003	0.027 ± 0.003	0.044 ± 0.004	$0.020^{+0.015}_{-0.010}$	0.032 ± 0.014	0.010 ± 0.004	0.010 ± 0.003	0.010 ± 0.003
θ_{az}	134 ± 3	134 ± 3	121 ± 5	114 ± 4	131 ± 4	120^{+10}_{-19}	122^{+10}_{-20}	127 ± 7	122^{+10}_{-14}	118^{+11}_{-16}
f_{iso}	0.284 ± 0.017	0.239 ± 0.018	0.270 ± 0.020	0.250 ± 0.019	$0.328^{+0.025}_{-0.028}$	0.440 ± 0.025	0.241 ± 0.022	$0.237^{+0.022}_{-0.026}$	0.199 ± 0.021	0.230 ± 0.018
b	0.48 ± 0.04	0.53 ± 0.06	0.46 ± 0.05	0.49 ± 0.06	0.44 ± 0.05	1.8 ± 0.3	1.2 ± 0.5	1.1 ± 0.6	1.3 ± 0.8	1.5 ± 0.6
ϕ_0 $(\times 10^{-5})$	-2 ± 14	-7 ± 11	-36 ± 13	-47 ± 17	-6 ± 13	-55 ± 12	-55 ± 11	0 ± 9	15 ± 8	5 ± 8
Y	0.40 ± 0.08	0.35 ± 0.05	0.46 ± 0.09	0.89 ± 0.17	0.43 ± 0.07	$1.7^{+1.0}_{-0.7}$	2.5 ± 1.0	$0.42^{+0.24}_{-0.17}$	0.62 ± 0.20	$0.55^{+0.23}_{-0.19}$
Z	0.92 ± 0.05	0.96 ± 0.06	0.97 ± 0.05	1.02 ± 0.08	$1.07^{+0.11}_{-0.08}$	1.1 ± 0.3	1.4 ± 0.3	0.55 ± 0.08	0.60 ± 0.07	0.61 ± 0.07
θ_{tilt}	174.2 ± 0.9	174.2 ± 0.8	173.3 ± 1.0	170.9 ± 1.1	174.4 ± 0.8	120 ± 50	70 ± 40	70 ± 40	90 ± 40	70 ± 40
θ_{yaw}	-7.2 ± 2.4	$-8.1^{+2.9}_{-2.2}$	8 ± 4	7 ± 3	-4 ± 3	21^{+18}_{-12}	20^{+19}_{-11}	11 ± 8	18^{+14}_{-10}	28^{+15}_{-11}
F_1 (mJy)	0.0340 ± 0.0009	0.0398 ± 0.0011	0.0397 ± 0.0011	0.041 ± 0.0014	0.0234 ± 0.0009	0.157 ± 0.011	0.214 ± 0.012	0.194 ± 0.010	0.188 ± 0.009	0.192 ± 0.009
F_{disc} (mJy)	0.0337 ± 0.0019	0.0180 ± 0.0010	0.0221 ± 0.0014	0.0214 ± 0.0015	0.0186 ± 0.0011	0.101 ± 0.016	0.090 ± 0.014	0.079 ± 0.012	0.053 ± 0.013	0.056 ± 0.013
F_{bs} (mJy)	0.095 ± 0.0020	0.0887 ± 0.0021	0.0893 ± 0.0019	0.0721 ± 0.0016	$0.0585^{+0.0016}_{-0.0019}$	0.233 ± 0.009	0.305 ± 0.010	0.306 ± 0.008	0.319 ± 0.013	0.010 ± 0.003
F_2 (mJy)	0.0160 ± 0.0011	0.00293 ± 0.00027	$0.00323^{+0.00026}_{-0.00023}$	0.00330 ± 0.00022	0.00092 ± 0.00009	0.052 ± 0.009	$0.008^{+0.009}_{-0.006}$	$0.008^{+0.008}_{-0.005}$	0.013 ± 0.008	0.009 ± 0.006
U_1	0.328	0.374	0.374	0.374	0.468	0.316	0.359	0.357	0.357	0.357

Table C.11: *Continued.*

Model fit	**SDSS 0901** – Simultaneous average eclipse fit					**V713 Cep** – Simultaneous individual eclipse fit				
q	0.182 ± 0.006					$0.244^{+0.009}_{-0.012}$				
$\Delta\phi$	0.05748 ± 0.00013					0.06775 ± 0.00006				
R_1/x_{L1}	0.0224 ± 0.0008					0.0235 ± 0.0005				
$\log h_1$	-12.8 ± 0.3					-9.50 ± 0.10				
$\log h_2$	-13.4 ± 0.5					-13.1 ± 0.3				
$\log \lambda$	-9.1 ± 0.5					-11.03 ± 0.11				
Eclipse no.	1/5	2/5	3/5	4/5	5/5	1/5	2/5	3/5	4/5	5/5
Cycle no.	–	–	–	–	–	3655	11	11	3655	11
Band	r'	r'	g'	g'	u'	i'	r'	g'	g'	u'
$R_{\mathrm{disc}}/x_{\mathrm{L1}}$	0.395 ± 0.013	0.454 ± 0.007	0.396 ± 0.010	0.453 ± 0.005	0.475 ± 0.011	$0.374^{+0.014}_{-0.018}$	$0.412^{+0.014}_{-0.008}$	0.418 ± 0.010	0.389 ± 0.012	0.422 ± 0.011
S/x_{L1}	0.039 ± 0.013	$0.022^{+0.015}_{-0.011}$	0.035 ± 0.013	$0.013^{+0.008}_{-0.004}$	$0.021^{+0.016}_{-0.009}$	0.011 ± 0.004	$0.0137^{+0.0022}_{-0.0017}$	$0.0131^{+0.0019}_{-0.0016}$	$0.011^{+0.006}_{-0.003}$	$0.0125^{+0.0023}_{-0.0018}$
θ_{az}	102 ± 20	112^{+11}_{-14}	105 ± 21	112^{+11}_{-16}	122^{+14}_{-20}	122^{+22}_{-26}	127 ± 6	127 ± 6	160^{+10}_{-40}	119 ± 5
f_{iso}	0.27 ± 0.06	0.21 ± 0.07	0.26 ± 0.06	0.20 ± 0.07	0.17 ± 0.07	$0.36^{+0.29}_{-0.24}$	0.28 ± 0.11	0.29 ± 0.11	$0.46^{+0.29}_{-0.23}$	$0.11^{+0.12}_{-0.08}$
b	1.0 ± 0.6	0.6 ± 0.4	1.2 ± 0.7	1.1 ± 0.6	1.6 ± 0.5	1.5 ± 0.5	$1.46^{+0.23}_{-0.27}$	$1.32^{+0.29}_{-0.32}$	1.2 ± 0.7	2.03 ± 0.25
ϕ_0 $(\times 10^{-5})$	4 ± 17	3 ± 14	0 ± 14	0 ± 9	34 ± 24	9 ± 12	-13 ± 9	-17 ± 4	11 ± 5	-33 ± 11
Y	$2.5^{+1.0}_{-1.3}$	$1.1^{+1.0}_{-0.6}$	2.2 ± 1.2	$0.9^{+0.7}_{-0.4}$	$1.4^{+1.1}_{-0.8}$	–	–	–	–	–
Z	2.3 ± 0.6	1.1 ± 0.3	2.3 ± 0.6	$0.96^{+0.27}_{-0.16}$	$1.2^{+0.6}_{-0.3}$	–	–	–	–	–
θ_{tilt}	90 ± 40	90 ± 50	100 ± 40	80 ± 50	100 ± 50	–	–	–	–	–
θ_{yaw}	57^{+21}_{-25}	31 ± 16	50^{+23}_{-26}	32 ± 16	20^{+23}_{-18}	–	–	–	–	–
F_1 (mJy)	$0.0267^{+0.0015}_{-0.0018}$	0.0191 ± 0.0010	$0.0313^{+0.0016}_{-0.0019}$	0.0225 ± 0.0010	0.0195 ± 0.0016	0.058 ± 0.004	0.079 ± 0.003	0.1057 ± 0.0028	$0.0911^{+0.0023}_{-0.0026}$	0.071 ± 0.005
F_{disc} (mJy)	0.018 ± 0.003	0.0114 ± 0.0027	0.0131 ± 0.0023	0.0079 ± 0.0018	0.0128 ± 0.0024	0.040 ± 0.004	0.079 ± 0.005	0.048 ± 0.004	0.021 ± 0.004	0.074 ± 0.005
F_{bs} (mJy)	0.027 ± 0.004	$0.0242^{+0.0027}_{-0.0019}$	0.024 ± 0.004	$0.0236^{+0.0025}_{-0.0021}$	0.022 ± 0.003	$0.0190^{+0.0028}_{-0.0021}$	0.0371 ± 0.0022	0.0364 ± 0.0019	$0.020^{+0.006}_{-0.003}$	0.0360 ± 0.0021
F_2 (mJy)	0.0107 ± 0.0024	0.0061 ± 0.0023	0.0019 ± 0.0012	0.0012 ± 0.0008	0.0017 ± 0.0011	$0.0695^{+0.0020}_{-0.0024}$	$0.0154^{+0.0026}_{-0.0029}$	$0.0031^{+0.0022}_{-0.0019}$	0.0035 ± 0.0018	0.0070 ± 0.0023
U_1	0.301	0.301	0.340	0.340	0.428	0.284	0.329	0.380	0.380	0.444

Table C.11: *Continued.*

Model fit	**SSS130413** – Simultaneous individual eclipse fit						**CSS110113** – Simultaneous average eclipse fit		
q	0.172 ± 0.008						0.105 ± 0.005		
$\Delta\phi$	0.06031 ± 0.00019						0.02767 ± 0.00025		
R_1/x_{L1}	0.0227 ± 0.009						0.0157 ± 0.0007		
$\log h_1$	$-7.68\,^{+0.19}_{-0.16}$						$-14.5\,^{+1.3}_{-0.4}$		
$\log h_2$	-8.31 ± 0.23						-15.0 ± 1.8		
$\log \lambda$	$-11.63\,^{+0.23}_{-0.19}$						$-13\,^{+5}_{-1}$		
Eclipse no.	1/6	2/6	3/6	4/6	5/6	6/6	1/3	2/3	3/3
Cycle no.	109	108	1	2	94	11176	–	–	–
Band	r'	g'	*KG5*	*KG5*	*KG5*	u'	r'	g'	u'
$R_{\mathrm{disc}}/x_{\mathrm{L1}}$	$0.453\,^{+0.014}_{-0.011}$	$0.444\,^{+0.013}_{-0.016}$	0.474 ± 0.019	0.459 ± 0.012	$0.438\,^{+0.011}_{-0.008}$	$0.489\,^{+0.023}_{-0.020}$	0.447 ± 0.006	0.450 ± 0.005	0.445 ± 0.010
S/x_{L1}	0.047 ± 0.013	0.027 ± 0.011	0.050 ± 0.013	0.048 ± 0.013	0.044 ± 0.013	0.033 ± 0.013	$0.021\,^{+0.016}_{-0.013}$	$0.021\,^{+0.015}_{-0.011}$	0.024 ± 0.015
θ_{az}	$133\,^{+7}_{-12}$	117 ± 12	120 ± 11	$129\,^{+7}_{-10}$	129 ± 8	137 ± 17	125 ± 6	120 ± 7	$126\,^{+10}_{-17}$
f_{iso}	0.22 ± 0.04	0.32 ± 0.06	0.31 ± 0.04	0.29 ± 0.03	0.33 ± 0.04	0.11 ± 0.04	$0.253\,^{+0.023}_{-0.020}$	0.243 ± 0.019	0.25 ± 0.04
b	1.70 ± 0.24	1.81 ± 0.24	0.79 ± 0.14	0.92 ± 0.14	$0.82\,^{+0.13}_{-0.16}$	1.13 ± 0.21	0.7 ± 0.6	0.4 ± 0.4	1.0 ± 0.8
ϕ_0 $(\times 10^{-5})$	-40 ± 30	$-53\,^{+24}_{-21}$	$10\,^{+26}_{-18}$	-12 ± 19	-11 ± 22	0 ± 40	-25 ± 21	-25 ± 16	0 ± 40
Y	0.56 ± 0.19	0.57 ± 22	0.51 ± 0.24	0.5 ± 0.3	$0.63\,^{+0.25}_{-0.22}$	0.6 ± 0.3	1.2 ± 0.6	1.0 ± 0.5	$1.5\,^{+1.2}_{-0.8}$
Z	1.3 ± 0.3	$1.02\,^{+0.29}_{-0.22}$	1.34 ± 0.24	$1.32\,^{+0.27}_{-0.21}$	1.4 ± 0.3	1.1 ± 0.4	0.91 ± 0.24	0.9 ± 0.3	1.0 ± 0.3
θ_{tilt}	$145\,^{+16}_{-22}$	$145\,^{+17}_{-26}$	$145\,^{+16}_{-25}$	$146\,^{+15}_{-20}$	$140\,^{+17}_{-24}$	$151\,^{+18}_{-17}$	50 ± 30	50 ± 30	60 ± 30
θ_{yaw}	20 ± 11	6 ± 13	19 ± 11	11 ± 10	12 ± 9	5 ± 17	26 ± 9	31 ± 9	$18\,^{+18}_{-15}$
F_1 (mJy)	0.207 ± 0.020	0.259 ± 0.020	0.300 ± 0.012	0.292 ± 0.015	0.268 ± 0.015	0.299 ± 0.023	0.0189 ± 0.0009	0.0219 ± 0.0006	$0.0188\,^{+0.0015}_{-0.0020}$
F_{disc} (mJy)	0.204 ± 0.028	0.198 ± 0.023	0.106 ± 0.016	0.157 ± 0.020	$0.120\,^{+0.021}_{-0.018}$	0.257 ± 0.027	0.006 ± 0.003	$0.0031\,^{+0.0017}_{-0.0014}$	$0.0072\,^{+0.0024}_{-0.0027}$
F_{bs} (mJy)	0.43 ± 0.04	$0.29\,^{+0.018}_{-0.014}$	$0.377\,^{+0.029}_{-0.026}$	$0.398\,^{+0.027}_{-0.020}$	$0.338\,^{+0.027}_{-0.022}$	0.39 ± 0.03	0.0366 ± 0.0017	0.0333 ± 0.0016	0.0241 ± 0.0015
F_2 (mJy)	0.073 ± 0.016	0.018 ± 0.007	0.029 ± 0.007	0.019 ± 0.007	0.025 ± 0.007	0.011 ± 0.003	0.014 ± 0.004	$0.0044\,^{+0.0018}_{-0.0022}$	$0.0025\,^{+0.0025}_{-0.0017}$
U_1	0.275	0.326	0.315	0.315	0.315	0.374	0.291	0.326	0.419

Table C.11: *Continued.*

Model fit	**Z Cha** – Simultaneous individual eclipse fit						**DV UMa** – Simultaneous average eclipse fit		
q	0.189 ± 0.004						0.170 ± 0.006		
$\Delta\phi$	0.05347 ± 0.00012						0.06346 ± 0.00009		
R_1/x_{L1}	0.0215 ± 0.0005						0.0119 ± 0.0007		
$\log h_1$	-6.38 ± 0.17						-14.13 ± 0.29		
$\log h_2$	-7.44 ± 0.22						-14.2 ± 0.5		
$\log \lambda$	-12.00 ± 0.19						$-13.8\,^{+1.2}_{-0.9}$		
Eclipse no.	1/6	2/6	3/6	4/6	5/6	6/6	1/3	2/3	3/3
Cycle no.	27237	29571	27237	27518	29571	27237	–	–	–
Band	i'	r'	g'	g'	g'	u'	i'	g'	u'
$R_{\mathrm{disc}}/x_{\mathrm{L1}}$	0.412 ± 0.006	0.422 ± 0.007	0.403 ± 0.006	0.485 ± 0.006	0.419 ± 0.005	0.408 ± 0.006	0.463 ± 0.005	0.461 ± 0.003	0.461 ± 0.006
S/x_{L1}	0.0119 ± 0.0019	0.0170 ± 0.0025	0.0098 ± 0.0017	$0.0107\,^{+0.0017}_{-0.0012}$	$0.0140\,^{+0.0022}_{-0.0028}$	0.015 ± 0.003	$0.012\,^{+0.011}_{-0.004}$	0.010 ± 0.003	$0.012\,^{+0.011}_{-0.005}$
θ_{az}	127 ± 7	130 ± 5	115 ± 7	99 ± 11	131 ± 5	$113\,^{+10}_{-13}$	114 ± 7	112 ± 5	87 ± 15
f_{iso}	0.24 ± 0.04	0.185 ± 0.020	0.22 ± 0.05	$0.278\,^{+0.024}_{-0.027}$	0.165 ± 0.017	0.24 ± 0.05	0.238 ± 0.013	0.207 ± 0.006	0.178 ± 0.015
b	0.38 ± 0.03	1.72 ± 0.15	1.50 ± 0.09	2.28 ± 0.13	2.18 ± 0.13	1.43 ± 0.09	0.8 ± 0.4	1.7 ± 0.4	2.2 ± 0.3
ϕ_0 $(\times 10^{-5})$	-23 ± 20	$29\,^{+14}_{-17}$	-31 ± 14	-14 ± 12	37 ± 12	29 ± 20	-36 ± 13	-31 ± 5	-32 ± 12
Y	0.93 ± 0.19	0.92 ± 0.14	0.99 ± 0.16	0.96 ± 0.17	0.82 ± 0.10	0.56 ± 0.18	1.1 ± 0.4	0.7 ± 0.3	$1.0\,^{+0.8}_{-0.5}$
Z	0.71 ± 0.06	0.74 ± 0.05	0.74 ± 0.05	0.79 ± 0.05	0.74 ± 0.06	0.91 ± 0.11	$0.75\,^{+0.17}_{-0.09}$	0.72 ± 0.06	$0.88\,^{+0.26}_{-0.14}$
θ_{tilt}	121 ± 14	97 ± 13	140 ± 11	132 ± 13	78 ± 12	95 ± 15	110 ± 30	$101\,^{+19}_{-22}$	80 ± 30
θ_{yaw}	11 ± 7	11 ± 5	14 ± 6	37 ± 11	18 ± 4	30 ± 11	19 ± 7	24 ± 5	54 ± 16
F_1 (mJy)	0.457 ± 0.022	0.651 ± 0.028	0.748 ± 0.022	0.792 ± 0.025	0.822 ± 0.024	0.624 ± 0.025	0.0193 ± 0.0015	0.0333 ± 0.0013	0.0300 ± 0.0027
F_{disc} (mJy)	0.51 ± 0.05	0.53 ± 0.04	0.227 ± 0.023	0.175 ± 0.023	0.290 ± 0.027	0.46 ± 0.04	$0.0213\,^{+0.0023}_{-0.0020}$	0.0106 ± 0.0016	0.0171 ± 0.0029
F_{bs} (mJy)	0.91 ± 0.04	1.22 ± 0.03	1.08 ± 0.04	0.97 ± 0.03	1.30 ± 0.04	1.03 ± 0.05	0.0667 ± 0.0014	0.0790 ± 0.0011	$0.0672\,^{+0.0020}_{-0.0017}$
F_2 (mJy)	0.77 ± 0.05	0.41 ± 0.04	0.261 ± 0.022	0.285 ± 0.019	0.218 ± 0.027	0.115 ± 0.015	0.0794 ± 0.0018	0.0065 ± 0.0011	$0.0043\,^{+0.0012}_{-0.0015}$
U_1	0.279	0.330	0.391	0.391	0.391	0.433	0.183	0.248	0.341

Table C.11: *Continued.*

Model fit	**SSS100615** – Simultaneous average eclipse fit		
q	$0.094^{+0.004}_{-0.008}$		
$\Delta\phi$	0.05544 ± 0.00014		
R_1/x_{L1}	0.0208 ± 0.0011		
$\log h_1$	-13.2 ± 1.1		
$\log h_2$	-15^{+2}_{-5}		
$\log \lambda$	$-8.4^{+1.6}_{-2.3}$		
Eclipse no.	1/3	2/3	3/3
Cycle no.	–	–	–
Band	r'	g'	u'
$R_{\mathrm{disc}}/x_{\mathrm{L1}}$	$0.40^{+0.04}_{-0.01}$	$0.402^{+0.023}_{-0.012}$	$0.397^{+0.026}_{-0.022}$
S/x_{L1}	$0.023^{+0.019}_{-0.007}$	0.036 ± 0.015	$0.045^{+0.012}_{-0.019}$
θ_{az}	156^{+13}_{-6}	159^{+12}_{-22}	155 ± 15
f_{iso}	0.31 ± 0.06	0.27 ± 0.08	$0.25^{+0.13}_{-0.07}$
b	$0.6^{+0.8}_{-0.4}$	$1.0^{+1.0}_{-0.7}$	$0.7^{+0.9}_{-0.5}$
ϕ_0 ($\times 10^{-5}$)	-16 ± 9	-22 ± 7	-6 ± 21
Y	–	–	–
Z	–	–	–
θ_{tilt}	–	–	–
θ_{yaw}	–	–	–
F_1 (mJy)	0.0326 ± 0.0013	0.0392 ± 0.0013	0.0273 ± 0.0018
F_{disc} (mJy)	0.0087 ± 0.0029	0.0053 ± 0.0019	0.007 ± 0.004
F_{bs} (mJy)	0.017 ± 0.003	0.016 ± 0.004	0.017 ± 0.005
F_2 (mJy)	0.0067 ± 0.0022	0.0020 ± 0.0014	0.0051 ± 0.0027
U_1	312	349	467

Table C.11: *Continued.*

Appendix D

System Parameters for Supplementary Systems

The following table includes the system parameters for supplementary systems included in Chapter 8.

System	$P_{\rm orb}$ (d)	q	M_1 ($M_\odot$)	M_2 ($M_\odot$)	R_2 ($R_\odot$)	Method	Ref.
SDSS J1433+1011	0.054240679(2)	0.0661(7)	0.865(5)	0.0571(7)	0.1074(4)	EM(U)	1
SDSS J1507+5230	0.04625828(4)	0.0647(18)	0.892(8)	0.0575(20)	0.0969(11)	EM(U)	1
SDSS J1035+0551	0.0570067(2)	0.0571(10)	0.835(9)	0.0475(12)	0.1047(8)	EM(U)	1
CTCV J2354−4700	0.065550270(1)	0.1097(8)	0.935(31)	0.101(3)	0.1463(16)	EM(U)	1
SDSS J1152+4049*	0.0677497026(3)§	0.155(6)	0.560(28)	0.087(6)	0.142(3)	EM(U)	1
SDSS J0903+3300	0.059073543(9)	0.113(4)	0.872(11)	0.099(4)	0.1358(20)	EM(U)	1
SDSS J1227+5139	0.062959041(7)	0.1115(16)	0.796(18)	0.0889(25)	0.1365(13)	EM(U)	1
XZ Eri	0.061159491(5)	0.118(3)	0.769(17)	0.091(4)	0.1350(18)	EM(U)	1
SDSS J1502+3334	0.05890961(5)	0.1099(7)	0.709(4)	0.0781(8)	0.1241(3)	EM(U)	1
SDSS J1501+5501*	0.05684126603(21)§	0.101(10)	0.767(27)	0.077(10)	0.122(5)	EM(U)	1
CTCV J1300−3052*	0.0889406998(17)§	0.240(21)	0.736(14)	0.177(21)	0.215(8)	EM(U)	1
OU Vir	0.072706113(5)	0.1641(13)	0.703(12)	0.1157(22)	0.1634(10)	EM(U)	1
DV UMa*	0.0858526308(7)§	0.1778(22)	1.098(24)	0.196(5)	0.2176(18)	EM(U)	1
SDSS J1702+3229	0.10008209(9)	0.248(5)	0.91(3)	0.223(10)	0.252(4)	EM(U)	1
KIS J1927+4447	0.165308(5)	0.570(11)	0.69(7)	0.39(4)	0.432(15)	EM(U)	2,3
IP Peg	0.1582061029(3)	0.48(1)	1.16(2)	0.55(2)	0.466(6)	EM(U)	4
EX Dra	0.20993718(2)	0.75(5)	0.71(4)	0.53(1)	0.565(4)	EM	5
SDSS J1006+2337*	0.185913107(13)§	0.51(8)	0.78(12)	0.40(10)	0.47(4)	EM	6
CSS111003† (Te 11)	0.120971471(9)§	0.236(6)	1.18(11)	0.28(3)	0.314(11)	EM	7
HS 0220+0603†	0.14920775(8)	0.54(3)	0.87(9)	0.47(5)	0.427(15)	EM	8
1RXS J0644+3344†	0.26937431(22)	0.80(2)	0.73(7)	0.58(6)	0.690(24)	EM	9,10
SDSS J0756+0858†	0.1369745(4)	0.47(9)	0.60(12)	0.28(5)	0.338(20)	EM	11

Table D.1: System parameters for supplementary systems included in Chapter 8 (Figures 8.1–8.7). The second-to-last column indicates the method used to obtain system parameters: EM – eclipse modelling (U – using ULTRACAM/ULTRASPEC data), CPT – contact phase timing, RV – radial velocity, GR – gravitational redshift, SM – spectrophotometric modelling. For consistency, all R_2 values were calculated using equation 8.3 (ensuring all systems follow the same period-density relation). References: (1) Savoury et al. (2011), (2) Scaringi, Groot & Still (2013), (3) Littlefair et al. (2014), (4) Copperwheat et al. (2010), (5) Shafter & Holland (2003), (6) Southworth et al. (2009), (7) Miszalski et al. (2016), (8) Rodríguez-Gil et al. (2015), (9) Sing et al. (2007), (10) Hernandez et al. (2017), (11) Tovmassian et al. (2014), (12) Steeghs et al. (2003), (13) Horne, Wood & Stiening (1991), (14) Wood & Horne (1990), (15) Littlefair et al. (2008), (16) Baptista et al. (2003), (17) Borges & Baptista (2005), (18) Araujo-Betancor et al. (2003), (19) Patterson et al. (2005), (20) Baptista & Bortoletto (2008), (21) Baptista, Steiner & Cieslinski (1994), (22) Thorstensen (2000), (23) Wade & Horne (1988), (24) Echevarría et al. (2016), (25) Arnold, Berg & Duthie (1976), (26) Echevarría, de la Fuente & Costero (2007), (27) Horne, Welsh & Wade (1993), (28) Thoroughgood et al. (2005), (29) Rolfe, Haswell & Patterson (2000), (30) Rodríguez-Gil et al. (2001), (31) Peters & Thorstensen (2006), (32) Arenas et al. (2000), (33) Robinson (1974), (34) Welsh et al. (2007), (35) Thoroughgood et al. (2004), (36) Patterson (1998), (37) Steeghs et al. (2001), (38) Steeghs et al. (2007), (39) van Amerongen et al. (1987), (40) Smith, Haswell & Hynes (2006), (41) Szkody & Brownlee (1977), (42) Gänsicke et al. (2006a).

*Updated system parameters produced in this work (Table 7.1), †System parameters published post-2013 (start of this work), §$P_{\rm orb}$ from this work

System	$P_{\rm orb}$ (d)	q	M_1 ($\rm M_\odot$)	M_2 ($\rm M_\odot$)	R_2 ($\rm R_\odot$)	Method	Ref.
IY UMa*	0.07390892818(21)§	0.125(8)	0.79(4)	0.10(1)	0.158(5)	CPT	12
HT Cas	0.0736471745(5)§	0.15(3)	0.61(4)	0.09(2)	0.152(11)	CPT	13
OY Car*	0.06312092545(24)§	0.102(3)	0.84(4)	0.086(5)	0.1354(26)	CPT	14,15
V2051 Oph	0.06242785751(8)§	0.19(3)	0.78(6)	0.15(3)	0.161(11)	CPT	16
V4140 Sgr	0.0614296779(9)	0.125(15)	0.73(8)	0.092(16)	0.136(8)	CPT	16,17
DW UMa	0.136606499(3)	0.28(4)	0.73(3)	0.21(3)	0.304(14)	CPT	18,19
UU Aqr	0.1638049430	0.30(7)	0.67(14)	0.20(7)	0.34(4)	CPT	20,21
GY Cnc*	0.175442399(6)§	0.41(4)	0.82(14)	0.33(7)	0.42(3)	RV	22
Z Cha*	0.0744992631(3)§	0.149(4)	0.84(9)	0.125(14)	0.171(6)	RV	23
EX Hya†	0.068233843(1)	0.13(2)	0.78(3)	0.10(2)	0.150(10)	RV	24
U Gem	0.17690617(6)	0.35(5)	1.20(5)	0.42(4)	0.456(14)	RV	25,26
DQ Her	0.193620897	0.66(4)	0.60(7)	0.40(5)	0.485(20)	RV	27
V347 Pup	0.231936060(6)	0.83(5)	0.63(4)	0.52(6)	0.603(23)	RV	28
V348 Pup	0.101838931(14)	0.31(6)	0.65(13)	0.20(4)	0.246(16)	RV	29,30
V603 Aql	0.13820103(8)	0.24(5)	1.2(2)	0.29(4)	0.341(16)	RV	31,32
EM Cyg	0.290909(4)	0.77(4)	1.00(12)	0.77(8)	0.797(28)	RV	33,34
AC Cnc	0.30047747(4)	1.02(4)	0.76(3)	0.77(5)	0.827(18)	RV	35
V363 Aur	0.32124187(8)	1.17(7)	0.90(6)	1.06(11)	0.97(4)	RV	35
WZ Sge	0.0566878460(3)	0.057(18)	0.85(4)	0.049(15)	0.105(11)	RV,GR	36,37,38
VW Hyi	0.074271038(14)	–	0.71(22)	–	–	GR	39,40
AM Her	0.128927(2)	–	0.78(15)	–	–	SM	41,42

Table D.1: *Continued.*